

Physics Area - PhD course in
Theory and Numerical Simulation of Condensed Matter

Simulating non-equilibrium dynamics and finite temperature physics: efficient representations for matrix product states

Thesis submitted for the degree of
Doctor Philosophiae

Candidate:

Lucas Kohn

Advisor:

Giuseppe E. Santoro

Academic Year 2020-2021



Abstract

Experimental advances have made it possible to realize and control quantum many-body systems, allowing the experimental study of non-equilibrium phenomena. Due to the Hilbert space growing exponentially with the number of particles, advanced numerical techniques are usually required to understand many-body effects at the theoretical level.

In this thesis, we address the question of how to efficiently simulate the non-equilibrium dynamics of many-body systems using matrix product states (MPS). In particular, we consider quantum systems in interaction with macroscopic environments, as they appear in Anderson impurity problems, quantum thermodynamics, or open quantum systems.

We develop a low-entanglement representation of the environment with only short-range interactions, perfectly suitable for simulations with MPS. We further show that an interleaved ordering of tight-binding chains can significantly reduce the creation of entanglement, as opposed to an intuitive implementation of the Hamiltonian's geometry. Our approach allows long-time simulations and an analysis of the environmental dynamics, in which, after a sudden quench, we find clear signatures of many-body effects. We employ our techniques to compute spectral functions of impurity models, with possible applications to dynamical mean-field theory impurity solvers, and to calculate dissipation in the non-equilibrium Anderson model with explicit time-dependence, as relevant for ongoing experiments with oscillating tip atomic force microscopes.

Acknowledgements

First, I would like to thank my supervisor Giuseppe Santoro for his guidance through this PhD, his helpfulness, and the freedom to work on what interests me. Not only did I learn a lot about physics, but I believe that his suggestions also helped me to develop on a personal level. I would like to thank Erio Tosatti for including me into the ERC project. Due to this project we started to work on fermionic systems, which now make up a big part of the thesis. Further, I am very grateful to my former supervisor Simone Montangero for his support, and for bringing me into the topic of tensor networks. I remember the first time we met to discuss about the topic of the Bachelor thesis, where I just said something like 'I do not know exactly what I want to work on, but I do not want to do any programming'. Well, things have changed a little, and I couldn't be happier with the 'numerics' path I have taken. Thank you also to Uli Schollwöck and Dario Tamascelli for being the referees of my thesis.

I would like to thank all my CM colleagues at SISSA, and in particular the PhD4PMI group, who made the time in Trieste very enjoyable. I am also very grateful to all my friends in my hometown, where I am always welcome whenever I find the time to pass by. Finally, I would like to thank my family for giving me the possibility to do whatever I wanted to do in life, and for taking care of everything around me, allowing me to focus on studying whenever necessary.

The research presented in this thesis was supported by EU Horizon 2020 under ERC-ULTRADISS, Grant Agreement No. 834402.

Publications

This thesis reports — in Chap. 3, 4, and 5 — results from the following publications and preprints:

- [1] L. Kohn and G. E. Santoro, *Efficient mapping for Anderson impurity problems with matrix product states*, *Phys. Rev. B* **104**, 014303 (2021)
- [2] L. Kohn and G. E. Santoro, *Quenching the Anderson impurity model at finite temperature: Entanglement and bath dynamics using matrix product states*, [arXiv:2107.02807](https://arxiv.org/abs/2107.02807) (2021)

Still unpublished material is reported in Chap. 6 and 7. During the course of the PhD, I have further authored or contributed to the following publications, which will not be discussed in this thesis.

- [3] L. Kohn, P. Silvi, M. Gerster, M. Keck, R. Fazio, G. E. Santoro, and S. Montangero. *Superfluid-to-Mott transition in a Bose-Hubbard ring: Persistent currents and defect formation*, *Phys. Rev. A* **101**, 023617 (2020)
- [4] L. Arceci, L. Kohn, A. Russomanno, and G. E. Santoro, *Dissipation assisted Thouless pumping in the Rice–Mele model*, *JSTAT* **2020**, 043101 (2020)

Contents

1. Introduction	1
1.1. Challenges in the simulation of many-body dynamics	2
1.2. Macroscopic environments and tensor networks	3
1.2.1. Fermionic environments	5
1.2.2. Bosonic environments	8
1.3. Overview of the thesis	9
2. Matrix product states techniques	11
2.1. Graphical notation for tensors	12
2.2. Many-body states in matrix product form	13
2.3. Schmidt decomposition and entanglement entropy	18
2.4. Variational ground state search: DMRG	21
2.5. Time evolution: TDVP	26
2.6. Jordan-Wigner transformation	30
3. Anderson model and simulation techniques	33
3.1. Single impurity Anderson model	34
3.1.1. Discrete SIAM	34
3.1.2. SIAM in the continuum	36
3.2. Chain mapping I: Discretization plus Lanczos	37
3.2.1. Bath discretization	37
3.2.2. Lanczos chain mapping	42
3.3. Chain mapping II: Orthogonal Polynomials	44
3.3.1. Theory of orthogonal polynomials	44
3.3.2. Chain mapping for the Anderson impurity model	46
3.4. Example: Chain mapping at $T = 0$	49
3.5. The issue of the chain mapping	51
3.6. A fermionic thermo-field transformation	52
3.7. Thermofield chain mapping	55
3.8. Example: Chain coefficients at finite T	55
3.9. Summary and discussion of simulation techniques	56
4. Quenching the Anderson impurity model at finite temperature	59
4.1. How to order sites in the MPS	60

4.2.	Results: Impurity, bath and entanglement dynamics	61
4.2.1.	Noninteracting case $U = 0$	61
4.2.2.	Interacting case $U > 0$	67
4.3.	Conclusions	72
4.4.	Additional information	73
4.4.1.	Numerical details and parameters	73
4.4.2.	Calculating the conduction occupation density	73
4.4.3.	Starting from an occupied impurity	74
4.4.4.	TDVP beyond nearest neighbor hopping	74
4.4.5.	Convergence with Bond dimension	76
5.	Spectral functions from MPS simulations of the Anderson impurity model	77
5.1.	Green's functions	78
5.2.	$T > 0$ equilibrium state and Green's functions	79
5.3.	Main results	81
5.4.	Analysis of the equilibration scheme	83
5.4.1.	Noninteracting case $U = 0$	83
5.4.2.	Interacting case at zero temperature	86
5.4.3.	Effect of finite temperature at $U = 2.5\pi\Gamma$	87
5.4.4.	Quantitative analysis of the equilibration time τ	88
5.4.5.	Summary and discussion of the equilibration step	90
5.5.	Benchmark against Numerical Renormalization Group results	91
5.6.	Summary and conclusions	91
6.	Dissipation in the driven Anderson impurity model	93
6.1.	Model and setting of the problem	94
6.1.1.	Protocol and dissipation	94
6.1.2.	Dissipation for a sudden quench	96
6.2.	Preliminary results	97
6.2.1.	Equilibrium impurity occupation	97
6.2.2.	Dissipation	98
6.3.	Spectral functions	100
6.4.	Discussion and outlook	100
7.	Simulating non-equilibrium open quantum systems with MPS	103
7.1.	Introduction	103
7.2.	Dissipative Landau-Zener-Stückelberg interferometer	105
7.2.1.	Coherent LZS interferometer	105
7.2.2.	Dissipative LZS	106
7.3.	Methods	108
7.3.1.	Thermofield transformation	109
7.3.2.	Merging the baths	110
7.3.3.	Chain mapping	111

7.4. Results: Dissipative Stückelberg interference	113
7.4.1. Effect of the coupling operator \hat{A}	117
7.4.2. Sub- and Super-ohmic spectral functions	117
7.5. Optimal annealing velocity	118
7.6. Conclusions	119
7.7. Outlook	120
8. Conclusions	123
8.1. Future perspectives	124
A. Tensor network operations and algorithmic details	129
A.1. Reshaping	129
A.2. Singular value decomposition for tensors	130
A.3. Solving a TDVP equation	131
B. Additional details for Chapter 5	135
B.1. Parameters and numerical details	135
B.1.1. Performance dependence on bath size	136
B.1.2. Convergence with bond dimension D	137
B.2. Comparison with the star geometry	138
B.3. Linear prediction	139
B.3.1. Example: Symmetric Anderson impurity model	142
C. Additional details for Chapter 7	143
C.1. Proof that the Gibbs state is represented by the thermofield vacuum . .	143
C.2. Bloch vector and Schmidt decomposition	144
C.3. Numerical details and parameters	145

1. Introduction

Quantum mechanics is the theory describing matter and light on the atomic scale, which “*appears peculiar and mysterious to everyone*”, borrowing Feynman’s words. Even a single quantum particle can show remarkable effects that contradict our classical intuition, such as the emergence of interference fringes upon passing through a double slit. When bringing together several quantum particles, novel effects emerge, due to the interaction of individual objects. Experimental progress in the preparation, control and measurement of quantum many-body systems has made it possible to observe purely quantum phenomena, such as the superfluid to Mott phase transition in ultracold atomic gases [5]. Starting from the investigation of equilibrium physics, it is nowadays even possible to study not only equilibrium phenomena such as phase transitions, but one can also explore the non-equilibrium dynamics [6], even with explicit time-dependent driving [7]. However, dealing with many-body systems is generally a very difficult task on the theoretical side, since most models of interest cannot be solved analytically. Moreover, the exponential increase of the Hilbert space size puts strong limitations on treatments based on the exact diagonalization of Hamiltonians. Hence, more involved numerical techniques are required for the vast majority of problems, such as Quantum Monte Carlo (QMC) [8], Numerical Renormalization Group (NRG) [9] for impurity problems, Dynamical Mean Field Theory (DMFT) for strongly correlated materials [10], or variational approaches inspired by machine learning [11], to name just a few.

Particularly relevant to the present thesis is an algorithm introduced by Steven White in 1992: the density-matrix renormalization group (DMRG) [12, 13]. DMRG is currently one of the most powerful algorithms to simulate low dimensional quantum systems. The essential idea of the method is an iterative procedure, where, for a given subsystem, only the most relevant states are kept at each step. White’s key idea was to select the states to be retained as the highest-weight eigenstates of the reduced density matrix of the subsystem considered, rather than those of lowest energy: see Ref. [14] for a more detailed discussion of these issues. Nowadays, the success of DMRG is understood in the variational framework of matrix product states (MPS) — also known as *tensor trains* in the mathematics community [15] —, which can efficiently represent quantum states with sufficiently low entanglement [16, 17]. This has led to generalizations of MPS, which go under the name of “tensor networks” [18, 19], the most prominent tensor network structures being Projected Entangled Pair States (PEPS) [20–23] for 2D systems, and hierarchical networks such as tree tensor networks

(TTN) [24–27] and the multi-scale entanglement renormalization ansatz (MERA) [28].

Initially designed to deal with pure quantum states at zero temperature, even finite temperature systems can now be treated within the MPS framework, either by purification [29] or by the direct tensor network representation of the density matrix [30, 31]. Tensor networks have found widespread applications in various fields of physics, such as the study of quantum phases and transitions [32], non-equilibrium dynamics [6, 33], as impurity solver for dynamical mean field theory [34–40], or to understand the role of quantum effects in biological systems [41]. Remarkably, they have even spread out of pure physics and have found applications in quantum chemistry [42], machine learning [43–45] and even medicine [46]. A concise review of different tensor network structures, algorithms and applications can be found in Ref. [19]. Similar to the experimental developments, the field of tensor network/ DMRG has expanded into the study of real-time dynamics. Starting with the time evolving block decimation algorithm (TEBD) [47–49], there are now many techniques available to study the non-equilibrium dynamics of many-body systems [50].

1.1. Challenges in the simulation of many-body dynamics

Consider a many-body system composed of two subsystems A and B , with Hilbert space $\mathcal{H}_A \otimes \mathcal{H}_B$. The Schmidt decomposition [51][Chap.2] allows us to decompose a pure many-body state $|\psi\rangle$ as

$$|\psi\rangle = \sum_{j=1}^{\chi} \lambda_j |\phi_j^A\rangle \otimes |\phi_j^B\rangle,$$

where $\{|\phi_j^A\rangle\}$ and $\{|\phi_j^B\rangle\}$ are orthonormal states belonging to \mathcal{H}_A and \mathcal{H}_B , while λ_j are real positive numbers — the so-called Schmidt coefficients — with the normalization condition of $|\psi\rangle$ implying that $\sum_j \lambda_j^2 = 1$. Here the sum over j runs up to the a value χ — the so-called Schmidt rank — which can be shown to be smaller than the smallest of the Hilbert space dimensions of A and B , $\chi \leq \min(\dim \mathcal{H}_A, \dim \mathcal{H}_B)$. The entanglement between the two subsystems is quantified by the von Neumann entropy of the reduced density matrix $\hat{\rho}_A = \text{Tr}_B |\psi\rangle\langle\psi|$, which can be shown to be directly expressed in terms of the Schmidt coefficients as

$$S = -\text{Tr}_A \hat{\rho}_A \log \hat{\rho}_A = -\sum_{j=1}^{\chi} \lambda_j^2 \log \lambda_j^2. \quad (1.1)$$

To get an estimate of S , suppose that only the first $D < \chi$ Schmidt coefficients λ_j contribute significantly to S , while all $\lambda_{j>D}$ are small enough to be neglected. Assuming also that the Schmidt coefficients which contribute are all equal, hence $\lambda_{j \leq D}^2 \approx D^{-1}$,

one can estimate the entanglement entropy to be $S = \log(D)$. As we will see later on in more detail, D is the number of states kept in a tensor network and determines the complexity of the simulations. Consequently, the required numerical resources scale with the entanglement entropy as $D \propto e^S$: It is this exponential scaling of D that requires us to keep the entanglement as low as possible.

Ground states of low dimensional Hamiltonians with short-ranged interactions are often only slightly entangled, due to the “area-law” for the entanglement entropy [52]: the bipartite entanglement grows only with the size of the boundary separating the two subsystems, hence a constant for one-dimensional systems¹. However, in non-equilibrium dynamics, there is no fundamental law that limits the entanglement growth versus t , the simulation time, and indeed one often finds S to grow linearly with t , leading to an exponential increase of the required numerical resources. Hence, non-equilibrium simulations are often severely limited in the number of particles, the reachable time in real-time dynamics, the physical parameters such as the strength of interactions or temperature, or the explicit form of the time-dependence. For this reason, it is crucial to understand the origin of the entanglement increase, to develop strategies leading to more efficient simulations.

In general, different factors can affect the entanglement in a tensor network. For example, one can apply unitary transformations to the model to change basis, which might lead to improved connectivity or to geometries that are better suited for tensor network treatments. Furthermore, one can engineer the network structure to capture the geometry of the model or to take into account the dynamics of physical processes. Indeed, it has been recently shown that the entanglement growth in quantum transport between two baths can be significantly reduced through appropriate engineering of the tensor network structure and ordering of the sites [53]. Devising similar strategies for the systems of interest to us — impurity models in the presence of large macroscopic baths — will be one a *leitmotiv* of the present thesis.

1.2. Macroscopic environments and tensor networks

In this thesis, we deal with a special class of many-body systems: quantum systems that are coupled to macroscopic environments. The Hamiltonian describing these systems consists of three terms:

$$\hat{H} = \hat{H}_{\text{sys}} + \hat{H}_{\text{int}} + \hat{H}_{\text{bath}} , \quad (1.2)$$

as visualised in Fig. 1.1. In general, the system can range from a single particle system, such as a single fermionic mode or a two-level system, to a general many-body system that can be treated through tensor network techniques. \hat{H}_{int} models the interaction

¹On the contrary, for general quantum states the entanglement is expected to scale with the volume of the subsystem.

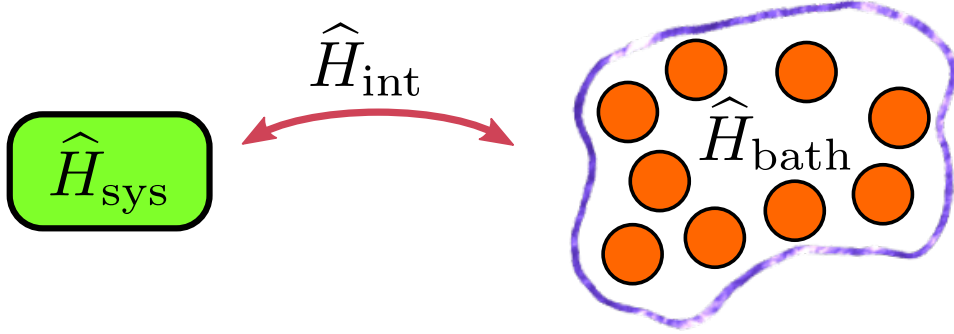


Figure 1.1.: Quantum system interacting with macroscopic environment: In this thesis we consider quantum systems built from a small system with Hamiltonian \hat{H}_{sys} , and a macroscopic environment \hat{H}_{bath} , modeled as a set of free particles. They are coupled through some interaction \hat{H}_{int} that is not required to be weak and which can exchange particles and/or energy between system and environment.

between system and environment, and depending on the model, can lead to exchange of particles or energy between the two. It is this interaction that is responsible for the creation of (quantum) correlations between system and environment. The last term, \hat{H}_{bath} , describes the environmental bath, which is often assumed to consist of noninteracting particles or modes:

$$\hat{H}_{\text{bath}} = \sum_k \epsilon_k \hat{b}_k^\dagger \hat{b}_k, \quad (1.3)$$

where \hat{b}_k can be either a bosonic or fermionic destruction operator. Correspondingly, the interaction term is often modelled as

$$\hat{H}_{\text{int}} = \sum_k \left(\hat{A}_k \otimes \hat{b}_k + \text{H.c.} \right), \quad (1.4)$$

where \hat{A}_k is a suitable system operator coupling to the bath mode \hat{b}_k . Physical examples for environmental bosons are photons or phonons, while fermions appear when describing the conduction electrons in metals. Due to the macroscopic number of bath modes, however, numerical simulations can be very challenging. Our main interest in this thesis concerns the question of how to simulate these systems efficiently when the system-environment correlations cannot be neglected and weak-coupling assumptions fail.

In general, there are different ways to represent the bath. As detailed later, one can map the bath Hamiltonian from the so-called *star geometry* into a *chain geometry*, where only a single bath mode interacts with the system [39, 54, 55]. The price to pay is that the transformed bath modes are not independent anymore: the transformation leads to nearest-neighbor couplings, as visualised in Fig. 1.2.

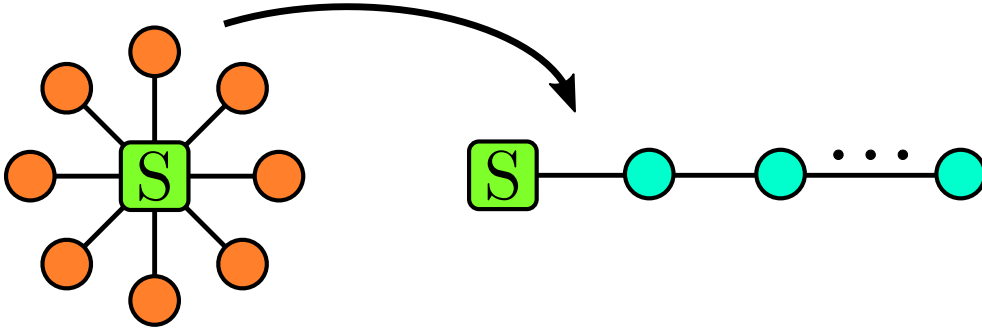


Figure 1.2.: Mapping from star to chain geometry: A set of free particles interacting with a quantum system S can be unitarily transformed into a chain with nearest-neighbor couplings, where only a single bath site interacts with the system.

1.2.1. Fermionic environments

Macroscopic fermionic environments play a major role in several areas of condensed matter physics. For instance, the Kondo effect explains the resistance minimum of metallic conductors [56, 57]. It emerges from the interaction of a localized impurity embedded in a sea of electrons and is theoretically described by the Anderson impurity model [58]

$$\hat{H} = \underbrace{\sum_{\sigma} \varepsilon_d \hat{n}_{\sigma} + U \hat{n}_{\uparrow} \hat{n}_{\downarrow}}_{\hat{H}_{\text{sys}}} + \underbrace{\sum_{k,\sigma} V_k \left(\hat{d}_{\sigma}^{\dagger} \hat{c}_{k\sigma} + \hat{c}_{k\sigma}^{\dagger} \hat{d}_{\sigma} \right)}_{\hat{H}_{\text{int}}} + \underbrace{\sum_{k,\sigma} \epsilon_k \hat{c}_{k\sigma}^{\dagger} \hat{c}_{k\sigma}}_{\hat{H}_{\text{bath}}} . \quad (1.5)$$

Here, the first term represents a local impurity, with $\hat{d}_{\sigma}^{\dagger}$ creating an electron of spin $\sigma = \uparrow, \downarrow$ in the impurity orbital, $\hat{n}_{\sigma} = \hat{d}_{\sigma}^{\dagger} \hat{d}_{\sigma}$ the number operator, and U the on-site Hubbard repulsion. The second term describes the hybridization interaction, with matrix element V_k , between the impurity orbital and a sea of conduction electrons — $\hat{c}_{k\sigma}^{\dagger}$ creating an electron with energy ϵ_k in the conduction band —, allowing electrons to hop from the impurity into the bath and vice-versa. The final term describes the bath of free electrons, with kinetic energy ϵ_k being measured with respect to the chemical potential $\mu = 0$.

The Kondo physics has been observed experimentally in a variety of situations, for instance in quantum dot systems [59, 60]. Dynamical properties and quantum transport can be studied experimentally [61, 62] and theoretically [53, 63], by employing two fermionic environments with a temperature gradient or an electric voltage between them. Theoretically, quantum transport is often studied by setting up the environments (leads) at a certain temperature and chemical potential, and connecting them to some quantum system that acts as a bridge to transport energy and/or particles. The initial state is usually set to be a separable state, and interactions between the system and the leads are abruptly turned on at $t = 0$, in a setting that is known as *quantum quench*.

One of our goals in this thesis is to efficiently simulate the non-equilibrium dynamics

after such a quantum quench. This is a two-step procedure: (i) One initializes some state at time $t < 0$, e.g. a pure state $|\psi_0\rangle$. Often, $|\psi_0\rangle$ is taken to be the ground state of the model Hamiltonian $\widehat{H}(\{\underline{h}^{\text{ini}}\})$ for a set of initial physical parameters $\{\underline{h}^{\text{ini}}\}$. (ii) These parameters are suddenly changed at $t = 0$ to some final values $\{\underline{h}^{\text{fin}}\}$. Since the initial state will generally not be an eigenstate of $\widehat{H}_{\text{fin}} \equiv \widehat{H}(\{\underline{h}^{\text{fin}}\})$, it evolves non-trivially as

$$|\psi(t)\rangle = e^{-i\widehat{H}_{\text{fin}}t/\hbar}|\psi_0\rangle .$$

Sudden quench descriptions are a valid approximation whenever the system parameters can be changed on time scales much shorter than the typical equilibration time with which the quantum state would adjust to the change. The opposite of a sudden quench is an adiabatic evolution [64], where physical parameters are changed slowly enough to keep the quantum system in equilibrium at all times.

Preparing thermal states is a delicate task for tensor network methods. In this thesis, we employ the so-called *thermofield transformation*, which allows for a very efficient and easy to prepare representation of the environmental thermal state $\rho_{\text{bath}} \propto e^{-\widehat{H}_{\text{bath}}/k_B T}$. It is based on the idea of purification, which can be best understood from the following example. Consider two spin-1/2 particles A and B in the entangled singlet state

$$|\psi\rangle = \frac{1}{\sqrt{2}}(|\uparrow_A\downarrow_B\rangle - |\downarrow_A\uparrow_B\rangle) .$$

If we trace out one of the spins, let's say B , the quantum state of spin A will be mixed with reduced density matrix $\hat{\rho}_A$,

$$\hat{\rho}_A = \text{Tr}_B |\psi\rangle\langle\psi| = \frac{1}{2}\mathbb{1} ,$$

which is the infinite temperature state. As detailed later, the thermofield transformation follows a similar idea to represent thermal states of free particles at any temperature [65, 66]. The transformation, however, leads to two independent environments that need to be simulated. As discussed above, one possibility is to map them into a chain geometry. In this thesis we show, among other things, that at finite temperatures the entanglement creation can be significantly reduced through an interleaved ordering of the chains, which allows reaching much longer simulation times.

Another key area where fermionic environments play a crucial role is the dynamical mean-field theory (DMFT) approach to strongly correlated materials. In essence, DMFT maps — by averaging out spatial fluctuations around a given site — a lattice Hamiltonian, such as a Hubbard model, into an Anderson impurity problem, which has to be solved through a self-consistency loop. The challenging part of the program is to solve the impurity model, which requires finding the single-particle Green's function. Several methods to calculate the impurity spectral function $\text{Im}G(\omega)$ — the crucial ingredient in the self-consistency DMFT loop [10] — have been developed, all of them with their pros and cons. Exact diagonalization — requiring a severe truncation of

the conduction electron degrees-of-freedom — is still one of the most popular impurity solvers for DMFT [10, 67]. Continuous-time Monte Carlo [68–70] can deal with multiple band models, but can suffer from sign problems and requires analytic continuation to the real frequency axis. The Numerical Renormalization Group (NRG) [9, 71–74] works directly on the real frequency axis and is particularly accurate at low frequencies. Recently, three orbital models have been tackled using NRG [75–78]. Finally, matrix product state (MPS) solvers based on DMRG [12] — a very accurate approach for one-dimensional systems [14, 17, 18] — work at zero temperature, both on the imaginary [34, 35] and on the real [36–40] frequency axis.

In order to get the impurity spectral function $\text{Im} G(\omega)$ at zero temperature, it is necessary to calculate the so-called *greater* Green’s function

$$iG_{\sigma}^{>}(t) = e^{iE_0 t/\hbar} \langle \psi_0 | \hat{d}_{\sigma} e^{-i\hat{H}t/\hbar} \hat{d}_{\sigma}^{\dagger} | \psi_0 \rangle ,$$

where $|\psi_0\rangle$ is the ground state, with energy E_0 . The evaluation of this expression implies a strategy similar to that of a quantum quench. It involves two steps: (i) The system needs to be prepared in its ground state $|\psi_0\rangle$, followed by the application of $\hat{d}_{\sigma}^{\dagger}$: This is analogous to the change of system parameters in a quench. (ii) The resulting state $\hat{d}_{\sigma}^{\dagger}|\psi_0\rangle$ needs to be evolved in time, and the overlap with $\langle \psi_0 | \hat{d}_{\sigma}$ computed. Hence, in practice we face very similar challenges in sudden quenches and in the calculation of Green’s functions: Tensor-network-based impurity solvers on the real-frequency axis are limited by the growth of entanglement. The best strategy known so far for the multi-orbital case is to mimic the Hamiltonian structure with the tensor network, hence, geometrically separating the baths corresponding to different orbitals [40]. To optimize the tensor network geometry in presence of multiple orbitals, one needs to understand the entanglement dynamics of the essential building block, the single impurity Anderson model. In this thesis, we show that a separation of filled and empty electron modes, followed by a chain mapping, can reduce the entanglement as compared to previous attempts. This method immediately generalizes to the thermofield approach for finite temperatures.

Turning to finite temperature, the calculation of the Green’s function requires now

$$iG_{\sigma}^{>}(t) = \text{Tr} \left(e^{i\hat{H}t/\hbar} \hat{d}_{\sigma} e^{-i\hat{H}t/\hbar} \hat{d}_{\sigma}^{\dagger} \hat{\rho} \right) .$$

The crucial point to notice here is that we need to initialize the system in its thermal state at some temperature T , $\hat{\rho} \propto e^{-\hat{H}/k_B T}$. As mentioned above, we will employ a thermofield transformation to deal with $T > 0$. However, this approach has one bottleneck for our application: It only allows to prepare the bath of free electrons in the thermal state, but not the thermal state of the full model including the localized system \hat{H}_{sys} and the interaction \hat{H}_{int} . We show that this problem can be solved by a conceptually very simple idea: We can turn on the interaction between the localized system and the thermal environment at time $t = 0$, and let them equilibrate for a while. The state in the long-time limit can then be used as the thermal state: We

show that this approach yields quantitatively correct spectral functions. Notice that this approach should not be confused with the thermalization of closed quantum many-body systems [79–83], where observables after a quench are found to behave as in thermal equilibrium: In this case, there is no actual thermal bath, but the system rather can be seen to act as its own environment in the thermodynamic limit, and hence the resulting effective temperature depends on the initial state. In our scenario, instead, a certain temperature is directly enforced through the thermal bath.

1.2.2. Bosonic environments

Bosonic environments appear in a variety of physical systems. The most widespread application is to open quantum systems [84–86]: The dynamics of any real quantum system is unavoidably affected by its environment, as perfect isolation is never possible. Even though dissipation might turn out beneficial in certain scenarios [4, 87, 88], in most cases the coupling to the environment is undesirable, and poses a great challenge in experimental setups, slowing down progress in fields such as quantum information processing and quantum simulation [89–91]. Hence, it is key to understand the underlying detrimental effects and physical processes, to develop strategies to reduce their negative impact.

On the theoretical side, it is challenging to model and simulate thermal baths, which are often modelled as a set of quantum harmonic oscillators [92], due to their macroscopic number of degrees of freedom. The minimal model in this context is the *spin-boson model* [93]. The spin-boson model describes a single two-level system coupled to a thermal bath. The total Hamiltonian has the form of Eq. (1.2), where the system Hamiltonian is

$$\hat{H}_{\text{sys}} = \frac{h}{2}\hat{\sigma}^z + \frac{\Delta}{2}\hat{\sigma}^x, \quad (1.6)$$

with $\hat{\sigma}^{x,y,z}$ the usual Pauli matrices. The eigenstates of $\hat{\sigma}^z$ can be thought of as two macroscopic states, with energy difference h , coupled by a tunnelling term Δ . The bath Hamiltonian is as in Eq. (1.3), with \hat{b}_k the destruction operator of a set of harmonic oscillators with energy $\epsilon_k = \hbar\omega_k$. The interaction is modelled by Eq. (1.4), with $\hat{A}_k = \alpha_k\hat{\sigma}^z$, α_k being a coupling constant between the system operator $\hat{\sigma}^z$ and the harmonic oscillators [93, 94]. ²

Often, it proves convenient to approximate the dynamics by taking into account the effects of the environment only approximately. For instance, the assumption of weak system-bath coupling allows for theoretical simplifications, including Markov and/or Born approximations, which require that system-bath correlations can be neglected [84, 85]. As a result, the quantum system is described by a density matrix,

²Notice that the coupling along $\hat{\sigma}^z$ is general enough: if we had another operator, we simply could apply a unitary transformation to go back to Eq. (1.6) with a proper change of h and Δ .

whose non-unitary dynamics is governed by a so-called Master equation, containing terms to mimic the environmental effects. The most prominent examples are the Bloch-Redfield and Lindblad master equations [95, 96]. However, the weak coupling assumption poses severe limitations on the physical systems that can be studied, as non-Markovian effects play an important role in many areas of physics [97], such as quantum thermodynamics [98, 99] or electronic transport in biological systems [41, 100, 101]. Recently, an experimental device based on a superconducting artificial atom has been realized, which is strongly coupled to an electromagnetic continuum [102], thereby realizing the famous spin-boson model [86, 93]. Any kind of weak coupling assumption would fail in describing this system.

In these scenarios, more involved techniques are needed [103], such as hierarchical equations of motion [104, 105] or the quasi-adiabatic propagator path integral [106, 107]. In this thesis, we explore the possibility to carry out non-equilibrium simulations with explicit time dependence using MPS, which is relevant for already realized experimental systems [7]. In particular, we consider a two-level system described by the Hamiltonian in Eq. (1.6) with explicitly time-dependent $\hat{\sigma}_z$ coupling, $h \rightarrow h(t)$, as it has been realized experimentally [7]. As a pedagogical example, we study the dynamics of a dissipative Stückelberg interferometer [108], where $h(t)$ is driven linearly back and forth. This driving leads to avoided crossings in the eigen-energies when $h(t) = 0$, and interference is observed as a consequence of different phase accumulation of ground and excited state in between avoided crossings.

To carry out numerical simulations, we employ a technique recently developed by Tamascelli *et al.* [109], which shares several aspects with the method we use in the fermionic case. It allows us to simulate exactly the dynamics of system and bath, and hence does not contain any fundamental limitations regarding coupling strength α_k in the system-bath interaction, the bath temperature, or the time-dependence $h(t)$ of the quantum system. This is particularly important when approaching new physical regimes, where system-bath correlations play a major role. We further demonstrate the capabilities of the method through simulations in the strong-coupling regime, with periodic sinusoidal driving $h(t)$ as employed in Ref. [7].

1.3. Overview of the thesis

We start this thesis with an introduction, in Chapter 2, to matrix product states (MPS), since the MPS representation of quantum many-body states will be employed throughout the entire thesis. In particular, we show how any many-body state can be written as an MPS, and we explain why and when this representation is efficient. The remainder of the chapter is devoted to two major MPS algorithms, the density matrix renormalization group algorithm for the calculation of ground states, and the time-dependent variational principle to carry our real-time evolution.

In Chapter 3 we introduce the single impurity Anderson model (SIAM) and we discuss various simulation techniques suitable for treatment with MPS. More in detail, we show how the star-like Hamiltonian can be mapped into a chain, which is a well-known transformation regularly employed for numerical simulations. Additionally, we introduce a novel low entanglement transformation, combining the advantages of star and chain geometry. To expand this technique towards finite temperatures, we employ the so-called thermofield transformation, to represent finite temperature density matrices as pure states.

Chapter 4 analyzes the dynamics of the entanglement in the MPS after a quantum quench in the finite temperature SIAM, employing the techniques of Chapter 3. We pay special attention to the ordering of the MPS and show that an interleaved geometry — combining the two chains emerging from the thermofield transformation — significantly reduces the entanglement growth at finite temperature as compared to an intuitive implementation, allowing for longer and more efficient simulations. We further study the dynamics of the free fermion bath, which reveals clear signatures of the Kondo effect in the quench dynamics.

As a second application, we show that the technique can be employed to efficiently compute finite temperature spectral functions in Chapter 5. Importantly, we provide evidence that our chain mapping leads to lower entanglement as compared to previously applied techniques at zero temperature, which is particularly relevant for applications as impurity solvers for dynamical mean-field theory.

Chapter 6 is devoted to the issue of dissipation in the driven SIAM. The periodic time-dependent driving of the impurity leads to an absorption of energy — also called dissipation — which is transported from the impurity into the macroscopic bath. Such a process is relevant for ongoing experiments with atomic force microscopes, where the contribution of the Kondo effect to dissipation is investigated. We discuss the general mechanism of dissipation from a theoretical point of view and present preliminary results for the case where the impurity energy level is affected by external driving.

In Chapter 7 we consider the case of a bosonic environment. This is particularly relevant in the context of open quantum systems, to take into account effects caused by the presence of an environment. We recapitulate the methods used to simulate the bosonic bath, and apply them to the problem of a dissipative quantum interferometer, exploring the method's applicability to time-dependent problems. We show that interference effects decay rapidly as dissipation is turned on, but can be partially restored upon tweaking the annealing velocity.

We conclude the thesis in Chapter 8 with a summary of the work, open questions, and a discussion of ideas for future research.

2. Matrix product states techniques

Tensor networks (TN) are a class of variational *Ansätze*, designed to efficiently represent quantum many-body states with low entanglement. Out of this class, matrix product states (MPS) are the simplest and most popular TN, with tensors ordered in a chain geometry, which is particularly suitable to deal with one-dimensional systems. The natural extension of MPS to two dimensions are projected entangled pair states (PEPS) [20, 21] and iPEPS [22] — for systems which are finite or in the thermodynamic limit, respectively —, with tensors arranged on a 2D (square) lattice and connections (bond links) to nearest neighbors. This arrangement shows a favorable scaling for the entanglement entropy, but the optimization of the tensors and the calculation of observables turns out to be rather challenging [23]. Tree tensor networks (TTN) are hierarchical networks without loops, and can therefore be evaluated and optimized efficiently [24]. TTN have proven useful in dealing with 1D systems with periodic boundary conditions [25] and 2D systems [26, 27]. Lastly, the multi-scale entanglement renormalization ansatz (MERA) is essentially a TTN with additional unitary tensors — known as disentanglers — to reduce short-range entanglement. MERA has proven particularly useful in the study of many-body systems at quantum criticality [28].

In this thesis, we restrict ourselves to MPS, since the systems of interest are all quasi-one-dimensional. In general, there are two major tasks where MPS are employed: (i) equilibrium calculations, where the goal is to determine the ground state of a given quantum system; (ii) out-of-equilibrium calculations, where the task is to follow the Schrödinger dynamics of a given model Hamiltonian. Regarding equilibrium simulations — task (i) —, MPS for systems with open boundary conditions can be efficiently optimized through the DMRG algorithm [12, 13], a major advantage of MPS as compared to more complex TN structures such as PEPS. On the other hand, many algorithms have been developed over the last years to deal with the time evolution of MPS — task (ii) —, all of them with their own pros and cons. An extensive review with examples and comparisons can be found in Ref. [50]. Here, we only provide a short overview of several important methods and their basic idea.

One of the most used time-evolution techniques is the time-evolving block decimation (TEBD) [47–49], which is particularly useful for short-ranged Hamiltonians. It relies on a Trotter splitting of the time-evolution operator [110, 111]. In each evolution step, the application of two-site gates to the MPS is followed by a subsequent truncation using a Singular Value Decomposition (SVD), in order to retain the MPS structure and limit its dimension.

Similar to the idea of TEBD, the $W^{I,II}$ -method approximates the time-evolution operator \hat{U} [112]. It exploits the matrix product operator (MPO) format of the Hamiltonian to represent \hat{U} as an MPO as well. The time-evolution operator can then be applied to the MPS, to evolve the quantum state. The major advantage of this method as compared to TEBD is its applicability to long-ranged systems. As an alternative, one can directly approximate the application of the time-evolution operator on the state to find the time evolved MPS. In this approach, \hat{U} is not constructed explicitly. For example, this can be done using Krylov subspace techniques [113, 114], with a method known as global Krylov algorithm [50]. While it can be computationally expensive, it also allows for long-range interactions. In this thesis we employ the time-dependent variational principle (TDVP) [115–117] technique — to be discussed in more detail below —, as it has proven to be highly efficient and accurate [50], and can deal with long-range interaction.

The purpose of this chapter is to provide an introduction to MPS, with detailed explanations on how and why MPS algorithms work. The chapter is structured as follows. In the first section, we introduce the graphical notation for tensors and tensor networks, totally equivalent to mathematical equations, but significantly easier to read and understand. In Section 2.2 we show how any quantum many-body state can be represented in MPS form. This procedure is very instructive to understand the connection of a quantum state with its MPS representation and will provide a first introduction to the tensor operations carried out in TN algorithms. The Schmidt decomposition [51][Chap.2] of a quantum state, discussed in Section 2.3, is one of the essential keys to understand the success of TN techniques. We show how any many-body state can be decomposed using a singular value decomposition (SVD), and we relate the result to the entanglement entropy of the corresponding bipartition and the MPS representation. In Section 2.4 and Section 2.5 we provide details on the two MPS algorithms most relevant for this thesis, namely DMRG for ground-state search and TDVP for time evolution. In the final section, we discuss the Jordan-Wigner transformation as a method to deal with fermionic particles.

2.1. Graphical notation for tensors

In the field of TN it is common to represent tensor objects and networks using a graphical notation. The graphical representation has a one-to-one correspondence to mathematical equations but is usually much simpler to read. Before discussing any of the TN basics, let us introduce this notation. A tensor is represented by a geometric object like a circle, rectangle, square, or triangle. In this thesis, we will use squares/rectangles with round corners for general tensors, and triangles for tensors with additional orthogonality properties, as discussed later on. Each tensor has a certain number of indices r , which is called the *rank of the tensor*. For each of the indices, we attach a line (or "leg") to the tensor symbol, as visualized in Fig. 2.1(a) for a

$$\begin{aligned}
 \text{a)} \quad A_{i_1} &= \boxed{A} \downarrow_{i_1} & B_{k_1, k_2, k_3} &= \begin{array}{c} \boxed{B} \\ \downarrow_{k_2} \\ \text{---}_{k_1} \quad \text{---}_{k_3} \end{array} \\
 \text{b)} \quad \sum_j A_j C_j &= \boxed{A} \text{---}_j \boxed{C} & \sum_{k_3} B_{k_1, k_2, k_3} D_{k_3, l} &= \begin{array}{c} \boxed{B} \text{---}_{k_3} \boxed{D} \\ \downarrow_{k_2} \quad \downarrow_l \\ \text{---}_{k_1} \end{array}
 \end{aligned}$$

Figure 2.1.: Graphical notation for tensors and tensor contractions. a) Graphical representation of a rank-1 tensor A (vector) and a rank-3 tensor B , with elements A_{i_1} and B_{k_1, k_2, k_3} , respectively. b) Contraction of two rank-1 tensors A and C (scalar product), and contraction of a rank-3 tensor B and a rank-2 tensor D . In the contraction we sum over the connected indices, while open legs represent indices of the new tensor after contraction.

rank-1 and a rank-3 tensor. One of the most important tensor operations is the so-called *contraction*, which is basically a generalization of scalar products, matrix-vector products, or matrix-matrix products. In the graphical convention, we sum over all internal indices (legs) that are connected to two (contracted) tensors. For instance, the left-hand side of Fig. 2.1(b) corresponds to a vector-vector product, where we sum over the common index of the two vectors. Since there are no external (or “open”) legs, the result is just a scalar. On the right-hand side of Fig. 2.1(b) we visualize the contraction of a rank-3 with a rank-2 tensor: They have one internal leg which is summed over. The result will be a rank-3 tensor, where the indices correspond to the open legs of the two original tensors.

2.2. Many-body states in matrix product form

In this section, we discuss how to obtain the MPS representation for any arbitrary quantum many-body state, following Ref. [17]. The procedure is purely theoretical and never carried out in practice, as it is highly inefficient. It is, however, very instructive and helps understanding basic ideas and operations used in TN-based algorithms.

Let us consider a many-body system with L sites, each with a Hilbert space of local dimension d . Let $\{|i\rangle, i = 1 \cdots d\}$ be a local orthonormal basis of states. For example, $d = 2$ for spin-1/2 particles, and the local basis states might be taken to be eigenstates of $\hat{\sigma}^z$: $\{|\uparrow\rangle, |\downarrow\rangle\}$. Any quantum state can be written in the form

$$|\psi\rangle = \sum_{i_1, \dots, i_L=1}^d C_{i_1, \dots, i_L} |i_1, \dots, i_L\rangle, \quad (2.1)$$

with coefficient tensor C_{i_1, \dots, i_L} — a rank- L tensor — and L -site many-body product states $|i_1, \dots, i_L\rangle = |i_1\rangle \otimes \cdots \otimes |i_L\rangle$. Notice that the number of elements of C scales exponentially with L , limiting an exact treatment of many-body systems to small system sizes. A matrix product state is a specific way to represent the coefficient tensor

C , which can be very efficient if the state has sufficiently low bipartite entanglement. Before discussing how an MPS is obtained from a general many-body state, let us introduce the singular value decomposition (SVD) [51][Chap.2], which will play a major role in the following.

i **Singular value decomposition.** The SVD is a matrix decomposition that can be carried out for any arbitrary complex $m \times n$ matrix. For $A \in \mathbb{C}^{m,n}$ it is given by

$$A = UDV^\dagger, \quad (2.2)$$

which is equivalent to the element-wise notation

$$A_{i,j} = \sum_{k,l} U_{i,k} D_{k,l} V_{l,j}^\dagger, \quad (2.3)$$

with $U \in \mathbb{C}^{m,m}$ and $V^\dagger \in \mathbb{C}^{n,n}$ unitary, and $D \in \mathbb{R}^{m,n}$ diagonal with positive ordered elements, called singular values, $\sigma_1 \geq \sigma_2 \geq \dots \geq \sigma_{\min(m,n)}$. In practice, the SVD can be carried out using well-established numerical routines (LAPACK).

Starting from the coefficient tensor C , its MPS representation is obtained by carrying out the following steps:

- (i) We reshape C into a matrix, see Appendix A.1 for details, with indices i_1 and joint index (i_2, \dots, i_L) , and carry out an SVD of the corresponding matrix $C_{i_1, (i_2, \dots, i_L)}$. More details on the SVD of tensors, together with examples, are presented in Appendix A.2. The tensor C is hence decomposed as

$$C_{i_1, \dots, i_L} = \sum_{k_1, j} A_{i_1, k_1}^{(1)} D_{k_1, j}^{(1)} \tilde{B}_{j, i_2, \dots, i_L}^{(1)}. \quad (2.4)$$

Note that the matrices $A^{(1)}$ and $\tilde{B}^{(1)}$ as obtained from the SVD are unitary, while $D^{(1)}$ is diagonal, with positive real elements. The decomposition is graphically shown in Fig. 2.2(a,b). The big rectangle in Fig. 2.2(a) represents the coefficient tensor C , while Fig. 2.2(b) visualises the right hand side of Eq. (2.4): The tensor $A^{(1)}$ has two legs, representing the physical index i_1 and the so-called bond-index or bond-link k_1 . The diagonal tensor $D^{(1)}$ has two bond-indices k_1 and j , and no physical index. Last, $\tilde{B}^{(1)}$ has a single bond-index j and all remaining physical indices i_2, \dots, i_L .

- (ii) In the next step we carry out the sum over j explicitly and define the tensor $B_{k_1, i_2, \dots, i_L}^{(1)} = \sum_j D_{k_1, j}^{(1)} \tilde{B}_{j, i_2, \dots, i_L}^{(1)}$. We say that $D^{(1)}$ is contracted into $\tilde{B}^{(1)}$. Then the coefficients C are given by the expression

$$C_{i_1, \dots, i_L} = \sum_{k_1} A_{i_1, k_1}^{(1)} B_{k_1, i_2, \dots, i_L}^{(1)}, \quad (2.5)$$

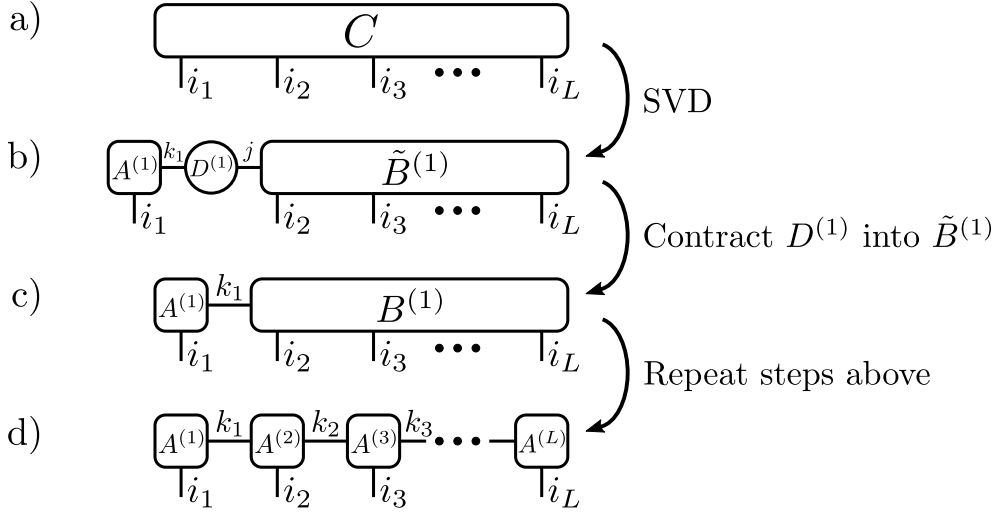


Figure 2.2.: Representing many-body states in MPS form. a) The tensor C with physical indices i_1, \dots, i_L encodes the many-body state of a quantum system with L particles or sites (see Eq. (2.1)). (a→b) After reshaping the tensor C into a matrix with indices i_1 and joint index (i_2, \dots, i_L) we decompose it via SVD, see Eq. (2.4). (b→c) We contract the diagonal tensor $D^{(1)}$ into $\tilde{B}^{(1)}$ to obtain $B^{(1)}$. (c→d) Starting from $B^{(1)}$ the procedure is repeated until we arrive at the MPS form of the state, where each tensor has just a single physical index.

as visualised in Fig. 2.2(c).

(iii) From here on, the procedure is simply repeated, and in each step, a physical index is taken out from the big tensor on the right. However, note that for the next SVD we need to reshape $B^{(1)}$ into a matrix with joint indices (k_1, i_2) and (i_3, \dots, i_L) . In contrast to the previous step, where the column index was just i_1 , it now contains a bond-index as well, in order to connect to the previous tensor. The left matrix obtained from the SVD is then reshaped into a three-leg tensor $A^{(2)}$ and is the second tensor in the MPS. After repeated applications of the SVD and consecutive contraction of the singular values to the right, we end up with the matrix product state

$$C_{i_1, \dots, i_L} = \sum_{k_1, \dots, k_{L-1}} A_{i_1, k_1}^{(1)} A_{k_1, i_2, k_2}^{(2)} A_{k_2, i_3, k_3}^{(3)} \cdots A_{k_{L-1}, i_L}^{(L)}, \quad (2.6)$$

graphically illustrated in Fig. 2.2(d).

Gauge freedom. While any MPS uniquely represents a quantum state, individual tensors $A^{(1)}, \dots, A^{(L)}$ are not unique. Consider for instance the tensor $A^{(2)}$ with physical index i_2 and bond indices k_1 and k_2 , visualised in Fig. 2.3. We could reshape the tensor into a matrix with indices k_1 and joint index (i_2, k_2) , and carry out an SVD, such that

$$A_{k_1, i_2, k_2}^{(2)} = \sum_{l, m} U_{k_1, l} D_{l, m} V_{m, i_2, k_2}^\dagger.$$

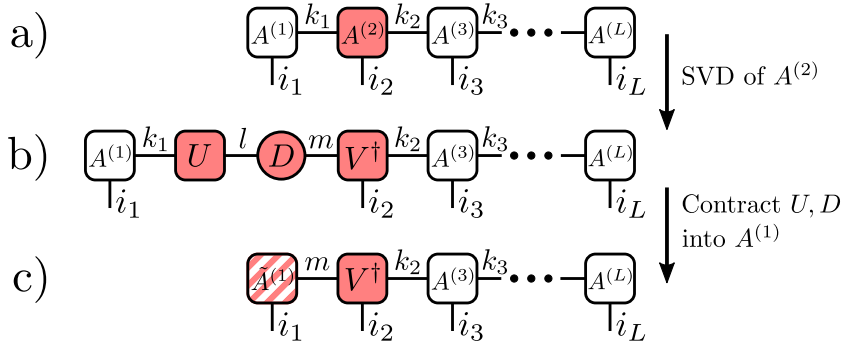


Figure 2.3.: Gauge freedom in MPS. a) Arbitrary MPS representing a quantum state. (a→b) Perform SVD of $A^{(2)} = UDV^\dagger$ and insert the decomposition into the MPS. (b→c) Contract U, D into $A^{(1)}$, to get the new tensor $\tilde{A}^{(1)}$. The quantum state is identical to the initial one, but tensors $A^{(1)} \rightarrow \tilde{A}^{(1)}$ and $A^{(2)} \rightarrow V^\dagger$ have been modified.

Now it is possible to replace $A^{(2)}$ in the MPS by this decomposition, Fig. 2.3(b), and we can contract the tensors U and D into the neighboring tensor $A^{(1)}$, see Fig. 2.3(c). The quantum state represented by the MPS is still the same, however, the tensors have changed. This gauge freedom is very important for the DMRG and TDVP algorithms presented later on. For this reason, we discuss here the most important choices for the MPS gauge.

In the so-called *left-canonical gauge* all tensors $A^{(m)}$ with corresponding physical indices i_m — except for the last one with physical index i_L — satisfy the left-orthogonality condition

$$\text{Left-orthogonality condition: } \sum_{k_{m-1}, i_m} A_{k_{m-1}, i_m, k_m}^{(m)} \left(A_{k_{m-1}, i_m, k'_m}^{(m)} \right)^* = \delta_{k_m, k'_m}. \quad (2.7)$$

Notice that the first tensor $A^{(1)}$ only has two indices and no left bond index k_{m-1} . In graphical notation, left-orthogonal tensors are drawn as a triangle pointing to the right, as visualized in Fig. 2.4. Hence, an MPS in left-canonical gauge (see Fig. 2.5(a)) is represented by a chain of tensors pointing towards the last one, which does not satisfy any orthogonality condition.

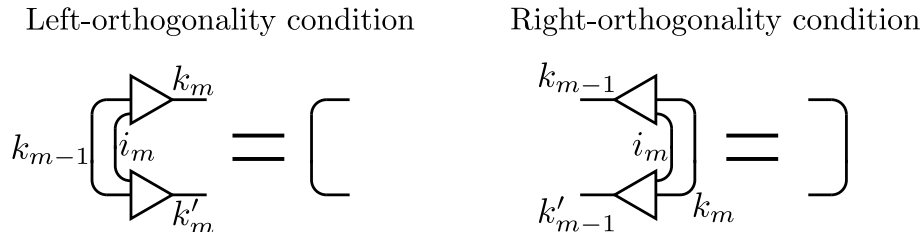


Figure 2.4.: Orthogonality conditions. Graphical representation of the left and right orthogonality conditions, Eq. (2.7) and Eq. (2.8). Left (right) orthogonal tensors are represented as triangles pointing to the right (left). When a tensor is contracted with its conjugate over the "incoming" legs, it results in an identity, represented by a line.

i

Practical remark. The procedure described above to build an MPS from the coefficient tensor C yields an MPS in the left-canonical gauge since all but the last tensor are given by unitary matrices as obtained from the SVD. In practical applications, it is often necessary to bring an MPS into (left-) canonical form. This can be achieved in the following way: Starting from the leftmost tensor, one carries out consecutive SVDs (or alternatively QR-decompositions for improved efficiency), where after each decomposition the left SVD-tensor U replaces the decomposed tensor, while singular values D and right tensor V^\dagger are contracted into the next tensor. The kept tensor U comes from an SVD, hence it is unitary and satisfies Eq. (2.7).

The so-called *right-canonical gauge*, on the other hand, is basically the opposite. Here, all tensors but the first (physical index i_1) satisfy the right-orthogonality condition, Fig. 2.4,

$$\text{Right-orthogonality condition: } \sum_{i_m, k_m} A_{k_{m-1}, i_m, k_m}^{(m)} \left(A_{k'_{m-1}, i_m, k_m}^{(m)} \right)^* = \delta_{k_{m-1}, k'_{m-1}}. \quad (2.8)$$

Graphically, right-orthogonal tensors are represented as triangles pointing to the left, and hence an MPS in right-canonical gauge points towards the first tensor, see Fig. 2.5(b). Similar to the left-orthogonal MPS, we can obtain a right orthogonal MPS through consecutive applications of the SVD: Starting from the rightmost tensor, the tensor containing the singular values is always contracted to the left.

Finally, the mixed-canonical gauge is a combination of left- and right-canonical gauge, and has a well-defined center tensor $A^{(m)}$ with physical index i_m , also called *orthogonality center* in the following. Here, all tensors on the left of the orthogonality center ($A^{(1)}, \dots, A^{(m-1)}$) are left-orthogonal, while tensors on the right ($A^{(m+1)}, \dots, A^{(L)}$) are right orthogonal. An MPS in mixed canonical form is written as

$$\begin{aligned} |\psi\rangle &= \sum_{\substack{i_1, \dots, i_L \\ k_1, \dots, k_{L-1}}} A_{i_1, k_1}^{(1)} A_{k_1, i_2, k_2}^{(2)} \dots A_{k_{L-1}, i_L}^{(L)} |i_1, i_2, \dots, i_L\rangle \\ &= \sum_{k_{m-1}, i_m, k_m} A_{k_{m-1}, i_m, k_m}^{(m)} |\phi_{k_{m-1}}^{(A)}\rangle |i_m\rangle |\phi_{k_m}^{(B)}\rangle, \end{aligned} \quad (2.9)$$

where $|\phi_{k_{m-1}}^{(A)}\rangle$ and $|\phi_{k_m}^{(B)}\rangle$ are sets of orthonormal states for the corresponding region of the MPS, and are defined as

$$|\phi_{k_{m-1}}^{(A)}\rangle = \sum_{\substack{i_1, \dots, i_{m-1} \\ k_1, \dots, k_{m-2}}} A_{i_1, k_1}^{(1)} \dots A_{k_{m-2}, i_{m-1}, k_{m-1}}^{(m-1)} |i_1, \dots, i_{m-1}\rangle \quad (2.10)$$

$$|\phi_{k_m}^{(B)}\rangle = \sum_{\substack{i_{m+1}, \dots, i_L \\ k_{m+1}, \dots, k_{L-1}}} A_{k_m, i_{m+1}, k_{m+1}}^{(m+1)} \dots A_{i_L, k_{L-1}}^{(L)} |i_{m+1}, \dots, i_L\rangle. \quad (2.11)$$

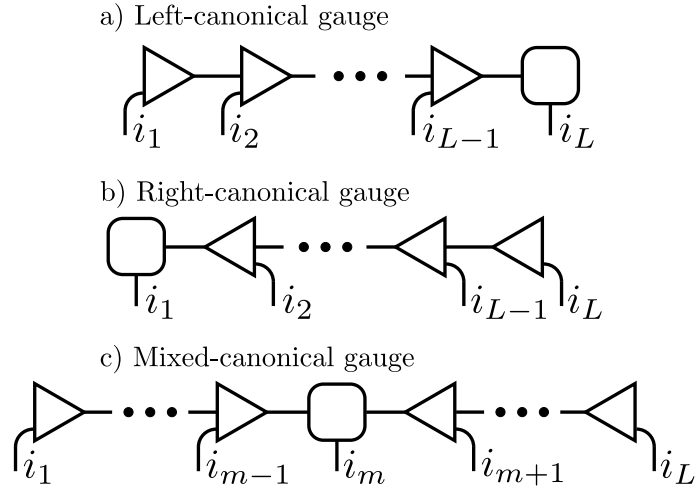


Figure 2.5.: Canonical MPS gauges. a) In the left-canonical gauge all tensors but the rightmost (physical index i_L) satisfy the left-orthogonality condition Eq. (2.7). b) In the right-canonical gauge all tensors but the leftmost (physical index i_1) satisfy the right-orthogonality condition Eq. (2.8). c) MPS in mixed-canonical gauge with respect to the tensor with physical index i_m . Tensors on the left are left-orthogonal, while tensors on the right are right-orthogonal.

Notice that $|\phi_{k_{m-1}}^{(A)}\rangle$ and $|\phi_{k_m}^{(B)}\rangle$ are orthonormal sets of states: this follows easily from the fact that they are constructed from left- and right-orthogonal tensors, respectively. In the graphical notation, all tensors of a mixed canonical MPS point towards the orthogonality center, see Fig. 2.5(c). The mixed-canonical gauge is obtained from any MPS through consecutive applications of SVDs, starting from the first and last tensor independently until reaching the required tensor $A^{(m)}$.

As mentioned before, the canonical gauges can represent the same quantum state with different tensors in the MPS, with specific features that make them more suited for certain operations.

2.3. Schmidt decomposition and entanglement entropy

We have seen previously that any quantum many-body state can be written as an MPS. However, MPS provide an efficient representation for a certain class of states only, as we discuss in this section. The Schmidt-decomposition separates a many-body system into two subsystems, which we label with A and B . Let the full Hilbert space be $\mathcal{H} = \mathcal{H}_A \otimes \mathcal{H}_B$. For a pure quantum state $|\psi\rangle \in \mathcal{H}$ it reads

$$|\psi\rangle = \sum_j \lambda_j |\phi_j^A\rangle \otimes |\phi_j^B\rangle, \quad (2.12)$$

where $\{|\phi_j^A\rangle\}$ and $\{|\phi_j^B\rangle\}$ are orthonormal bases for \mathcal{H}_A and \mathcal{H}_B , respectively, and $\sum_j \lambda_j^2 = 1$. The last relation ensures the correct normalization of $|\psi\rangle$. Such a de-

composition can always be obtained from the full coefficient tensor C in Eq. (2.1) by an appropriate application of the SVD. For instance, consider two subsystems with physical indices i_1, \dots, i_m and i_{m+1}, \dots, i_L . The SVD on the coefficient tensor with appropriately joint indices is

$$C_{(i_1, \dots, i_m), (i_{m+1}, \dots, i_L)} = \sum_j U_{(i_1, \dots, i_m), j} \lambda_j V_{j, (i_{m+1}, \dots, i_L)}^\dagger,$$

and hence Eq. (2.1) becomes

$$|\psi\rangle = \sum_j \lambda_j \sum_{i_1, \dots, i_L} U_{i_1, \dots, i_m, j} V_{j, i_{m+1}, \dots, i_L}^\dagger |i_1, \dots, i_m\rangle \otimes |i_{m+1}, \dots, i_L\rangle. \quad (2.13)$$

Comparing with Eq. (2.12) we identify $|\phi_j^A\rangle = \sum_{i_1, \dots, i_m} U_{i_1, \dots, i_m, j} |i_1, \dots, i_m\rangle$ and $|\phi_j^B\rangle = \sum_{i_{m+1}, \dots, i_L} V_{j, i_{m+1}, \dots, i_L}^\dagger |i_{m+1}, \dots, i_L\rangle$. Note that these states are orthonormal by construction, as U and V^\dagger result from the SVD, and are therefore unitary.

The entanglement entropy S quantifies the entanglement of pure quantum states $|\psi\rangle$ between subsystems A and B . In terms of the corresponding reduced density matrices $\hat{\rho}_A = \text{Tr}_B |\psi\rangle\langle\psi|$ and $\hat{\rho}_B = \text{Tr}_A |\psi\rangle\langle\psi|$, it is defined as the von Neumann entropy of either of the two ¹

$$S \equiv -\text{Tr}_A (\hat{\rho}_A \log \hat{\rho}_A) = -\text{Tr}_B (\hat{\rho}_B \log \hat{\rho}_B). \quad (2.14)$$

Using the Schmidt decomposition, Eq. (2.12), it directly follows that the entanglement entropy is determined by the singular values λ_j through

$$S = -\sum_j \lambda_j^2 \log \lambda_j^2. \quad (2.15)$$

Connection to matrix product states. Consider an MPS in mixed canonical gauge (see Fig. 2.6(a)) with orthogonality center $A^{(m)}$ and corresponding physical index i_m . The SVD of the orthogonality center with joint index (k_{m-1}, i_m) and k_m is

$$A_{k_{m-1}, i_m, k_m}^{(m)} = \sum_j U_{k_{m-1}, i_m, j} \lambda_j V_{j, k_m}^\dagger.$$

We insert this decomposition into the MPS form (see Eq. (2.6)) to find

$$|\psi\rangle = \sum_{\substack{i_1, \dots, i_L \\ k_1, \dots, k_{L-1}}} \sum_j A_{i_1, k_1}^{(1)} \cdots A_{k_{m-2}, i_{m-1}, k_{m-1}}^{(m-1)} U_{k_{m-1}, i_m, j} \lambda_j V_{j, k_m}^\dagger A_{k_m, i_{m+1}, k_{m+1}}^{(m+1)} \cdots A_{k_{L-1}, i_L}^{(L)} \\ \times |i_1, \dots, i_m\rangle \otimes |i_{m+1}, \dots, i_L\rangle$$

with graphical representation in Fig. 2.6(b). This MPS is still in mixed-canonical gauge, with orthogonality center being the diagonal matrix with elements $\lambda_{j,j} \equiv \lambda_j$ as

¹One can easily show that the two expressions indeed coincide.

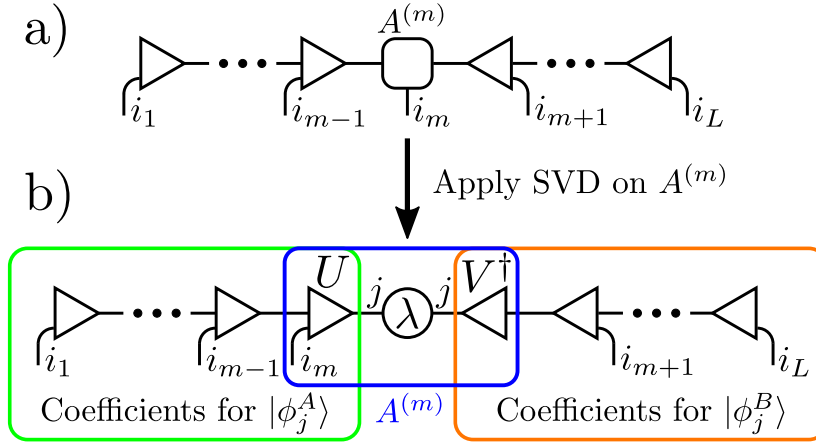


Figure 2.6.: Schmidt decomposition of an MPS. a) MPS in mixed-canonical gauge with orthogonality center $A^{(m)}$. b) MPS obtained after decomposing $A^{(m)}$ with an SVD. The tensor is replaced by its decomposition, encircled in blue. The MPS remains in mixed-canonical form, where the orthogonality center is the diagonal matrix of the SVD, with elements $\lambda_{j,j} \equiv \lambda_j$. The green and orange boxes contain the coefficients to build states $|\phi_j^A\rangle$ and $|\phi_j^B\rangle$ of subsystems A and B , respectively.

obtained from the SVD. We realize that this is the Schmidt decomposition of the state $|\psi\rangle$, with

$$\begin{aligned}
 |\phi_j^A\rangle &= \sum_{\substack{i_1, \dots, i_m \\ k_1, \dots, k_{m-1}}} A_{i_1, k_1}^{(1)} \cdots A_{k_{m-2}, i_{m-1}, k_{m-1}}^{(m-1)} U_{k_{m-1}, i_m, j} |i_1, \dots, i_m\rangle \\
 |\phi_j^B\rangle &= \sum_{\substack{i_{m+1}, \dots, i_L \\ k_m, \dots, k_{L-1}}} V_{j, k_m}^\dagger A_{k_m, i_{m+1}, k_{m+1}}^{(m+1)} \cdots A_{k_{L-1}, i_L}^{(L)} |i_{m+1}, \dots, i_L\rangle.
 \end{aligned}$$

Note that this is true because the MPS is in mixed-canonical gauge, and hence the tensors to the left of the diagonal matrix λ are left-orthogonal, while those to the right are right-orthogonal. This implies that the states of sets $\{|\phi_j^A\rangle\}$ and $\{|\phi_j^B\rangle\}$ are orthonormal.

i

Summary. The Schmidt decomposition of any bipartition that requires a single cut of the MPS is easy to find: First, we need to bring the MPS in mixed-canonical form with orthogonality center at the cut of the bipartition. Then an appropriate SVD yields the Schmidt decomposition with Schmidt coefficients λ_j , from which we can calculate the entanglement entropy S using Eq. (2.15).

Area laws and truncation of an MPS. We have previously seen how any quantum many-body state can be brought into an MPS form. However, so far it is not clear how and when the representation of a state in MPS form can be computationally efficient. Here, the so-called *area laws* for the entanglement entropy play a crucial role. A system

is said to satisfy an area law if the entanglement between two subsystems scales with the size of the boundary between them, rather than with the volume of the subsystems. For one-dimensional systems, this means that the entanglement is bound by a constant since the size of the boundary (two points) is independent of the system size. Area laws are known to hold for a variety of systems. In 1D, for instance, ground states of gapped Hamiltonians with local interactions are known to satisfy the area law [52].

Let us discuss the implications of area laws on the efficiency of the MPS representation. Recall that the entanglement entropy is connected to the distribution of Schmidt coefficients λ_j , see Eq. (2.15). Generally speaking, the entanglement entropy tends to be small if the Schmidt coefficients decay fast, while, on the contrary, high entropy is associated with slowly decaying Schmidt coefficients: the maximum possible entropy occurs for a flat distribution of the $\{\lambda_j\}$. Even though there is no direct implication, the opposite is usually true as well: States with low entanglement show a rapid decay of Schmidt coefficients, and hence, only a few λ_j s contribute significantly. This allows us to truncate the sum in Eq. (2.12), keeping only the largest D Schmidt coefficients, while discarding the remaining states having a low probability. The number of kept states D is called *bond dimension* and defines the size of the tensors in the MPS: Each tensor — except the first and last one — has three indices, two of them being bond indices and one being the physical index. The dimension of the bond indices, however, equals the number of kept states D , see Fig. 2.6(b). Hence, any tensor has at most D^2d elements, where d is the local physical dimension ($d = 2$ for spin 1/2 particles). Consequently, the MPS representation is very efficient whenever the many-body state can be well approximated with a low bond dimension D , which is the case when the entanglement between bipartitions of the system is low.

2.4. Variational ground state search: DMRG

As discussed previously, TN techniques originate from the Density Matrix Renormalization Group (DMRG) algorithm introduced by White [12, 13], who used it to study the ground state of lattice models. To date, DMRG for MPS is likely the most popular TN algorithm to study equilibrium properties of quantum many-body systems. In this section, we discuss in some detail the DMRG algorithm in the language of MPS for closed finite systems governed by a Hamiltonian \hat{H} . Our goal, in particular, is to find the ground state $|\psi_0\rangle$ of the time-independent Schrödinger equation,

$$\hat{H}|\psi_0\rangle = E_0|\psi_0\rangle, \quad (2.16)$$

and the corresponding ground state energy E_0 . The ground state energy is the minimum possible eigenvalue of \hat{H} , which, according to the variational principle, is found

by minimizing the energy expectation value over all quantum states $|\psi\rangle$:

$$E_0 = \min_{|\psi\rangle} \frac{\langle\psi|\widehat{H}|\psi\rangle}{\langle\psi|\psi\rangle} \quad (2.17)$$

When employing the MPS *Ansatz*, however, we restrict our variational space to a subspace of the Hilbert space, and hence, the variational energy will generally be higher than the true ground state energy. The variational space is set by the MPS bond dimension D , and our goal is to find the optimal MPS therein. Assume that we start with some randomly initialized MPS, with a given bond dimension D . An approximation to the ground state is found by optimizing the tensor elements such that the energy of the corresponding quantum state is minimal. However, optimizing *all* tensor elements at the same time is computationally demanding and therefore impractical. To circumvent this issue, DMRG uses the following strategy: Instead of optimizing all MPS elements simultaneously, only one or two tensors are optimized at a time, leading to the 1-site or 2-site version of DMRG, respectively. In general, the single-site DMRG is much more efficient as it acts on only one tensor of the network, while the 2-site version is working on two contracted tensors.²

In the following, we restrict our discussion to the 2-site version of DMRG, since, due to its simplicity, it is our method of choice for practical applications. We are going to discuss the essential building block of the DMRG algorithm, by showing how one can optimize two consecutive tensors. Clearly, this is not enough to find the globally best MPS: the full algorithm that exploits this building block will be presented at the end of the section.

Optimizing two consecutive tensors. Imagine an MPS consisting of tensors $A^{(1)}, \dots, A^{(L)}$, and suppose we want to optimize $A^{(m)}$ and its neighbor $A^{(m+1)}$. Consider the MPS to be in mixed-canonical gauge with orthogonality center $A^{(m)}$ (or $A^{(m+1)}$). This means that tensors on the left hand side of $A^{(m)}$ are left-orthogonal and tensors on the right hand side of $A^{(m+1)}$ are right-orthogonal, see Eq. (2.7) and Eq. (2.8). First, we compute the contraction of $A^{(m)}$ and $A^{(m+1)}$, which yields the tensor $T^{(m)}$ to be optimized:

$$T_{k_{m-1}, i_m, i_{m+1}, k_{m+1}}^{(m)} = \sum_{k_m} A_{k_{m-1}, i_m, k_m}^{(m)} A_{k_m, i_{m+1}, k_{m+1}}^{(m+1)} \quad (2.18)$$

Consider now the numerator and denominator of Eq. (2.17). Since the MPS is in mixed-canonical gauge, the normalization $\langle\psi|\psi\rangle$ is fully encoded in the orthogonality center, see Fig. 2.7(b). Hence, the denominator depends only on the variational tensor $T^{(m)}$, via

$$\langle\psi|\psi\rangle = |\mathbf{T}^{(m)}|^2, \quad (2.19)$$

²On the other hand, the standard single-site version is plagued by convergence issues, in particular when symmetries are encoded explicitly in the TN, since it is impossible to resize different symmetry sectors. Further progress, most notably subspace expansions, however, has cured this downside by temporarily expanding the bond links of the tensor to be optimized [118–120].

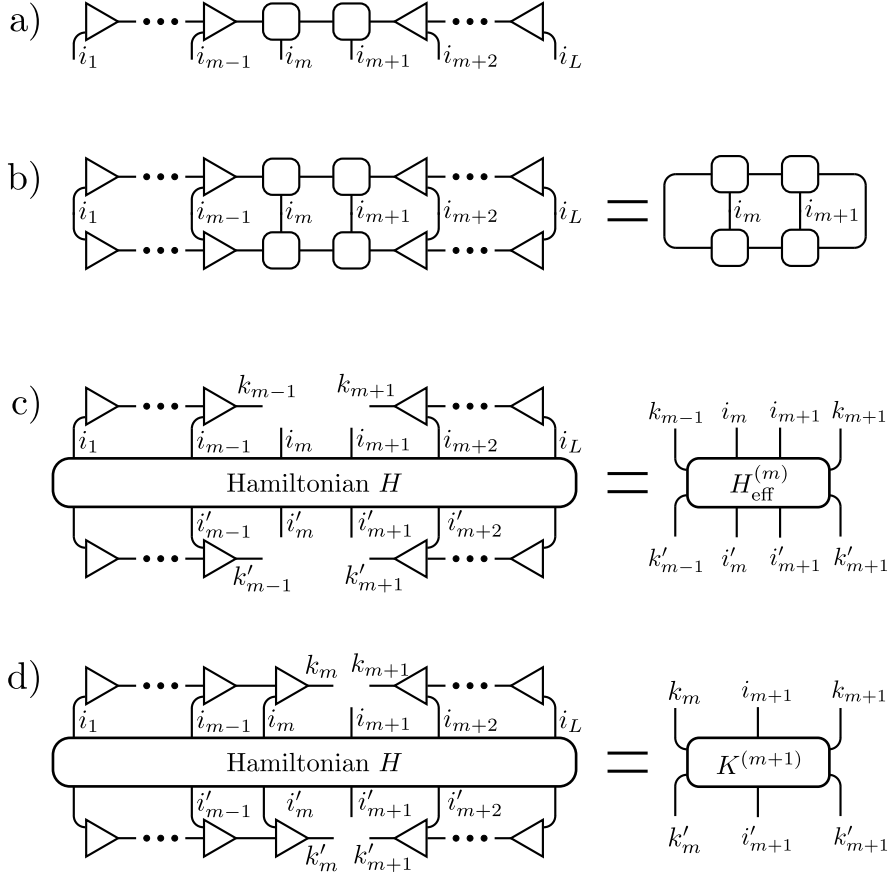


Figure 2.7.: Effective Hamiltonian for MPS in mixed-canonical gauge. a) MPS in mixed canonical gauge with respect to tensors $A^{(m)}$ and $A^{(m+1)}$. b) Scalar product $\langle \psi | \psi \rangle$ for an MPS in mixed canonical gauge. Due to the right- and left-orthogonality property of the tensors, the scalar product depends only on the orthogonality center. c) Effective Hamiltonian $\hat{H}_{\text{eff}}^{(m)}$ for the MPS with 2-site orthogonality center in panel (a): Tensors $A^{(m)}$ and $A^{(m+1)}$ are taken out from the MPS, while all remaining tensors are contracted into the Hamiltonian \hat{H} . d) Effective Hamiltonian $K^{(m+1)}$ for the single site orthogonality center $A^{(m+1)}$ as required by the TDVP algorithm. It is presented here already for better comparison with panel (c): Notice that $K^{(m+1)}$ can easily be obtained by contracting $A^{(m)}$ into $\hat{H}_{\text{eff}}^{(m)}$ from above and below.

where $\mathbf{T}^{(m)}$ is the vectorised tensor $T^{(m)}$. Notice that any tensor can be reshaped into a vector by merging the indices. Technical details and an example for this are provided in Appendix A.1. On the other hand, the numerator of Eq. (2.17) is the energy expectation value of the Hamiltonian for state $|\psi\rangle$. Hence the Hamiltonian must be sandwiched in between the MPS representing $|\psi\rangle$. This can be written as

$$\langle \psi | \hat{H} | \psi \rangle = (\mathbf{T}^{(m)})^\dagger \hat{H}_{\text{eff}}^{(m)} \mathbf{T}^{(m)}, \quad (2.20)$$

with effective Hamiltonian $\hat{H}_{\text{eff}}^{(m)}$ obtained in the following way: The full expectation value $\langle \psi | \hat{H} | \psi \rangle$ is the contraction of the MPS into the Hamiltonian from above (ket) and below (bra). Removing the tensor $T^{(m)}$ from the expectation value in both the bra and the ket yields the effective Hamiltonian $\hat{H}_{\text{eff}}^{(m)}$ (see Fig. 2.7(c)). Upon multiplication of

$\widehat{H}_{\text{eff}}^{(m)}$ with $T^{(m)}$ from above and below one obtains, once again, the energy expectation value, see Eq. (2.20). Notice that in Fig. 2.7 the Hamiltonian is drawn as a single block for simplicity, while in practice it is represented by a matrix product operator³ [17]. Hence, an upper bound for the ground state energy is

$$E' = \min_{T^{(m)}} \frac{(\mathbf{T}^{(m)})^\dagger \widehat{H}_{\text{eff}}^{(m)} \mathbf{T}^{(m)}}{|\mathbf{T}^{(m)}|^2}, \quad (2.21)$$

with minimization over the variational tensor $T^{(m)}$. Notice that E' is larger than the true ground state energy E_0 , as the minimization is carried out only over a subset of possible quantum states. The optimization problem is solved when $\mathbf{T}^{(m)}$ is the eigenvector of $\widehat{H}_{\text{eff}}^{(m)}$ corresponding to the smallest eigenvalue:

$$\widehat{H}_{\text{eff}}^{(m)} \mathbf{T}^{(m)} = E' \mathbf{T}^{(m)} \quad (2.22)$$

In practice, one often applies iterative approaches, such as the Davidson algorithm [121], to compute the lowest eigenvalue with the corresponding eigenvector numerically.

i

Warning: It is only in tensor networks without loops, such as open boundary conditions MPS or TTNs that the optimization leads to a standard eigenvalue problem. In the more general case, e.g in periodic boundary MPS, PEPS or MERA, the optimization results in a generalized eigenvalue problem, which can be much more difficult to solve [23].

After the optimal tensor $T^{(m)}$ is found, we need to restore the state to the MPS format: Indeed, recall that $T^{(m)}$ has been built from the two tensors $A^{(m)}$ and $A^{(m+1)}$, and hence needs to be split into two tensors again. This is achieved using the SVD, where the number of kept singular values, and hence the dimension of the tensors, can be chosen and adapted during the simulation. Assume that the SVD yields singular values $\lambda_1, \dots, \lambda_M$, ordered in descending order. Usually one uses a combination of two criteria for the truncation:

- (i) One keeps only the largest r singular values, where r is chosen such that the discarded ones have a summed weight of less than some error threshold w_t ,

$$\sum_{j=r+1}^M \lambda_j^2 < w_t. \quad (2.23)$$

³The MPO representation of an operator is similar to the MPS representation of a state, where however, each tensor has two physical indices instead of one. Here, it is only important to know that an efficient MPO representation can be obtained for basically any Hamiltonian of interest, even in presence of long-range interactions, and hence we simply represent the Hamiltonian by a single tensor.

- (ii) If r is larger than the so-called bond dimension D , only the largest D singular values are kept.

The two criteria follow a different strategy. (i) sets an upper bound for the error, but can lead to a strong growth of the matrix dimensions. Instead, (ii) sets an upper bound for the matrix dimensions, but does not control the error. Hence, sometimes only criterion (i) is used, see Ref. [39] for example. In either case, it is necessary to check that the result converges with respect to the control parameter w_t or D .

Algorithm 1: 2-site DMRG for MPS

- 1: **for** $s = 1, \#\text{Sweeps}$ **do**
- 2: **for** $m = 1, L - 1$ **do**
- 3: Make $A^{(m)}$ the MPS' orthogonality center
- 4: Find $T^{(m)}$ through contraction of $A^{(m)}$ and $A^{(m+1)}$
- 5: Compute effective Hamiltonian $\widehat{H}_{\text{eff}}^{(m)}$ for $T^{(m)}$
- 6: Find lowest energy eigenvector $\mathbf{T}^{(m)}$ of $\widehat{H}_{\text{eff}}^{(m)}$
- 7: Decompose $T^{(m)}$ via SVD into $A^{(m)}$ and $A^{(m+1)}$, gauge on $A^{(m+1)}$
- 8: **end for**
- 9: **end for**

Optimize the full MPS using the DMRG algorithm. Now that we know how a pair of consecutive tensors is optimized, we can discuss the full DMRG algorithm, sketched in Algorithm 1 above. It basically contains two nested loops in which tensors are optimized. In the inner loop, we optimize all pairs of neighboring tensors in the MPS. Usually, this is done by starting from the left end of the MPS, sweeping towards the right end, and optimizing one pair after the other. In general, the order in which tensors are optimized is not crucial. However, the pair to optimize must be the orthogonality center of the MPS, since otherwise Eq. (2.19) is not true, which finally would lead to a generalized eigenvalue problem instead of a standard one. Notice that for the special case where the pair to optimize involves the first or last tensor of the MPS, the MPS is required to be in right- or left-canonical gauge, respectively. In the outer loop, we simply repeat the entire procedure for several sweeps to reach convergence.

To illustrate the algorithm, we graphically show in Fig. 2.8 several steps carried out in a DMRG sweep for a system with $L = 4$. Starting from right-orthogonal MPS (panel a), one contracts the two leftmost tensors, $A^{(1)}$ and $A^{(2)}$, to obtain $T^{(1)}$ (panel b), see Eq. (2.18). Afterwards, the corresponding effective Hamiltonian $\widehat{H}_{\text{eff}}^{(1)}$ is built, in order to find the optimal tensor for $T^{(1)}$, given by the lowest energy eigenvector of $\widehat{H}_{\text{eff}}^{(1)}$. We then need to restore the MPS format by decomposing the optimized $T^{(1)}$ via SVD. Notice that the singular values are directly contracted into the right tensor, such that $A^{(2)}$ is the new orthogonality center of the MPS. These steps are then repeated until the entire MPS is optimized, with one more optimization step shown in Fig. 2.8.

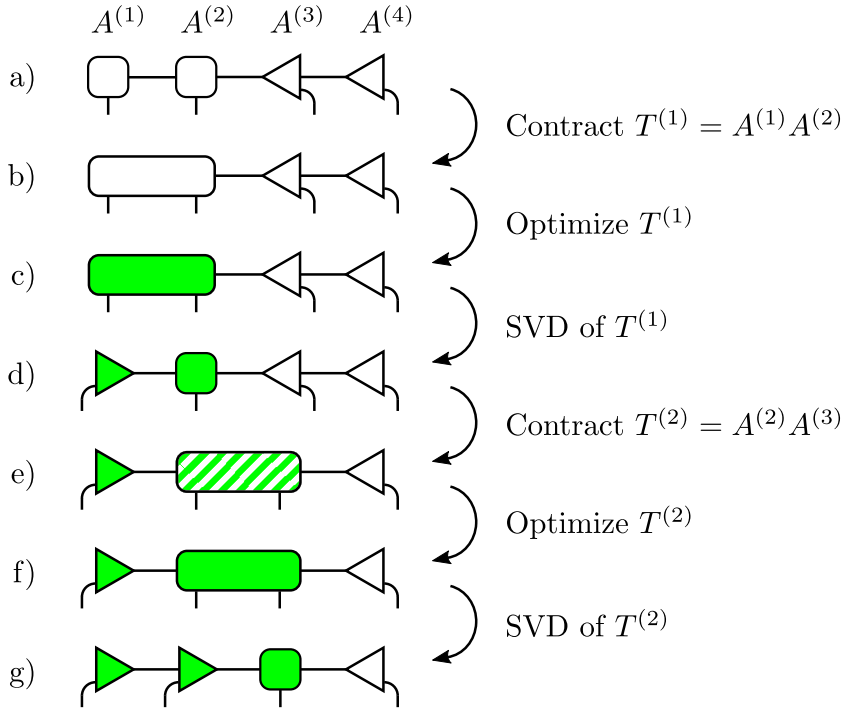


Figure 2.8.: Several steps of a DMRG sweep for $L = 4$ sites. (a→b) Starting from a right orthogonal MPS ($A^{(2)}$ is not required right orthogonal), we contract $A^{(1)}$ and $A^{(2)}$ to build the two-site block $T^{(1)}$. (b→c) We build the effective Hamiltonian $\hat{H}_{\text{eff}}^{(1)}$, Fig. 2.7, and optimize $T^{(1)}$ by computing the lowest energy eigenvector of $\hat{H}_{\text{eff}}^{(1)}$, see Eq. (2.22). Optimized tensor is coloured in green. (c→d) Compute SVD of optimized $T^{(1)}$ and contract singular values into the right tensor, $A^{(2)}$, becoming the new orthogonality center of the MPS. (d→e) Contract $A^{(2)}$ and $A^{(3)}$ to get $T^{(2)}$. The block is partially colored as one of the two building blocks was optimized. (e→f) Optimize $T^{(2)}$ using corresponding effective Hamiltonian $\hat{H}_{\text{eff}}^{(2)}$. (f→g) Decompose $T^{(2)}$ via SVD. Afterwards, continue in the same way until all tensors in the MPS are optimized.

2.5. Time evolution: TDVP

While an earlier version of the time-dependent variational principle (TDVP) algorithm was developed already a decade ago [115], it has caught widespread attention only recently after further algorithmic improvements have been made [116, 117]. Since then, TDVP has been established as one of the most popular methods to carry out the time evolution of MPS. As we will see, the algorithm is very similar to DMRG, and hence only minor changes need to be made to implement TDVP starting from a DMRG code [117]. Just like DMRG, TDVP sweeps through the entire MPS, updating only individual tensors or blocks of two consecutive tensors at a time, making the algorithm highly efficient. In contrast to TEBD, TDVP naturally allows for long-range interactions, without the need to swap sites. Similar to DMRG it can be employed efficiently in any tensor network structure that does not contain loops, such as tree tensor networks [3, 122] or MPS with optimized boson basis [123]. Due to its importance in

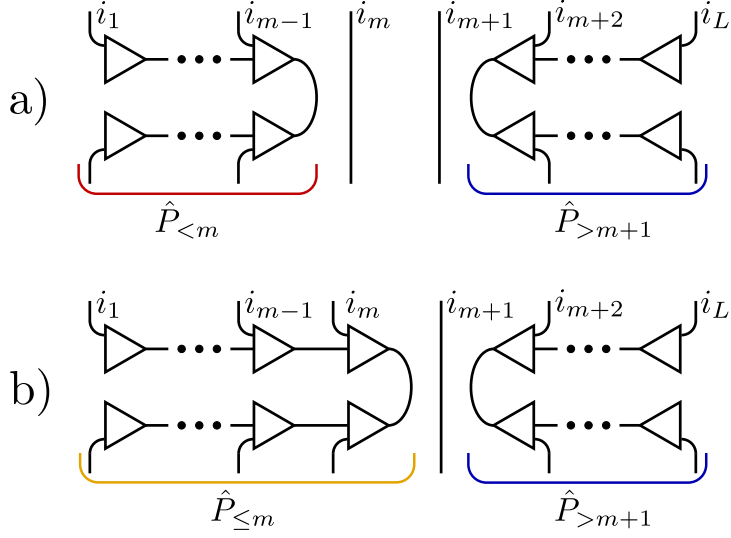


Figure 2.9.: 2-site TDVP projectors for an MPS. a) Projectors in the first sum of Eq. (2.27). The projector consists of two projectors, $\hat{P}_{<m}$ and $\hat{P}_{>m+1}$, acting on physical sites $1, \dots, m-1$ and $m+2, \dots, L$, respectively. They are built from the MPS in mixed canonical gauge with orthogonality center $A^{(m)}$ or $A^{(m+1)}$. b) Second term projector of Eq. (2.27). As compared to panel (a), the left projector includes a projection for tensor $A^{(m)}$ and has to be built from the MPS with orthogonality center $A^{(m+1)}$.

this thesis, we are going to discuss TDVP for MPS in some detail here.

Our goal is to solve the time-dependent Schrödinger equation

$$i\hbar \frac{\partial}{\partial t} |\psi(t)\rangle = \hat{H} |\psi(t)\rangle, \quad (2.24)$$

where $|\psi(t)\rangle$ is represented in MPS form. Consider now a small discrete time step Δt . The state at time $t + \Delta t$ can be written as $|\psi(t + \Delta t)\rangle = |\psi(t)\rangle + \frac{\Delta t}{i\hbar} \hat{H} |\psi(t)\rangle$. However, in MPS form this state will generally require a larger bond dimension than $|\psi(t)\rangle$. The TDVP tackles this issue by projecting the right-hand side of Eq. (2.24) onto the tangent space of the MPS, by introducing the tangent space projector $\hat{P}_{|\psi}$. We will provide details for this projector on the next pages. The Schrödinger equation, supplemented with the projection operator, then becomes

$$i\hbar \frac{\partial}{\partial t} |\psi(t)\rangle = \hat{P}_{|\psi} \hat{H} |\psi(t)\rangle. \quad (2.25)$$

In the single-site version of TDVP, only variations of individual tensors are allowed, which means that only one tensor can be changed at a time. In practice, this leads to an algorithm that does not allow for a dynamical increase of the bond dimension [117]. However, this can be problematic for non-equilibrium dynamics with growing entanglement, as the growth of entanglement requires to increase the bond dimension. To overcome this issue, one can allow for more general variations in the MPS. Rather than restricting to variations in individual tensors — leading to the single-site version of TDVP — we can allow variations that leave the original MPS manifold (see discussion

in Ref. [117]), and hence can describe an enlarged set of states. For example, consider a bond with bond dimension D , connecting two neighboring tensors. We can contract the two tensors and allow for arbitrary variations in this larger tensor, which is somehow similar to the application of a nearest-neighbor operator in TEBD. Clearly, such an idea requires an SVD with truncation to restore the original MPS format, allowing, however, for a dynamical adjustment of the bond dimension D . This strategy is called the *two-site version* of TDVP. Two-site TDVP has been proven to be both very efficient and accurate in many scenarios [50] and has therefore been employed in our simulations. In the following, we restrict the discussion on TDVP to the 2-site version: the single-site version is very similar [116, 117, 123].

Consider a quantum many-body system with L lattice sites, described by a MPS in mixed canonical gauge with orthogonality center $A^{(m+1)}$. We write the state as

$$|\psi\rangle = \sum_{k_m, i_m, k_{m+1}} A_{k_m, i_m, k_{m+1}}^{(m+1)} |\phi_{k_m}^{(1:m)}\rangle |i_{m+1}\rangle |\phi_{k_{m+1}}^{(m+2:L)}\rangle, \quad (2.26)$$

where $\{|\phi_{k_m}^{(1:m)}\rangle\}_{k_m}$ and $\{|\phi_{k_{m+1}}^{(m+2:L)}\rangle\}_{k_{m+1}}$ are orthonormal sets of quantum states describing the states of sites $1, \dots, m$ and $m+2, \dots, L$, and are built from left-orthogonal MPS tensors $A^{(1)}, \dots, A^{(m)}$ and right-orthogonal tensors $A^{(m+2)}, \dots, A^{(L)}$, respectively. The 2-site TDVP projector is given by [117]

$$\hat{P}_{|\psi\rangle} = \sum_{m=1}^{L-1} \underbrace{\hat{P}_{<m} \otimes \mathbb{1}_m \otimes \mathbb{1}_{m+1} \otimes \hat{P}_{>m+1}}_{\hat{P}_m^{(+)}} - \sum_{m=1}^{L-2} \underbrace{\hat{P}_{\leq m} \otimes \mathbb{1}_{m+1} \otimes \hat{P}_{>m+1}}_{\hat{P}_m^{(-)}}, \quad (2.27)$$

where $\hat{P}_{<m}$, $\hat{P}_{\leq m}$, and $\hat{P}_{>m+1}$ are projectors onto the reduced density matrix of the corresponding MPS region [117], namely:

$$\hat{P}_{<m} = \sum_{k_{m-1}} |\phi_{k_{m-1}}^{(1:m-1)}\rangle \langle \phi_{k_{m-1}}^{(1:m-1)}| \quad (2.28)$$

$$\hat{P}_{\leq m} = \sum_{k_m} |\phi_{k_m}^{(1:m)}\rangle \langle \phi_{k_m}^{(1:m)}| \quad (2.29)$$

$$\hat{P}_{>m+1} = \sum_{k_{m+1}} |\phi_{k_{m+1}}^{(m+2:L)}\rangle \langle \phi_{k_{m+1}}^{(m+2:L)}| \quad (2.30)$$

Notice that states $|\phi_{k_{m-1}}^{(1:m-1)}\rangle$ — not introduced so far — are constructed from left-orthogonal tensors $A^{(1)}, \dots, A^{(m-1)}$ in the same way as states $|\phi_{k_m}^{(1:m)}\rangle$, with the only difference that they only describe sites $1, \dots, m-1$, excluding site m . The projectors are visualized in Fig. 2.9. We observe that $\hat{P}_m^{(+)}$ is acting on all physical indices except i_m and i_{m+1} , while $\hat{P}_m^{(-)}$ acts additionally on i_m . Knowing the projector, our goal is to solve the TDVP equation in Eq. (2.25). The essential idea is to split the equation using a so-called *Lie-Trotter splitting* [124], and solve it for just a single term of the

projector at a time. The splitting leads to the following system of equations:

$$\begin{aligned}
 i\hbar \frac{\partial}{\partial t} |\psi(t)\rangle &= +\hat{P}_1^{(+)} \hat{H} |\psi(t)\rangle \\
 i\hbar \frac{\partial}{\partial t} |\psi(t)\rangle &= -\hat{P}_1^{(-)} \hat{H} |\psi(t)\rangle \\
 i\hbar \frac{\partial}{\partial t} |\psi(t)\rangle &= +\hat{P}_2^{(+)} \hat{H} |\psi(t)\rangle \\
 i\hbar \frac{\partial}{\partial t} |\psi(t)\rangle &= -\hat{P}_2^{(-)} \hat{H} |\psi(t)\rangle \\
 &\vdots
 \end{aligned} \tag{2.31}$$

Here, we can solve one equation after the other [116]. Notice that there are two types of differential equations, corresponding to the two types of projectors in Eq. (2.27). Until now, the differential equations still contain some time-dependence for the *entire* MPS. However, it has been shown in Ref. [116] that the differential equations can be solved by making only the non-projected tensors time-dependent, while keeping all the remaining ones constant (see also Appendix A.3 for more details). Hence, the two types of equations are reduced to

$$i\hbar \frac{d}{dt} \mathbf{T}^{(m)} = + \hat{H}_{\text{eff}}^{(m)} \mathbf{T}^{(m)} \tag{2.32}$$

$$i\hbar \frac{d}{dt} \mathbf{A}^{(m+1)} = - K^{(m+1)} \mathbf{A}^{(m+1)}. \tag{2.33}$$

Here, $\mathbf{T}^{(m)}$ is the vectorized two-site orthogonality center of the MPS, built from tensors $A^{(m)}$ and $A^{(m+1)}$, Eq. (2.18), and $\hat{H}_{\text{eff}}^{(m)}$ is the corresponding effective Hamiltonian known already from DMRG, see Fig. 2.7(c). In the second line, $\mathbf{A}^{(m+1)}$ is the vectorized tensor $A^{(m+1)}$, and $K^{(m+1)}$ is the corresponding effective Hamiltonian, obtained when contracting $A^{(m)}$ into $\hat{H}_{\text{eff}}^{(m)}$, see Fig. 2.7(d). These differential equations can be solved employing Krylov subspace techniques [113] to compute the result of the application of the operator exponential on a state [50, 114], without the need to calculate the operator exponential explicitly. Notice the negative sign in the second line, which leads to an evolution *backward* in time. Furthermore, it needs to be stressed that after solving a differential equation like Eq. (2.32), we need to perform an SVD on $T^{(m)}$, in order to restore the MPS format, see also Appendix A.3.

Algorithm 2: 2-site TDVP for MPS

- 1: **for** $m = 1, L - 1$ **do**
- 2: Make $A^{(m)}$ the MPS' orthogonality center
- 3: Find $T^{(m)}$ through contraction of $A^{(m)}$ and $A^{(m+1)}$, Eq. (2.18)
- 4: Compute effective Hamiltonian $\widehat{H}_{\text{eff}}^{(m)}$
- 5: Evolve $T^{(m)}$ according to Eq. (2.32)
- 6: Decompose $T^{(m)}$ via SVD into $A^{(m)}$ and $A^{(m+1)}$, gauge on $A^{(m+1)}$
- 7: **if** $m \neq L - 1$ **then**
- 8: Compute effective Hamiltonian $K^{(m+1)}$
- 9: Evolve $A^{(m+1)}$ backwards according to Eq. (2.33)
- 10: **end if**
- 11: **end for**

We have now discussed all the building blocks to formulate the 2-site TDVP algorithm, which is summarized in Algorithm 2 for an evolution by one time step Δt . As pointed out in Ref. [117], the TDVP algorithm is closely connected to the DMRG algorithm: In both of them, a single optimization (DMRG) or time evolution step (TDVP) is achieved by sweeping through the MPS. In each sweep, the MPS is optimized/evolved through operations acting *locally* on the MPS. While in DMRG a pair of neighboring tensors is optimized by solving an eigenvalue problem for its effective Hamiltonian, in TDVP the very same effective Hamiltonian determines its time evolution. Additionally, TDVP contains a backward evolution step, for which there is no counterpart in DMRG. Just like for DMRG, we show in Fig. 2.10 the first steps of a TDVP sweep. As compared to DMRG, Fig. 2.8, all steps up to panel (d) are the same, where only the optimization is replaced by the time evolution. Before proceeding with the next block of tensors, however, TDVP requires the backward evolution of the right tensor after the SVD (d→e).

i

Remarks. In practice it can be beneficial to use a symmetric choice, with time step $\Delta t/2$ for the left-to-right sweep and an additional right-to-left sweep with $\Delta t/2$ as well, to reduce the time step error [50, 117, 122]. Furthermore, there are various possibilities to combine the single-site and two-site versions to further improve efficiency. For example, one can employ the different versions for different parts of a tensor network [122]. Alternatively, one can start the time evolution with the 2-site version until the maximum bond dimension is reached and then continue with single-site TDVP.

2.6. Jordan-Wigner transformation

The quantum many-body simulation of quantum particles such as spin-1/2 or bosons is straightforward with Tensor Networks, due to the commutator vanishing for different

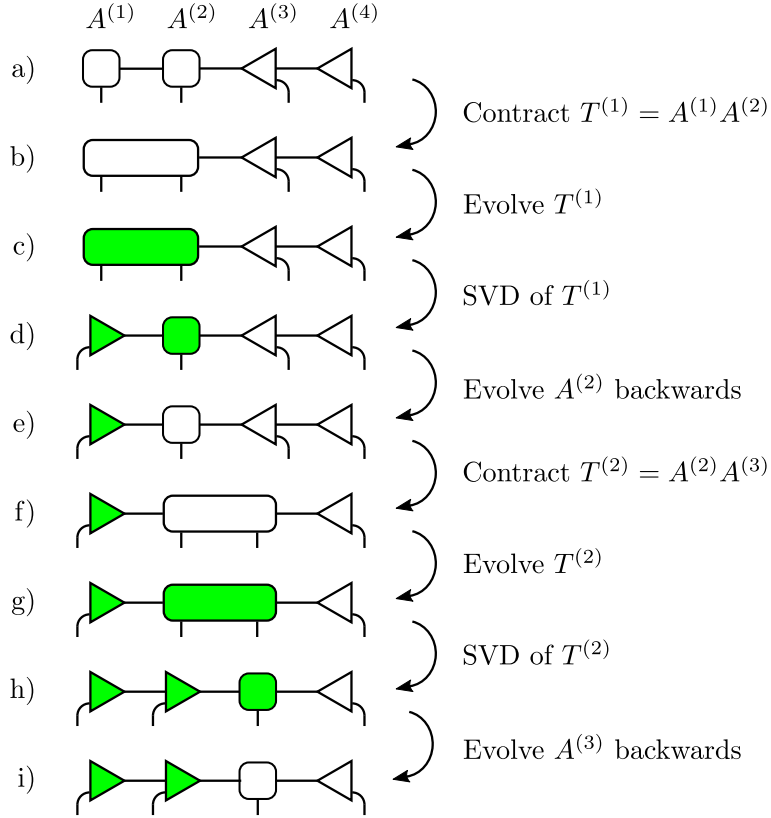


Figure 2.10.: Several steps of a TDVP sweep for $L = 4$ sites. (a→b) Starting from a right orthogonal MPS ($A^{(2)}$ is not required right orthogonal), we contract $A^{(1)}$ and $A^{(2)}$ to build the two-site block $T^{(1)}$. (b→c) We build the effective Hamiltonian $\hat{H}_{\text{eff}}^{(1)}$, Fig. 2.7(c), and evolve $T^{(1)}$ in time by solving the differential equation in Eq. (2.32). The evolved tensor is colored in green. (c→d) Compute SVD of evolved tensor $T^{(1)}$ and contract singular values into the right tensor, becoming the new orthogonality center of the MPS. (d→e) Find the effective Hamiltonian $K^{(2)}$ for $A^{(2)}$, see Fig. 2.7(d), and evolve $A^{(2)}$ backwards in time by solving Eq. (2.33). (e→f) Contract $A^{(2)}$ and $A^{(3)}$ to get $T^{(2)}$. (f→g) Evolve $T^{(2)}$ using corresponding effective Hamiltonian $\hat{H}_{\text{eff}}^{(2)}$. (g→h) Decompose $T^{(2)}$ via SVD. (h→i) Evolve $A^{(3)}$ backwards in time using $K^{(3)}$. Afterward, continue in the same way until all tensors in the MPS are evolved. Notice that there is no backward evolution for the last tensor.

lattice sites. When dealing with fermions, however, the situation changes drastically due to the change of sign when exchanging two fermions as required by the anti-commutator $\{\hat{c}_i, \hat{c}_j^\dagger\} = \delta_{i,j}$, where $\{\hat{A}, \hat{B}\} = \hat{A}\hat{B} + \hat{B}\hat{A}$. The most prominent way to deal with this issue in one dimension is the so-called *Jordan-Wigner transformation* [125], a unitary transformation which maps spinless fermions into spin-1/2 particles. Let us define two operators

$$\sigma_j^+ = \exp\left(+i\pi \sum_{k=1}^{j-1} \hat{c}_k^\dagger \hat{c}_k\right) \hat{c}_j^\dagger \quad (2.34)$$

$$\sigma_j^- = \exp\left(-i\pi \sum_{k=1}^{j-1} \hat{c}_k^\dagger \hat{c}_k\right) \hat{c}_j. \quad (2.35)$$

Notice that this transformation is non-local as it acts on all sites with index $k < j$ simultaneously. We can easily show that these operators satisfy the commutation relations $[\sigma_l^-, \sigma_j^+] = \delta_{l,j}$ and $[\sigma_l^-, \sigma_j^-] = [\sigma_l^+, \sigma_j^+] = 0$, characteristic for spin-1/2 particles. The spin sites are built from two basis states $|\uparrow\rangle$ and $|\downarrow\rangle$, with operators $\sigma^+ = |\uparrow\rangle\langle\downarrow|$ and $\sigma^- = |\downarrow\rangle\langle\uparrow|$ exchanging between the basis states. These operators are the spin-equivalent of the fermionic creation and annihilation operators, \hat{c}^\dagger and \hat{c} , respectively. The inverse transformation is given by

$$\hat{c}_j^\dagger = \exp\left(-i\pi \sum_{k=1}^{j-1} \sigma_k^+ \sigma_k^-\right) \sigma_j^+ \quad (2.36)$$

$$\hat{c}_j = \exp\left(+i\pi \sum_{k=1}^{j-1} \sigma_k^+ \sigma_k^-\right) \sigma_j^- . \quad (2.37)$$

Using the inverse transformation we can show that the fermionic number operator, $\hat{n}_j = \hat{c}_j^\dagger \hat{c}_j$, and nearest-neighbor hopping terms take the simple form

$$\hat{c}_j^\dagger \hat{c}_j = \sigma_j^+ \sigma_j^- \quad (2.38)$$

$$\hat{c}_j^\dagger \hat{c}_{j+1} = \sigma_j^+ \sigma_{j+1}^- \quad (2.39)$$

$$\hat{c}_{j+1}^\dagger \hat{c}_j = \sigma_{j+1}^+ \sigma_j^- . \quad (2.40)$$

However, the transformation of operators $\hat{c}_l^\dagger \hat{c}_j$ is non-trivial in general. Assuming $l < j$ we observe an additional string operator in the spin-basis, which acts on all sites in between the two operators \hat{c}_l^\dagger and \hat{c}_j :

$$\hat{c}_l^\dagger \hat{c}_j = \sigma_l^+ \exp\left(+i\pi \sum_{k=l+1}^{j-1} \sigma_k^+ \sigma_k^-\right) \sigma_j^- . \quad (2.41)$$

Hence, fermionic models with only nearest-neighbor hopping terms can easily be implemented using the Jordan-Wigner transformation with no further complications. On the other hand, terms with interaction range > 1 require the implementation of the string operators, where local operators are acting on the two interacting sites and all sites in between. When using the MPO representation, such string operators can lead to a more complex representation of the Hamiltonian, which, however, is still possible. In our simulations, we use the iTensor library [126], which handles fermionic operators and the resulting string operators automatically.

3. Anderson model and simulation techniques

The Anderson model is one of the most prominent models in condensed matter physics. Introduced to study the effect of a magnetic impurity in a metal [58], and the emerging Kondo effect [56, 57], it finds applications in various fields. In the framework of dynamical mean-field theory (DMFT), the single-impurity Anderson model (SIAM) serves as a building block to study strongly correlated materials [10, 127]. Coupled to an additional bath, the SIAM provides a simple playground to study quantum transport through the impurity, induced by a temperature gradient or an electric voltage between the leads [53, 63], as realizable with quantum dots [61, 62].

The most popular techniques used so far to study the Anderson model are exact diagonalization (ED), Quantum Monte Carlo [68–70], Wilson’s numerical renormalization group (NRG) [9, 71–73, 76, 128] and tensor-network-based methods [34–40, 63], all of them with their own advantages and disadvantages. ED is numerically exact and has equal resolution on all energy scales, but is usually limited in the number of conduction modes that can be treated. Monte-Carlo-based methods and NRG are very successful in calculating equilibrium properties, such as the impurity Green’s function for DMFT applications. However, simulating real-time dynamics is more challenging. Matrix product states (MPS), or tensor-network methods in general, are well suited to deal with one-dimensional systems [14, 17]: ground states of 1D models with short-range interactions are known to follow an area law for the entanglement entropy [52], making tensor networks a very efficient tool for equilibrium simulations. However, when simulating the dynamics, e.g. after a sudden quench, the entanglement typically grows in time, often even linearly. This results in an exponential increase of the required numerical resources.

Hence, for real-time simulations employing MPS, it is crucial to reduce the entanglement as much as possible. For the Anderson model, a very natural idea to represent the conduction modes would be to apply Wilson’s chain mapping [128]: free electrons are represented by a tight-binding chain, which is well suited for NRG calculations and was believed to be the best strategy for MPS simulations as well, due to the interactions being short range. However, it has been shown that simulations in the so-called “star-geometry”, avoiding Wilson’s chain mapping, show significantly less entanglement [39]. In this chapter, we introduce the Anderson model, which is the model of interest in

the following chapters, and we discuss the various possibilities to simulate it, with a focus on ideas suitable for MPS. In addition to the discussion of previously employed methods, we introduce an idea that combines the advantages of the tight-binding chain mapping and the star geometry, which can even be generalized to finite temperatures.

This chapter is structured as follows. In Section 3.1 we introduce the single impurity Anderson model, both in its discrete variant and the continuum, where the latter is obtained from the discrete one in the thermodynamic limit. The connection between the two is established in Section 3.2, where we show how to discretize the continuum. Furthermore, we show how the star-like Anderson model can be transformed into a tight-binding chain, which is well suited for numerical simulations. We then show in Section 3.3 an alternative method to carry out the chain mapping directly from the continuum, which is based on orthogonal polynomials. Section 3.4 is devoted to an example of the chain mapping at zero temperature, where we compare the two aforementioned methods. Following this, we discuss in Section 3.5 some of the issues one encounters in practical simulations when employing the chain mapping. Discussing the zero temperature case only up to this point, we show how one can deal with finite temperatures in Section 3.6, with corresponding chain mapping being presented in Section 3.7. We conclude the chapter with an example for the finite temperature chain mapping, Section 3.8, and a summary with a discussion about the different simulation methods suitable for MPS, see Section 3.9.

3.1. Single impurity Anderson model

We start the chapter by introducing the essential model of this thesis, the single impurity Anderson model (SIAM). We present the SIAM in the discrete version, as is usually done, and in the continuum, which is useful for practical simulations. We moreover establish a connection between the discrete and continuum formulation of the SIAM, and discuss practical aspects of simulations in the star geometry.

3.1.1. Discrete SIAM

The single impurity Anderson model (SIAM) [58] consists of a single spin-full impurity orbital hybridizing with a bath of free conduction electrons:

$$\hat{H}_{\text{SIAM}}(t) = \hat{H}_{\text{loc}}(t) + \hat{H}_{\text{hyb}} + \hat{H}_{\text{cond}} \quad (3.1)$$

The local Hamiltonian describes the localized impurity embedded in the bath of conduction electrons,

$$\hat{H}_{\text{loc}}(t) = \sum_{\sigma} \varepsilon_d(t) \hat{d}_{\sigma}^{\dagger} \hat{d}_{\sigma} + U(t) \hat{n}_{\uparrow} \hat{n}_{\downarrow}, \quad (3.2)$$

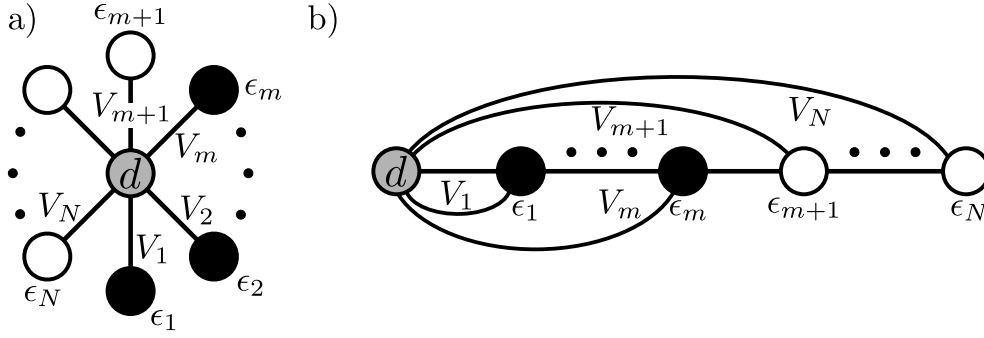


Figure 3.1.: SIAM in star geometry. a) Graphical representation of the single impurity Anderson model. The localized impurity, labeled by "d", is coupled to a bath of free electron modes, labeled through their index k , with corresponding energies ϵ_k . Bath modes below the Fermi energy E_f (black circles) are filled at $T = 0$, while modes above E_f are empty (white circles). The hybridization interaction with coupling coefficient V_k allows electrons to hop from the bath into the impurity and vice-versa. b) For simulations with MPS, the bath modes are organized as a one-dimensional chain, with artificial long-range interactions [39].

where \hat{d}_σ^\dagger creates an electron with spin $\sigma = \uparrow, \downarrow$ in the impurity orbital, $\hat{n}_\sigma = \hat{d}_\sigma^\dagger \hat{d}_\sigma$ is the number operator, and U the on-site Hubbard repulsion. Here we could allow for a time-dependent impurity level $\varepsilon_d(t) = E_d(t) - \mu$, where μ denotes the chemical potential of the conduction electron bath, and even for a time-dependent $U(t)$, for possible applications to non-equilibrium problems. The impurity-bath hybridization term models the interaction of the impurity with the conduction electrons, see Fig. 3.1(a), and is given by:

$$\hat{H}_{\text{hyb}} = \sum_{\sigma} \sum_k V_k \left(\hat{d}_\sigma^\dagger \hat{c}_{k,\sigma} + \hat{c}_{k,\sigma}^\dagger \hat{d}_\sigma \right) \quad (3.3)$$

where V_k is a (real) hybridization matrix element and $\hat{c}_{k,\sigma}^\dagger$ creates a conduction electron in an orbital labeled by k . The conduction electrons are assumed to be free, and hence are described by the Hamiltonian

$$\hat{H}_{\text{cond}} = \sum_{k,\sigma} \epsilon_k \hat{c}_{k,\sigma}^\dagger \hat{c}_{k,\sigma}. \quad (3.4)$$

Here ϵ_k denotes energies referred to the conduction electron chemical potential μ . The interactions between impurity and conduction electrons are characterized by a "star" geometry, see Fig. 3.1(a). In the star geometry, we can directly simulate the SIAM using matrix product states. To this end, one organizes the impurity and the bath sites as a one-dimensional chain, with artificial long-range interaction [39], as visualized in Fig. 3.1(b). A more detailed discussion of the simulation strategies, however, will follow in the next sections.

Symmetries in the SIAM

Let us briefly discuss the symmetries of the Anderson model here, see also section 2.3.1 of Ref. [129]. Clearly, the model is symmetric in spin, and hence invariant under the transformation

$$\hat{c}_{k,\sigma} \longrightarrow \hat{c}_{k,-\sigma} . \quad (3.5)$$

This implies that in equilibrium and during time evolution with spin-symmetric initial state observables are the same for spin-up and spin-down. This symmetry would be broken in the presence of a magnetic field B , where the local impurity Hamiltonian would be supplemented by a term like $B(\hat{n}_\uparrow - \hat{n}_\downarrow)$. One can easily show that for parameters satisfying the conditions

$$\varepsilon_d = -U/2 , \quad V_k = V_{-k} , \quad \epsilon_k = -\epsilon_{-k} \quad (3.6)$$

the SIAM is particle-hole (PH) symmetric [129], meaning that it is invariant under the transformation

$$\hat{c}_{k,\sigma} \longrightarrow \hat{c}_{-k,\sigma}^\dagger \quad \text{and} \quad \hat{d}_\sigma \longrightarrow -\hat{d}_\sigma^\dagger . \quad (3.7)$$

Essentially, the conditions boil down to a symmetric hybridization function and a symmetric choice for the local impurity levels. The PH-symmetric case is extremely useful for benchmarks of numerical methods since certain values of observables are known exactly due to the symmetry. For example, in equilibrium and at PH-symmetry, the impurity population is always $\langle \hat{n}_\sigma \rangle = 1/2$ per spin.

3.1.2. SIAM in the continuum

Previously we have introduced the SIAM with discrete conduction electron modes. However, as we approach the thermodynamic limit, it is reasonable to employ a continuum representation for the electron bath. Denoting the half-bandwidth by W , we work with energy dimensionless units $x = \epsilon/W$. In the continuum limit [9, 130], with some more details given in the next section, we replace the sum over k -modes by an integral, $\sum_k \rightarrow \int dx$, and we substitute the hybridization couplings and dispersion with their continuum versions, $V_k \rightarrow V(x)$, $\epsilon_k \rightarrow g(x)$. The fermionic operators become $\hat{c}_{k\sigma} \rightarrow \hat{c}_\sigma(x)$, with a Dirac-delta anti-commutation relationship

$$\{\hat{c}_\sigma(x), \hat{c}_{\sigma'}^\dagger(x')\} = \delta_{\sigma,\sigma'} \delta(x - x') .$$

Hence, we recast the kinetic term as:

$$\hat{H}_{\text{cond}} = W \sum_\sigma \int_{-1}^1 dx g(x) \hat{c}_\sigma^\dagger(x) \hat{c}_\sigma(x) \quad (3.8)$$

Similarly, the hybridization term is given by

$$\hat{H}_{\text{hyb}} = W \sum_{\sigma} \int_{-1}^1 dx V(x) \left(\hat{d}_{\sigma}^{\dagger} \hat{c}_{\sigma}(x) + \text{H.c.} \right). \quad (3.9)$$

Remarkably enough, the dispersion $g(x)$ and the hybridization couplings $V(x)$ are not completely independent. Instead, the conduction electron bath is characterized by only a single function $\Delta(\omega)$, the hybridization function. $\Delta(\omega)$ is related to $V(x)$ and $g(x)$ through the relation [130]

$$\frac{dx(\omega)}{d\omega} V^2(x(\omega)) = \frac{\Delta(\omega)}{\pi}, \quad (3.10)$$

where $x(\omega) = g^{-1}(\omega)$ is the inverse of $g(x)$, such that $g(g^{-1}(\omega)) = \omega$. For bosonic baths, the role of the hybridization function is taken by the so called *spectral density*, as will be discussed in more detail in Chapter 7.

3.2. Chain mapping I: Discretization plus Lanczos

In principle, it is possible to simulate the Anderson model — after an appropriate discretization — directly in the star geometry, using exact diagonalization, for instance. However, advanced methods such as the Numerical Renormalization Group (NRG), require a mapping of the conduction electrons from the star geometry into a tight-binding chain with nearest-neighbor couplings only. Similarly, a chain structure can be well employed in TN simulations, as dealing with short-range couplings is usually easier than working with long-range interactions. For this reason, let us discuss in some detail different possibilities to carry out the chain mapping of the electron bath. In this section, we first show how the discrete version of the SIAM is obtained when discretizing its continuum counterpart. We then map the discrete model into a chain using Lanczos' tridiagonalization algorithm, to obtain the chain representation of the bath.

3.2.1. Bath discretization

Let us now establish a relation between the Anderson impurity model in the continuum limit, see Section 3.1.2, and its discretized version as given in Eq. (3.1). To this end, we discuss two different ideas to discretize the continuum bath. The first method is rather simple, and introduces the conceptual idea for the discretization, while the second one is slightly more involved, but leads to an improved approximation of the original bath.

Simple discretization. We start from the continuum SIAM in Section 3.1.2, and we choose the linear dispersion relation $g(x) = x$, with inverse $x(\omega) = g^{-1}(\omega) = \omega$. Notice, that we take ω to be dimensionless. According to Eq. (3.10), this implies $V^2(x) = \Delta(x)/\pi$. We discretize the support $[-1, 1]$ of x , into intervals I_k centered around some discrete values x_k , with interval length $L_k = \Delta x_k$. In each interval we can define a Fourier basis:

$$\psi_{k,n}(x) = \begin{cases} \frac{1}{\sqrt{L_k}} e^{i2\pi n x/L_k} & \text{for } x \in I_k \\ 0 & \text{otherwise} \end{cases} \quad (3.11)$$

where $n = 0, \dots, \infty$. Being a complete orthonormal basis, we can introduce a set of discrete operators $\hat{c}_{k,n}$ through the unitary transformation

$$\hat{c}_{k,n} = \int_{-1}^1 dx \psi_{k,n}^*(x) \hat{c}(x), \quad (3.12)$$

whose inverse is

$$\hat{c}(x) = \sum_k \sum_{n=0}^{\infty} \psi_{k,n}(x) \hat{c}_{k,n}. \quad (3.13)$$

Notice that we have dropped spin indices, since they are irrelevant here and in the following. Employing this transformation, we can rewrite the Hamiltonian in terms of the (infinitely many) discrete modes. For instance, the term entering the hybridization coupling reads

$$\begin{aligned} W \int_{-1}^1 dx V(x) \hat{c}(x) &= \sum_k \sum_{n=0}^{\infty} W \int_{-1}^1 dx V(x) \psi_{k,n}(x) \hat{c}_{k,n} \\ &= \sum_k \sum_{n=0}^{\infty} V_{k,n} \hat{c}_{k,n} \quad \text{with} \\ V_{k,n} &\stackrel{\text{def}}{=} W \int_{-1}^1 dx V(x) \psi_{k,n}(x). \end{aligned} \quad (3.14)$$

Until now, the transformation is still exact but contains an infinite number of Fourier contributions. The usual approximation — which becomes exact in the limit $L_k \rightarrow 0$ — is to drop all Fourier harmonics with $n > 0$, keeping only the constant term $\psi_{k,n=0}$. This is valid because for $L_k \rightarrow 0$ we can approximate $V(x)$ as a constant in each interval I_k , and hence, only the constant term of $\psi_{k,n}$ survives in the integral. For the hybridization term, we then find

$$W \int_{-1}^1 dx V(x) \hat{c}(x) \xrightarrow{L_k \rightarrow 0} \sum_k V_k \hat{c}_k, \quad (3.15)$$

where we have introduced a short notation for the fermion operator $\hat{c}_{k,n=0}$,

$$\hat{c}_k = \hat{c}_{k,n=0} = \frac{1}{\sqrt{L_k}} \int_{I_k} dx \hat{c}(x), \quad (3.16)$$

and the hybridization coupling $V_{k,n=0}$:

$$V_k = V_{k,n=0} = \frac{W}{\sqrt{L_k}} \int_{I_k} dx V(x) \quad (3.17)$$

Applying the very same approximation, we drop all $n \neq 0$ terms in the conduction Hamiltonian, which then becomes

$$W \int_{-1}^1 dx x \hat{c}^\dagger(x) \hat{c}(x) \xrightarrow{L_k \rightarrow 0} \sum_k \epsilon_k \hat{c}_k^\dagger \hat{c}_k, \quad (3.18)$$

where the discrete energies are given by

$$\epsilon_k = \frac{W}{L_k} \int_{I_k} dx x. \quad (3.19)$$

Advanced discretization. In the previous paragraph, we argued that only the zeroth Fourier component survives in the limit $L_k \rightarrow 0$. Hence, dropping all the remaining components introduces an error, for finite L_k . In this section, we discuss an improved discretization scheme, following Refs. [9, 130]. In contrast to the above strategy, here it will not be an approximation that only the zeroth component of the Fourier expansion couples to the impurity. This is achieved in the following way. Due to Eq. (3.10) we have the freedom to choose $V(x)$ to be *stepwise constant* in each interval I_k : the energy dependence of the hybridization function $\Delta(\omega)$ is fully encoded in $g(x)$ and its inverse $x(\omega)$, while $V(x)$ is kept constant in each discretization interval. We choose $V^2(x)$ to take the mean value of $\Delta(\omega)/\pi$ in each interval:

$$V^2(x \in I_k) = \tilde{V}_k^2 = \frac{1}{\pi L_k} \int_{I_k} d\omega \Delta(\omega) \quad (3.20)$$

By exploiting the decomposition of $\hat{c}(x)$, Eq. (3.13), and the stepwise constant nature of $V(x)$, the hybridization term becomes

$$\int_{-1}^1 dx V(x) \hat{c}(x) = \sum_k \sum_{n=0}^{\infty} \tilde{V}_k \int_{-1}^1 dx \psi_{k,n}(x) \hat{c}_{k,n}. \quad (3.21)$$

Now we realize that $\psi_{k,n}(x)$ is the only non-constant term in the integral: Only the $n = 0$ component contributes. This is the improvement as compared to the last paragraph, where $n > 0$ terms only vanished in the limit of small intervals. Since $\int_{-1}^1 dx \psi_{k,n}(x) = \sqrt{L_k} \delta_{n,0}$ we obtain

$$W \int_{-1}^1 dx V(x) \hat{c}(x) = W \sum_k \sqrt{L_k} \tilde{V}_k \hat{c}_k = \sum_k V_k \hat{c}_k, \quad (3.22)$$

with discrete hybridization couplings

$$V_k^2 = W^2 L_k \tilde{V}_k^2 = \frac{W^2}{\pi} \int_{I_k} d\omega \Delta(\omega). \quad (3.23)$$

Let us turn to the free conduction modes now. Inserting the decomposition of $\hat{c}(x)$ and $\hat{c}^\dagger(x)$ we find:

$$\int_{-1}^1 dx g(x) \hat{c}^\dagger(x) \hat{c}(x) = \int_{-1}^1 dx g(x) \sum_{k,k'} \sum_{n,n'=0}^{\infty} \psi_{k,n}^*(x) \psi_{k',n'}(x) \hat{c}_k^\dagger \hat{c}_{k'} \quad (3.24)$$

Notice that up to this point no approximation has been made. In the next step, however, we carry out the same approximation as in the last paragraph, dropping all terms with $n > 0$. There are two arguments for this approximation [9]:

- (i) The impurity couples only to the $n = 0$ state, while $n > 0$ states contribute only through their coupling to the $n = 0$ state.
- (ii) The coupling between $n = 0$ and $n > 0$ states vanishes as $L_k \rightarrow 0$, and hence the approximation becomes exact. For a more detailed discussion of these issues, we refer to Refs. [9, 130].

Dropping all terms with $n, n' \neq 0$ we have

$$\int_{-1}^1 dx g(x) \hat{c}^\dagger(x) \hat{c}(x) = \int_{-1}^1 dx g(x) \sum_{k,k'} \psi_{k,n=0}^*(x) \psi_{k',n=0}(x) \hat{c}_k^\dagger \hat{c}_{k'} \quad (3.25)$$

$$= \sum_k \frac{1}{L_k} \int_{I_k} dx g(x) \hat{c}_k^\dagger \hat{c}_k . \quad (3.26)$$

Here, we have used that $\psi_{k,n=0}(x) = 0$ for $x \notin I_k$, which implies $\psi_{k,n=0}^*(x) \psi_{k',n=0}(x) = \delta_{k,k'}/L_k$. Hence, the discrete version of the conduction term is given by

$$W \int_{-1}^1 dx g(x) \hat{c}^\dagger(x) \hat{c}(x) = \sum_k \epsilon_k \hat{c}_k^\dagger \hat{c}_k , \quad (3.27)$$

with discrete energies

$$\epsilon_k = \frac{W}{L_k} \int_{I_k} dx g(x) . \quad (3.28)$$

When fixing the hybridization coupling $V(x)$ in Eq. (3.20), we have simultaneously defined $g(x)$ and its inverse $x(\omega)$ through Eq. (3.10), since the hybridization function $\Delta(x)$ is fixed. Now one might think that, in order to find the discrete energies, we need to solve Eq. (3.10) for $x(\omega)$ and invert it to obtain $g(x)$. However, it turns out that this is not the case. Instead, we can simply calculate them as [9, 130]

$$\epsilon_k = W \frac{\int_{I_k} d\omega \Delta(\omega) \omega}{\int_{I_k} d\omega \Delta(\omega)} = \frac{W^3}{\pi V_k^2} \int_{I_k} d\omega \Delta(\omega) \omega . \quad (3.29)$$

Let us prove that this is indeed equal to Eq. (3.28). We start from Eq. (3.10), with constant $V^2(x(\omega)) = \tilde{V}_k^2 = W^{-2} L_k^{-1} V_k^2$ as chosen previously. Hence, Eq. (3.10) becomes

$$\frac{dx(\omega)}{d\omega} W^{-2} L_k^{-1} V_k^2 = \frac{\Delta(\omega)}{\pi} . \quad (3.30)$$

We insert this into the right hand side of Eq. (3.29) and find

$$\frac{W^3}{\pi V_k^2} \int_{I_k} d\omega \Delta(\omega) \omega = \frac{W}{L_k} \int_{I_k} d\omega \frac{dx(\omega)}{d\omega} \omega. \quad (3.31)$$

We can now use the substitution $\omega = g(x)$ to make x the variable of integration, and hence

$$\frac{W^3}{\pi V_k^2} \int_{I_k} d\omega \Delta(\omega) \omega = \frac{W}{L_k} \int_{I_k} dx \frac{dg(x)}{dx} \frac{\partial x(\omega(x))}{\partial \omega(x)} g(x) \quad (3.32)$$

$$= \frac{W}{L_k} \int_{I_k} dx g(x), \quad (3.33)$$

where we have used that $x(\omega) = g^{-1}(\omega)$ is the inverse of $g(x)$. This proves the equivalence of Eq. (3.28) and Eq. (3.29): the latter can be easily evaluated to find the discrete energies ϵ_k in practice.

i

Summary. In this section we have shown how to transform the Anderson impurity model in the continuum

$$\hat{H}_{\text{SIAM}} = \hat{H}_{\text{loc}} + W \sum_{\sigma} \left[\int_{-1}^1 dx V(x) \left(\hat{d}_{\sigma}^{\dagger} \hat{c}_{\sigma}(x) + \text{H.c.} \right) + \int_{-1}^1 dx g(x) \hat{c}_{\sigma}^{\dagger}(x) \hat{c}_{\sigma}(x) \right]$$

into its discrete version

$$\hat{H}_{\text{SIAM}} = \hat{H}_{\text{loc}} + \sum_{k,\sigma} V_k \left(\hat{d}_{\sigma}^{\dagger} \hat{c}_{k,\sigma} + \hat{c}_{k,\sigma}^{\dagger} \hat{d}_{\sigma} \right) + \sum_{k,\sigma} \epsilon_k \hat{c}_{k,\sigma}^{\dagger} \hat{c}_{k,\sigma}.$$

We have provided two possibilities for the discretization:

(i) One can choose $g(x) = x$, which, by Eq. (3.10), gives $V^2(x) = \Delta(x)/\pi$. The discretization then leads to hybridization and energy coefficients

$$V_k = \frac{W}{\pi \sqrt{\Delta x_k}} \int_{I_k} dx \Delta(x) \quad \text{and} \quad \epsilon_k = \frac{W}{\Delta x_k} \int_{I_k} dx x.$$

(ii) We can choose $V^2(x \in I_k) = (\pi L_k)^{-1} \int_{I_k} dx \Delta(x)$ to be step-wise constant, obtaining

$$V_k^2 = \frac{W^2}{\pi} \int_{I_k} dx \Delta(x) \quad \text{and} \quad \epsilon_k = W \frac{\int_{I_k} dx \Delta(x) x}{\int_{I_k} dx \Delta(x)}.$$

Linear and logarithmic discretization. So far we have always assumed that we have some given intervals I_k . In principle, we are free to choose them at will, as long as their length L_k is sufficiently small. In practice, there are two popular discretization schemes, namely linear and logarithmic discretization. In the linear discretization scheme, intervals I_k are all equally sized, meaning that $L_k = L$ is independent of k , providing

equal resolution over the spectrum. On the other hand, logarithmic discretization is particularly useful when dealing with low-energy phenomena, and is typically employed in NRG simulations [9]. In this case, we take intervals $I_k = [x_{k+1}, x_k]$ with $x_k = \Lambda^{-k}$, and hence, $L_k = \Lambda^{-k}(1 - \Lambda^{-1})$. The parameter Λ is the discretization parameter, and the continuum limit is recovered for $\Lambda \rightarrow 1$.

3.2.2. Lanczos chain mapping

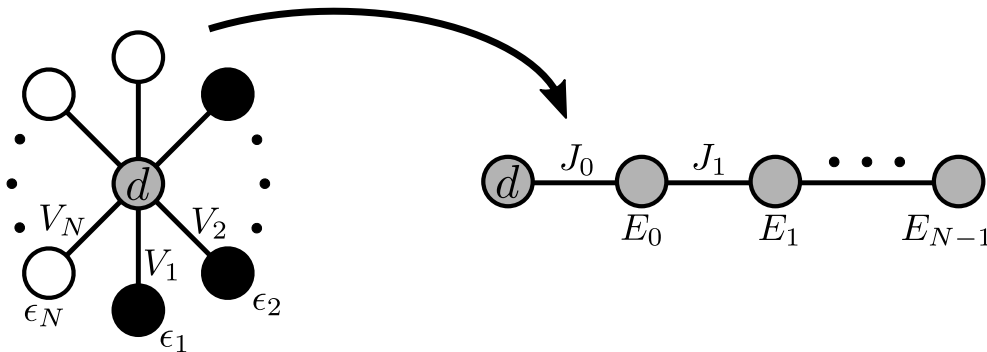


Figure 3.2.: Mapping from star to chain geometry. Starting from a discretized conduction electron bath with N sites, hybridization couplings V_k and corresponding on-site energies ϵ_k , the star-like Anderson model is mapped into a one-dimensional chain. In the chain, only the first bath mode \hat{a}_0 couples to the impurity, while all remaining chain sites are coupled to their nearest-neighbors.

In the previous section, we have seen how the continuum bath of the Anderson impurity model can be discretized into a finite number of bath modes. In this form, the impurity interacts with all bath modes, while the bath modes do not interact with each other directly. The “geometry” of the Hamiltonian looks like a star, with the impurity, in the middle, connected to all bath sites, see Fig. 3.2: it is called the “*star geometry*”. However, when simulating the model using numerical techniques such as NRG or TN techniques, it is often beneficial to have short-range couplings. Employing the Lanczos tridiagonalization algorithm, it is possible to map the star-like bath into a chain, Fig. 3.2. Here, only the first bath site is interacting with the impurity, while the remaining bath sites couple with their nearest neighbors. Let us now briefly discuss how this mapping works from a mathematical viewpoint. The Hamiltonian for the bath term — after truncation of the bath modes — is given in matrix notation as

$$\hat{H}_{\text{cond}} = \hat{\mathbf{c}}^\dagger \mathbb{H}_{\text{cond}} \hat{\mathbf{c}} = \begin{pmatrix} \hat{c}_1^\dagger & \hat{c}_2^\dagger & \dots & \hat{c}_N^\dagger \end{pmatrix} \begin{pmatrix} \epsilon_1 & 0 & \dots & 0 \\ 0 & \epsilon_2 & & \vdots \\ \vdots & & \ddots & 0 \\ 0 & \dots & 0 & \epsilon_N \end{pmatrix} \begin{pmatrix} \hat{c}_1 \\ \hat{c}_2 \\ \vdots \\ \hat{c}_N \end{pmatrix}, \quad (3.34)$$

where we have dropped spin indices as usual. In the first step, we want to simplify the hybridization term, $\sum_k V_k \hat{d}^\dagger \hat{c}_k$, by introducing a new bath mode \hat{a}_0 that captures the

entire hybridization interaction. We define

$$\hat{a}_0 = J_0^{-1} \sum_k V_k \hat{c}_k, \quad (3.35)$$

with $J_0 = \sqrt{\sum_k V_k^2}$ to ensure the correct normalization, $\{\hat{a}_0, \hat{a}_0^\dagger\} = \mathbb{1}$. The hybridization Hamiltonian then takes the simple form

$$\hat{H}_{\text{hyb}} = J_0 \left(\hat{d}^\dagger \hat{a}_0 + \text{H.c.} \right). \quad (3.36)$$

The chain mapping can then be performed by transforming the matrix \mathbb{H}_{cond} as $\mathbb{H}_{\text{cond}} = \mathbb{Q}^\dagger \mathbb{H}'_{\text{cond}} \mathbb{Q}$, where \mathbb{Q} is an orthogonal matrix and $\mathbb{H}'_{\text{cond}}$ is tridiagonal

$$\mathbb{H}'_{\text{cond}} = \begin{pmatrix} \alpha_0 & \beta_1 & 0 & \dots & 0 \\ \beta_1 & \alpha_1 & \beta_2 & & \vdots \\ \vdots & \beta_2 & \alpha_2 & \ddots & 0 \\ & & \ddots & \ddots & \beta_{N-1} \\ 0 & \dots & 0 & \beta_{N-1} & \alpha_{N-1} \end{pmatrix}. \quad (3.37)$$

This transformation can be obtained employing Lanczos' algorithm. Choosing the initial vector $Q_{1,k} = J_0^{-1} V_k$ we ensure that \hat{a}_0 is defined as above. Hence, we can rewrite the conduction electron Hamiltonian as

$$\hat{H}_{\text{cond}} = \hat{\mathbf{c}}^\dagger \mathbb{Q}^\dagger \mathbb{H}'_{\text{cond}} \mathbb{Q} \hat{\mathbf{c}} = \hat{\mathbf{a}}^\dagger \mathbb{H}'_{\text{cond}} \hat{\mathbf{a}}, \quad (3.38)$$

with $\hat{\mathbf{a}} = \mathbb{Q} \hat{\mathbf{c}}$. Due to the tridiagonal form of $\mathbb{H}'_{\text{cond}}$, the conduction Hamiltonian transforms into a chain with only nearest-neighbor couplings

$$\hat{H}_{\text{cond}} = \sum_{n=1}^{N-1} \left(J_n \hat{a}_n^\dagger \hat{a}_{n-1} + \text{H.c.} \right) + \sum_{n=0}^{N-1} E_n \hat{a}_n^\dagger \hat{a}_n, \quad (3.39)$$

where energies $E_n = \alpha_n$ and couplings $J_{n>0} = \beta_n$ are easily obtained from Lanczos algorithm.

i

Warning. It is well known that Lanczos' algorithm is intrinsically unstable. For the practical application here, however, there is a brute force way to circumvent the problem: We can simply carry out calculations with extremely high numerical precision. For example, we have employed floating-point numbers with ≈ 200 digits using the variable precision arithmetic (VPA) in Matlab. After finding the Lanczos coefficients it is then possible to diagonalize the matrix with the chain coefficients, from which one obtains the corresponding Hamiltonian parameters in star geometry. Clearly, those coefficients should match the original ones we started with. This is a simple check to ensure that the chain parameters have been calculated correctly.

i

Summary. Using Lanczos' tridiagonalization algorithm we have discussed how the discrete Anderson impurity model can be transformed from the star-geometry to the chain-geometry, where the spinful Hamiltonian

$$\hat{H}_{\text{SIAM}} = \hat{H}_{\text{loc}} + \sum_{\sigma} \left(J_0 \left(\hat{d}_{\sigma}^{\dagger} \hat{a}_{0,\sigma} + \text{H.c.} \right) + \sum_{n=1}^{N-1} \left(J_n \hat{a}_{n,\sigma}^{\dagger} \hat{a}_{n-1,\sigma} + \text{H.c.} \right) + \sum_{n=0}^{N-1} E_n \hat{a}_{n,\sigma}^{\dagger} \hat{a}_{n,\sigma} \right) \quad (3.40)$$

is essentially one-dimensional, and consists of nearest-neighbor terms only. The on-site energies and hopping rates in the chain are related to the hybridization couplings and Lanczos coefficients as

$$J_0 = \sqrt{\sum_k V_k^2}, \quad J_{n \geq 1} = W \beta_n, \quad E_{n \geq 0} = W \alpha_n. \quad (3.41)$$

3.3. Chain mapping II: Orthogonal Polynomials

In this section, we discuss another possibility to carry out the chain mapping of the Anderson impurity model. In contrast to the previous section, this technique is directly applied to the continuum version of the SIAM and does not require an explicit discretization. Hence, discretization errors are in principle absent in this approach, see also Ref.[131], at the cost of an infinitely long chain. In practical applications, the chain needs to be truncated, often with negligible additional errors. The chain mapping is performed by employing a unitary transformation based on orthogonal polynomials. For this reason, we first discuss some crucial theoretical basics of orthogonal polynomials. Later, we show explicitly how the SIAM is transformed from the star to the chain geometry.

3.3.1. Theory of orthogonal polynomials

Let us discuss some of the essential theory of orthogonal polynomials required in the following section. Here, and later, we follow Refs. [54, 55, 132], where the orthogonal polynomial chain mapping has been introduced for open quantum systems. We start by defining the inner product of two real polynomials p and q as

$$\langle p, q \rangle = \int_a^b p(x) q(x) d\mu(x), \quad (3.42)$$

where $d\mu(x)$ denotes a positive measure $d\mu(x) = V^2(x) dx$. Of course, it is not by accident that we have denoted the function in the measure by $V(x)$, but this will become clear later. Two polynomials $p(x)$ and $q(x)$ are said to be orthogonal with respect to the

measure $d\mu(x)$, if $\langle p, q \rangle = 0$. The inner product induces a norm for the polynomials, given by $\|p\| = \sqrt{\langle p, p \rangle}$.

Given some measure function $V^2(x)$, we construct a set of orthogonal polynomials using a Gram-Schmidt orthogonalization procedure for the basis functions $1, x, x^2, \dots$. The whole procedure does indeed show some similarities to the Lanczos' algorithm employed in the last section. We start by constructing a set of orthogonal *monic polynomials*, i.e., with the coefficient of maximal degree equal to one, which we denote by $\pi_n(x)$. Obviously, $\pi_n(x)$ is related to the corresponding normalized polynomials $p_n(x)$ through $p_n(x) = \pi_n(x)/\|\pi_n\|$ and $\pi_n(x)$ can be obtained from $p_n(x)$ through division by the leading coefficient a_n of $p_n(x)$, $\pi_n(x) = p_n(x)/a_n$.

Suppose we have constructed a set of such orthogonal polynomials, and we have the corresponding monic polynomials $\{\pi_n\}$. The difference $\pi_{n+1} - x\pi_n$ is a polynomial of degree $\leq n$, and hence can be expanded in terms of the monic polynomials as

$$\pi_{n+1}(x) - x\pi_n(x) = \sum_{k=0}^n c_k \pi_k(x). \quad (3.43)$$

Our goal is now to find all expansion coefficients c_k . Due to the orthogonality property of the polynomials, we can find the coefficient c_n by taking the scalar product of Eq. (3.43) with π_n ,

$$\langle \pi_n, \pi_{n+1} - x\pi_n \rangle = \langle \pi_n, \sum_{k=0}^n c_k \pi_k \rangle = c_n \langle \pi_n, \pi_n \rangle, \quad (3.44)$$

and hence

$$c_n = -\frac{\langle \pi_n, x\pi_n \rangle}{\langle \pi_n, \pi_n \rangle}. \quad (3.45)$$

We can proceed in the same way to obtain the coefficient c_{n-1} . We now take the scalar product with π_{n-1} , which yields

$$c_{n-1} = -\frac{\langle \pi_{n-1}, x\pi_n \rangle}{\langle \pi_{n-1}, \pi_{n-1} \rangle} = -\frac{\langle x\pi_{n-1}, \pi_n \rangle}{\langle \pi_{n-1}, \pi_{n-1} \rangle} = -\frac{\langle \pi_n, \pi_n \rangle}{\langle \pi_{n-1}, \pi_{n-1} \rangle}. \quad (3.46)$$

Notice that in the scalar product we can simply move x from the ket into the bra as they are simply multiplied, see Eq. (3.42). Further, we have employed that $x\pi_{n-1}$ can be expanded in monic polynomials up to degree n , where only π_n survives in the scalar product with unit expansion coefficient. In the next step, we notice that all remaining coefficients, given just like before as

$$c_{l < n-1} = -\frac{\langle \pi_l, x\pi_n \rangle}{\langle \pi_l, \pi_l \rangle} = -\frac{\langle x\pi_l, \pi_n \rangle}{\langle \pi_l, \pi_l \rangle} = -\frac{\langle \pi_{l+1}, \pi_n \rangle}{\langle \pi_l, \pi_l \rangle} = 0, \quad (3.47)$$

disappear exactly since $\langle \pi_{l+1}, \pi_n \rangle = 0$ for $l < n - 1$. Hence, we find that the sum in Eq. (3.43) has just two nonzero terms. So, we obtain the so called three-term recurrence relation:

$$\pi_{n+1}(x) - x\pi_n(x) = c_{n-1} \pi_{n-1}(x) + c_n \pi_n(x) \quad (3.48)$$

It relates a monic polynomial π_{n+1} to the previous two, π_n and π_{n-1} . Notice the similarity with Lanczos' algorithm, where a new Lanczos vector is expressed in terms of the previous two.

i

Recurrence relation for orthogonal polynomials. Given a measure $d\mu(x)$, the corresponding set of orthogonal monic polynomials satisfies the three-term recurrence relation

$$\pi_{n+1}(x) = (x - \alpha_n)\pi_n(x) - \beta_n\pi_{n-1}(x) \quad \forall n \geq 0, \quad (3.49)$$

with $\pi_{-1}(x) = 0$, and α_n and β_n given by

$$\alpha_n = -c_n = \frac{\langle \pi_n, x\pi_n \rangle}{\langle \pi_n, \pi_n \rangle} \quad \text{and} \quad \beta_n = -c_{n-1} = \frac{\langle \pi_n, \pi_n \rangle}{\langle \pi_{n-1}, \pi_{n-1} \rangle}. \quad (3.50)$$

The normalized polynomials are then obtained by $p_n(x) = \pi_n(x)/\|\pi_n\|$. For the chain mapping it will be important to find the recurrence coefficients α_n and β_n for a given $d\mu(x)$, which is related to the hybridization function, while the polynomials are not needed explicitly. These coefficients can be obtained analytically for some special cases [54], but are usually calculated numerically [133, 134]. For a weighting function $V^2(x)$ with finite support $[a, b]$, it can be shown that α_n and β_n converge as $\alpha_n \rightarrow (a + b)/2$ and $\beta_n \rightarrow (b - a)^2/16$ for $n \rightarrow \infty$ [54].

The recurrence relation in Eq. (3.49) can also be formulated for normalized polynomials and is given by [54]

$$p_{n+1}(x) = (C_n x - A_n)p_n(x) - B_n p_{n-1}(x) \quad \forall n \geq 0, \quad (3.51)$$

where again $p_{-1}(x) = 0$. The coefficients A_n, B_n and C_n are related to the coefficients α_n and β_n in Eq. (3.49) through the equations

$$A_n = \frac{\alpha_n}{\sqrt{\beta_{n+1}}}, \quad B_n = \sqrt{\frac{\beta_n}{\beta_{n+1}}}, \quad C_n = \frac{1}{\sqrt{\beta_{n+1}}}. \quad (3.52)$$

These relations will be used in the next section.

3.3.2. Chain mapping for the Anderson impurity model

Let us now discuss how orthogonal polynomials can be employed to map the continuum Anderson impurity model into a chain with nearest-neighbor interactions. The first thing we notice is that there is a well defined combination of operators that couples to the system

$$\hat{a}_0 = J_0^{-1} W \int_{-1}^{+1} dx V(x) \hat{c}(x), \quad (3.53)$$

where J_0 is a normalization factor such that

$$\mathbb{1} = \{\hat{a}_0, \hat{a}_0^\dagger\} = J_0^{-2} W^2 \int_{-1}^{+1} dx V^2(x) \implies J_0 = W \sqrt{\int_{-1}^{+1} dx V^2(x)}. \quad (3.54)$$

Question

How can we extend this \hat{a}_0 to a complete *discrete* set of operators $\{\hat{a}_n, n = 0, \dots, \infty\}$ made from appropriate combinations of the original $\hat{c}(x)$?

The solution to this question is a unitary transformation based on orthogonal polynomials. We can define new fermionic modes a_n as a linear combination of the continuum modes $\hat{c}(x)$,

$$\hat{a}_n = \int_{-1}^{+1} dx U_n(x) \hat{c}(x) \quad \text{for } n = 0 \dots \infty, \quad (3.55)$$

and impose the canonical commutation relations¹:

$$\begin{aligned} \{\hat{a}_n, \hat{a}_m^\dagger\} &= \int_{-1}^{+1} \int_{-1}^{+1} dx dy U_n(x) U_m(y) \overbrace{\{\hat{c}(x), \hat{c}^\dagger(y)\}}^{\delta(x-y)} \\ &= \int_{-1}^{+1} dx U_n(x) U_m(x) = \delta_{n,m} \end{aligned} \quad (3.56)$$

We see that the canonical commutation relationships are obeyed *if and only if* the $\{U_n(x)\}$ are *orthogonal polynomials*. It turns out that the correct choice the transformation $U_n(x)$ is [54]

$$U_n(x) = V(x) p_n(x), \quad (3.57)$$

where $\{p_n(x)\}$ is a set of orthonormal polynomials with respect to the measure $d\mu(x) = V^2(x) dx$. The inverse transformation can be written explicitly and is given by

$$\hat{c}(x) = \sum_{n=0}^{\infty} U_n(x) \hat{a}_n. \quad (3.58)$$

To verify this, simply multiply both sides by $U_m(x)$ and integrate. We now check how the transformation allows to rewrite the Hamiltonian in the new basis. Let us start with the hybridization term:

$$\hat{H}_{\text{hyb}} = W \int_{-1}^{+1} dx V(x) \left(\hat{d}^\dagger \hat{c}(x) + \text{H.c.} \right) \quad (3.59)$$

¹Notice that $\{\hat{a}_n, \hat{a}_m\} = \{\hat{a}_n^\dagger, \hat{a}_m^\dagger\} = 0$ due to the anti-commutation relations of the original operators $\hat{c}(x)$ and $\hat{c}^\dagger(x)$, independently of the explicit choice of $U_n(x)$.

We insert the transformation in Eq. (3.58) for the fermionic operators $\hat{c}(x)$ and $\hat{c}^\dagger(x)$, and use that $U_n(x) = V(x)p_n(x)$ to find:

$$\begin{aligned}\hat{H}_{\text{hyb}} &= W \sum_{n=0}^{\infty} \int_{-1}^{+1} dx V^2(x) p_n(x) \left(\hat{d}^\dagger \hat{a}_n + \text{H.c.} \right) \\ &= J_0 \underbrace{\sum_{n=0}^{\infty} \int_{-1}^{+1} dx V^2(x) p_0 p_n(x)}_{\langle p_0, p_n \rangle} \left(\hat{d}^\dagger \hat{a}_n + \text{H.c.} \right) \\ &= J_0 \left(\hat{d}^\dagger \hat{a}_0 + \text{H.c.} \right)\end{aligned}\quad (3.60)$$

Here, we have used that $p_0 = W/J_0$ is just a constant and only the constant polynomial survives the integral, due to their orthogonality property. Notice that $J_0/W = p_0^{-1} = \sqrt{\int_{-1}^{+1} dx V^2(x)}$ as expected. Consider now the bath Hamiltonian, where we choose $g(x) = x$ for a reason that will become clear shortly:

$$\hat{H}_{\text{cond}} = W \int_{-1}^{+1} dx x \hat{c}^\dagger(x) \hat{c}(x) \quad (3.61)$$

Notice that according to Eq. (3.10) this choice for $g(x)$ implies $V^2(x) = \Delta(x)/\pi$. Again, we first insert the transformation for the operators $\hat{c}(x)$ and $\hat{c}^\dagger(x)$ (see Eq. (3.58)), finding:

$$\hat{H}_{\text{cond}} = W \sum_{n,m=0}^{\infty} \int_{-1}^{+1} dx x V^2(x) p_n(x) p_m(x) \hat{a}_m^\dagger \hat{a}_n \quad (3.62)$$

We cannot directly employ the orthogonality property of the polynomials, due to the additional factor x in the integral. However, the choice $g(x) = x$ allows us to exploit the three-term recurrence relation of the orthogonal polynomials, see Eq. (3.51). We can solve it for the term $x p_n(x)$:

$$x p_n(x) = \frac{B_n}{C_n} p_{n-1}(x) + \frac{A_n}{C_n} p_n(x) + \frac{1}{C_n} p_{n+1}(x) \quad (3.63)$$

Inserting into the integral we get:

$$\hat{H}_{\text{cond}} = W \sum_{n,m=0}^{\infty} \int_{-1}^{+1} dx V^2(x) p_m(x) \left(\frac{B_n}{C_n} p_{n-1}(x) + \frac{A_n}{C_n} p_n(x) + \frac{1}{C_n} p_{n+1}(x) \right) \hat{a}_m^\dagger \hat{a}_n \quad (3.64)$$

Now we can use the orthogonality relations and carry out the sum over m , since the integration brings Krönecker delta's for the three terms²:

$$\hat{H}_{\text{cond}} = W \sum_{n=0}^{\infty} \left(\frac{B_{n+1}}{C_{n+1}} \hat{a}_n^\dagger \hat{a}_{n+1} + \frac{A_n}{C_n} \hat{a}_n^\dagger \hat{a}_n + \frac{1}{C_n} \hat{a}_{n+1}^\dagger \hat{a}_n \right) \quad (3.65)$$

²We also shift the index in the first term, $n \rightarrow n+1$, as the $n=0$ contribution of the first term in Eq. (3.64) vanishes: ($p_{-1} = 0$).

Using the relation between the coefficients A_n, B_n, C_n and α_n, β_n given in Eq. (3.52), we finally get the bath Hamiltonian in the desired tight-binding form:

$$\hat{H}_{\text{cond}} = W \sum_{n=0}^{\infty} \left(\sqrt{\beta_{n+1}} \left(\hat{a}_n^\dagger \hat{a}_{n+1} + \hat{a}_{n+1}^\dagger \hat{a}_n \right) + \alpha_n \hat{a}_n^\dagger \hat{a}_n \right) \quad (3.66)$$

Summary. Here we have shown how to map the SIAM in the continuum, see Section 3.1.2, into an infinitely long-tight binding chain using orthogonal polynomials as introduced in Refs. [54, 55]. Reinstalling spin indices, the final form of the Hamiltonian is

$$\begin{aligned} \hat{H}_{\text{SIAM}} = \hat{H}_{\text{loc}} &+ \sum_{\sigma} J_0 \left(\hat{d}_{\sigma}^\dagger \hat{a}_{0,\sigma} + \text{H.c.} \right) \\ &+ \sum_{\sigma} \sum_{n=1}^{\infty} \left(J_n \hat{a}_{n,\sigma}^\dagger \hat{a}_{n-1,\sigma} + \text{H.c.} \right) + \sum_{\sigma} \sum_{n=0}^{\infty} E_n \hat{a}_{n,\sigma}^\dagger \hat{a}_{n,\sigma}, \end{aligned} \quad (3.67)$$

where:

$$J_{n=0} = W \sqrt{\int_{-1}^{+1} dx V^2(x)} \quad J_{n \geq 1} = W \sqrt{\beta_n} \quad E_{n \geq 0} = W \alpha_n \quad (3.68)$$

Recall that $V(x)$ is defined through the hybridization function as $V^2(x) = \Delta(x)/\pi$. The Hamiltonian looks the same as in Eq. (3.40), which was obtained from Lanczos chain mapping. The difference, however, is the infinitely long chain, while in Lanczos mapping the number of bath sites is finite from the beginning, due to discretization and truncation. When using orthogonal polynomials instead, we have to truncate the chain appropriately, usually done in such a way that no excitation reaches the end of the chain [123]. For practical simulations we need find the recurrence coefficients $\alpha_{n \geq 0}$ and $\beta_{n \geq 1}$ for the measure $d\mu(x) = V^2(x) dx$. In most cases, this will be done numerically, by employing the routines presented in Refs. [133, 134]. Once the recurrence coefficients are known, we have all the chain parameters and we can simulate the Anderson model in the chain representation.

3.4. Example: Chain mapping at $T = 0$

To illustrate the chain mapping, let us consider an explicit example. As in the following chapters, we employ a semi-circular hybridization function

$$V^2(x) = \frac{1}{\pi} \Delta(\epsilon = Wx) = \frac{\Gamma}{W\pi} \sqrt{1-x}, \quad (3.69)$$

see Fig. 3.3(a), with W the half-bandwidth and Γ the hybridization coupling strength. In the thermodynamic (continuum) limit, the corresponding chain coefficients are analytically known to be $J_n = W/2$ and $E_n = 0$ [135]. Numerically we carry out the

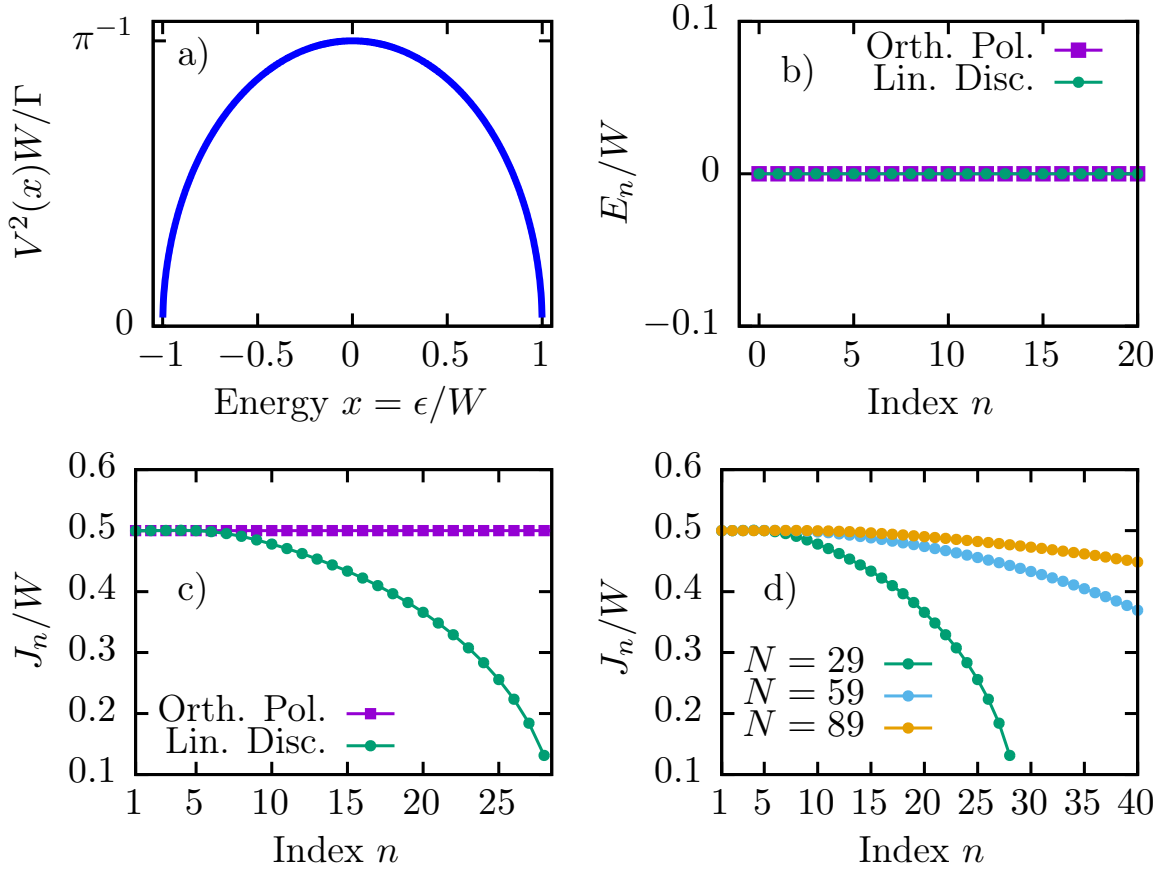


Figure 3.3.: Chain coefficients for semi-circular hybridization function. a) Semi-circular hybridization function $V^2(x) = \Gamma\sqrt{1-x}/W\pi$, where chain coefficients are analytically known to be $J_n = W/2$ and $E_n = 0$ [135]. b,c) On-site energies E_n (b) and nearest neighbor couplings J_n (c) of chain sites as obtained from linear discretization plus Lanczos with $N = 29$, and orthogonal polynomials. d) Dependence of the couplings on the number of bath sites N when using simple linear discretization.

chain mapping by employing two different methods: (i) We discretize the bath using the simple discretization scheme with constant interval length L_k , the so-called linear discretization, and map the discrete star-like Hamiltonian to a chain using Lanczos' algorithm. (ii) We carry out the chain mapping exploiting orthogonal polynomials. In Fig. 3.3(b) we see that the on-site energies E_n of the chain sites are the same for linear discretization with $N = 29$ bath sites and orthogonal polynomials, $E_n = 0$, in agreement with the values expected for the thermodynamic limit. Using orthogonal polynomials, which indeed work in the continuum limit, we find the numerical results for the nearest neighbor couplings to match the theoretic expectation $J_n = W/2$, see Fig. 3.3(c). The linear discretization, however, shows deviations from the analytic and orthogonal polynomial results, due to the finite discretization prior to the chain mapping. As we increase the number of sites, and by that making the discretization finer, the coupling coefficients approach the value $J_n = W/2$ expected in the thermodynamic limit, as shown in Fig. 3.3(d).

3.5. The issue of the chain mapping

In this section, we briefly discuss the issue of the chain mapping, that causes problems in practical simulations with tensor networks. To understand the issue, suppose we have a bath of discrete conduction electron modes at $T = 0$, which are decoupled from the impurity. The ground state of the free electrons is given by the Fermi sea state

$$|\text{FS}\rangle = \prod_k^{\epsilon_k < 0} \hat{c}_k^\dagger |0\rangle, \quad (3.70)$$

where all electron modes with energy ϵ_k below the chemical potential $\mu = 0$ are occupied, while modes with energy $\epsilon_k > 0$ are empty. As usual, $|0\rangle$ denotes the vacuum state with no electrons. It is clear that this state is very simple in the star geometry: It is just a product state with no correlations between different modes, and hence it can be represented by an MPS with bond dimension $D = 1$. Furthermore, the ground state can be trivially set up, without the need for an explicit ground-state search. As discussed previously, the star geometry can be mapped into a chain with only nearest-neighbor interaction, which was believed to be beneficial for tensor network simulations. Hence, the chain geometry has been used regularly in practical simulations, and is employed sometimes even today [36–38, 63, 136]. However, this mapping brings one major disadvantage: It builds new fermionic bath modes as a linear combination of all original bath modes, thereby mixing occupied and empty bath modes. Hence, the Fermi sea is not a trivial product state in the chain geometry but is indeed entangled: it has partially filled chain sites. For MPS simulations, unfortunately, this is very detrimental as it strongly increases the numerical costs [39]. Moreover, in contrast to the star geometry, finding the ground state of the bath in the chain geometry requires a full DMRG ground-state search.

Let us now discuss how to circumvent this problem of the original chain mapping. Simply notice that all problems are caused by the mixing of occupied and empty conduction modes. Hence, a reasonable strategy is to separate them before mapping them into a chain, as has proven beneficial in Lanczos exact diagonalization calculations already [67]. We can simply write the bath Hamiltonian as a sum of occupied and empty modes (again, without spin indices, at $T = 0$ and decoupled impurity)

$$\sum_k \epsilon_k \hat{c}_k^\dagger \hat{c}_k = \sum_k^{\epsilon_k < 0} \epsilon_k \hat{c}_k^\dagger \hat{c}_k + \sum_k^{\epsilon_k > 0} \epsilon_k \hat{c}_k^\dagger \hat{c}_k = \sum_k \epsilon_k \hat{f}_{2k}^\dagger \hat{f}_{2k} + \sum_k \epsilon_k \hat{f}_{1k}^\dagger \hat{f}_{1k}. \quad (3.71)$$

Here, we have introduced two new fermions \hat{f}_{1k} and \hat{f}_{2k}

$$\hat{f}_{1k} = \hat{c}_k \text{ if } \epsilon_k > 0 \quad \text{and} \quad \hat{f}_{2k} = \hat{c}_k \text{ if } \epsilon_k < 0, \quad (3.72)$$

to make the separation of modes explicit also in the notation. Hence, the hybridization term becomes

$$\sum_k V_k \left(\hat{d}^\dagger \hat{c}_k + \text{H.c.} \right) = \sum_k V_{1k} \left(\hat{d}^\dagger \hat{f}_{1k} + \text{H.c.} \right) + \sum_k V_{2k} \left(\hat{d}^\dagger \hat{f}_{2k} + \text{H.c.} \right), \quad (3.73)$$

with $V_{1k} = V_k \Theta(\epsilon_k)$ and $V_{2k} = V_k \Theta(-\epsilon_k)$, where $\Theta(\cdot)$ is the Heaviside theta function. The essential idea is now to carry out independent chain mappings for \hat{f}_{1k} and \hat{f}_{2k} . This will lead to two independent chains, both of them coupled to the impurity. Since the chain mapping is carried out only for occupied (empty) modes, also the chains will be fully occupied (empty) in the bath ground state. Hence, the mixing can be avoided. Details of the chain mapping will be presented in the next section, after generalizing the approach to finite temperatures.

3.6. A fermionic thermo-field transformation

Simulating systems at finite temperature is usually a challenging task for tensor network techniques. While originally designed to simulate pure states at zero temperature, matrix product states — or tensor networks in general — can be adapted to represent density matrices as well [29, 30]. The generalization of MPS to represent a density matrix is a matrix product operator (MPO). Theoretically, it is then rather simple to prepare the thermal state of a quantum system. Given some Hamiltonian \hat{H} , the thermal state at temperature T is $\hat{\rho} \propto e^{-\hat{H}/k_B T}$. Hence, one simply needs to initialize the infinite temperature density matrix $\mathbb{1}$, and evolve it in imaginary time [41]. Numerically, however, this can be very resource-demanding.

Alternatively, there is another idea to represent mixed states. Suppose we have some Hamiltonian \hat{H} acting on the systems Hilbert space \mathcal{H}_S . We can then enlarge \mathcal{H}_S by an ancillary \mathcal{H}_A , forming a new Hilbert space $\mathcal{H}_S \otimes \mathcal{H}_A$. The idea is then to find a pure quantum state $|T\rangle$ in the enlarged Hilbert space such that tracing out the ancillary space leads to the required thermal state, $\hat{\rho}_S = \text{Tr}_A |T\rangle \langle T|$. This method is sometimes referred to as *purification* [17, 29]. A variant of purification, the so-called thermofield transformation, will be employed throughout this thesis.

Let us briefly summarize the thermofield transformation in the present context [65, 66]. First, we rename the physical conduction modes, $\hat{c}_{k\sigma} \rightarrow \hat{c}_{1k\sigma}$, by adding the additional index '1'. We then add ancillary fermions, denoted by $\hat{c}_{2k\sigma}$, supplementing the conduction Hamiltonian with an ancillary bath term:

$$\hat{H}_{\text{cond}} \rightarrow \sum_{k,\sigma} \epsilon_k \left(\hat{c}_{1k\sigma}^\dagger \hat{c}_{1k\sigma} - \hat{c}_{2k\sigma}^\dagger \hat{c}_{2k\sigma} \right) = \sum_{k,\sigma} \epsilon_k \left(\hat{c}_{1k\sigma}^\dagger \hat{c}_{1k\sigma} + \hat{c}_{2k\sigma} \hat{c}_{2k\sigma}^\dagger \right) - \sum_{k,\sigma} \epsilon_k. \quad (3.74)$$

The ancillary fermions $\hat{c}_{2k\sigma}$ do not couple to either the impurity or the physical conduction electrons, and therefore will not affect the dynamics. Dropping spin indices for a while, we introduce two new fermionic operators as linear combinations of physical and ancillary fermionic operators, through the unitary (orthogonal) thermofield transformation [63, 65, 66, 136]

$$\begin{pmatrix} \hat{f}_{1k} \\ \hat{f}_{2k} \end{pmatrix} = \begin{pmatrix} \cos \theta_k & -\sin \theta_k \\ \sin \theta_k & \cos \theta_k \end{pmatrix} \begin{pmatrix} \hat{c}_{1k} \\ \hat{c}_{2k}^\dagger \end{pmatrix} = \mathbb{O} \begin{pmatrix} \hat{c}_{1k} \\ \hat{c}_{2k}^\dagger \end{pmatrix}, \quad (3.75)$$

with inverse given by:

$$\begin{pmatrix} \hat{c}_{1k} \\ \hat{c}_{2k}^\dagger \end{pmatrix} = \begin{pmatrix} \cos \theta_k & \sin \theta_k \\ -\sin \theta_k & \cos \theta_k \end{pmatrix} \begin{pmatrix} \hat{f}_{1k} \\ \hat{f}_{2k} \end{pmatrix} = \mathbb{O}^{-1} \begin{pmatrix} \hat{f}_{1k} \\ \hat{f}_{2k} \end{pmatrix} \quad (3.76)$$

Note that the transformation includes an additional particle-hole transformation on \hat{f}_{2k} as compared to the original formulation [65, 66], in order to maintain the particle number conservation of the Hamiltonian [63]. Hence, in absence of the impurity, the thermal state is not represented by the vacuum state of \hat{f}_{1k} and \hat{f}_{2k} , but rather by the vacuum $|\emptyset_1\rangle$ of \hat{f}_{1k} and the fully occupied state $|F_2\rangle$ of \hat{f}_{2k} , which in the following we will denote by $|\emptyset_1\rangle \otimes |F_2\rangle = |\emptyset_1, F_2\rangle$. Using Eq. (3.76) we can show that the number operator $\hat{n}_{1k} = \hat{c}_{1k}^\dagger \hat{c}_{1k}$ of the physical fermions transforms as

$$\hat{c}_{1k}^\dagger \hat{c}_{1k} = \cos^2(\theta_k) \hat{f}_{1k}^\dagger \hat{f}_{1k} + \sin^2(\theta_k) \hat{f}_{2k}^\dagger \hat{f}_{2k} + \cos(\theta_k) \sin(\theta_k) \left(\hat{f}_{1k}^\dagger \hat{f}_{2k} + \hat{f}_{2k}^\dagger \hat{f}_{1k} \right). \quad (3.77)$$

Hence, the average physical electron occupation in the state $|\emptyset_1, F_2\rangle$ is

$$\langle \emptyset_1, F_2 | \hat{c}_{1k}^\dagger \hat{c}_{1k} | \emptyset_1, F_2 \rangle = \sin^2(\theta_k). \quad (3.78)$$

To enforce that these follow the thermal distribution, given by the Fermi function $f_F(\epsilon)$, we simply need to choose [136]:

$$\sin^2(\theta_k) \equiv f_F(\epsilon_k) = \frac{1}{e^{\beta\epsilon_k} + 1} \quad (3.79)$$

i

Remark: the $T = 0$ case. At zero temperature the Fermi function becomes a step function, $f_F(\epsilon_k) \xrightarrow{T \rightarrow 0} \Theta(-\epsilon_k)$, and hence the thermofield transformation is simply

$$\begin{cases} \hat{f}_{1k} = \hat{c}_{1k} & \text{and} & \hat{f}_{2k} = \hat{c}_{2k}^\dagger & \text{for } \epsilon_k > 0 \\ \hat{f}_{1k} = -\hat{c}_{2k}^\dagger & \text{and} & \hat{f}_{2k} = \hat{c}_{1k} & \text{for } \epsilon_k < 0 \end{cases}, \quad (3.80)$$

which separates occupied and empty modes precisely as we did in the last section, see Eq. (3.72). Notice that at $T = 0$ the ancillary bath, described through the \hat{c}_{2k} modes, is totally irrelevant.

Knowing how to prepare the thermal state in the basis of the bath modes \hat{f}_{1k} and \hat{f}_{2k} , we transform the Hamiltonian into this basis, by using the unitary transformation in Eq. (3.76). The hybridization term (still ignoring spin indices) becomes

$$\sum_k V_k \hat{d}^\dagger \hat{c}_{1k} = \sum_k \left(V_{1k} \hat{d}^\dagger \hat{f}_{1k} + V_{2k} \hat{d}^\dagger \hat{f}_{2k} \right), \quad (3.81)$$

with $V_{1k} = V_k \cos \theta_k$ and $V_{2k} = V_k \sin \theta_k$, as visualized in Fig. 3.4. Originally coupled to the physical conduction electrons only, the impurity now interacts with both transformed modes, \hat{f}_{1k} and \hat{f}_{2k} , with renormalized temperature-dependent couplings V_{1k}

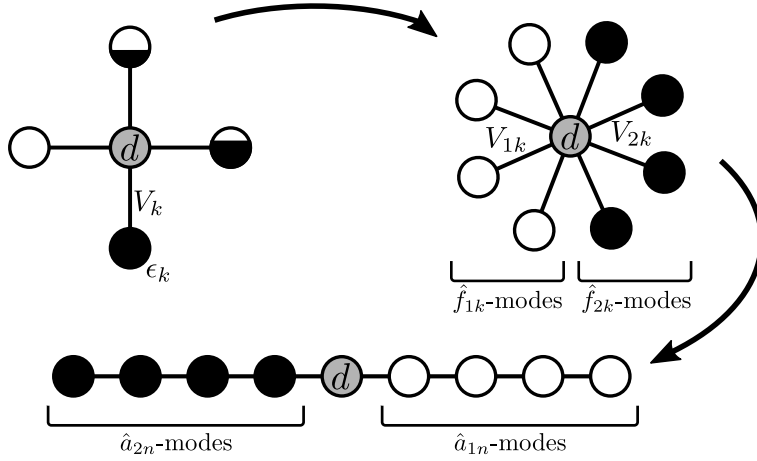


Figure 3.4.: Thermofield transformation. At finite temperature, free conduction modes \hat{c}_{1k} are partially occupied. The thermofield transformation maps the mixed thermal state $\hat{\rho} \propto e^{-\hat{H}_{\text{cond}}/k_B T}$ of the bath into a pure state $|\emptyset_1, F_2\rangle$ of an enlarged Hilbert space, with new fermionic modes \hat{f}_{1k} and \hat{f}_{2k} as defined in Eq. (3.75). They are coupled to the impurity with effective couplings $V_{1k} = V_k \cos \theta_k$ and $V_{2k} = V_k \sin \theta_k$, respectively, where $\sin^2(\theta_k) = f_F(\epsilon_k)$. In the thermal state, \hat{f}_{1k} -modes are completely empty, while \hat{f}_{2k} -modes are fully occupied. The two baths can be mapped into independent chains, see Section 3.7.

and V_{2k} . Hence, the temperature-dependent thermofield transformation encodes finite temperature into the hybridization couplings, while the state in the basis of fermions \hat{f}_{1k} and \hat{f}_{2k} is independent of T . The conduction term including the ancillary bath, Eq. (3.74), without the irrelevant constant term $\sum_k \epsilon_k$, transforms as

$$\sum_k \epsilon_k \left(\hat{c}_{1k}^\dagger \hat{c}_{1k} + \hat{c}_{2k}^\dagger \hat{c}_{2k} \right) = \sum_k \epsilon_k \left(\hat{f}_{1k}^\dagger \hat{f}_{1k} + \hat{f}_{2k}^\dagger \hat{f}_{2k} \right), \quad (3.82)$$

where we used the fact that \mathbb{O} is orthogonal and the 2×2 form of the Hamiltonian was simply $\epsilon_k \mathbb{1}_2$, hence unchanged by the rotation.

i

Summary. The thermofield transformation is given by Eq. (3.75). Reinstalling spin indices, the hybridization coupling becomes

$$\hat{H}_{\text{hyb}} = \sum_\sigma \sum_k \left(V_{1k} \hat{d}_\sigma^\dagger \hat{f}_{1k\sigma} + V_{2k} \hat{d}_\sigma^\dagger \hat{f}_{2k\sigma} + \text{H.c.} \right), \quad (3.83)$$

where $V_{1k} = V_k \cos \theta_k$ and $V_{2k} = V_k \sin \theta_k$ are temperature-dependent couplings, with $\sin^2(\theta_k) = f_F(\epsilon_k)$. For the free electron term we have:

$$\hat{H}_{\text{cond}} = \sum_\sigma \sum_k \epsilon_k \left(\hat{f}_{1k\sigma}^\dagger \hat{f}_{1k\sigma} + \hat{f}_{2k\sigma}^\dagger \hat{f}_{2k\sigma} \right) \quad (3.84)$$

Hence, the thermofield transformation leads to two independent baths, both coupled only to the impurity. The crucial improvement is the efficient representation of the

thermal state of the conduction electrons. In the new basis, its purification is given by a pure state $|\emptyset_1, F_2\rangle$ of the extended system, with fermion modes $\hat{f}_{1k\sigma}$ empty, and $\hat{f}_{2k\sigma}$ -modes completely filled.

3.7. Thermofield chain mapping

When employing the thermofield method we need to simulate two independent baths of free fermions — one empty (\hat{f}_{1k}) and one completely filled (\hat{f}_{2k}) —, both interacting with the impurity only. While in principle a direct simulation in the star geometry — using artificial long-range interactions, as discussed in Section 3.1 — would be possible, we focus on the chain geometry in this section. Notice that the two baths have different hybridization functions, defined through the couplings $V_{1k} = V_k \cos \theta_k$ and $V_{2k} = V_k \sin \theta_k$. If we employ the orthogonal polynomial chain mapping³ after changing to a continuum description, see Section 3.1.2, we define new fermions

$$\hat{a}_{c\sigma} = \int_{-1}^1 dx U_{cn}(x) \hat{f}_{c\sigma}(x), \quad (3.85)$$

where $U_{cn}(x) = V_c(x) p_{cn}(x)$ as discussed in Section 3.3. Notice that U, V and p have an additional index, corresponding to the empty ($c = 1$) and filled ($c = 2$) bath. The final form of the Hamiltonian transformed into a Wilson's chain is

$$\begin{aligned} \hat{H}_{\text{SIAM}} &= \hat{H}_{\text{loc}} + \sum_{\sigma} \sum_{c=1}^2 J_{c,0} \left(\hat{d}_{\sigma}^{\dagger} \hat{a}_{c0,\sigma} + \hat{a}_{c0,\sigma}^{\dagger} \hat{d}_{\sigma} \right) \\ &+ \sum_{\sigma} \sum_{c=1}^2 \sum_{n=1}^{\infty} \left(J_{c,n} \hat{a}_{cn,\sigma}^{\dagger} \hat{a}_{c(n-1),\sigma} + \text{H.c.} \right) + \sum_{\sigma} \sum_{c=1}^2 \sum_{n=0}^{\infty} E_{c,n} \hat{a}_{cn,\sigma}^{\dagger} \hat{a}_{cn,\sigma}, \end{aligned} \quad (3.86)$$

where $c = 1, 2$ denotes the two chains associated to \hat{f}_{1k} (and hybridization V_{1k}) and \hat{f}_{2k} (and hybridization V_{2k}). The geometry of the Hamiltonian is visualized in Fig. 3.4.

3.8. Example: Chain coefficients at finite T

Let us now discuss an example for the chain mapping at finite temperature that will be particularly important in the next chapters. In Fig. 3.5 we show the two renormalized couplings $V_c^2(x)$ in the continuum limit for the semi-circular hybridization $V^2(x) = \Gamma \sqrt{1-x^2}/\pi W$, and the corresponding chain coefficients $J_{c,n}$ and $E_{c,n}$. We clearly see that after only a few sites the chain coefficients converge towards the values expected from the theory of orthogonal polynomials⁴: At $T = 0$ the renormalized hybridization functions have support $[0, 1]$ ($V_1(x)$) and $[-1, 0]$ ($V_2(x)$), hence the couplings

³Of course, Lanczos chain mapping would work as well.

⁴For $V^2(x)$ with support $[a, b]$, the orthogonal polynomial recurrence coefficients converge as $\alpha_n \rightarrow (a+b)/2$ and $\beta_n \rightarrow (b-a)^2/16$ for $n \rightarrow \infty$, see Section 3.3.1, and $J_{n \geq 1} = W \sqrt{\beta_n}$, $E_{n \geq 0} = W \alpha_n$.

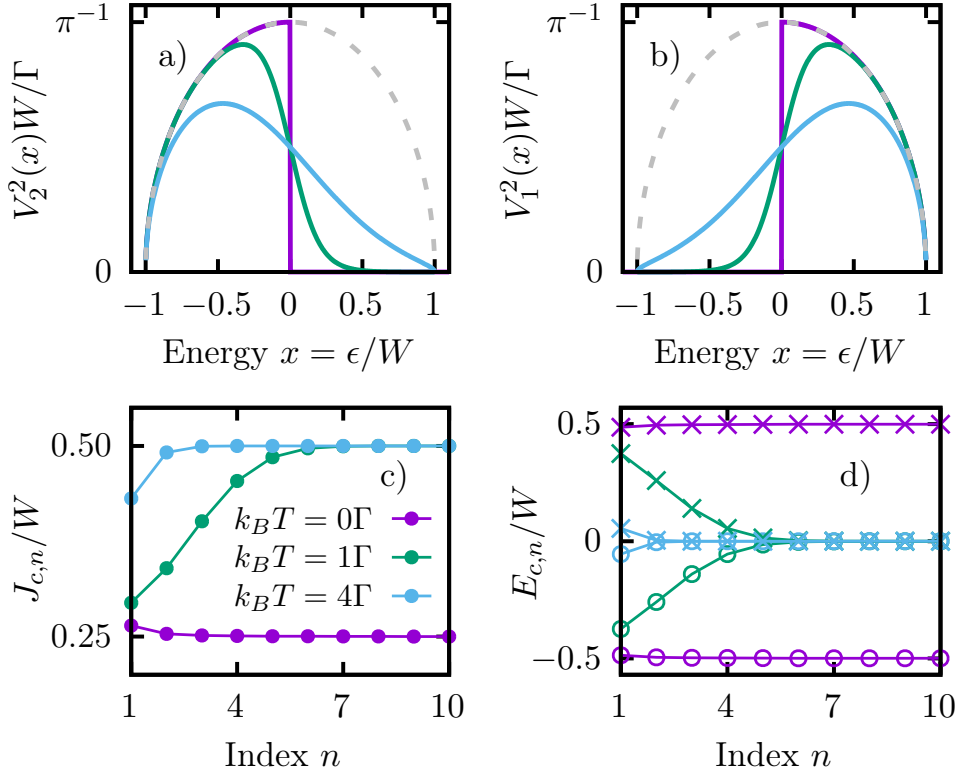


Figure 3.5.: Chain coefficients for semi-circular hybridization at finite temperature. (a,b) Renormalized hybridization couplings $V_2^2(x) = V^2(x)\sin^2(\theta)$ (a) and $V_1^2(x) = V^2(x)\cos^2(\theta)$ (b) for different temperatures T (see legend panel (c)), where $\sin^2(\theta) = f_F(x)$ is the Fermi function, to ensure the correct distribution of bath electrons, and $V^2(x) = \Gamma\sqrt{1-x^2}/\pi W$ (dashed line). c) Couplings $J_{c,n}$ along the initially empty ($c = 1$) and fully occupied ($c = 2$) chains. d) On-site energies $E_{1,n}$ (crosses) and $E_{2,n}$ (open circles). Here, $J_{1,n} = J_{2,n}$ and $E_{2,n} = -E_{1,n}$ due to the symmetric hybridization function, $V(x) = V(-x)$. All chain coefficients were calculated using the orthogonal chain mapping technique.

converge as $J_{c,n} \rightarrow W/4$, while for the on-site energies $E_{1,n} \rightarrow W/2$ and $E_{2,n} \rightarrow -W/2$. For $T > 0$ instead, both $V_1(x)$ and $V_2(x)$ have support $[-1, 1]$, implying $J_{c,n} \rightarrow W/2$ and $E_{c,n} \rightarrow 0$ for $n \rightarrow \infty$. For reasons of numerical convergence, it can be beneficial to truncate the support of $V_c(x)$ for the calculation of the chain coefficients, to eliminate regions where $V_c(x)$ falls below computational precision. This typically happens at low temperatures, where the Fermi function has tails with very small values.

3.9. Summary and discussion of simulation techniques

Let us summarize this chapter and discuss the different possibilities to simulate the single impurity Anderson model utilizing MPS. There are two major cases that we need to distinguish: $T = 0$, where any state we deal with is a pure state, and $T > 0$, where the state is mixed.

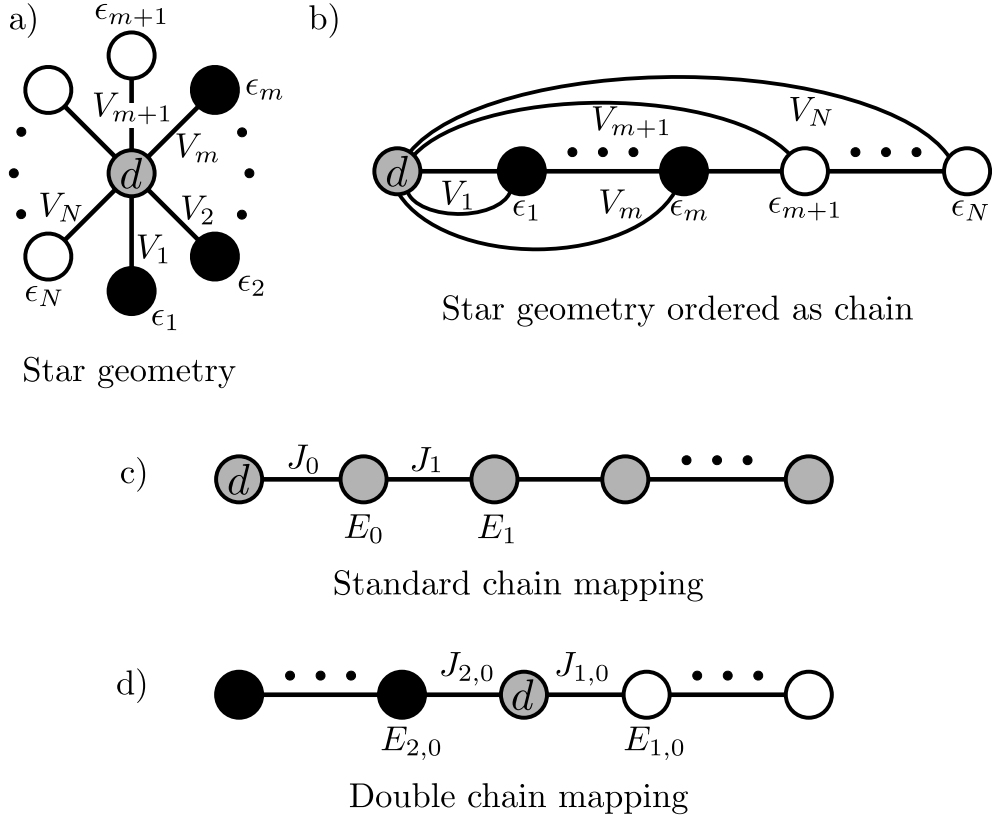


Figure 3.6.: Possible geometries to simulate the SIAM. a) SIAM in star geometry. Black and white circles represent filled and empty bath modes, respectively. b) Star geometry represented on a one-dimensional chain with artificial long-range interaction. c) Standard chain mapping: All bath modes are mapped into a single chain, leading to partially filled chain sites (grey color) d) Filled and empty modes are mapped into independent chains, preserving the “totally filled/empty” property. This structure is naturally encountered when employing the thermofield transformation plus chain mapping.

Zero Temperature. At zero temperature any quantum state is pure, and hence can be represented using standard tensor network techniques, even though the representation is not necessarily efficient. So far there have been two different geometries to simulate the SIAM at $T = 0$:

- (i) The star-like Hamiltonian, see Fig. 3.6(a), can be mapped into a chain with artificial long-range interaction, Fig. 3.6(b), where the impurity interacts with all remaining sites. The advantage of the star geometry is the efficient representation of the conduction electrons’ ground state, which is simply a product state, with filled modes below the Fermi energy E_f and empty modes above E_f . Hence, it can be represented in an MPS very efficiently, and the bath ground state can be initialized without the need for numerical optimization. If the ground state of impurity plus bath is required, one can carry out a numerical ground-state search using DMRG. However, the star geometry comes at the cost of introducing long-range interactions in the MPS, which can be more difficult to deal with,

even though from an entanglement point of view this is not a problem [39].

- (ii) The second very common possibility is the chain geometry, visualized in Fig. 3.6(c), which is obtained from the star through unitary transformations, see Section 3.2 and Section 3.3. The clear advantage of the chain geometry is that it contains only nearest-neighbor interaction, which is particularly well suited for NRG and tensor network simulations. However, as pointed out in Ref. [39], the chain geometry is significantly more entangled in the bath ground state as compared to the star, due to the mixing of filled and empty modes, leading to an increased numerical cost in MPS based simulations. Moreover, the ground state of the bath —either coupled to the impurity or not— has to be calculated numerically using DMRG.

However, we can design a third possibility, to combine the advantages of the two previous techniques:

- (iii) Rather than mapping the *entire* bath into a single chain, we separate filled and empty modes, and map them into independent chains, see Section 3.5 and Section 3.7, as visualized in Fig. 3.6(d). This geometry contains only nearest-neighbor interaction, while at the same time the bath ground state is a product state just like in the star geometry.

Finite Temperature. Let us discuss how the three possibilities generalize at finite temperatures, where we need to describe mixed states.

- (i) For the star geometry, Fig. 3.6(a) and Fig. 3.6(b), there are essentially two ways to deal with finite temperature. First, one could move from an MPS description of the state to an MPO, to represent a density matrix. The thermal state of either the bath alone or bath plus impurity would then be obtained through imaginary time evolution. Alternatively, one could employ the thermofield transformation to efficiently represent the thermal state of the conduction electrons as a pure state. It is an open question how exactly the bath sites should be ordered in the MPS to keep the entanglement low during real-time dynamics.
- (ii) For the single-chain approach there is just one way to deal with finite temperature. One needs to employ an MPO to represent the mixed state, and thermal states have to be prepared using imaginary time evolution, as was done in [41].
- (iii) When mapping the bath into two chains, we can proceed as for the star geometry. In principle, we can map the Hamiltonian into two chains, by separating modes below and above the chemical potential, and then use imaginary time evolution to prepare the thermal state. However, it is unclear how this idea would perform in practice as it has not been employed so far. Instead, the thermofield plus chain mapping approach allows for a very efficient representation and preparation of the conduction mode thermal state. We will discuss it in the next chapter.

4. Quenching the Anderson impurity model at finite temperature

In this chapter, we study the out-of-equilibrium real-time dynamics — more precisely, a quantum quench — of the single impurity Anderson model at finite temperature. We will focus, in particular, on the entanglement along the corresponding MPS representation and the analysis of the fermionic bath. The content of this chapter is published in Ref. [2].

More in detail, we consider an impurity and a half-filled conduction band, which are initially decoupled from each other. We suddenly turn on, at time $t = 0$, the hybridization coupling, evolving the system with a constant Hamiltonian \hat{H}_{SIAM} , where

$$\hat{H}_{\text{SIAM}} = \sum_{\sigma} \varepsilon_d \hat{d}_{\sigma}^{\dagger} \hat{d}_{\sigma} + U \hat{n}_{\uparrow} \hat{n}_{\downarrow} + \sum_{k,\sigma} V_k \left(\hat{d}_{\sigma}^{\dagger} \hat{c}_{k\sigma} + \hat{c}_{k\sigma}^{\dagger} \hat{d}_{\sigma} \right) + \sum_{k,\sigma} \epsilon_k \hat{c}_{k\sigma}^{\dagger} \hat{c}_{k\sigma},$$

see Chapter 3. As discussed previously, we employ a thermofield transformation to deal with finite temperatures, Section 3.6, and we map the two emerging baths into two independent chains, Section 3.7. The final Hamiltonian we simulate, see Section 3.7, is

$$\begin{aligned} \hat{H}_{\text{SIAM}} = \hat{H}_{\text{loc}} &+ \sum_{\sigma} \sum_{c=1}^2 J_{c,0} \left(\hat{d}_{\sigma}^{\dagger} \hat{a}_{c0,\sigma} + \hat{a}_{c0,\sigma}^{\dagger} \hat{d}_{\sigma} \right) \\ &+ \sum_{\sigma} \sum_{c=1}^2 \sum_{n=1}^{\infty} \left(J_{c,n} \hat{a}_{cn,\sigma}^{\dagger} \hat{a}_{cn-1,\sigma} + \text{H.c.} \right) + \sum_{\sigma} \sum_{c=1}^2 \sum_{n=0}^{\infty} E_{c,n} \hat{a}_{cn,\sigma}^{\dagger} \hat{a}_{cn,\sigma}. \end{aligned}$$

Recall that c labels the two chains, which are empty ($c = 1$) or filled ($c = 2$) in the thermal state. We initialize the system in the state $|\psi_0\rangle = |0\rangle \otimes |\emptyset_1, F_2\rangle$, where $|0\rangle$ is the impurity vacuum and $|\emptyset_1, F_2\rangle$ is the thermal state of the conduction electrons, represented as a pure state in the extended Hilbert space. For the hybridization of the impurity with the conduction electrons, we choose a semi-circular form, $V^2(x) = \Gamma\sqrt{1-x^2}/\pi W$, where $x = \epsilon/W$ is the dimensionless energy, and W half the bandwidth, see also Section 3.8 for the corresponding chain coefficients. Throughout this chapter, we fix the hybridization coupling Γ such that $W = 10\Gamma$.

The chapter is organized as follows. We first discuss different possible orderings of sites in the MPS. Section 4.2 illustrates the results we have obtained, concerning, in particular, the SIAM in the Kondo regime. In our approach, the dynamics of the entire system, including the conduction modes, is simulated, and hence we also have

information about the quantum state of the bath. By analyzing the bath state we find signatures of the Kondo effect in the quench dynamics. We particularly discuss the dynamics of the entanglement along the MPS for different chain orderings. In Section 4.3, we summarize our results and draw our conclusions. In the final sections, we provide some additional information on the numerical simulations, including numerical convergence checks and simulations with an alternative initial state.

4.1. How to order sites in the MPS

To carry out simulations using MPS there is one more decision to make: How to order the chain sites in the MPS. This question is crucial for the simulation, since it affects the entanglement structure in the MPS, and therefore has a major impact on the performance, as we will see. Three different possibilities have been considered, and will be discussed below:

- A) The most intuitive idea is to employ fermionic sites with spin degree of freedom, i.e. spinful fermionic sites, with the impurity placed in the middle of the MPS. The two chains, for empty and filled modes, are both connected to the impurity, one to the left and one to the right (see Fig. 4.1(a)). In this way, there are only nearest-neighbor interactions in the MPS, and each tensor represents both spin up and spin down states, with local (physical) dimension $d = 4$, corresponding to states $|0\rangle, |\uparrow\rangle, |\downarrow\rangle, |\uparrow\downarrow\rangle$. This choice reflects the interaction structure of the Hamiltonian.
- B) The second possibility is obtained by reordering the tensors of structure **A**. Here, the impurity is placed at the very first site of the MPS. The subsequent sites represent the two chains, with chain sites corresponding to the filled and empty chain, in an alternating fashion. Since the interaction within the two chains is nearest-neighbor, the interaction in the MPS is now up to next-nearest neighbors. The impurity is interacting with the first site of the filled chain (second tensor in Fig. 4.1(b)) and the first site of the empty chain (third tensor in Fig. 4.1(b)). The idea behind this structure is the following. Imagine that during the dynamics an electron moves from the filled into the empty chain, creating an entangled particle-hole pair. Such a particle-hole pair will be traveling along the MPS without being much spatially separated in structure **B**, while a long-ranged entanglement is certainly required in structure **A**. Similar interleaved geometries were recently used to study quantum transport [137] and 1D systems with periodic boundary conditions [138, 139].
- C) The third structure follows the idea of structure **B**. However, instead of working with spinful sites, we build the MPS with spinless sites, separating spin-up and spin-down degrees of freedom. This idea is suggested by the structure of the Hamiltonian: Spin-up and spin-down modes interact only at the impurity site. It

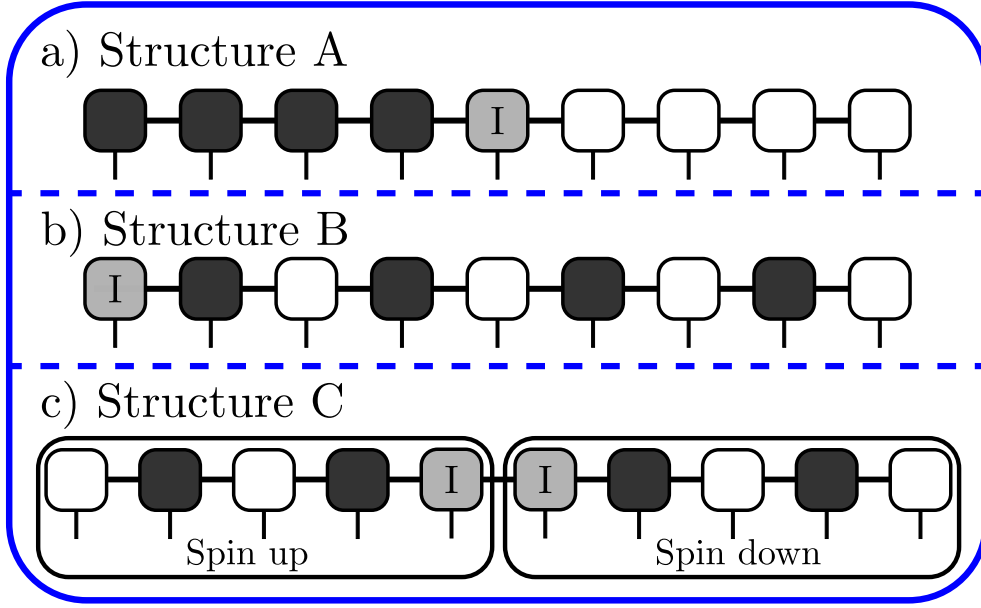


Figure 4.1.: Different possibilities to order the sites in the MPS. The impurity is visualized in light grey and empty (filled) chain sites are coloured in white (black). **A)** Structure suggested by the Hamiltonian, with spinful fermionic sites (local dimension $d = 4$). Filled (left) and empty (right) chains are separated and connected to the impurity, placed in the middle of the MPS. The interaction is only nearest neighbor. **B)** Interleaved ordering, with the impurity on the left and alternating filled and empty chain sites. In the MPS the couplings become next-nearest neighbor. **C)** Same as **B)**, with separated spin components. The local sites are spinless (local dimension $d = 2$).

is well known that spatially separating the spins can be beneficial for numerical simulations [38, 40, 53].

4.2. Results: Impurity, bath and entanglement dynamics

In the following, we study the dynamics of the SIAM, with a special focus on the evolution of the entanglement entropy for the different MPS structures, see Fig. 4.1. Since we simulate the entire dynamics, we not only analyze the dynamics of the impurity, but also investigate how the population of the bath modes changes over time.

4.2.1. Noninteracting case $U = 0$

For $U = 0$ the Anderson model reduces to the so-called “resonant level model”, where spin degrees of freedom are decoupled, and the model is fully quadratic in the fermions. Hence, we can forget about the spin index and consider spinless fermions

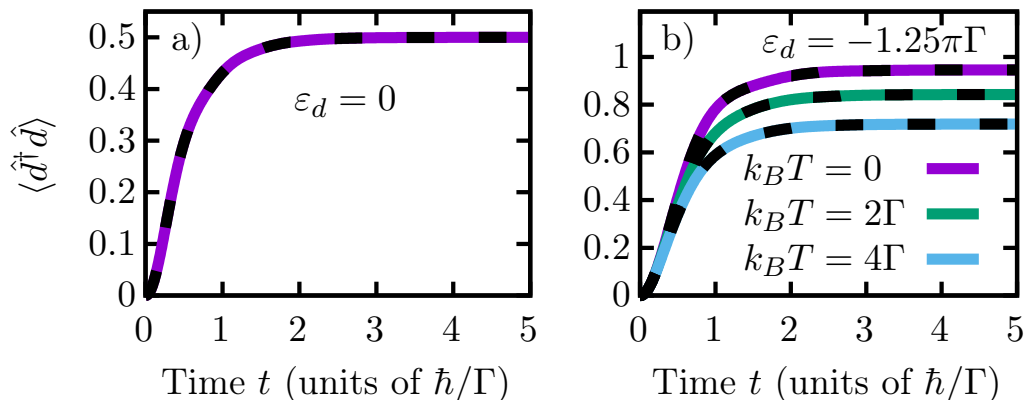


Figure 4.2.: Impurity dynamics in the noninteracting case. (a,b) Dynamics of the $U = 0$ impurity occupation $\langle \hat{d}^\dagger \hat{d} \rangle$ for impurity energy level $\varepsilon_d = 0$ (a) and $\varepsilon_d = -1.25\pi\Gamma$ (b) at different temperatures T . The dynamics is independent of T for $\varepsilon_d = 0$. Dashed lines represent results obtained from exact diagonalization, with linear discretization and 400 bath sites. MPS results were obtained using the structure **B** of Fig. 4.1.

instead. In this case structures **A** and **B** in Fig. 4.1 are simplified, and we use fermionic sites with local dimension $d = 2$. Structure **C** will not be considered.

Impurity occupation. First, let us discuss the quench dynamics of the impurity occupation. We compare our results obtained from the MPS approach using structure **B** with exact diagonalization (ED) results, finding perfect agreement between the two methods. Since the impurity is initially empty, it starts to fill up at $t \geq 0$, as shown in Fig. 4.2. For $\varepsilon_d = 0$, see Fig. 4.2(a), we observe a very smooth convergence towards $\langle \hat{d}^\dagger \hat{d} \rangle = 1/2$, a value consistent with the particle-hole symmetry of the final Hamiltonian. In this case, moreover, the dynamics is independent of temperature. For $\varepsilon_d = -1.25\pi\Gamma$, instead, as the impurity level lies below the Fermi energy $\epsilon_f = 0$, the impurity occupation converges towards a temperature-dependent steady-state value $\langle \hat{d}^\dagger \hat{d} \rangle > 1/2$, see Fig. 4.2(b). As expected, the equilibrium occupation goes towards $\langle \hat{d}^\dagger \hat{d} \rangle = 1/2$ as temperature increases.

Conduction electron density. We have seen that the initially empty impurity is populated during the dynamics. Particle number conservation implies that the conduction modes lose exactly the number of electrons that is gained by the impurity. Our method computes the dynamics of the entire system, including the conduction modes. Hence, we are able to study also the dynamics of the bath. Here we focus on the occupation of the conduction modes, although other quantities might be calculated as well. More in detail, the quantity we calculate is the time-dependent expectation value

$$\Delta\rho_k(t) = \langle \psi(t) | : \hat{c}_{1k}^\dagger \hat{c}_{1k} : | \psi(t) \rangle \quad (4.1)$$

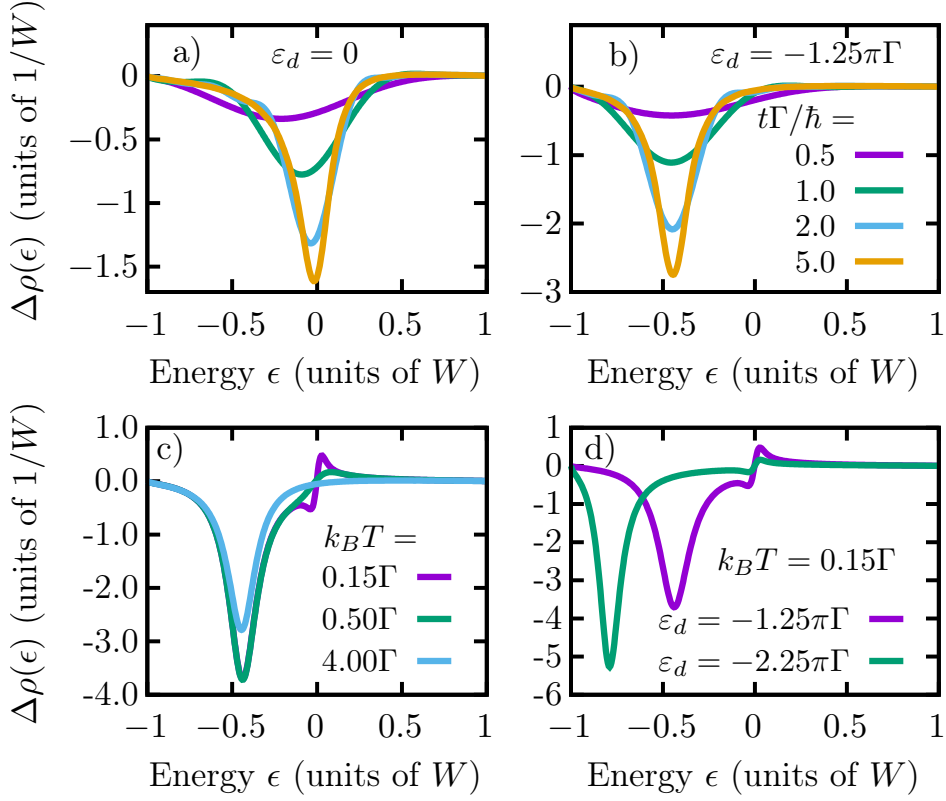


Figure 4.3.: Bath dynamics in the noninteracting case. (a,b) Conduction band occupation density $\Delta\rho(\epsilon, t)$ at different times t , for $\epsilon_d = 0$ (a) and $\epsilon_d = -1.25\pi\Gamma$ (b) at temperature $k_B T = 4\Gamma$. A well defined negative peak close to the impurity energy level appears. (c+d) Converged $\Delta\rho(\epsilon)$ in the long-time limit for different temperatures T (c) and ϵ_d (d). At low temperatures a kink at the Fermi energy ϵ_f emerges (c), which is reduced as the impurity energy level moves away from ϵ_f (d).

of the conduction electron occupation number operator

$$:\hat{c}_{1k}^\dagger \hat{c}_{1k}: \stackrel{\text{def}}{=} \hat{c}_{1k}^\dagger \hat{c}_{1k} - \langle \psi_0 | \hat{c}_{1k}^\dagger \hat{c}_{1k} | \psi_0 \rangle.$$

Here, subtracting the initial state value is a device, akin to normal ordering, which takes care of the infinite number of electrons in the bath, and captures only the change in conduction electron density induced by the hybridization.

Details on the practical evaluation of this expression are given in Section 4.4.2. In the continuum limit, we calculate $\Delta\rho(x, t)$ in dimensionless energy units, $x = \epsilon/W$. We show it in panels (a) and (b) of Fig. 4.3, for a temperature $k_B T = 4\Gamma$. Starting from $\Delta\rho(x, t = 0) \equiv 0$, we observe the growth of a peak close to the impurity level energy ϵ_d , similarly to what has been found for the Spin-Boson model [123]. Note that $\Delta\rho$ is predominantly negative, since particle conservation requires

$$\langle \psi(t) | \hat{d}^\dagger \hat{d} | \psi(t) \rangle = - \int_{-1}^{+1} dx \Delta\rho(x, t)$$

at any time. As temperature is reduced, Fig. 4.3(c), we observe the appearance of a kink at the Fermi energy ϵ_f , which we easily understand in the limit $T \rightarrow 0$: The

conduction bath is completely filled below the Fermi energy, and empty above. The tail of the spectral weight — corresponding to the local impurity level — drains some of the initially occupied modes below ϵ_f , and provokes the occupation of some initially empty modes above ϵ_f . As we move the impurity level further away from the Fermi energy, lowering the spectral weight at ϵ_f , the kink is clearly reduced in size, as shown in Fig. 4.3(d). Once again, we benchmarked our calculations through comparison with ED data (not shown). As we will show later on, $\Delta\rho(x,t)$ can even contain information about many-body physics, in particular the Kondo effect.

Entanglement. We now turn to the analysis of the entanglement dynamics. To quantify the amount of entanglement we calculate the entanglement entropy S_l (see Eq. (1.1)) between the first l sites of the MPS and the rest of the system. Since our initial state $|\psi_0\rangle = |0\rangle \otimes |\emptyset_1, F_2\rangle$ — an empty impurity and the bath in the thermal state — is represented by a product state, the entanglement is zero along the MPS for $t = 0$. For $t > 0$, excitations — particles in the empty chain or holes in the filled chain — are created in the vicinity of the impurity. Hence, we observe the entanglement to grow (see Fig. 4.4) starting from the impurity’s position in the MPS. Notice that the impurity is placed in the middle of the MPS for structure **A** and on the left in structure **B**. The region of nonzero entanglement is growing during the dynamics in a light-cone-like fashion, due to the spreading of excitations along the chains. We note a slight asymmetry in the entanglement of structure **A**, due to the initial state: Since we start with an empty impurity, and the particle number is conserved, only the filled chain is able to interact with the impurity at $t = 0$, leading to an initial entanglement predominantly between impurity and filled chain. Overall, we find the entanglement’s magnitude to be similar for both MPS structures at $T = 0$.

At higher temperature, $k_B T = 4\Gamma$ (see Fig. 4.4(c,d)), we note that entanglement is spreading faster. Hence, longer chains are needed, independently of the MPS structure. However, the most striking effect of a higher temperature is the significant increase of entanglement in structure **A**: While structure **B** shows similar entanglement as for $T = 0$, we observe a massive increase in structure **A**, mostly in the middle of the MPS, indicating a strongly increasing entanglement between the empty and filled chain.

We define the maximum entanglement entropy $S_{\max} = \max_l S_l$ along the MPS, and study its behaviour versus the simulation time t . For $k_B T = 4\Gamma$ we find (see Fig. 4.4(e)) that S_{\max} increases linearly in t for structure **A**, while, after some initial increase, it stays almost constant for structure **B**. An entanglement entropy which increases linearly in t requires the bond dimension to grow exponentially in time, and thus strongly limits the accessible simulation times. As shown in Fig. 4.4(f), the entanglement highly depends on temperature for the structure **A**. These observations are in agreement with the findings of Ref. [140]. At $T = 0$ the effective hybridization functions $V_1^2(x)$ and $V_2^2(x)$ only touch at the Fermi energy $x = 0$ (see Fig. 4.5(a)). In this case, Ref. [140] found the entanglement entropy to grow only logarithmically. At $T > 0$, instead, the

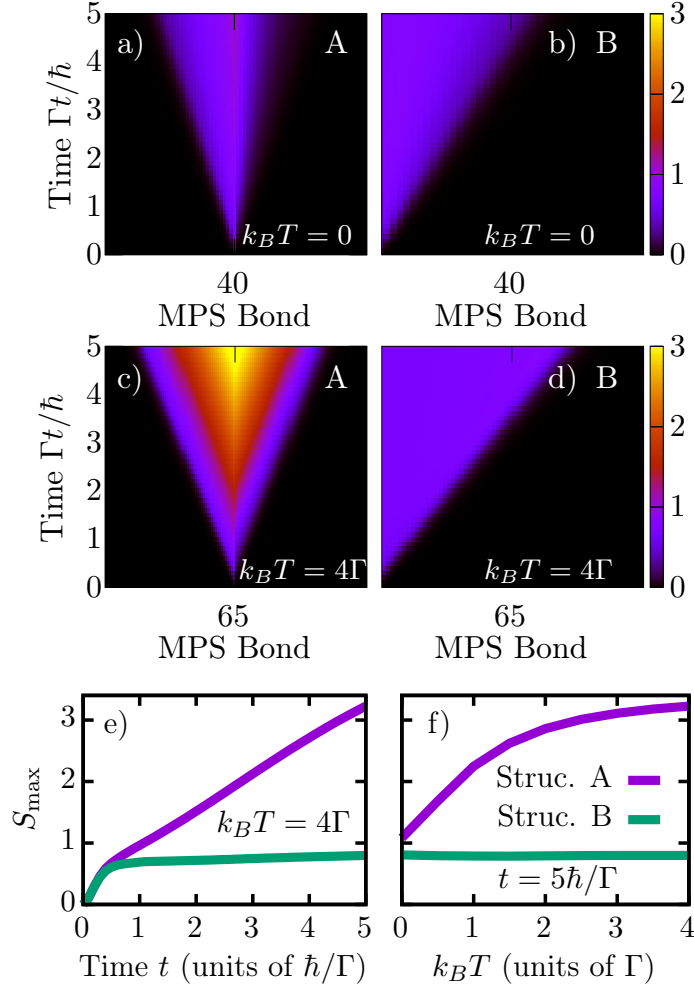


Figure 4.4.: Entanglement dynamics in the noninteracting case. Color plots: Dynamics of the entanglement entropy within the MPS in the noninteracting case $U = 0$. Structures **A** (a+c) and **B** (b+d) are considered, with conduction electrons at temperature $T = 0$ (a+b) and $T = 4\Gamma$ (c+d). (e+f) Maximum entanglement entropy S_{\max} along the MPS as a function of time at fixed temperature $k_B T = 4\Gamma$ (e) and as a function of temperature at fixed time $t = 5\hbar/\Gamma$ (f). Structure **A** shows significantly stronger entanglement growth as temperature increases, while structure **B** has almost no entanglement growth and is independent of temperature.

hybridization functions do overlap on a finite interval, see Fig. 4.5(b), leading to linear entanglement growth [140]. Remarkably, merging the two chains, as we suggested in structure **B**, Fig. 4.1(b), results in a temperature-independent maximum entanglement (see Fig. 4.4(f)).

To add further intuition for this behavior, we measure the total number of particles in the initially empty chain, through the average of the corresponding number operator (written here for spinless fermions, for simplicity):

$$\langle \psi(t) | \hat{N}_1 | \psi(t) \rangle = \sum_{n=0}^{\infty} \langle \psi(t) | \hat{a}_{1,n}^\dagger \hat{a}_{1,n} | \psi(t) \rangle \quad (4.2)$$

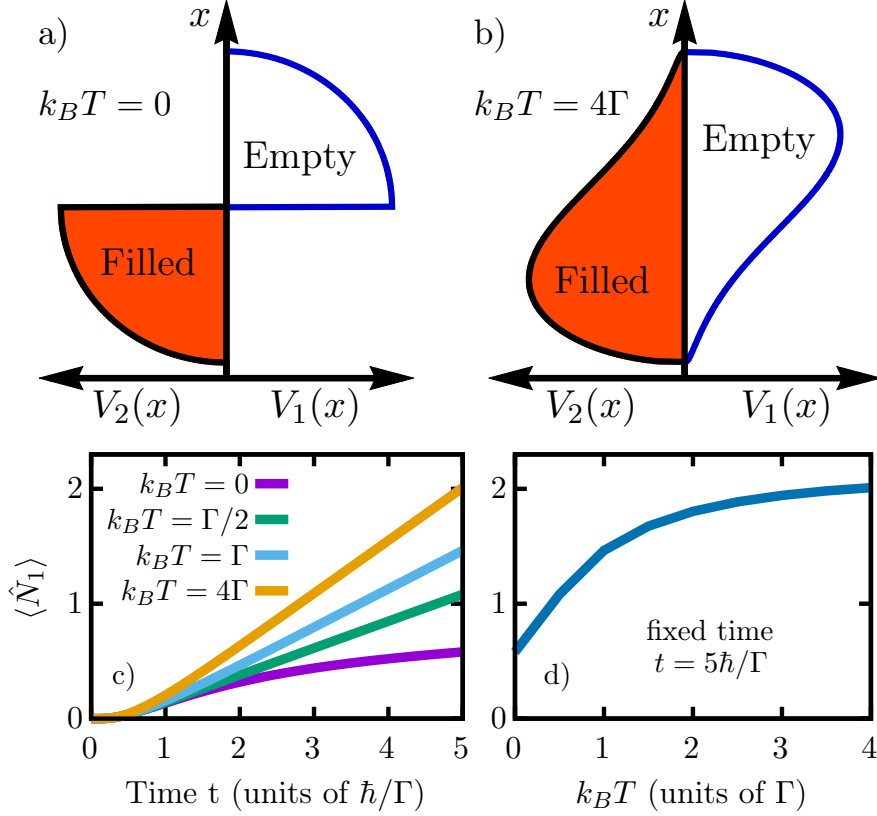


Figure 4.5.: Hybridization overlap and particle movement. (a,b): Effective hybridization functions $V_2(x)$ and $V_1(x)$ for the filled and empty bath, respectively, at temperatures $k_B T = 0$ (a) and $k_B T = 4\Gamma$ (b). $x = \epsilon/W$ is the dimensionless energy. At zero temperature, the effective hybridization functions do not overlap, touching only at the Fermi energy ($x = 0$). For $T > 0$ they do have a nonzero overlap, allowing particles to travel from the filled to the empty bath. (c,d): Total number of electrons in the initially empty chain $\langle \psi(t) | \hat{N}_1 | \psi(t) \rangle$ as a function of time for increasing temperature $k_B T$ (c), and at fixed time $t = 5\hbar/\Gamma$ as a function of temperature $k_B T$ (d). Notice that $\langle \hat{N}_1 \rangle$ is independent of the MPS structure.

$\langle \psi(t) | \hat{N}_1 | \psi(t) \rangle$ counts how many particles flow from the filled chain — after passing through the impurity — into the empty chain “1”. Fig. 4.5(c) shows that $\langle \hat{N}_1 \rangle$ increases linearly in time at finite temperature and sub-linearly at $k_B T = 0$, similar to the entanglement in Ref. [140]. Fig. 4.5(d) shows that the temperature dependence of $\langle \hat{N}_1 \rangle$ at fixed time $t = 5\hbar/\Gamma$ agrees qualitatively well with our findings for the entanglement, see Fig. 4.4(f). Notice that any particle leaving the filled chain “2” creates a hole there. Hence, the dynamics creates particle-hole pairs: particles created in the empty chain “1” and holes in the filled chain “2”. Our results suggest that such particle-hole pairs carry the entanglement, leading to an overall entanglement growth between the two chains.

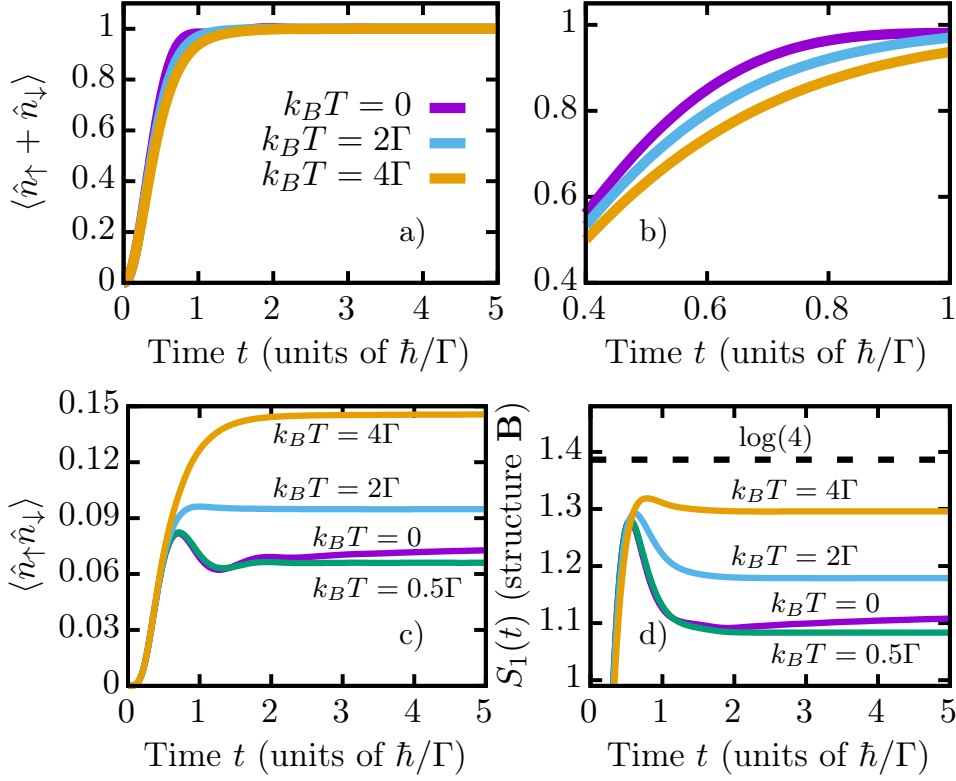


Figure 4.6.: Impurity dynamics at $U = 2.5\pi\Gamma$. (a,b) Dynamics of the total impurity occupation $\langle \hat{n}_\uparrow + \hat{n}_\downarrow \rangle$ for $U = 2.5\pi\Gamma$ for the particle-hole symmetric choice $\varepsilon_d = -U/2$. (c) Double occupancy $\langle \hat{n}_\uparrow \hat{n}_\downarrow \rangle$. (d) Entanglement entropy between impurity and bath, S_1 . Dashed line in (d) indicates the theoretically maximum value of the entanglement entropy, $S_1 = \log(4)$. Data are obtained the using MPS ordering structure **B** (see Fig. 4.1).

4.2.2. Interacting case $U > 0$

Turning on the on-site interaction, we need to consider spinful fermions, with spin-up and spin-down electrons in the impurity interacting through Coulomb repulsion U . Let us start with a brief analysis of the dynamics, with fixed interaction $U = 2.5\pi\Gamma$ and energy level $\varepsilon_d = -1.25\pi\Gamma$, where the model is particle-hole symmetric ($U = -2\varepsilon_d$) with an estimated Kondo temperature $k_b T_K = 0.07\Gamma$. Hence, the impurity occupation — starting again from zero — converges towards $\langle \hat{d}_\sigma^\dagger \hat{d}_\sigma \rangle \rightarrow 1/2$ for both spin-up and spin-down at any temperature, with total impurity occupation $\langle \hat{n}_\uparrow + \hat{n}_\downarrow \rangle \rightarrow 1$ (see Fig. 4.6(a)). In contrast to the non-interacting case, however, the dynamics of the impurity occupation does show some small temperature dependence before reaching convergence, as visualized by an appropriate zoom-in, see Fig. 4.6(b). The double occupancy, shown in Fig. 4.6(c), is equivalent to the probability to find the impurity in the filled state $|\uparrow\downarrow\rangle$, and shows a clear (non-monotonic) temperature dependence in its final value. Note that the curve for $k_B T = 0$ converges much more slowly than the remaining ones. We believe that the slow convergence — and, connected to that, also the non-monotonicity in temperature — is related to the building up of the Kondo

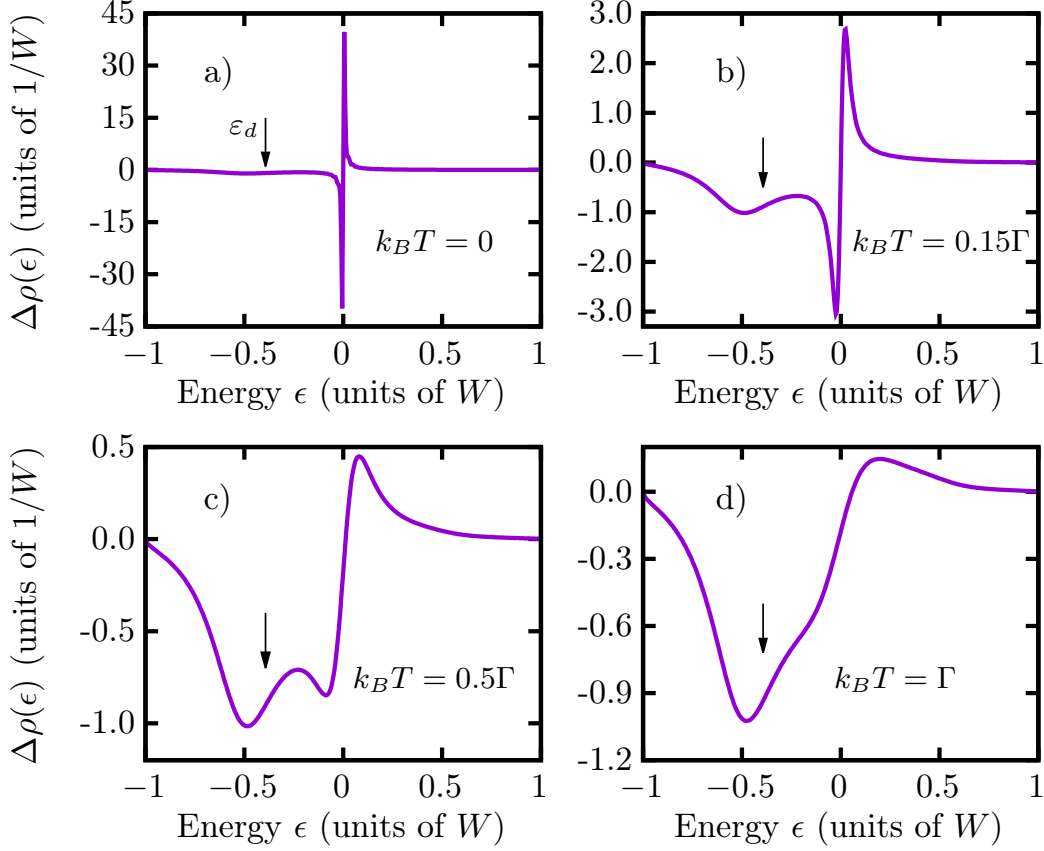


Figure 4.7.: Bath dynamics at $U = 2.5\pi\Gamma$. Conduction electron occupation density $\Delta\rho(\epsilon, t)$ of spin-up conduction modes (spin-down is equivalent) at temperatures $T = 0$ (a), $k_B T = 0.15\Gamma$ (b), $k_B T = 0.5\Gamma$ (c) and $k_B T = \Gamma$ (d). Curves are taken at times $t = 30\hbar/\Gamma$ ($k_B T = 0$), $t = 15\hbar/\Gamma$ ($k_B T = 0.15\Gamma$), $t = 10\hbar/\Gamma$ ($k_B T = 0.5\Gamma$) and $t = 5\hbar/\Gamma$ ($k_B T = \Gamma$). For $T > 0$ they are converged with respect to time and do not change anymore. Peaks are observed close to the impurity level $\epsilon_d = -1.25\pi\Gamma$, marked through arrows, and for low temperatures around the Fermi energy, indicating the presence of the Kondo effect. The Kondo temperature is $k_B T_K \approx 0.07\Gamma$.

effect, for which slow convergence of the Greens function has been observed previously at low temperatures [1][supplementary material]. Similar behavior is found for the entanglement entropy between the impurity and the free electron bath, including the non-monotonic temperature dependence and the slow convergence for $T = 0$. Notice that, as temperature gets higher, the entanglement entropy tends towards its maximum possible value $S_1 = \log(4)$.

Conduction electron density. In the non-interacting case, we saw that the conduction electron occupation density $\Delta\rho(\epsilon, t)$ — see Eq. (4.1) — develops a (negative) peak around the impurity energy level at ϵ_d . In the interacting case, we find signatures of the Kondo peak at low temperatures. The Kondo effect manifests itself through two peaks of opposite sign around the Fermi energy $\epsilon_f = 0$, which are similar to the kink

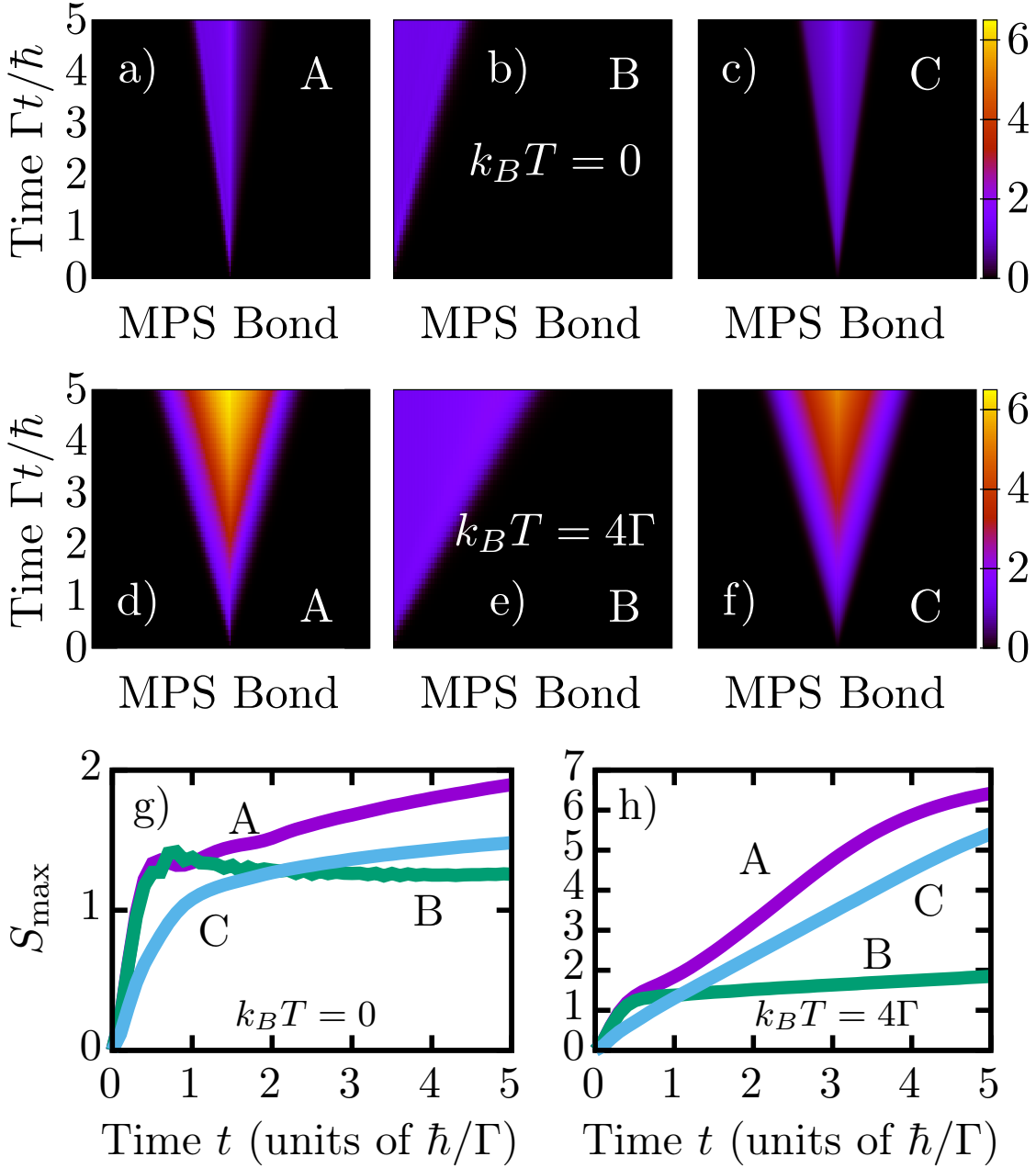


Figure 4.8.: Entanglement dynamics at $U = 2.5\pi\Gamma$. Temporal evolution of the entanglement entropy along the MPS at temperatures $k_B T = 0$ (a-c) and $k_B T = 4\Gamma$ (d-f), for structures **A**, **B**, and **C**, as illustrated in Fig. 4.1, at fixed interaction $U = 2.5\pi\Gamma$, for the particle-hole symmetric case $\varepsilon_d = -U/2$. Bottom: Dynamics of the maximum entanglement entropy S_{\max} at fixed $k_B T = 4\Gamma$ (g) and temperature dependence of S_{\max} at the final simulation time $t = 5\hbar/\Gamma$ (h). In panel (h) the curve for structure **A** is a lower bound for S_{\max} , as convergence with respect to the bond dimension has not been reached (see Section 4.4.5). Filled and empty chains are made of 90 sites each.

at $U = 0$, but significantly more pronounced. Hence, the increased impurity spectral weight around the Fermi energy — due to the formation of the Kondo cloud singlet — results in two peaks of different sign in $\Delta\rho(\epsilon, t \rightarrow \infty)$, see Fig. 4.7. As we increase T above the Kondo temperature $k_B T_K \approx 0.07\Gamma$, the two peaks close to ϵ_f disappear, just like the Kondo peak in the impurity spectral function, leaving peaks corresponding to the impurity level. Note that at $U > 0$ there is a second impurity level at $\epsilon_d + U$, corresponding to a fully occupied impurity. This state is not probed in our scenario, since we are starting from an empty impurity, and the doubly occupied state has little impact on the dynamics. However, we can probe this level starting from the fully occupied impurity (see Section 4.4.3 for details). It is worth mentioning that the convergence of $\Delta\rho(\epsilon, t)$ with respect to time is strongly temperature-dependent, with faster convergence for higher temperatures, again, similarly to the convergence of the Green's function [1]. At $T = 0$ we did not even reach convergence at time $t = 30\hbar/\Gamma$, where peaks at $\epsilon = 0$ are still growing.

Entanglement. Turning to the entanglement, we investigate all MPS orderings illustrated in Fig. 4.1, where, additionally to structures **A** and **B**, we now consider structure **C** with spatially separated spin-up and spin-down.

For $T = 0$, we find similarly low entanglement for all structures, as shown in Fig. 4.8(a-c). Once again, for $k_B T = 4\Gamma$, we observe the entanglement to grow strongly for structure **A**, with a maximum entropy that increases linearly in time. On the contrary, for our mixed structure **B** the entanglement stays significantly lower, see Fig. 4.8(h), although a slight increase in time is also visible here. For structure **C**, where spin-up sites are separated from spin-down sites, the entanglement structure is similar to the one of structure **A**, with a massive entanglement growth during the dynamics. Interestingly, the blow-up of entanglement is observed in the middle of the MPS, suggesting that spin-up and spin-down sites are getting heavily entangled at higher temperatures. Hence, the separation of spins unavoidably leads to strong entanglement growth, independent of the explicit structure used to represent the bath. This might affect all finite temperature generalizations of approaches exploiting a spatial separation, like the one recently developed by Rams *et al.* to simulate transport through an impurity [53].

Let us now investigate the effect of different physical model parameters. To simplify the discussion we focus on the maximum entanglement entropy encountered during the dynamics up to time $t = 5\hbar/\Gamma$, while the general entanglement structure along the MPS was observed to be similar to that discussed previously. Fig. 4.9 shows the temperature dependence of the maximum entanglement entropy for $U = 0.5\pi\Gamma$ (a) and for the particle-hole symmetric choice $U = 2.5\pi\Gamma$ (b). For both values of U , we observe a strong temperature dependence for structure **A**, while structure **B** is significantly less sensitive to temperature, similarly to what we found in the noninteracting case. Structure **C**, instead, shows little T -dependence for small interactions, but strong dependence for

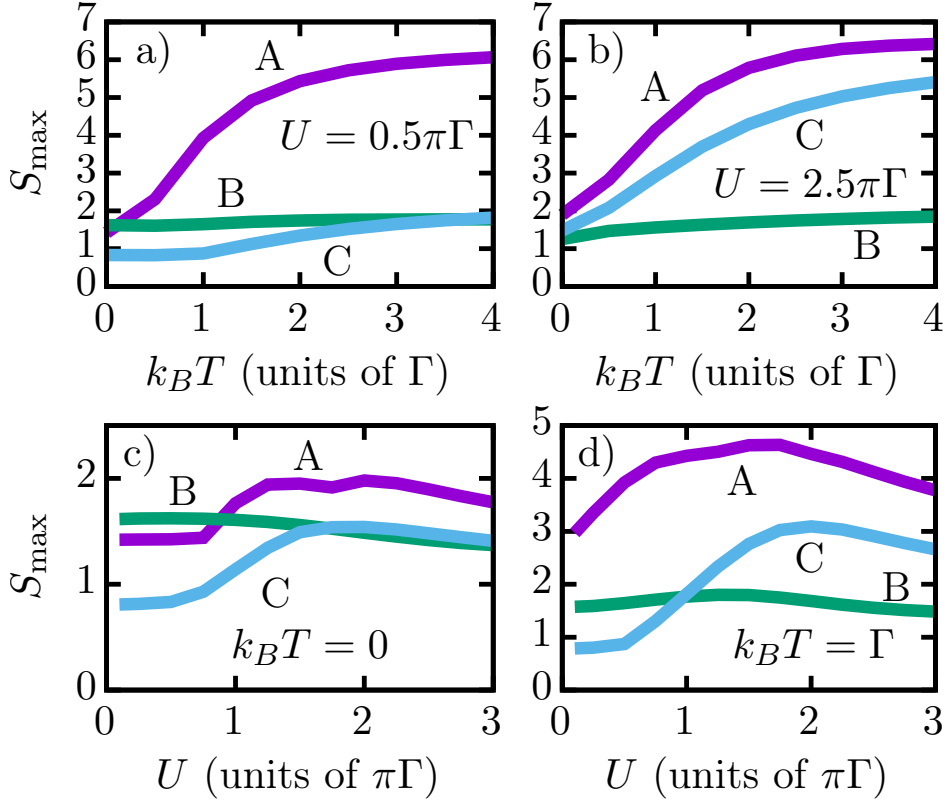


Figure 4.9.: Maximum entanglement entropy. S_{\max} along the MPS as a function of temperature $k_B T$ (a,b) and interaction U (c,d), at fixed time $t = 5\hbar/\Gamma$ for MPS structures **A**, **B**, and **C** (see Fig. 4.1). In panels (a,b) we fix the interaction to $U = 0.5\pi\Gamma$ (a) and $U = 2.5\pi\Gamma$ (b), while in panels (c,d) temperatures $k_B T = 0$ (c) and $k_B T = \Gamma$ (d) are kept constant. Here $\epsilon_d = -1.25\pi\Gamma$.

$U = 2.5\pi\Gamma$. This behavior is easy to understand. We have seen in Fig. 4.8 that the entanglement for $U = 2.5\pi\Gamma$ and $k_B T = 4\Gamma$ grows strongly in between spin-up and spin-down modes. At $U = 0$, however, spin-up and down are decoupled. Therefore, at low values of U , the entanglement growth between the opposite spins is still modest.

To analyze the effect of the interaction in more detail, we show the maximum entanglement entropy as a function of U in the bottom row of Fig. 4.9. Structures **A** and **C** display a non-monotonic behavior with maximum entanglement in the order of $U/\Gamma \approx (1 \div 2)$, while the spinful interleaved ordering **B** is rather independent from the interaction. Hence, from an entanglement point of view, structure **A** never seems advantageous. The interleaved ordering with spin splitting, structure **C**, shows low entanglement at weak coupling and low temperatures. In several scenarios, including high temperature at intermediate interactions, however, the entanglement grows strongly for orderings **A** and **C**, while structure **B** can capture the dynamics much more efficiently.

4.3. Conclusions

We have studied the dynamics of the quenched Anderson model in a wide range of temperatures T and interactions U . By employing the chain geometry for the two conduction electron baths emerging from the thermofield approach, we have shown that the entanglement can dramatically depend on the ordering of the chain sites in the MPS.

While at zero temperature all orderings considered show slow-to-modest entanglement growth, the situation changes dramatically at higher temperature: entanglement strongly grows if either the empty/filled chains or sites with different spin are spatially separated. Instead, merging the chains with alternating empty and filled sites — such that the interaction terms in the MPS are next-nearest neighbor — leads to significantly lower entanglement growth, allowing for much longer simulations with low numerical resources. For the separation of filled/empty chains, we have reasoned that the growing entanglement is due to the increased rate at which particle-hole pairs are created, following from the overlap of effective hybridization functions at finite temperature. Our analysis has shown that, in non-equilibrium situations, it is not necessarily beneficial to mimic the Hamiltonian structure in the MPS. Instead, the ongoing physical processes, such as the movement of particles, determine the entanglement properties.

Notice that a further simplification is possible if two conditions are met: (i) the system-bath coupling factorizes, meaning that it can be written as $\hat{A} \otimes \hat{B}$, where \hat{A} and \hat{B} are solely acting on the system and the environment, respectively. (ii) the chemical potential lies at the bottom of the environmental band modes, such that the bath modes are empty in the bath's ground state. Then the two continuum baths are equivalent to a single bath with modified hybridization function [109], which can be mapped into a single chain. In this way, one avoids the problem of growing entanglement between the two chains. Such a scenario can often be found in the context of open quantum systems, see also Chapter 7.

Furthermore, we have shown that the analysis of the conduction bath — available when simulating the full dynamics of system and “environment” — can reveal interesting many-body physics, like the Kondo-effect. As an outlook for further research, it would be interesting to study how the star geometry would perform at finite temperatures. Our results suggest that the separation of filled and empty baths would lead to strong entanglement growth also in the star-geometry. However, a mixed ordering according to the energy of the modes might be a low-entanglement candidate for the star geometry.

4.4. Additional information

4.4.1. Numerical details and parameters

We have carried out simulations using the 2-site version of the time-dependent variational principle (TDVP) [50, 115–117], which, in combination with the matrix product operator representation of the Hamiltonian, allows us to deal with next-nearest neighbor interaction. Using TDVP, it would also be possible to simulate more complicated networks [3, 122, 123], which would be needed to split both spin degrees of freedom and empty/filled chains. Depending on the MPS ordering, we use bond dimensions between $D = 150$ and $D = 1600$ to reach convergence (see Section 4.4.5) and a total truncated weight w_t — the summed probability of discarded states — of $w_t = 10^{-12}$ for the truncation of the MPS. We further employ a minimum bond dimension $D_{\min} \approx 10$, keeping even states with low probability, to reduce the projection error of TDVP (see Section 4.4.4 for details). The time-step is fixed to be $\Delta t = 0.1\hbar/W$. We explicitly exploit the particle-number conservation of the Hamiltonian to speed up simulations. In practice, we must use a finite number of chain sites. We choose the number of sites such that no excitation — being either a particle in the empty chain or a hole in the filled chain — reaches the end of the chain (see also Ref. [123]). For simulations up to time $t = 5\hbar/\Gamma$, we typically use about 100 sites for each chain.

4.4.2. Calculating the conduction occupation density

Here we provide details in the calculation of the residual bath occupation density $\Delta\rho(x, t)$. The starting point is the transformation of $:\hat{c}_{1k}^\dagger\hat{c}_{1k}:=\hat{c}_{1k}^\dagger\hat{c}_{1k}-\langle\psi_0|\hat{c}_{1k}^\dagger\hat{c}_{1k}|\psi_0\rangle$, see Eq. (3.77), which leads to:

$$:\hat{c}_{1k}^\dagger\hat{c}_{1k}:=\cos^2(\theta_k):f_{1k}^\dagger\hat{f}_{1k}:+\sin^2(\theta_k):f_{2k}^\dagger\hat{f}_{2k}:+\cos(\theta_k)\sin(\theta_k)(:f_{1k}^\dagger\hat{f}_{2k}:+\text{H.c.}).$$

Next, observe that since $|\psi_0\rangle=|\emptyset_1, F_2\rangle$ we have $:f_{1k}^\dagger\hat{f}_{1k}:=\hat{f}_{1k}^\dagger\hat{f}_{1k}$, and $:f_{1k}^\dagger\hat{f}_{2k}:=\hat{f}_{1k}^\dagger\hat{f}_{2k}$. However,

$$:f_{2k}^\dagger\hat{f}_{2k}:=\hat{f}_{2k}^\dagger\hat{f}_{2k}-1=-\hat{f}_{2k}\hat{f}_{2k}^\dagger.$$

Hence, in the continuum limit we get:

$$\begin{aligned}\Delta\rho(x, t) &= \cos^2(\Theta)\langle\psi(t)|f_1^\dagger(x)\hat{f}_1(x)|\psi(t)\rangle-\sin^2(\Theta)\langle\psi(t)|f_2(x)\hat{f}_2^\dagger(x)|\psi(t)\rangle \\ &+ \cos(\Theta)\sin(\Theta)(\langle\psi(t)|f_1^\dagger(x)\hat{f}_2(x)|\psi(t)\rangle+\text{c.c.}),\end{aligned}$$

where we used the short notation $\Theta \equiv \Theta(x)$ for the continuum version of the thermofield angle (see Eq. (3.79)), defined through the Fermi function:

$$\sin^2(\Theta(x)) \equiv \frac{1}{e^{Wx/k_B T} + 1}. \quad (4.3)$$

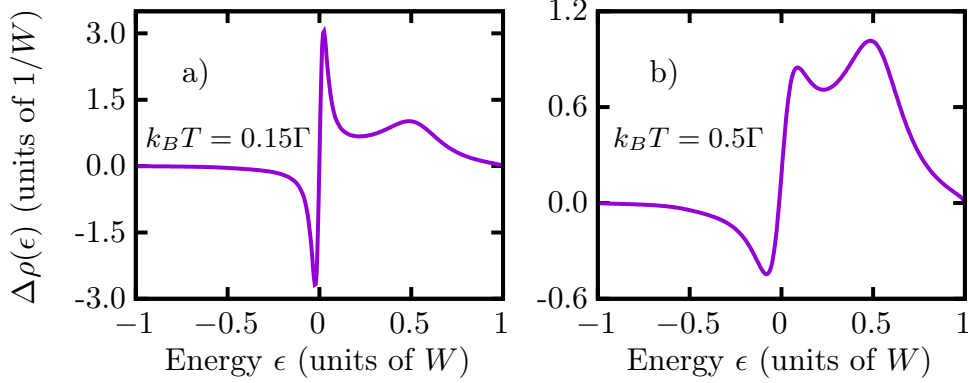


Figure 4.10.: Conduction electron occupation for initially filled impurity. $\Delta\rho(\epsilon, t)$ in the symmetric SIAM with $U = 2.5\pi\Gamma$, at temperatures $k_B T = 0.15\Gamma$ (a) and $k_B T = 0.5\Gamma$ (b). The initial state $|\psi_0\rangle$ is here a factorized state with doubly occupied impurity $|\uparrow\downarrow\rangle$ and conduction modes in the thermal state, $|\psi_0\rangle = |\uparrow\downarrow\rangle \otimes |\emptyset_1, F_2\rangle$. $\Delta\rho(\epsilon, t)$ is plotted for times $t = 15\hbar/\Gamma$ (a) and $t = 10\hbar$ (b), after which it does not change anymore.

The final transformation involves re-writing the $\hat{f}_c(x)$ in terms of orthogonal chain operators, see Eq. (3.58). One can show that the quantities involved in the expectation value are all well defined. For instance:

$$\hat{f}_2(x)\hat{f}_2^\dagger(x) = \sum_{n,m=0}^{\infty} U_{2,n}(x)U_{2,m}(x) \hat{a}_{2,n}\hat{a}_{2,m}^\dagger$$

Hence, by considering $\langle\psi(t)|\hat{a}_{2,n}\hat{a}_{2,m}^\dagger|\psi(t)\rangle$, one easily realises that these matrix elements vanish exactly for $n, m > \tilde{L}(t)$, where $\tilde{L}(t)$ is the effective distance reached by the excitations at time t . The infinite sums are therefore effectively cut-off by $\tilde{L}(t)$.

4.4.3. Starting from an occupied impurity

We have previously seen that the conduction bath occupation density $\Delta\rho(\epsilon, t)$ shows a peak corresponding to the impurity level ϵ_d (see Fig. 4.7). However, the second impurity level at energy $\epsilon_d + U$ has not been observed. The reason is that such a level corresponds to a double occupied state, which plays only a minor role in the dynamics when starting from an empty impurity. Here, we study $\Delta\rho(\epsilon, t)$ for the same dynamics as before, starting, however, from the doubly occupied impurity state $|\uparrow\downarrow\rangle$, see Fig. 4.10. We clearly observe the peak close to energy $\epsilon_d + U = 1.25\pi\Gamma = 0.125\pi W$, while peaks at energy ϵ_d — corresponding to the empty impurity state — are absent.

4.4.4. TDVP beyond nearest neighbor hopping

This section is devoted to an analysis of the projection error of the TDVP algorithm. Our structure \mathbf{A} contains at most nearest-neighbor interactions, and thus projection

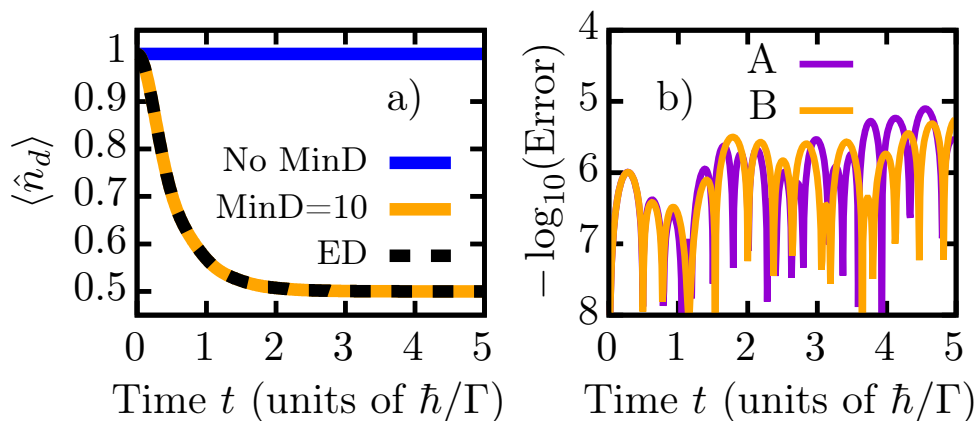


Figure 4.11.: Why we use a minimum bond dimension. a) Impurity occupation obtained when using **B**, at $U = 0$ and temperature $k_B T = 0$, for an initially occupied impurity. TDVP gets stuck due to the next-nearest neighbor interaction, as manifested by the constant impurity occupation. The problem is solved by setting a minimum bond dimension, and the dynamics agrees well with ED data. b) Error of the impurity occupation, calculated as the difference of MPS and ED data for structures **A** and **B**, by employing a minimum bond dimension $\text{MinD}=10$. Note that in structure **A** interactions are only nearest neighbor, and thus projection errors are absent.

errors are absent when using 2-site TDVP [50]. On the other hand, the Hamiltonians of structures **B** and **C** both contain mainly next-nearest neighbor terms, where projection errors do not vanish, in general. For simplicity, we restrict our analysis to the noninteracting case $U = 0$, where only structures **A** and **B** are relevant (structure **C** is equivalent to **B**). Similarly to the previous section, we initialize the impurity in the filled state $|1\rangle$ with one spinless fermion, and set the temperature to $T = 0$ to avoid strong entanglement growth in structure **A**.

We study the dynamics of the impurity occupation, which for $U = 0$ can easily be compared with exact diagonalization (ED) results. Without setting a minimum bond dimension we find TDVP to get stuck, as indicated by the horizontal curve in Fig. 4.11. Since the impurity is initially filled, the interaction term between impurity and the first filled chain site does not change the state. On the other hand, the impurity electron could move to the first empty chain site. In the MPS, however, this interaction is a next-nearest neighbor term, and since the initial state is a product state, this process is projected out by TDVP. Setting a minimum bond dimension for the state, we can enlarge the projector to avoid this issue. Indeed we find excellent agreement with ED data for the impurity occupation, see Fig. 4.11(b), with error similar to structure **A**, where projection errors do not play a role.

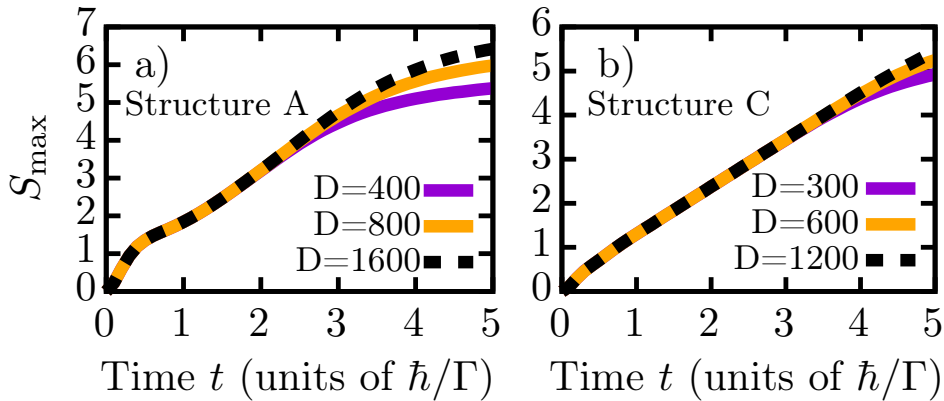


Figure 4.12.: Entanglement convergence with bond dimension. Dynamics of the maximum entanglement entropy along the MPS, S_{\max} , for different bond dimensions D and Structures **A** (panel a) and **C** (panel b), at temperature $k_B = 4\Gamma$. Even at bond dimension $D = 1600$, the entanglement entropy is clearly not converged at the end of the dynamics for structure **A**, while structure **C** is sufficiently converged at $D = 1200$.

4.4.5. Convergence with Bond dimension

The bond dimension D is the crucial numerical parameter in our simulations, as it sets an upper bound for the number of states kept. To ensure that the simulations deliver correct results we need to converge the quantity of interest with respect to the bond dimension. Here we study the convergence of the maximum entanglement entropy S_{\max} for the structures **A** and **C** (see Fig. 4.12). We omit details for structure **B** as results were converged already at $D = 150$. For structures **A** and **C** instead, we find significantly slower convergence, due to the higher entanglement. For structure **A** — separating filled and empty chains — S_{\max} is clearly not converged at the end of the simulation even with bond dimension $D = 1600$. Indeed the entanglement increase seems to be linear in time, but starts to flatten due to the insufficient bond dimension. However, the massive increase of computational costs prevents us from going to higher D . For structure **C**, instead, we are able to reach convergence using a bond dimension of $D = 1200$. Note that this is still significantly larger than bond dimension, $D = 150$, required for structure **B**, and longer simulations would be impossible due to the required exponentially increasing bond dimension.

5. Spectral functions from MPS simulations of the Anderson impurity model

In this chapter, we demonstrate the effectiveness of the previously developed strategies for the calculation of Green's functions. The material contained in this chapter is published in Ref. [1]. Throughout this chapter we again consider the SIAM with semicircular hybridization function, see Chapter 4, and we focus on the Kondo regime.

Let us summarize the crucial aspects of the strategies discussed in the preceding chapters. We have discussed that a direct simulation in the star-geometry, see Fig. 5.1(a,b), is possible through an appropriate ordering of the MPS sites with artificial long-range interactions. In the chain geometry instead, Fig. 5.1(c), the Hamiltonian consists of nearest-neighbor terms only. However, it has been shown that the mixing of filled and empty modes is highly detrimental for numerical simulations [39]. We have discussed in Section 3.5(d) that an independent chain mapping for filled and empty modes would resolve this issue, combining the advantages of the star and chain geometry. At the same time, this approach generalizes immediately to finite temperatures by employing the thermofield transformation, see Section 3.6. Due to the insights we got from quantum quenches in Chapter 4, we decided to use a mixed ordering of MPS sites also in this chapter, Fig. 5.1(e), to reduce the entanglement creation at finite temperatures.

The chapter is organized as follows. First, in Section 5.1 we introduce the objects of interest, the retarded Green's function and the spectral function, and discuss how to calculate them at zero temperature. The finite temperature case is presented in Section 5.2, which requires an advanced strategy to obtain the equilibrium state and the Green's function. In Section 5.3 we provide some results for the spectral function and the entanglement entropy for different Hamiltonian structures. In Section 5.4 we analyze and justify the equilibration scheme employed for the preparation of equilibrium states at finite T . Next, we provide benchmarks against NRG in Section 5.5. Conclusions are drawn, with a small summary of the results, in Section 5.6. Finally, additional technical details are given in Appendix B, including an interesting comparison between our chain mapping approach and the star geometry, see Appendix B.2.

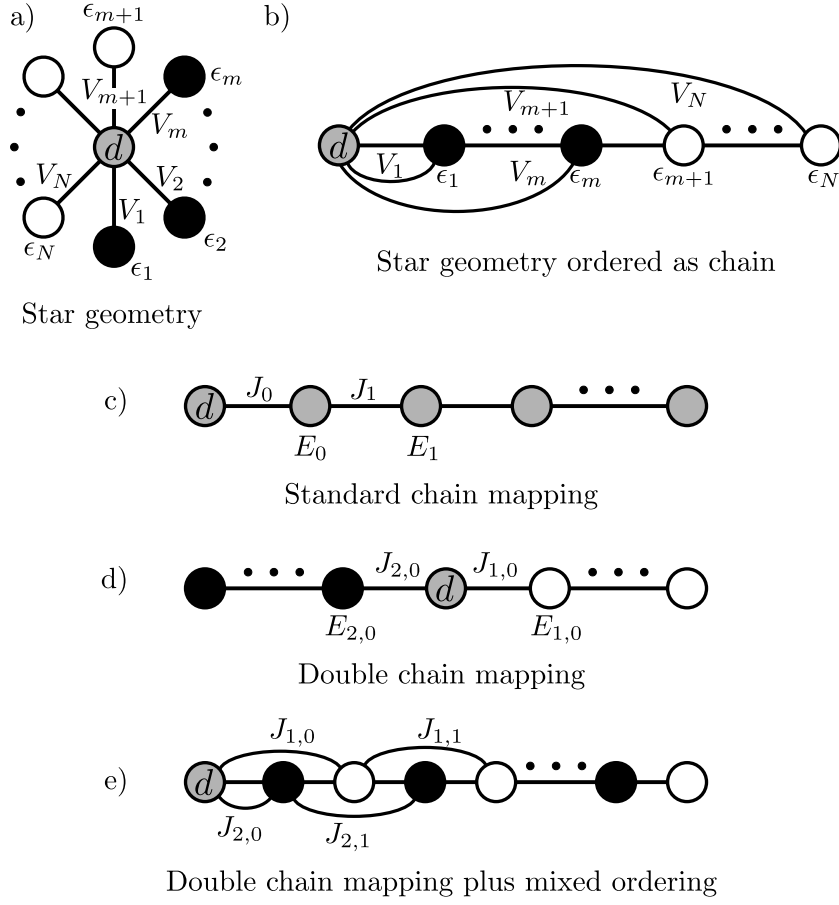


Figure 5.1.: a) Star-like representation of the SIAM. The impurity orbital “d” hybridizes with a half-filled bath of conduction electrons. Here and below, grey circles denote partially filled orbitals, black/white fully-occupied/empty ones. b) The topologically equivalent chain with long-range hoppings, with orbitals ordered according to their increasing energy ϵ_k . c) The bath is mapped into a 1D chain with nearest-neighbor couplings, mixing filled and empty orbitals. d) Structure **A** of Fig. 4.1: Separate chain mapping for filled and empty modes. e) Structure **B** of Fig. 4.1: Interleaved MPS ordering, with alternating filled and empty sites, leading to next-nearest neighbor couplings.

5.1. Green’s functions

In the following we are interested in the retarded Green’s function

$$G_\sigma^R(t) = -i\Theta(t) \text{Tr}_s \left(\{ \hat{d}_\sigma(t), \hat{d}_\sigma^\dagger(0) \} \hat{\rho}_s \right), \quad (5.1)$$

where $\hat{d}_\sigma(t)$ is the Heisenberg impurity operator, $\hat{\rho}_s$ the thermal density matrix of the system, Tr_s the trace over the system, $\Theta(\cdot)$ the Heaviside function and $\{\cdot, \cdot\}$ denotes the anti-commutator. The Fourier transform of the $G_\sigma^R(t)$ provides the experimentally accessible spectral function

$$A_\sigma(\omega) = -\frac{1}{\pi} \text{Im} \int_{-\infty}^{\infty} dt e^{i\omega t} G_\sigma^R(t). \quad (5.2)$$

To calculate G_σ^R in Eq. (5.1) we first split it as $G_\sigma^R(t) = \Theta(t) (G_\sigma^>(t) - G_\sigma^<(t))$, where

$$iG_\sigma^>(t) = \text{Tr}_s(\hat{d}_\sigma(t)\hat{d}_\sigma^\dagger(0)\hat{\rho}_s) \quad \text{and} \quad iG_\sigma^<(t) = -\text{Tr}_s(\hat{d}_\sigma^\dagger(0)\hat{d}_\sigma(t)\hat{\rho}_s) \quad (5.3)$$

are the greater and lesser Green's functions, respectively, calculated in separate simulations. For the discussion we focus on $iG_\sigma^>(t)$, as $G_\sigma^<(t)$ deserves similar comments.

Zero temperature. In general, $\hat{\rho}_s$ is the state where impurity and bath are in thermal equilibrium. Physically, equilibrium can be established by starting from a state where impurity and bath are isolated, by slowly turning on the hybridization between the two, see also Ref. [74]. At $T = 0$, however, there is a short-cut, and $\hat{\rho}_s$ can be obtained by a DMRG ground state (GS) search [38–40]. In particular, the equilibrium density operator is simply the projector on the ground state $|E_0\rangle$, $\hat{\rho}_s = |E_0\rangle\langle E_0|$. After writing explicitly the time dependence of the Heisenberg operators and carrying out the trace we get:

$$iG_\sigma^>(t) = \langle E_0 | \hat{d}_\sigma e^{-i\hat{H}t/\hbar} \hat{d}_\sigma^\dagger | E_0 \rangle e^{iE_0t/\hbar}. \quad (5.4)$$

Here, E_0 is the ground state energy of $|E_0\rangle$.

i

Practical remark. Notice that one can split the time-evolution operator to write the Green's function as

$$iG_\sigma^>(t) = \langle E_0 | \hat{d}_\sigma e^{-i\hat{H}t/2\hbar} e^{-i\hat{H}t/2\hbar} \hat{d}_\sigma^\dagger | E_0 \rangle e^{iE_0t/\hbar}.$$

Hence, instead of evolving $\hat{d}_\sigma^\dagger | E_0 \rangle$ up to time t one can carry out two separate simulations for the bra and the ket, one up to $t/2$ (ket) and one backwards in time up to $-t/2$ (bra). In practice, this can be beneficial if the entanglement grows strongly during the simulations, as longer simulation times can be reached [40].

5.2. $T > 0$ equilibrium state and Green's functions

While at $T = 0$ we can use DMRG to find the equilibrium state, for finite $T > 0$ we cannot do that. Following the previous idea of a real-time equilibration, the thermal state $\hat{\rho}_s$ is obtained through a TDVP evolution, with total equilibration times τ that increase with the interaction U and decrease with temperature T , as detailed later. In practice, this involves three steps:

- 1) we initialize a state with empty impurity $|0\rangle$ and “thermal” conduction electrons, with an MPS pure state $|\psi_0\rangle = |0\rangle \otimes |\emptyset_1, F_2\rangle$;
- 2) We evolve the system by slowly ramping-up the local and hybridization terms as

$$\hat{H}_{\text{SIAM}}^{\text{eq}}(t) = w(t)(\hat{H}_{\text{loc}} + \hat{H}_{\text{hyb}}) + \hat{H}_{\text{cond}}, \quad (5.5)$$

with $w(t)$ starting from zero and linearly approaching one, see Fig. 5.2(a), until reaching \hat{H}_{SIAM} ;

- 3) We finally relax the system with \hat{H}_{SIAM} , getting to a final MPS pure state $|E\rangle$ effectively encoding the correct equilibrium state, such that $\hat{\rho}_S = \text{Tr}_A(|E\rangle\langle E|)$, where the trace is taken over the ancillary modes introduced with the thermofield transformation.

By employing the explicit form of the Heisenberg operators, we do some reordering within the trace to find for the greater Green's function, Eq. (5.3):

$$iG_\sigma^>(t) = \text{Tr}_{S+A} \left(e^{-i\hat{H}t/\hbar} \hat{d}_\sigma^\dagger |E\rangle\langle E| e^{i\hat{H}t/\hbar} \hat{d}_\sigma \right) \quad (5.6)$$

Note that in contrast to Eq. (5.1) we traced over both the physical fermions, subscript ‘‘S’’, and over the ancillary ones, subscript ‘‘A’’, as required by $\hat{\rho}_S$ [141]. Defining states $|\phi_L^>(t)\rangle = e^{-i\hat{H}t/\hbar} \hat{d}_\sigma^\dagger |E\rangle$ and $\langle\phi_R^>(t)| = \langle E| e^{i\hat{H}t/\hbar} \hat{d}_\sigma$, calculated by two independent TDVP evolutions, we finally rewrite

$$iG_\sigma^>(t) = \text{Tr} (|\phi_L^>(t)\rangle\langle\phi_R^>(t)|) = \langle\phi_R^>(t)|\phi_L^>(t)\rangle. \quad (5.7)$$

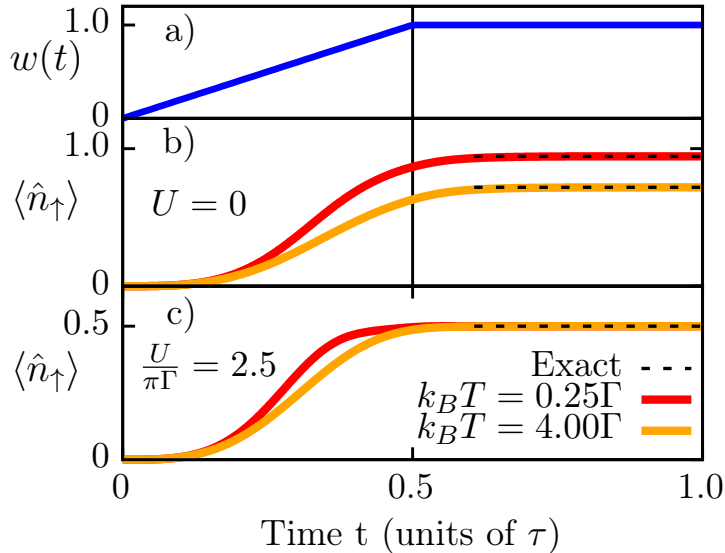


Figure 5.2.: a) Equilibration scheme employed to construct the thermal state of the system, see text for explanation. Local and hybridization terms are ramped-up linearly and kept constant for $t/\tau > 0.5$. Below: Evolution of $\langle\hat{n}_\uparrow\rangle$ for the noninteracting $U = 0$ (b) and particle-hole symmetric case $U = 2.5\pi\Gamma$ (c) at fixed impurity level energy $\varepsilon_d = -1.25\pi\Gamma$. Here $\tau = 8\hbar/\Gamma$ and bond dimension $D = 150$. Dashed lines represent exact equilibrium values obtained from exact diagonalization for $U = 0$, and the particle-hole symmetric value $\langle\hat{n}_\uparrow\rangle = \langle\hat{n}_\downarrow\rangle = 1/2$ for $U = 2.5\pi\Gamma = -2\varepsilon_d$.

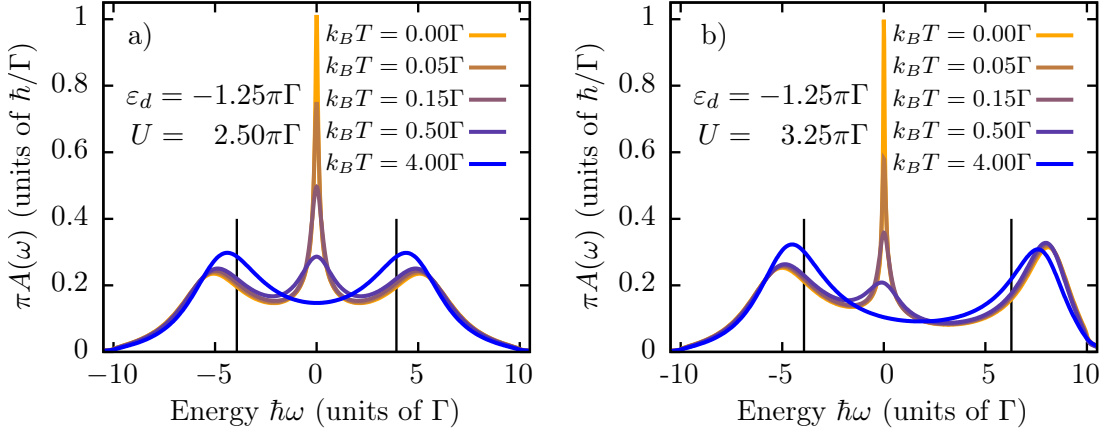


Figure 5.3.: Spectral function as obtained from the Fourier transform of the retarded Green’s function at different temperatures, showing the disappearance of the Kondo peak for increasing T . The interaction is $U = 2.5\pi\Gamma$ for the symmetric (a) and $U = 3.25\pi\Gamma$ for the non-symmetric case (b). Vertical lines mark impurity level energies at ε_d and $\varepsilon_d + U$. In the symmetric case, we estimate a Kondo temperature $k_B T_K \sim 0.07\Gamma$.

5.3. Main results

In our simulations we used a semi-elliptical fermion bath hybridization with half bandwidth W and coupling Γ , which in the continuum limit gives

$$\sum_k V_k^2 \delta(\epsilon - \epsilon_k) \rightarrow \frac{\Gamma}{\pi} \sqrt{1 - (\epsilon/W)^2}.$$

We fixed $W = 10\Gamma$ and the impurity energy level $\varepsilon_d = -1.25\pi\Gamma$. From here on we use Γ as our unit of energy. As discussed, our method involves two main blocks: First, we determine the equilibrium pure state $|E\rangle$ either by a direct DMRG GS-search ($T = 0$) or by a dynamical ramp-up, see Fig. 5.2(a), of \hat{H}_{loc} and \hat{H}_{hyb} ($T > 0$). Second, we calculate the Green’s function by TDVP evolutions starting from $|E\rangle$.

Equilibration. To test the first (equilibration) step we start from the empty impurity state $|\psi_0\rangle = |0\rangle \otimes |\emptyset_1, F_2\rangle$ and study the evolution of the spin-up impurity occupation $\langle \hat{n}_\uparrow \rangle$. We benchmark $\langle \hat{n}_\uparrow \rangle$ against exact values, for the noninteracting case ($U = 0$), Fig. 5.2(b), where exact diagonalization is possible, and for the particle-hole symmetric case ($\varepsilon_d = -1.25\pi\Gamma$, $U = 2.5\pi\Gamma$), Fig. 5.2(c), where the impurity is half-filled at any temperature $\langle \hat{n}_\uparrow \rangle = \langle \hat{n}_\downarrow \rangle = 1/2$. We find that $\langle \hat{n}_\uparrow \rangle$, starting from 0, converges to the exact values at the end of the equilibration in all cases. Further details on the equilibration step are given in Section 5.4.

Spectral function. Once the equilibrium state $|E\rangle$ is obtained, we calculate the Green’s function and — by means of a Fourier transform — the corresponding spectral

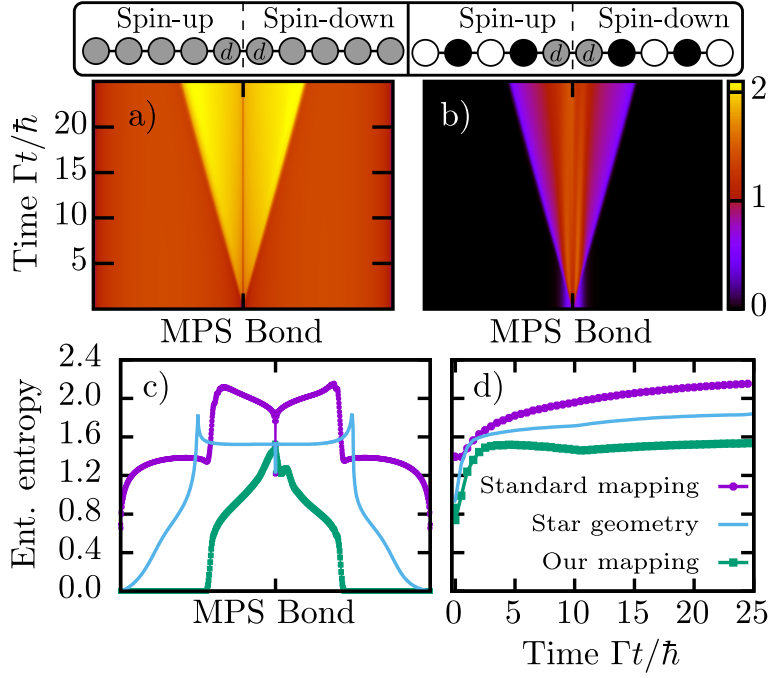


Figure 5.4.: Top: Evolution of the entanglement entropy along the MPS for the original chain method (a) and our work (b) in the symmetric SIAM at $T = 0$. Bottom: (c) The entanglement entropy at time $t = 25\hbar/\Gamma$ and (d) time-evolution of the maximum entropy for the original chain mapping, Fig. 5.1(c), our chain mapping, Fig. 5.1(e), and the star geometry, Fig. 5.1(b).

function $A(\omega)$. To obtain a smooth $A(\omega)$ we employ a “*linear prediction*” scheme [38, 141, 142] to extrapolate simulation data to longer times. In the symmetric case, at sufficiently strong repulsion U , we find two symmetrically located broad peaks due to the impurity close to energies ϵ_d and $\epsilon_d + U$, and a Kondo peak at the Fermi energy, see Fig. 5.3(a) [143]. We observe the disappearance of the Kondo peak as T increases. For the non-symmetric case of Fig. 5.3(b), at larger U , the Kondo peak becomes narrower but is still located at the Fermi energy. Our spectral functions are in excellent agreement with NRG results, see details in Section 5.5.

Entanglement. We now show how efficient is our mapping in terms of entanglement. We consider here $T = 0$, and we use the MPS structure **C** of Fig. 4.1, where spin degrees of freedom are spatially separated — which is known to be very efficient at $T = 0$ [38, 53, 144] — with spin-up on the left half of the MPS, spin-down on the right half, and the impurity in the middle. In principle, we could have carried out simulations with spinfull modes, ordered as in structure **B** of Fig. 4.1, as we did at finite temperature, or structure **A**. We have seen in the previous chapter that at $T = 0$ they all show similar behavior in the entanglement. However, the standard chain mapping approach to which we compare our results is impractically inefficient when working with spinfull fermions. Hence, we decided to employ spin-splitting in all approaches to allow for a fair comparison.

Fig. 5.4(a,b) show that our mapping leads to significantly lower entanglement entropy as compared to a standard chain mapping, with a characteristic “light-cone” spreading of entanglement, typical of short-ranged models. Fig. 5.4(c) shows a snapshot of the entanglement entropy across the whole MPS at time $t = 25\hbar/\Gamma$: interestingly, not only do we drastically improve on the standard chain mapping, but we also significantly improve on the star geometry, see Appendix B.2 for details. Fig. 5.4(d) shows the time-evolution of the maximum entanglement in the MPS: the original chain mapping, and also the star geometry, seem to show a logarithmic growth of entanglement, consistently with the analysis of Ref. [140], while the maximum entanglement entropy of our mapping seems to saturate, or in any case increase much more slowly.¹ Finally, let us mention that our method shows excellent scaling with the bath size, as increasing the number of sites will only lead to an extension of the zero entanglement region (see Fig. 5.4(b)) at the end of the chain, barely increasing the computational costs (see SM for details).

5.4. Analysis of the equilibration scheme

In this section, we provide a more detailed analysis of our evolution scheme employed to prepare the equilibrium state, which is then used for the calculation of the Green’s function. As explained previously, we expect the thermal conduction electrons to equilibrate with the impurity after bringing them into contact, hence converging towards the equilibrium state $|E\rangle$ we are looking for. In practice, we decided to smoothly turn on the local impurity and hybridization terms in a time-dependent fashion, see Fig. 5.2, in order to minimize the entanglement growth as compared to a sudden quench. In the following, we investigate this equilibration procedure in different scenarios. We first consider the noninteracting case, where we show that the hybridization energy converges towards the correct thermal value, and Green’s functions are reproduced correctly. Afterward, the effect of finite interaction U is studied at zero temperature, showing that stronger interactions lead to slower equilibration, but accurate Green’s functions can be obtained also for $U > 0$. The last subsections are devoted to the analysis of finite temperature effects, a quantitative analysis of the required equilibration time, and a summary including a qualitative discussion of the equilibration process.

5.4.1. Noninteracting case $U = 0$

At zero interaction, $U = 0$, the single impurity Anderson model (SIAM) reduces to the resonant level model and is solvable through exact diagonalization (ED), see

¹ For reference, our $T = 0$ simulations with bond dimension $D = 100$ and comparable accuracy required a CPU time of 15:31h in our chain geometry and 37:51h in the star geometry, on a single core of an Intel i7 9700K. These long computation times are due to the presence of a narrow Kondo peak, which requires us to calculate the Green’s function for long times.

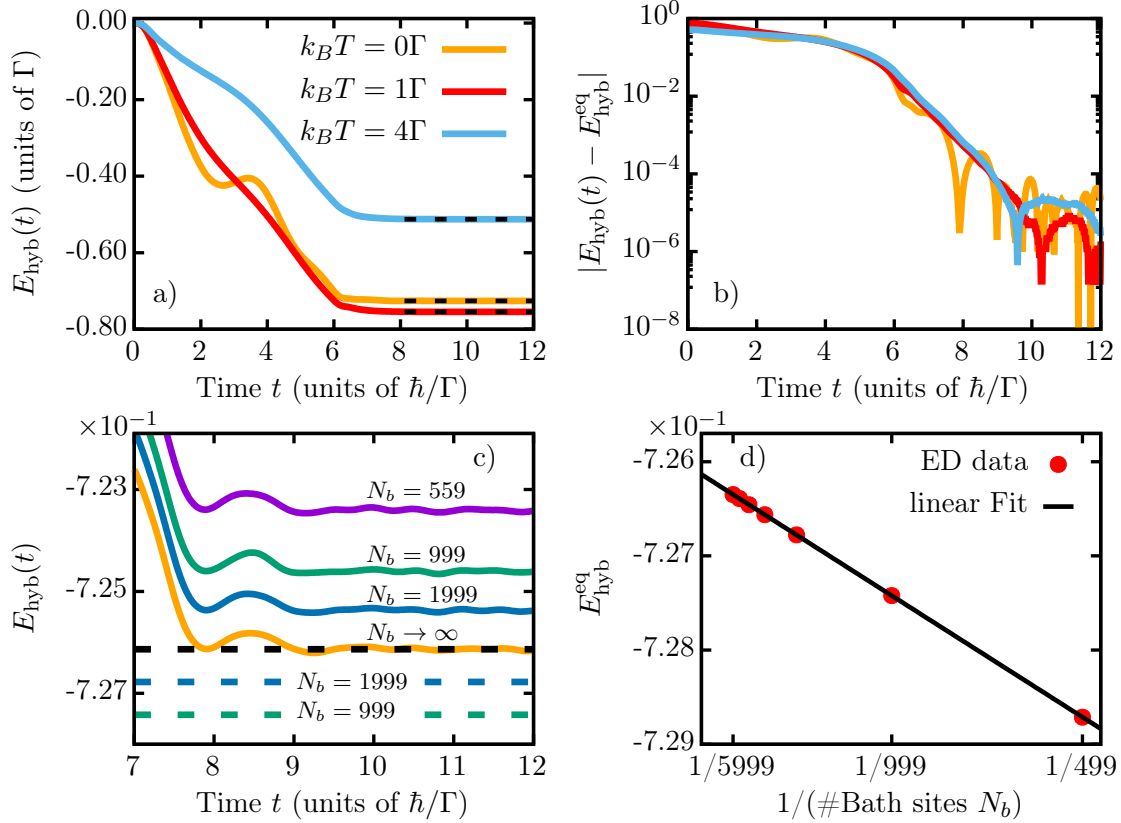


Figure 5.5.: Analysis of the equilibration scheme for the noninteracting case $U = 0$. a) Hybridization energy measured during equilibration with $\tau = 12\hbar/\Gamma$. Dashed lines correspond to hybridization energy in the thermal state as obtained from exact diagonalization. b) Difference between solid and dashed lines, showing excellent convergence of the hybridization energy. c) Size dependence of the hybridization energy at temperature $T = 0$. The fermionic bath is linearly discretized into N_b bath modes, and $N_b \rightarrow \infty$ is obtained using orthogonal polynomials for the equilibration (solid lines) and through extrapolation of finite-size data in exact diagonalization (ED, dashed horizontal lines). See text for comments on the various curves, in particular on the reason for the discrepancy between finite- N_b ED and MPS data. d) Extrapolation of finite-size data obtained from ED.

Ref. [145][Appendix A]. Hence, we are able to calculate expectation values not only in the ground state of the model, but also in the exact thermal state at any temperature T , to compare with our dynamical equilibration scheme. Previously we showed that the impurity occupation converges towards the thermal value. Here we would like to expand on this analysis. In particular, one quantity that we are able to compare is the hybridization energy, calculated as the expectation value $E_{\text{hyb}}(t) = \langle \psi(t) | \hat{H}_{\text{hyb}} | \psi(t) \rangle$ of the hybridization term

$$\hat{H}_{\text{hyb}} = \sum_{\sigma} \sum_k V_k \left(\hat{d}_{\sigma}^{\dagger} \hat{c}_{k,\sigma} + \text{H.c.} \right) = \sum_{\sigma} \sum_{c=1}^2 J_{c,0} \left(\hat{d}_{\sigma}^{\dagger} \hat{a}_{c,0,\sigma} + \text{H.c.} \right), \quad (5.8)$$

on the MPS state $|\psi(t)\rangle$ during equilibration. In Fig. 5.5(a) we show the time-dependence of the hybridization energy and the corresponding thermal state value

obtained through ED. For all temperatures, we find very smooth convergence and excellent agreement at the end of the dynamics (see also Fig. 5.5(b)).

At this point, let us briefly take a step away and discuss the effect of discretization. For ED, we generally use linear discretization with different numbers of bath modes N_b . For MPS simulations we use either linear discretization (plus Lanczos tridiagonalization) or orthogonal polynomials. In Fig. 5.5(c) we investigate the convergence of the hybridization energy for different discretizations at $T = 0$, with linear discretization being used for all curves with finite N_b . In the limit $N_b \rightarrow \infty$ — obtained using orthogonal polynomial discretization for the dynamics (orange curve) and extrapolation of finite-size ED data as presented in Fig. 5.5(d) — we observe excellent agreement between our MPS equilibration scheme and ED. The finite-size behavior, however, is clearly different for ED and the MPS dynamics. This can be understood from the following arguments. For the MPS dynamics, only chain sites sufficiently close to the impurity do have an impact on the hybridization energy, since any excitation created due to the interaction of impurity and fermion bath — being either a particle in the empty chain or a hole in the filled chain — is traveling at finite speed along the chain. Hence, it cannot reach chain sites too far away from the impurity by the end of the dynamics. On the other hand, in equilibrium simulations (DMRG or ED) *all* chain sites contribute to the equilibrium state, including those far away from the impurity and unreachable by the dynamics. The discrepancy at finite bath size N_b seen in Fig. 5.5(c) is therefore expected, and, in all of the energy comparisons, we consider the limit $N_b \rightarrow \infty$.

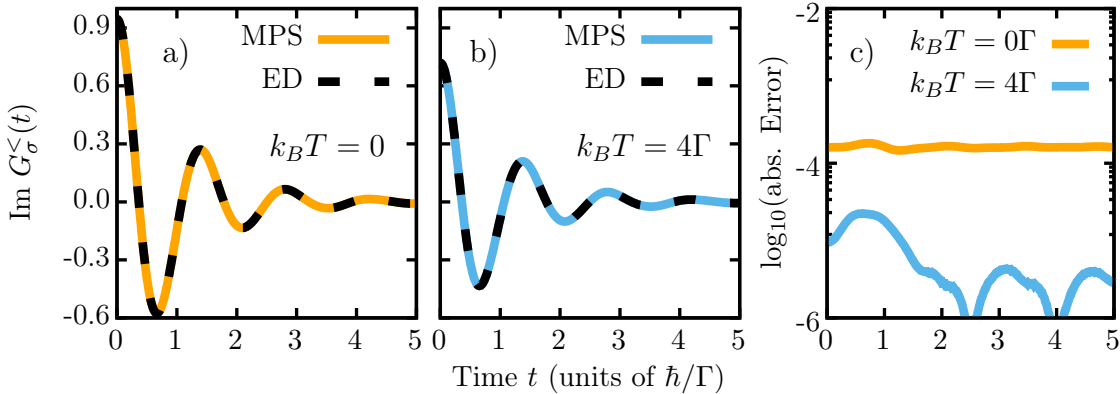


Figure 5.6.: (a+b) Imaginary part of the lesser impurity Green’s function for $U = 0$. Initial states to calculate $G_{\sigma}^{<}$ were prepared through equilibration with $\tau = 12\hbar/\Gamma$ (solid line) and exact diagonalization (ED, dashed line). c) Absolute error of the lesser Green’s function when using real-time equilibration as compared to ED results.

Let us turn to the object of interest: the Green’s function. For the comparison with ED, we focus on the lesser Green’s function $G_{\sigma}^{<}(t) = i \text{Tr}_s(\hat{d}_{\sigma}^{\dagger}(0)\hat{d}_{\sigma}(t)\hat{\rho}_s)$, since, in contrast to the retarded Green’s function, it *does* show temperature dependence even at $U = 0$. We compare the Green’s function obtained from ED, starting from the exact thermal state, with the one calculated with our MPS-based approach, where a

real-time equilibration is used to prepare the initial state. As shown in Fig. 5.6, we find excellent agreement, verifying that our approach correctly reproduces the temperature dependence of the Green's function.

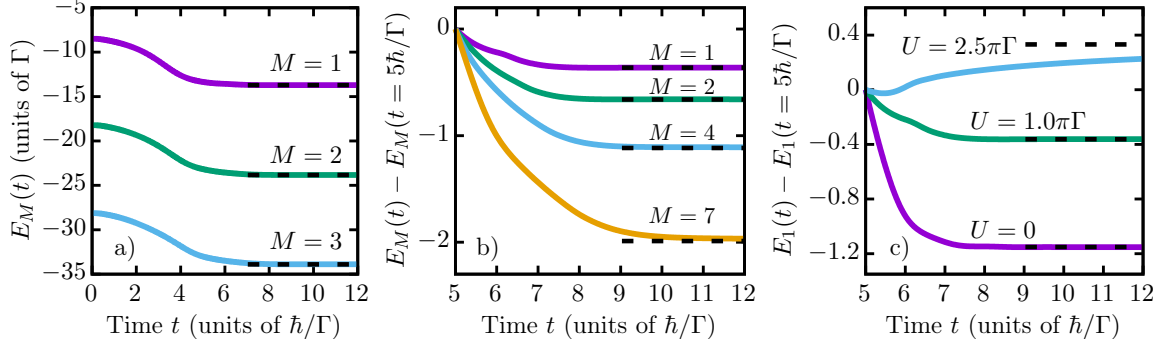


Figure 5.7.: Analysis of the equilibration scheme at fixed temperature $T = 0$. a) Dynamics of the partial energy for different M at fixed interaction $U = \pi\Gamma$ and $\tau = 12\hbar/\Gamma$. Dashed lines indicate ground state values extrapolated to the thermodynamic limit $N_b \rightarrow \infty$. b) Convergence behavior of partial energies. We subtract $E_M(t = 5\hbar/\Gamma)$ to have the same energy scale for all curves even with different M . c) Convergence of the partial energy E_1 for different interactions U . Stronger repulsion leads to slower equilibration.

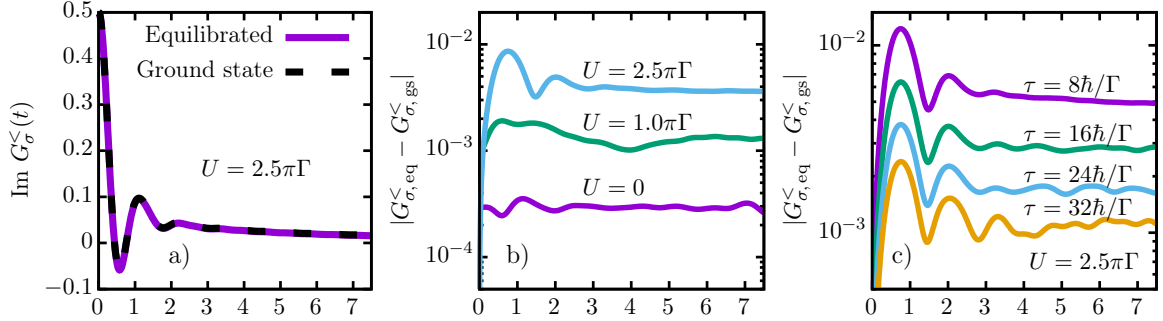


Figure 5.8.: a) Imaginary part of the lesser Green's function for $U = 2.5\pi\Gamma$ using the initial state obtained from equilibration (with $\tau = 32\hbar/\Gamma$) and DMRG ground state search. b) Error of the lesser Green's function obtained after equilibrating for $\tau = 12\hbar/\Gamma$ as compared to starting from the DMRG ground state. Stronger repulsion leads to slower equilibration, hence to larger errors in the Green's function. c) Error of $G_\sigma^<$ for different equilibration times at $U = 2.5\pi\Gamma$, which is found to decrease smoothly as we let the system equilibrate longer.

5.4.2. Interacting case at zero temperature

At $T = 0$ and finite interaction U , we can benchmark the equilibration procedure with the ground state as obtained from equilibrium DMRG calculations. We concentrate on the Green's function, as well as on the energy obtained by taking into account only chain sites at a finite distance from the impurity. The full SIAM with truncated

chain length (finite L) is given by

$$\widehat{H}_{\text{SIAM}}^{(L)} = \widehat{H}_{\text{loc}} + \widehat{H}_{\text{hyb}} + \sum_{\sigma} \sum_{c=1}^2 \left(\sum_{n=1}^{L-1} \left(J_{c,n} \hat{a}_{c,n,\sigma}^{\dagger} \hat{a}_{c,n-1,\sigma} + \text{H.c.} \right) + \sum_{n=0}^{L-1} E_{c,n} \hat{a}_{c,n,\sigma}^{\dagger} \hat{a}_{c,n,\sigma} \right).$$

We define the partial energies to be expectation values $E_M = \langle \psi(t) | \widehat{H}_{\text{SIAM}}^{(M)} | \psi(t) \rangle$, with $M \leq L$, such that only chain sites closest to the impurity are considered for the energy measurement. As expected, we find these partial energies to converge: for fixed $U = \pi\Gamma$ the final values are in perfect agreement with the corresponding expectation value in the DMRG ground state (see Fig. 5.7(a+b)). Similarly to the previous section, static DMRG data were obtained using linear discretization with various numbers of bath modes N_b , and were extrapolated to the thermodynamic limit employing a polynomial fitting function $E_M(N_b) = a(N_b)^{-c} + d$, with fitting parameters a, c, d . Zooming into the convergence behavior at the end of the equilibration (that is why we subtract $E_M(t = 5\hbar/\Gamma)$), we find that smaller M partial energies converge faster, implying that bath sites closer to the impurity equilibrate faster than sites further away. Investigating the effect of the interaction U , we find that stronger interactions lead to significantly slower equilibration (see Fig. 5.7(c)). Hence, longer evolution times are required to reach equilibrium. This behavior also impacts the accuracy of the Green's function, shown in Fig. 5.8(a). Comparing the Green's function obtained after the equilibration step with the one computed starting from the DMRG ground state, we observe larger deviations as U increases, see Fig. 5.8(b). Indeed, this error is due to insufficient equilibration and can be controlled through the equilibration time τ , Fig. 5.8(c). The longer the equilibration, the more accurate the Green's function. In practice, it is therefore important to converge the Green's function with respect to τ .

5.4.3. Effect of finite temperature at $U = 2.5\pi\Gamma$

In this section, we investigate the effect of temperature on the equilibration in the interacting case. We fix the interaction to be $U = -2\varepsilon_d = 2.5\pi\Gamma$, where at $T = 0$ we observed rather slow convergence of the partial energy and the Green's function with respect to the total equilibration time τ . We start by analyzing the convergence of the partial energy $E_{M=1}(t)$ at fixed $\tau = 14\hbar/\Gamma$ in Fig. 5.9. While at $T = 0$ $E_{M=1}(t)$ has not yet converged by the end of the equilibration dynamics, such convergence is achieved, significantly faster, at higher temperatures. These findings suggest that also the Green's function will converge much faster at finite temperature, as we will now show.

At both finite interaction and temperature — in contrast to the previous sections — we do not have any reference results to benchmark the time-dependence of the Green's function. For this reason, we use an alternative strategy to investigate convergence with τ : We calculate the difference $|G_{\sigma,\tau_1}^< - G_{\sigma,\tau_2}^<|$ of two Green's functions obtained after equilibration with different equilibration times τ_1 and τ_2 , where we fix $\tau_2 = \tau_1 + 2\hbar/\Gamma$. At convergence, this difference should vanish, since the Green's functions

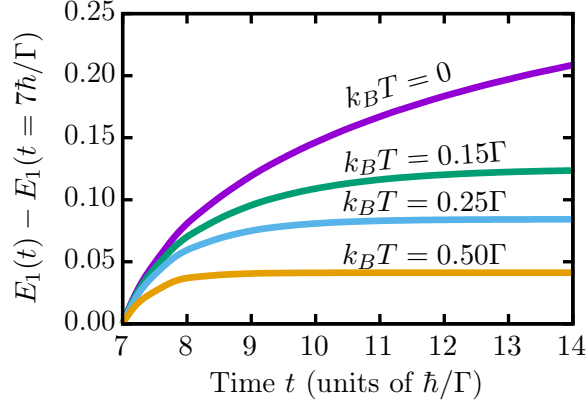


Figure 5.9.: Convergence of the partial energy $E_1(t)$ for fixed interaction $U = 2.5\pi\Gamma$ and equilibration time $\tau = 14\hbar/\Gamma$ at various temperatures. Higher temperature leads to significantly faster convergence.

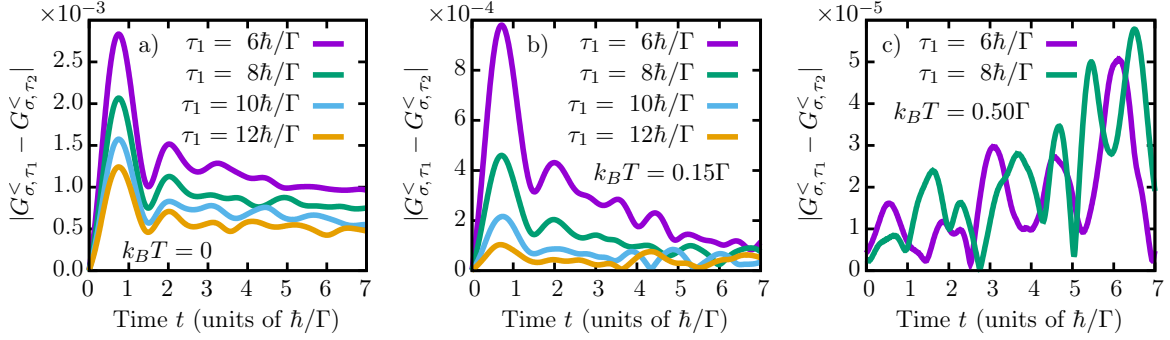


Figure 5.10.: Convergence of the Green's function is presented for temperatures $k_B T = 0$ (a), $k_B T = 0.15\Gamma$ (b) and $k_B T = 0.5\Gamma$ (c). Plots show the difference of two Green functions obtained after equilibrating for total time τ_1 and $\tau_2 = \tau_1 + 2\hbar/\Gamma$. Higher temperature leads to significantly reduced differences, indicating faster convergence of the equilibration with respect to τ .

become independent of the equilibration time. In Fig. 5.10 we show this convergence indicator for zero and finite temperature. We observe that for $T = 0$ it decreases as we increase τ_1 (and implicitly τ_2), as expected. At $T > 0$ we find the Green's function to converge significantly faster as compared to the zero temperature case (note the different scale of the y-axis). While at $k_B T = 0.15\Gamma$ our convergence indicator nicely decreases down to only 10^{-4} , for $k_B T = 0.5\Gamma$ it already stays below that value even for short equilibration times, with $\tau_1 = 6\hbar/\Gamma$.

5.4.4. Quantitative analysis of the equilibration time τ

We have seen previously that the system equilibrates faster at higher temperatures, while strong coupling U leads to slower equilibration. Here we quantify these effects and analyze the required equilibration time τ for different system parameters. To this

end, we calculate the Green's function after equilibrating for a sufficiently long time τ_{ref} , using it as a reference. We then calculate $G_{\tau'}^<(t)$ for various equilibration times τ' and calculate the absolute error with respect to the reference simulation. The minimum possible equilibration time with error less than $\varepsilon_{\text{err}} = 2 \times 10^{-3}$ is what we define to be the required equilibration time τ :

$$\tau = \min(\tau') \quad \text{such that} \quad \max_t |G_{\tau'}^<(t) - G_{\tau_{\text{ref}}}^<(t)| < \varepsilon_{\text{err}} \quad (5.9)$$

As expected from the previous discussions, we find the required equilibration time to grow as we lower temperature, see Fig. 5.11(a), where we identify two distinct regimes: At high temperatures $T \gg T_K$, where the Kondo effect is suppressed, the equilibration time shows a plateau, since the relevant energy scale is given by the local impurity level width Γ . Hence, one expects $\tau \propto \Gamma^{-1}$. For temperatures $T \gtrsim T_K$, where the Kondo effect plays a role, we observe power-law scaling, with $\tau \propto T^{-1}$, as obtained from the fit. For very low temperatures $T \ll T_K$, it is currently unclear how the equilibration time behaves since this regime is hard to reach. However, considering the smooth convergence of the Green's function (see Fig. 5.8), it seems possible that the equilibration criterion is satisfied for large τ even at $T = 0$. It is an open question if the observed behavior for the equilibration time is directly connected to Anderson's orthogonality catastrophe [146] and the absorption edge singularity [147].

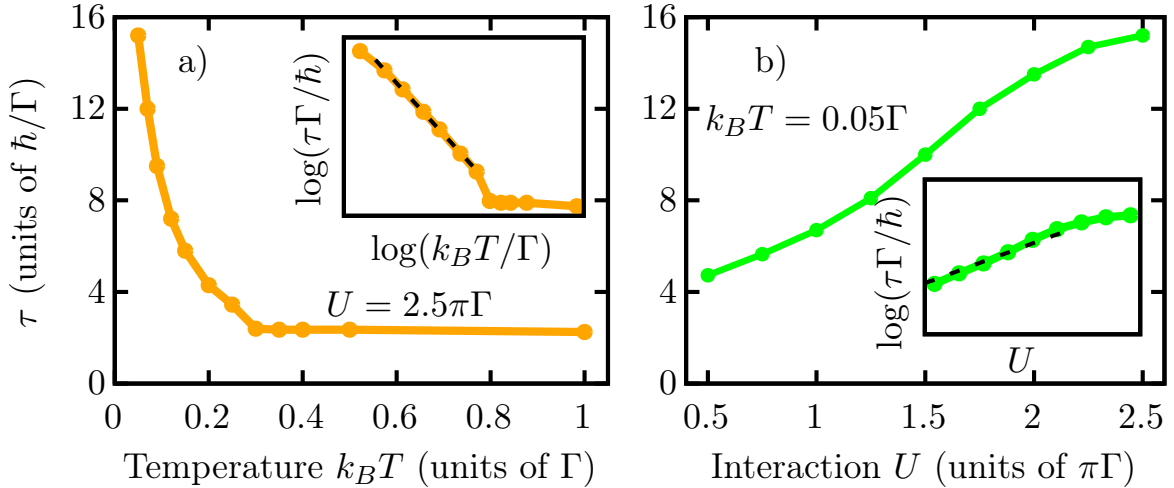


Figure 5.11.: a) Equilibration time as a function of temperature for the particle-hole symmetric Anderson model with $U = 2.5\pi\Gamma$. The inset shows the same data in a log-log plot, together with a polynomial fit for $0.07\Gamma \leq k_B T \leq 0.25\Gamma$, which yields $\tau \propto (k_B T)^{-1}$ (dashed line). b) Equilibration time versus interaction U at particle-hole symmetry and fixed temperature $k_B T = 0.05\Gamma$. Inset: Same data with log-linear axes, and exponential curve with $\tau \propto \exp(\frac{\pi U}{16\Gamma}) \propto 1/\sqrt{T_K}$ (dashed line).

As is well known, the Kondo temperature is exponentially small in the interaction

U at strong coupling [57], with

$$k_B T_K \sim \sqrt{\frac{2U\Gamma}{\pi^2}} \exp\left(-\frac{\pi U}{8\Gamma} + \frac{\pi\Gamma}{2U}\right), \quad (5.10)$$

for the symmetric case. Hence, it is not surprising that τ increases with U , as the narrow Kondo peak can be resolved only on long time scales. For $k_B T = 0.05\Gamma$, we find, see Fig. 5.11(b), the equilibration time τ to grow exponentially for moderately small U , where the corresponding Kondo temperature is still $T_K \gg T$. Taking the scaling of the Kondo temperature with U as in Eq. (5.10), our data seem to suggest a $\tau \propto 1/\sqrt{T_K}$ behavior. As the interaction U increases further, the exponential growth of τ is cut-off by temperature, when T_K becomes of the order of T . Further study would be needed to fully characterize and understand the scaling of the equilibration time in the whole parameter space of T and U .

5.4.5. Summary and discussion of the equilibration step

We have studied in detail the procedure we use to prepare the equilibrium state at finite temperature. We find that, after turning on the hybridization (and the local term), impurity occupation, hybridization energy, and more generally, partial energies (taking into account only chain sites closest to the impurity), converge towards their respective values in the exact equilibrium state. In particular, we focused on the cases of either zero interaction or zero temperature, where exact results for the equilibrium state are available, but we expect our conclusion to hold at finite interaction and temperature as well. We have quantitatively studied the required equilibration time and its dependence on U and T . We found that equilibration takes more and more time as the interaction U increases. On the other hand, increasing the temperature tends to speed up the equilibration process.

The qualitative picture we have in mind for the equilibration is that — in the chain geometry — fermionic sites locally converge towards their equilibrium state, with sites close to the impurity converging faster than sites further away. With this picture, we can discuss the issue of unitary dynamics versus equilibration. Since we consider a closed quantum system (consisting of impurity and bath fermions) with Hamiltonian dynamics only, the evolution is unitary. Hence, the quantum state contains information about the initial state at all times. At first sight, this might seem to be in contradiction with the idea of converging towards some equilibrium steady state. However, excitations — created in the chain sites connected to the impurity while/after turning on the hybridization — can travel along the (infinitely long) chain forever. Hence, they can carry information and residual energy of the initial state away from the impurity, while sites closer to the impurity can equilibrate. This is, in essence, a mechanism of *local thermalization*, as described in Ref. [148], where local here refers to the topology of the chain. It is important to note that the calculation of the Green's function requires the

application of creation/ annihilation operators at the impurity, which does not interfere with the non-equilibrated part of the state far away from the impurity. For this reason, we can obtain accurate Green's functions that do not contain any signs of the equilibration procedure.

5.5. Benchmark against Numerical Renormalization Group results

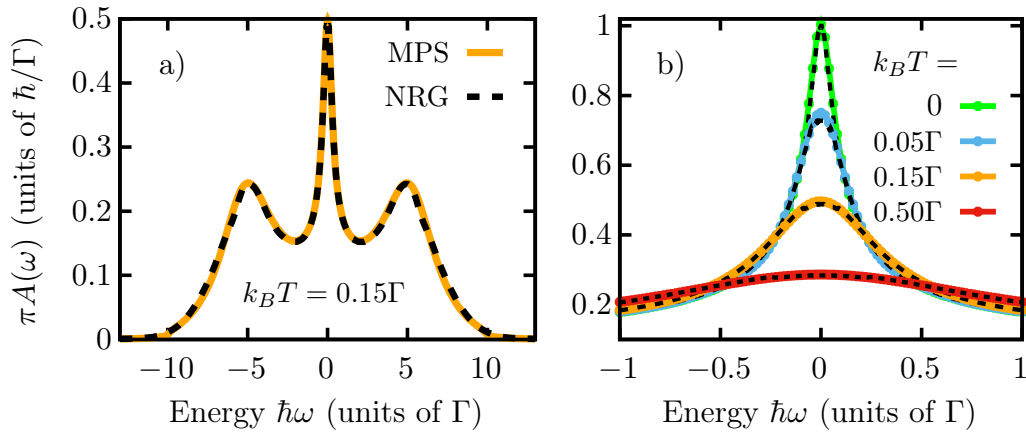


Figure 5.12.: a) Spectral function of the particle-hole symmetric Anderson model with $U = 2.5\pi\Gamma$ (Kondo temperature $k_B T_K \simeq 0.07\Gamma$) at temperature $k_B T = 0.15\Gamma$. b) Zoom into the Kondo peak at various temperatures. Solid lines correspond to our MPS calculations, while dashed black lines are obtained from NRG.

At non-zero interaction, we can benchmark our spectral functions against the numerical renormalization group (NRG) method. To perform NRG calculations, we used the 'full density matrix' method of the open-source library "NRG Ljubljana", based on the work of Ref. [72], with z -averaging parameter $N_z = 8$ and logarithmic discretization $\Lambda = 2$. We find an excellent agreement between NRG and our MPS results, see Fig. 5.12, where, in particular, we show that the Kondo peak is resolved correctly at all temperatures. Note that the Kondo peak is the most difficult feature to capture for our technique since it requires long time-evolutions. We further mention that we observe equally good agreement between MPS and NRG in the non-symmetric case with $U = 3.25\pi\Gamma$ (not shown).

5.6. Summary and conclusions

We presented an efficient chain-mapping-based method to simulate Anderson impurity models using matrix product states. Our method overcomes a major problem of

the original chain mapping, where mixing empty and filled sites led to large entanglement within the chain. Separating empty from filled sites and mapping them into separate chains, we drastically reduced the entanglement, providing significant performance improvements. In contrast to the star geometry, our method does not involve long-range couplings, but only next-nearest-neighbor terms.

Using a thermo-field transformation the idea neatly generalizes to finite temperatures, where we demonstrated its capabilities by studying the Kondo physics regime. Future research directions include the application to non-equilibrium dynamics, and the implementation of the DMFT loop, where multi-orbital problems are within reach [38, 40].

6. Dissipation in the driven Anderson impurity model

Atomic force (AFM) or scanning tunneling microscopes (STM) with nanoscale resolution have a long history in condensed matter physics, with outstanding capabilities in imaging and force measurements of material surfaces. Experimental progress has enabled the accurate measurement of dissipation in oscillating tips experiments [149–152], where energy is dissipated into the nanomechanical system due to the interaction of the oscillating tip and the sample underneath. The dissipated energy can then be used to investigate the sample, for example, to distinguish between a superconducting or metallic state [150].

Recently, it was suggested that the on and off switching of the Kondo effect through the oscillating tip might be detected in pendulum AFM dissipation measurements, where the cost to create or destroy the Kondo cloud should be in the order of the Kondo temperature $k_B T_K$ [153]. In this work, the Kondo switching has been modeled by turning on and off the hybridization interaction between the impurity and the free electrons in the metal. Due to the slow frequency of the oscillating tip, in the order of few kHz, it was assumed that the system equilibrates between switching on and off the Kondo effect. On the other hand, the switching itself has been assumed to be instantaneous, allowing to express the dissipation in terms of equilibrium quantities. The finite frequency case, discussed in Ref. [154], essentially confirmed that the Kondo effect should contribute to the dissipation with an energy per cycle of about $k_B T_K$.

Experimentally, the controlled switching of the Kondo effect has been realized in combined STM/ AFM experiments, by chemically changing the impurity spin between spin-1/2 (Kondo) and spin-1 (non-Kondo) [155], and should be possible also via mechanical lifting of the impurity [156], where dissipation measurements are possible.

In view of currently ongoing oscillating tip-based Force Microscopy (AFM) experiments [157], this chapter reports some theoretical early-stage work on the issue of nanomechanical dissipation in quantum impurity systems, discussing possible extensions of Refs. [153, 154]. In particular, we explore the possibilities to simulate the real-time dynamics, and hence the dissipation, of the SIAM with flexible driving and at any temperature, employing the approach developed in previous chapters. The material contained in this Chapter is still unpublished.

6.1. Model and setting of the problem

The essential physics that needs to be captured in the model is the Kondo effect. We will consider the single impurity Anderson model discussed in the previous chapters. We recall that it consists of three terms

$$\hat{H}_{\text{SIAM}} = \hat{H}_{\text{loc}} + \hat{H}_{\text{hyb}} + \hat{H}_{\text{cond}} . \quad (6.1)$$

The local term \hat{H}_{loc} describes the impurity

$$\hat{H}_{\text{loc}} = \sum_{\sigma} \varepsilon_d \hat{d}_{\sigma}^{\dagger} \hat{d}_{\sigma} + U \hat{n}_{\uparrow} \hat{n}_{\downarrow} + B(\hat{n}_{\uparrow} - \hat{n}_{\downarrow}) , \quad (6.2)$$

with energy level ε_d and on-site Coulomb repulsion U . In addition to the standard terms of the previous chapters, we also included a magnetic field B . As is well known, the magnetic field destroys the Kondo effect [57, 158] and hence provides a control parameter that allows us to extract the Kondo contribution to the dissipation. The impurity couples to conduction electrons through the hybridization interaction

$$\hat{H}_{\text{hyb}} = \sum_{\sigma} \sum_k V_k \left(\hat{d}_{\sigma}^{\dagger} \hat{c}_{k\sigma} + \hat{c}_{k\sigma}^{\dagger} \hat{d}_{\sigma} \right) ,$$

with spin-independent hybridization couplings V_k . The conduction electrons are, as usual, free fermions

$$\hat{H}_{\text{cond}} = \sum_{\sigma} \sum_k \epsilon_k \hat{c}_{k\sigma}^{\dagger} \hat{c}_{k\sigma} . \quad (6.3)$$

As mentioned in Section 3.1, the magnetic field breaks the spin-symmetry, and also particle-hole (PH) symmetry, if present. However, the model is invariant under the combined PH and spin-flip transformation

$$\hat{c}_{k,\sigma} \longrightarrow \hat{c}_{-k,-\sigma}^{\dagger} \quad \hat{d}_{\sigma} \longrightarrow -\hat{d}_{-\sigma}^{\dagger} , \quad (6.4)$$

provided we make the particle-hole symmetric choice $\varepsilon_d = -U/2$, $V_k = V_{-k}$, $\epsilon_k = -\epsilon_{-k}$. As before, we choose the hybridization to have a semi-circular shape, given in the continuum limit given by $V^2(x) = \Gamma\sqrt{1-x^2}/\pi W$, with hybridization coupling Γ , half-bandwidth W , and dimensionless energy $x = \epsilon/W$. While in absence of the magnetic field particle-hole symmetry implies $\langle \hat{n}_{\sigma} \rangle = 1/2$ for equilibrium states, in presence of B we have lower symmetry with $\langle \hat{n}_{\uparrow} + \hat{n}_{\downarrow} \rangle = 1$ for the impurity population.

6.1.1. Protocol and dissipation

We model the action of the tip as a periodic time-dependent shift of the energy level $\varepsilon_d \rightarrow \varepsilon_d(t)$, caused by electrostatic interactions between tip and impurity. A full cycle consists of the following four steps, as visualized in Fig. 6.1(a):

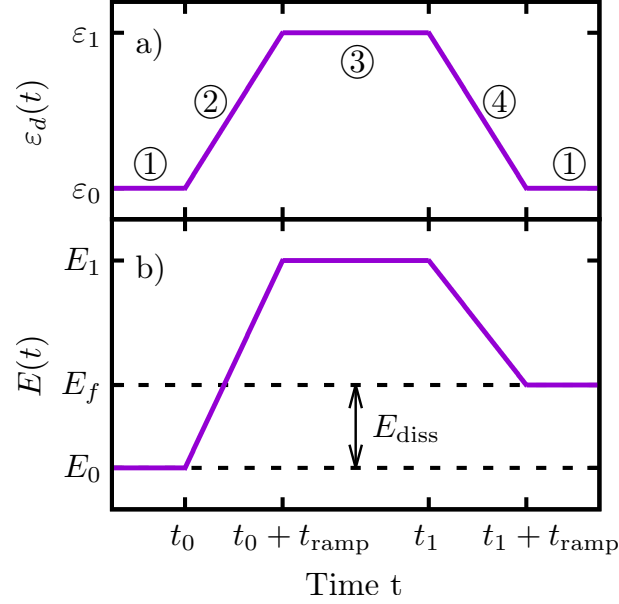


Figure 6.1.: Dissipation due to external driving. a) Time dependence of the impurity energy level during a single cycle. In steps ① and ③ the Hamiltonian is kept constant and the system equilibrates. In step ② the level is lifted from ε_0 to ε_1 in a time t_{ramp} , with linear time-dependence. In the last step ④ it is brought back to its original value ε_0 . b) Schematic time evolution of the total energy of the system. The dissipation E_{diss} is given by the energy difference at the beginning and the end of the cycle, and is absorbed by the infinitely large bath.

- ① The initial Hamiltonian with impurity energy level ε_0 is kept constant until the system has reached its equilibrium state. This stage models the tip far away from the impurity, where the Kondo effect is present. We expect that this is a reasonable approximation since the tip oscillation frequency is slow as compared to the relevant time scales of the Kondo impurity.
- ② The impurity energy level is raised (or lowered) linearly from ε_0 to ε_1 within a time t_{ramp} , modeling the tip approaching the impurity.
- ③ For simplicity, we let the system evolve until it reaches its new equilibrium state. In future research one could alternatively skip this step, assuming that no equilibration occurs when the tip is close to the impurity.
- ④ In the last step the impurity energy level is lowered (or raised) back to its original value ε_0 of step ①.

In Fig. 6.1(b) we schematically show the total energy $E(t)$ of the system within a single cycle. During the equilibration steps ① and ③, the total energy stays constant since the Hamiltonian is time-independent. In steps ② and ④ however, the energy can change due to the time-dependence of the impurity energy level, and hence, energy can be pumped into the impurity. Of course, the energy can then flow into the bath

due to the hybridization coupling. The dissipation per cycle, E_{diss} is defined as the net energy that is pumped into the system. It can be calculated as the difference between the energies E_0 and E_f at the beginning and at the end of the cycle:

$$E_{\text{diss}} = E_f - E_0 \quad (6.5)$$

One might ask the question of where the energy goes, and how a closed system can continuously absorb energy. The reason lies in the macroscopic (infinitely large) bath, which is able to take all the energy without ever heating up. This is particularly easy to understand if the bath is represented as a tight-binding chain, see Chapter 3. We can imagine that energy is pumped into the impurity, and then flows into the bath. Within the bath, the energy can continuously flow along the chain, and since the chain is infinitely long in the thermodynamic limit, it never comes back, and hence is lost forever in the infinity of the bath.

Let us discuss some practical aspects of the simulations: In steps ① and ③, one should evolve the system until it reaches its equilibrium state. However, the equilibrium state does not depend on the preceding dynamics, and therefore we can carry out steps ① + ② and steps ③ + ④ in separate simulations. In this case the dissipation is then calculated as

$$E_{\text{diss}} = (E(t_0 + t_{\text{ramp}}) - E(t_0)) + (E(t_1 + t_{\text{ramp}}) - E(t_1)) . \quad (6.6)$$

Notice that this reduces to the original definition if $E(t_0 + t_{\text{ramp}}) = E(t_1)$, which is the case when all steps are done in a single run, but is not necessarily true if the dynamics is split into two parts. At zero temperature there is one more simplification possible. Instead of calculating the equilibrium state through real-time evolution, we can simply use the DMRG algorithm to calculate the ground state of the system.

6.1.2. Dissipation for a sudden quench

Let us briefly discuss the special case where the ramp is sudden ($t_{\text{ramp}} = 0$). Assuming that the system is in its equilibrium state at the end of step ①, the sudden quench of ε_d in step ② causes the energy of the closed system to change by

$$\Delta E(\text{②}) = (\varepsilon_1 - \varepsilon_0) n(\text{①}), \quad (6.7)$$

where $n(\text{①}) = \langle \psi(t_0) | \hat{n}_\uparrow + \hat{n}_\downarrow | \psi(t_0) \rangle$ is the impurity particle occupation at the end of ①. Similarly, the change of energy in step ④ depends on the occupation $n(\text{③})$ at the end of step ③ through

$$\Delta E(\text{④}) = (\varepsilon_0 - \varepsilon_1) n(\text{③}) . \quad (6.8)$$

The dissipation is then given as the sum of the energy changes in steps ② and ④:

$$\begin{aligned} E_{\text{diss}} &= \Delta E(\text{②}) + \Delta E(\text{④}) \\ &= (\varepsilon_1 - \varepsilon_0) [n(\text{①}) - n(\text{③})] \end{aligned} \quad (6.9)$$

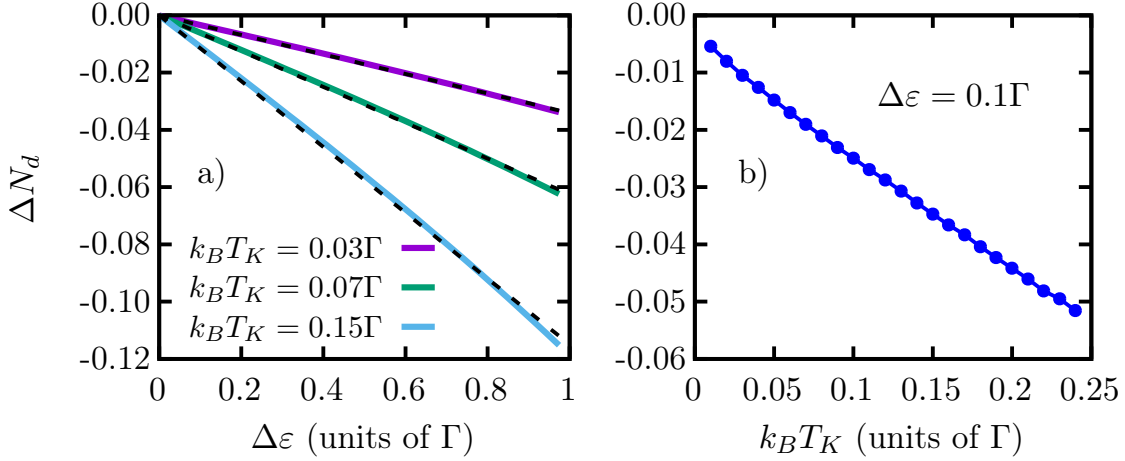


Figure 6.2.: Equilibrium (ground state) impurity occupation. a) Deviation from unit impurity filling, $\Delta N_d = \langle \hat{N}_d \rangle - 1$, in the ground state of the SIAM, as a function of the energy level shift $\Delta\varepsilon$ with respect to particle-hole symmetry, $\varepsilon_d = -U/2 + \Delta\varepsilon$. Dashed lines represent linear fits, and Kondo temperatures in the legend are estimated from the symmetric case $\Delta\varepsilon = 0$ using Eq. (6.10). The hybridization Γ is fixed to be 10% of the half-bandwidth W , $\Gamma = 0.1W$. b) ΔN_d as a function of the Kondo temperature at fixed $\Gamma = 0.1W$ and $\Delta\varepsilon = 0.1\Gamma$.

Hence, it is clear that, in the sudden quench scenario, the dissipation depends only on the equilibrium particle occupation of the impurity. This will be discussed in more detail in the next section.

6.2. Preliminary results

This section provides some preliminary results for the dissipation at zero temperature. The purpose of this analysis is to understand whether or not the dissipation shows signatures of the Kondo effect if the impurity energy level of the SIAM is periodically moved up and down.

6.2.1. Equilibrium impurity occupation

We study the equilibrium impurity occupation in the $T = 0$ ground state for different system parameters. For the symmetric SIAM with $\varepsilon_d = -U/2$ we find the impurity occupation $\langle \hat{N}_d \rangle = \langle \hat{n}_\uparrow + \hat{n}_\downarrow \rangle = 1$ to be independent of the magnetic field B (not shown), due to the particle-hole plus spin-flip symmetry discussed previously. Since the magnetic field does destroy the Kondo effect but does not affect the impurity occupation, it is clear that the impurity occupation alone does not contain information about the Kondo effect in the particle-hole symmetric case. For this reason we consider also the nonsymmetric case with $\varepsilon_d = -U/2 + \Delta\varepsilon$ and measure the deviation from unit

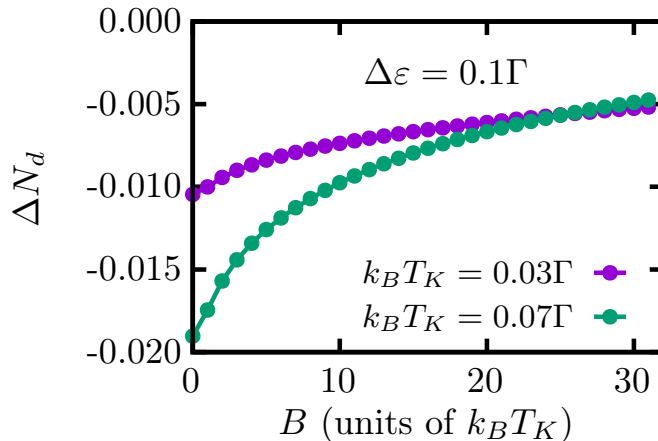


Figure 6.3.: Magnetic field dependence of the equilibrium impurity population. Deviation from unit filling, ΔN_d , as a function of the magnetic field B , at $\Delta\varepsilon = 0.1\Gamma$ and estimated Kondo temperature as indicated in the legend.

filling, $\Delta N_d = \langle \hat{N}_d \rangle - 1$, hoping to see some Kondo-related magnetic field dependence.

Let us first analyze how the impurity occupation depends on the various physical parameters of the model. We find ΔN_d to be linear in the deviation from particle-hole symmetry, $\Delta\varepsilon$, see Fig. 6.2(a). The slope, however, depends on the interaction, and hence the Kondo temperature, which we estimate as [159]

$$\frac{k_B T_K}{\Gamma} = \sqrt{\frac{2u}{\pi}} \exp\left(\frac{-\pi^2 u}{8} + \frac{1}{2u}\right). \quad (6.10)$$

at particle-hole symmetry. Here, $u = U/\pi\Gamma$ is the dimensionless interaction. Indeed ΔN_d shows a strong dependence on the Kondo temperature, see Fig. 6.2(b), with the magnitude of ΔN_d increasing with T_K . Hence, the results are indeed promising to find some Kondo-related dissipation. To further elaborate on this issue, we study the magnetic field dependence of ΔN_d . If ΔN_d is indeed related to the Kondo effect, we expect it to converge towards zero as we increase the magnetic field, as B destroys the Kondo effect. Indeed this is what we also find numerically, see Fig. 6.3, where the deviation from unit filling seems to decrease rapidly at small magnetic fields, but only slowly at strong fields $B > 10k_B T_K$, where the Kondo effect is not existent anymore.

6.2.2. Dissipation

Let us now turn to the main object of interest, the dissipation within a full cycle. The impurity energy level is periodically driven between ε_0 and ε_1 . We fix the initial level energy at particle-hole symmetry, $\varepsilon_0 = -U/2$, and lift it by $\Delta\varepsilon = 0.7\Gamma$, such that $\varepsilon_1 = -U/2 + 0.7\Gamma$.

We start our analysis considering the noninteracting case with $U = 0$. Here, the impurity spectral function has just a single peak, corresponding to the local level of the

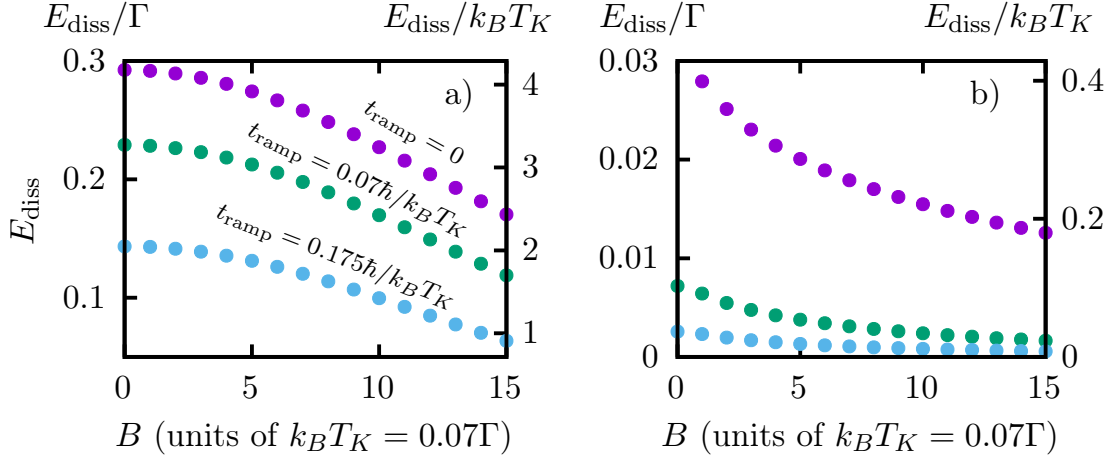


Figure 6.4.: Dissipation at finite ramp speed. Dissipation per cycle in the noninteracting $U = 0$ (a) and interacting case $U = 2.5\pi\Gamma$ at zero temperature, for different ramp times t_{ramp} . The impurity level is driven between the particle-hole symmetric value $\varepsilon_0 = -U/2$ and $\varepsilon_1 = \varepsilon_0 + \Delta\varepsilon$, with $\Delta\varepsilon = 0.7\Gamma (= 10k_B T_K)$ and Kondo temperature $k_B T_K = 0.07\Gamma$ in the interacting case. Dissipation is given in units of Γ (left scale) and in units of the Kondo temperature (right scale).

impurity, broadened due to the hybridization coupling, see Section 6.3(a). For a sudden quench ($t_{\text{ramp}} = 0$) and zero magnetic field B , we find the dissipation $E_{\text{diss}} = 0.29\Gamma$ to be in the order of the level shift $\Delta\varepsilon = 0.7\Gamma$. The dissipation decreases monotonically with the magnetic field, see Fig. 6.4(a), due to the opposite effect of the field on the spin-up and spin-down impurity levels. Furthermore, dissipation is reduced by slower annealing. This is generally expected in the limit of slow dynamics since dissipation vanishes for adiabatic ramps.

Let us now move to the interacting case with $U = 2.5\pi\Gamma$, and corresponding Kondo temperature $k_B T_K = 0.07\Gamma$ as obtained from Eq. (6.10). Again, the impurity level energy is lifted by $\Delta\varepsilon = 0.07\Gamma = 10k_B T_K$. The dissipation turns out to be significantly lower as compared to the noninteracting case, by about one order of magnitude for the sudden quench, see Fig. 6.4, however, being in the order of the Kondo temperature.

The magnetic field dependence of the dissipation at $t_{\text{ramp}} = 0$ follows the (inverse) behavior of the impurity population at ε_1 , since the occupation is field-independent at particle-hole symmetry $\varepsilon_d = \varepsilon_0$ and the dissipation is given by the difference in equilibrium occupations, Eq. (6.9). The decay of the dissipation with increasing ramp time turns out to be very rapid. In fact, the time scale on which dissipation disappears is clearly smaller than the Kondo time scale $\hbar/k_B T_K$, in contrast to what one would expect for the case of dissipation emerging from the Kondo effect. This issue will be discussed in the next section.

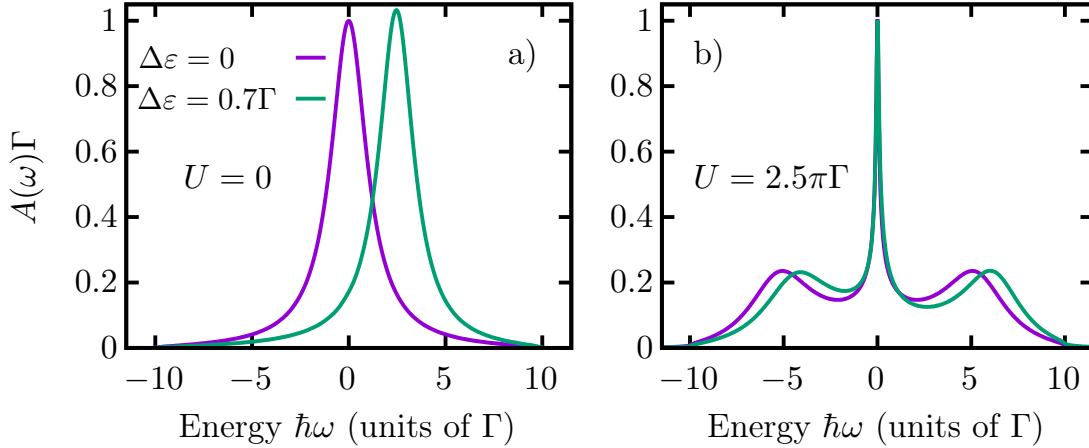


Figure 6.5.: Impurity spectral function for the SIAM. Zero temperature spectral function in the noninteracting $U = 0$ (a) and interacting case $U = 2.5\pi\Gamma$ (b), with Kondo temperature $k_B T_K = 0.07\Gamma$. Two different placements of the impurity energy level are considered, the particle-hole symmetric choice $\Delta\varepsilon = 0$ and $\Delta\varepsilon = 0.7\Gamma (= 10k_B T_K)$.

6.3. Spectral functions

To get a better understanding of the mechanisms leading to the observed dissipation, let us analyze the impurity spectral function $A(\omega)$, obtained from MPS calculations, as discussed in more detail in Chapter 5.

The noninteracting $U = 0$ spectral function has just a single peak, due to the local impurity level, see Fig. 6.5(a). The interacting $U = 2.5\pi\Gamma$ spectral function, see Fig. 6.5(b), shows two peaks corresponding to the local impurity levels at $\hbar\omega = \varepsilon_d$ and $\hbar\omega = \varepsilon_d + U$, and a Kondo peak at the baths Fermi energy, $\hbar\omega = 0$. By shifting the impurity energy level from $\Delta\varepsilon = 0$ to $\Delta\varepsilon = 10k_B T_K$ the two side-peaks move accordingly. However, the Kondo peak is barely affected. The overall change of the spectral function upon moving the impurity level is much more significant in the noninteracting case, which we expect to cause the much larger dissipation.

6.4. Discussion and outlook

In this chapter, we have discussed the concept of dissipation in the SIAM. Even though the model is a closed system, it continuously absorbs energy due to the periodic, external driving. The amount of absorbed energy can be measured as dissipation in oscillating tip experiments. Here, we have modeled the action of the tip on the impurity as an energy shift of the impurity energy level, due to electrostatic interactions, intending to detect signatures of the Kondo effect in the experimentally accessible dissipation. However, it turned out that shifting the impurity level leads to dissipation

which is mainly due to the side peaks of the spectral function, while the Kondo peak is rather insensitive to the position of the impurity energy level.

We believe that the Kondo effect creates signatures in the dissipation only if the Kondo peak in the instantaneous spectral function is strongly modified during the dynamics. For example, this can be achieved by modifying the hybridization coupling [153]: In the extreme case of $\Gamma \rightarrow 0$ the Kondo peak is getting narrower until it disappears, losing a lot of spectral weight. This indeed should be detectable in the dissipation, as done in Ref. [153] for the sudden quench case. It would be interesting to see how the dissipation then behaves for finite ramps, i.e. what is the time scale on which the adiabatic regime is reached. However, due to a lack of experimental results, it is currently unclear what exactly is the relevant mechanism in oscillating tip experiments.

7. Simulating non-equilibrium open quantum systems with MPS

In previous chapters, we have concentrated on the Anderson model, which describes an impurity interacting with a bath of free fermions. In this chapter we will consider the case of free bosons, which appears in the context of open quantum systems [84–86], quantum thermodynamics [98, 99] or in understanding electronic transport in biological systems [41, 100, 101]. Recent progress has made it possible to study the spin-boson model at strong coupling experimentally, with the spin implemented with a superconducting qubit, and the bosonic bath realized through the electromagnetic continuum of a one-dimensional waveguide [102]. Due to the high degree of control, it is now possible to investigate even scenarios with explicit time-dependence. Motivated by the experimental possibilities, we study here the applicability of the method recently developed by Tamascelli *et al.* [109] for explicitly time-dependent problems, applying it to the paradigmatic example of a Landau-Zener-Stückelberg interferometer [108].

7.1. Introduction

The superposition principle is a key ingredient in quantum computation algorithms, which, roughly speaking, profit from the ability to process multiple states at the same time. However, for these algorithms to work well, it is of crucial importance that the relative complex phase between states is well defined and controlled [160]. The dynamics of any real quantum system is unavoidably affected by its environment, and perfect isolation is never possible. Even though dissipation might turn out beneficial in certain scenarios [4, 87, 88], in most cases the coupling to the environment is undesirable, and poses a great challenge in the realization of quantum information processing and quantum simulation [89–91]. Hence, it is crucial to understand the physical processes and underlying detrimental effects associated with a quantum environment, in order to develop strategies to reduce their negative impact.

In this chapter, we revisit the problem of a single dissipative two-level system (TLS), which is driven back and forth over a Landau-Zener avoided crossing [161]. In absence of dissipation, this process shows interference effects as a consequence of the superposition principle, known as Stückelberg interference [108]. The interference, however, strongly depends on the phase coherence between the evolved states. Hence, it provides a simple

toy model to study the effect of dissipation on a microscopic level. Furthermore, the Landau-Zener-Stückelberg (LZS) interferometer has also been proposed as a scheme for the implementation of quantum gates in quantum computation [108, 162]. LZS interferometry can be realized in various experimental setups, such as single electron charge qubits [163], nitrogen-vacancies in diamond [164] or superconducting qubits [108].

On the theoretical side, it is challenging to model and simulate thermal baths, due to their macroscopic number of degrees of freedom. Hence, it can be convenient to approximate the dynamics, by taking the effects of the environment into account only effectively. For example, the assumption of weak system-bath coupling allows for theoretical simplifications, including Markov and/or Born approximations, which require that system-bath correlations can be neglected [84, 85]. As a result, the quantum system is described by a density matrix, whose non-unitary dynamics is governed by a so-called *quantum master equation*. The most prominent examples are the Redfield and Gorini-Kossakowski-Sudarshan-Lindblad, or Lindblad equation [95, 96]. However, the weak coupling assumption is not always valid, and non-Markovian effects can be relevant for the dynamics [97]. In these scenarios, more involved techniques are needed [103], such as hierarchical equations of motion (HEOM) [104, 105] or the quasi-adiabatic propagator path integral (QUAPI) [106, 107].

Previous theoretical studies of the LZS interferometer in presence of dissipation have focused on an effective description of the environment using Master equations [165] in the context of double quantum dot experiments, or by using Bloch equations including phenomenological relaxation times [108]. Here we follow a different approach. We explicitly model the environment as a set of (infinitely many) harmonic oscillators. The interaction, and consequently, the growth of entanglement between two-level system and bath leads to decoherence.

We show that the dissipative LZS interferometer has an optimal working point with respect to the annealing velocity, which emerges from the competition of coherent dynamics and dissipation. In absence of dissipation, interference effects are most pronounced for a certain well-defined annealing velocity, while dissipation generally favors fast annealing, to reduce the loss of coherence. Similar observations were made in the context of dissipative quantum annealing [166, 167].

The chapter is organized as follows. In Section 7.2 we introduce the model for the TLS and the bath, and we discuss Stückelberg interference for fully coherent dynamics. Details of the non-perturbative MPS-based method to simulate the full dynamics of TLS and bath are provided in Section 7.3. In Section 7.4 we discuss the effect of dissipation on the interference pattern and the state of the TLS, by analyzing its entanglement with the bath and its Bloch vector. We further show in Section 7.5 that the interferometer possesses an optimal working point with respect to the Landau-Zener annealing velocity, where the visibility of interference oscillations is maximum. We conclude the chapter in Section 7.6. Finally, we discuss and demonstrate further

possible research directions for strongly coupled and driven open quantum systems in Section 7.7. Additional technical information and details about the simulations can be found in Appendix C.

7.2. Dissipative Landau-Zener-Stückelberg interferometer

7.2.1. Coherent LZS interferometer

We study interference in quantum systems using a simple two-level system (TLS), with time-dependent Hamiltonian

$$\hat{H}_{\text{LZS}}(t) = -\frac{\Delta}{2}\hat{\sigma}_x - \frac{h(t)}{2}\hat{\sigma}_z. \quad (7.1)$$

The first term is time-independent, and defines the barrier/ transition rate between $\hat{\sigma}_z$ eigenstates $|\uparrow\rangle$ and $|\downarrow\rangle$. The second term carries the time-dependence, and controls the energy imbalance of $|\uparrow\rangle$ and $|\downarrow\rangle$. For our interference dynamics we choose

$$h(t) = \begin{cases} v(t - t_0) & t < t_0 + \tau/2 \\ v(t_0 + \tau - t) & t > t_0 + \tau/2, \end{cases} \quad (7.2)$$

as visualized in Fig. 7.1(a). The protocol is essentially composed of two consecutive Landau-Zener (LZ) sweeps. In each of them, the imbalance $h(t)$ changes linearly in time, with slopes v and $-v$ during the first ($t < t_0 + \tau/2$) and second LZ sweep ($t > t_0 + \tau/2$), respectively. The corresponding eigenenergies of ground and excited state show avoided level-crossings with minimum gap Δ at times $t = t_0$ and $t = t_0 + \tau$, when $h(t) = 0$, see Fig. 7.1(b).

Now, the idea of the interferometer is as follows. We initialize the system in its ground state at $t = 0$ and evolve in time according to $\hat{H}_{\text{LZS}}(t)$. In the vicinity of the first avoided crossing, the TLS gets excited, and hence its state $|\psi(t_0^+)\rangle$ after the transition is a superposition of instantaneous ground state $|\text{GS}(t_0)\rangle$ and excited state $|\text{EXC}(t_0)\rangle$,

$$|\psi(t_0^+)\rangle = \sqrt{P_{\text{gs}}}\text{GS}(t_0)\rangle + \sqrt{1 - P_{\text{gs}}}\text{e}^{i\phi}\text{EXC}(t_0)\rangle.$$

The probability to remain in the ground state, P_{gs} , depends on the velocity v at which we sweep over the avoided crossing. For a perfect, infinitely long LZ sweep with annealing velocity v it is given by [161]

$$P_{\text{gs,LZ}} = 1 - \text{e}^{\frac{-\pi\Delta^2}{2\hbar v}}. \quad (7.3)$$

After the first avoided crossing, an evolution crucial for interference follows. Due to their energy difference, $|\text{GS}\rangle$ and $|\text{EXC}\rangle$ accumulate different phases, leading to an

accumulated phase difference $\Delta\phi \approx \int_{t_0}^{t_0+\tau} dt \Delta E(t)$ at the second avoided crossing ($t = t_0 + \tau$). Here, $\Delta E(t)$ is the instantaneous energy gap between ground and excited state. Hence, the state immediately before the second transition at time $t = t_0 + \tau^-$ is

$$|\psi(t_0 + \tau^-)\rangle = \sqrt{P_{\text{gs}}}|GS(t_0 + \tau^-)\rangle + \sqrt{1 - P_{\text{GS}}}e^{i(\phi - \Delta\phi)}|EXC(t_0 + \tau^-)\rangle.$$

The relative phase of the states — depending on the interference time τ — massively affects the dynamics at the second avoided crossing, and thus the probability to end up in the ground or excited state. This is directly observed from the dynamics of the instantaneous ground state population $P_{\text{gs}}(t) = |\langle GS(t)|\psi(t)\rangle|^2$, see Fig. 7.2(a). As we change the interference time τ , the probability to end up in the ground state shows so-called Stückelberg oscillations, the signature of interference (see Fig. 7.2(b)). The oscillations are most pronounced when the state ends up in a 50:50 splitting of ground and excited state after the first LZ sweep, allowing for perfect constructive or destructive interference at the second avoided crossing. Using Eq. (7.3) the condition $P_{\text{gs,LZ}} = 1/2$ leads to the optimal annealing velocity

$$v_{\text{opt}} = \frac{\pi\Delta^2}{2\log(2)}, \quad (7.4)$$

in absence of dissipation, as has been used in Fig. 7.2.

7.2.2. Dissipative LZS

We study the effect of dissipation by coupling the TLS to a macroscopic environment at inverse temperature $\beta = 1/k_B T$. We consider the paradigmatic spin-boson model with Hamiltonian [93]

$$\hat{H} = \hat{H}_{\text{LZS}}(t) + \hat{H}_{\text{int}} + \hat{H}_{\text{B}}, \quad (7.5)$$

where $\hat{H}_{\text{LZS}}(t)$ is the (time-dependent) Hamiltonian for the TLS, while \hat{H}_{B} and \hat{H}_{int} describe the environment and its interaction to the TLS, respectively. We model the bath as a set of harmonic oscillators [168], which in our quantum mechanical framework is defined through the Hamiltonian

$$\hat{H}_{\text{B}} = \sum_k \epsilon_k \hat{b}_k^\dagger \hat{b}_k. \quad (7.6)$$

Here, the bosonic operators, with canonical commutation rules $[\hat{b}_k, \hat{b}_{k'}^\dagger] = \delta_{k,k'}$, create (\hat{b}_k^\dagger) or annihilate (\hat{b}_k) an excitation with energy ϵ_k in mode k . The interaction of the TLS and the bath is modeled with a standard spin-boson type of coupling. The Hamiltonian term is taken as a (tensor) product of an operator \hat{A} , acting solely on the TLS, and the sum of displacement operators $\hat{X}_k = \hat{b}_k + \hat{b}_k^\dagger$, acting on the bath modes. Hence, it can be written as

$$\hat{H}_{\text{int}} = \hat{A} \otimes \sum_k \lambda_k (\hat{b}_k + \hat{b}_k^\dagger). \quad (7.7)$$

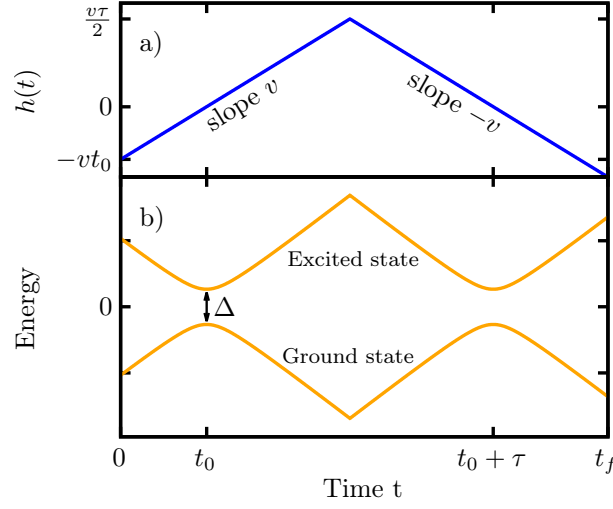


Figure 7.1.: LZS protocol and instantaneous eigenenergies. a) Time dependence of the $\hat{\sigma}_z$ coupling $h(t)$. The two-level system is driven linearly back and forth. b) Instantaneous eigenenergies $E(t) = \pm\sqrt{\Delta^2 + h^2(t)}/2$ of the two-level system, showing two consecutive Landau-Zener avoided crossings, with minimum gaps when $h(t) = 0$, at times $t = t_0$ and $t = t_0 + \tau$. The interference time τ controls the phase accumulation between the avoided crossing, and hence the interference. In practical simulations we fixed $t_0 = 2.5\hbar/\Gamma$ for the warm-up step up to the first avoided crossing, and $t_f - (t_0 + \tau) = 5\hbar/\Gamma$ for the relaxation step after the second avoided crossing. These values are chosen as small as possible such that the warm-up step is initially adiabatic, and to give the system enough time to relax after the second avoided crossing.

The bath and its interaction with the system is characterized by just a single function [130], the so called spectral function $\mathcal{J}(\omega) = \sum_k \lambda_k^2 \delta(\omega - \omega_k)$, which takes the role of the hybridization function in the Anderson model, see Chapter 3. Here, we assume the spectral function to be follow a power-law with a hard cut-off at ω_c ¹

$$\mathcal{J}(\omega) = 2\alpha\hbar^2\omega_c^{1-s}\omega^s \Theta(\omega_c - \omega) , \quad (7.8)$$

where Θ is the Heaviside function to set a hard high-energy cut-off ω_c , and α the system-bath coupling strength. For $s = 1$ the spectral function is called “ohmic”, while $s < 1$ and $s > 1$ defines sup- and super-ohmic spectral functions, respectively. At zero temperature and $s \leq 1$, the spin-boson model shows a quantum phase transition between a localized and a delocalized phase [93]. The critical coupling is $\alpha_c = 1$ for $s = 1$ and decreases with the exponent s [123]. Unless stated otherwise, we choose $\hat{A} = \hat{\sigma}_z$ for the system-bath interaction, an ohmic spectral function $s = 1$, and $v = v_{\text{opt}}$ for the annealing velocity, see Eq. (7.4).

¹An alternative more standard choice [93] employs an exponential cut-off function $e^{-\omega/\omega_c}$. The hard cut-off $\Theta(\omega_c - \omega)$ is chosen here because it is more convenient for the simulations, as the exponential cut-off requires to simulate high energy modes, and therefore smaller time steps are necessary.

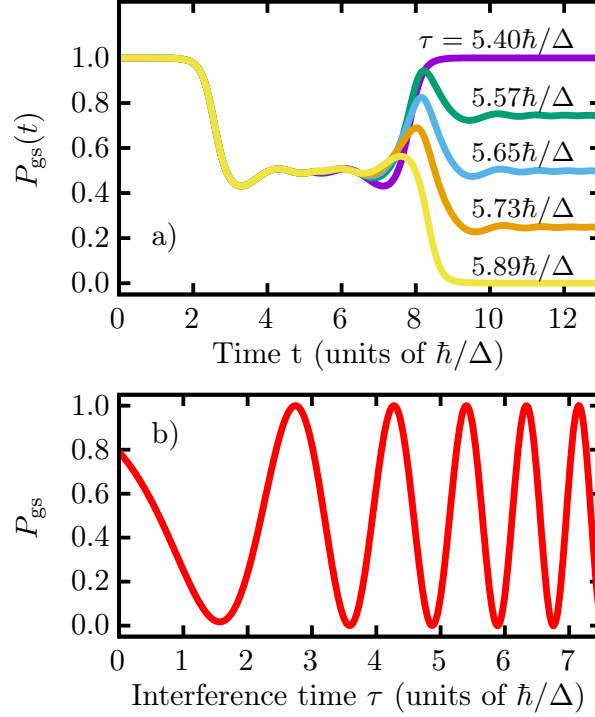


Figure 7.2.: Coherent LZS interference. a) Dynamics of the instantaneous ground state population in the LZS interferometer in absence of dissipation at different interference times τ . b) Ground state population at the end of the dynamics as a function of the interference time. The probability to find the system in its ground state shows perfect Stückelberg oscillations between zero and one.

7.3. Methods

Among the variety of methods to study the spin-boson model, we chose to employ a numerically exact technique based on matrix product states to simulate the full dynamics of the two-level system and the bath. In the following sections, we will present the method developed by Tamascelli *et al.* [109] to efficiently represent and simulate environments at finite temperature. However, we will go through a different derivation of the method, similar to that for the fermionic case [136]. The approach is based on the thermofield transformation introduced by Takahashi and Umezawa [65], which we used for the single impurity Anderson model in the previous chapters. It was first applied in the framework of MPS by de Vega *et al.* [66].

Before going into the details, let us sketch the idea again. Instead of writing the thermal state of the bath directly as a density matrix, the state is represented by a pure quantum state in an extended system, by introducing an ancillary bath, similar to the idea of purification [17, 29]. The thermofield transformation then transforms the physical and the ancillary baths into two novel baths, such that the thermal state is the vacuum state of the extended environment in the new basis. While de Vega *et al.* [66] were simulating the two baths after mapping them into two independent tight-binding

chains, in certain cases it is possible to recombine the environments before the chain mapping, ending up with just a single bath/chain, which is one of the important results of Ref. [109].

7.3.1. Thermofield transformation

In this section we show how to efficiently represent the thermal state of the bosonic bath using the thermofield transformation [65, 66]. As mentioned earlier, the thermal state is represented as pure state in an extended Hilbert space. Hence, we first supplement the bath Hamiltonian with ancillary bath modes \hat{b}_{2k} , such that

$$\hat{H}_B \rightarrow \hat{H}_B = \sum_k \epsilon_k \left(\hat{b}_{1k}^\dagger \hat{b}_{1k} - \hat{b}_{2k}^\dagger \hat{b}_{2k} \right). \quad (7.9)$$

Note that we renamed the original physical modes \hat{b}_k by adding the additional index '1', $\hat{b}_k \rightarrow \hat{b}_{1k}$. We then mix the physical and ancillary modes by defining new modes via the thermofield transformation [65, 66]

$$\begin{pmatrix} \hat{c}_{1k} \\ \hat{c}_{2k}^\dagger \end{pmatrix} = \begin{pmatrix} \cosh(\Theta_k) & -\sinh(\Theta_k) \\ -\sinh(\Theta_k) & \cosh(\Theta_k) \end{pmatrix} \begin{pmatrix} \hat{b}_{1k} \\ \hat{b}_{2k}^\dagger \end{pmatrix}, \quad (7.10)$$

whose inverse is

$$\begin{pmatrix} \hat{b}_{1k} \\ \hat{b}_{2k}^\dagger \end{pmatrix} = \begin{pmatrix} \cosh(\Theta_k) & \sinh(\Theta_k) \\ \sinh(\Theta_k) & \cosh(\Theta_k) \end{pmatrix} \begin{pmatrix} \hat{c}_{1k} \\ \hat{c}_{2k}^\dagger \end{pmatrix}. \quad (7.11)$$

Our goal is to represent the thermal state of the original physical system as the vacuum state of the extended transformed system. Using Eq. (7.11) it is easy to show that the occupation of the physical bosons is

$$\langle \emptyset | \hat{b}_{1k}^\dagger \hat{b}_{1k} | \emptyset \rangle = \sinh^2(\Theta_k), \quad (7.12)$$

where $|\emptyset\rangle$ is the vacuum state of the new bosons \hat{c}_{1k} and \hat{c}_{2k} . For the environment in the thermal state we require the population to follow the Bose-Einstein distribution f_B , and hence we take

$$\sinh^2(\Theta_k) \equiv f_B(\epsilon_k) = \frac{1}{e^{\beta\epsilon_k} - 1}. \quad (7.13)$$

A proof that the physical bath is indeed in a Gibbs state is presented in Appendix C.1.

Now that we know that the thermal state of the bath is represented by the vacuum state in the transformed basis, we can use Eq. (7.11) to transform the Hamiltonian to this basis. The free boson term becomes

$$\hat{H}_B = \sum_k \epsilon_k \left(\hat{c}_{1k}^\dagger \hat{c}_{1k} - \hat{c}_{2k}^\dagger \hat{c}_{2k} \right). \quad (7.14)$$

Hence, it describes free bosons with energies ϵ_k and $-\epsilon_k$ just as the original physical and ancillary baths. While the TLS couples only to the physical bath and not to the ancillary one, it interacts with both baths in the new basis:

$$\hat{H}_{\text{int}} = \hat{A} \otimes \sum_k \lambda_k \left(\cosh \Theta_k (\hat{c}_{1k} + \hat{c}_{1k}^\dagger) + \sinh \Theta_k (\hat{c}_{2k} + \hat{c}_{2k}^\dagger) \right) \quad (7.15)$$

Hence, the transformed Hamiltonian consists of two baths of free bosons, both of them coupled to the two-level system, and the thermal state of the physical environment is represented by the pure vacuum state of the two novel baths.

So far we have considered a discrete set of bath modes. In practice, however, we directly work in the continuum limit, where the role of the mode index k is taken by the continuous dimensionless variable $x = \omega/\omega_c$, with the cut-off frequency ω_c setting the maximum relevant energy scale of the environment. The continuum limit is obtained through the replacements $\sum_k \rightarrow \hbar\omega_c \int dx$, $\lambda_k \rightarrow \lambda(x)$, $\epsilon_k \rightarrow g(x)$, and $\Theta_k \rightarrow \Theta(x)$. More details on the discrete-to-continuum transformation can be found in Ref. [9] and Chapter 3. As mentioned before, the action of the bath on the TLS is characterized by the spectral function, which is related to the coupling function $\lambda(x)$ and the dispersion $g(x)$ via [54, 130]

$$\mathcal{J}(\omega) = \lambda^2(g^{-1}(\omega)) \frac{dg^{-1}(\omega)}{d\omega}, \quad (7.16)$$

where $g^{-1}(\omega)$ is the inverse of $g(x)$, just like in the fermionic case, see Eq. (3.10). The full Hamiltonian in the continuum limit is given by

$$\begin{aligned} \hat{H}(t) = \hat{H}_{\text{LZS}}(t) &+ \hbar\omega_c \int_0^1 dx x \left(\hat{c}_1^\dagger(x) \hat{c}_1(x) - \hat{c}_2^\dagger(x) \hat{c}_2(x) \right) \\ &+ \hbar\omega_c \hat{A} \otimes \int_0^1 dx \lambda(x) \left(\cosh(\Theta(x)) (\hat{c}_1^\dagger(x) + \hat{c}_1(x)) \right. \\ &\quad \left. + \sinh(\Theta(x)) (\hat{c}_2^\dagger(x) + \hat{c}_2(x)) \right), \end{aligned} \quad (7.17)$$

where we have chosen $g(x) = x$. This choice will turn out beneficial for the following steps.

7.3.2. Merging the baths

At this stage there are two possible routes we could follow:

- i) We can simulate the model with two baths, either in the star-geometry or in the chain geometry, with independent chain mappings for the two baths, as has been done in Ref. [66].
- ii) Since the system-bath coupling is a product of two self-adjoint operators and the chemical potential for the bath is zero, i.e. the bath is completely empty in its ground state, it is possible to merge the two baths into just a single one [109].

Here, we will employ method **(ii)**, since it requires us to simulate just a single bath.

In the following, we show the calculation on how this can be achieved, which is very similar to the fermionic case discussed in Ref. [136]. In the first step we carry out the substitution $x \rightarrow -x$ for all terms involving \hat{c}_2 or \hat{c}_2^\dagger operators:

$$\begin{aligned} \hat{H} = \hat{H}_{\text{LZS}} &+ \hbar\omega_c \int_0^1 dx x \hat{c}_1^\dagger(x) \hat{c}_1(x) + \hbar\omega_c \int_{-1}^0 dx x \hat{c}_2^\dagger(-x) \hat{c}_2(-x) \\ &+ \hbar\omega_c \hat{A} \otimes \int_0^1 dx \lambda(x) \cosh \Theta(x) \left(\hat{c}_1^\dagger(x) + \hat{c}_1(x) \right) \\ &+ \hbar\omega_c \hat{A} \otimes \int_{-1}^0 dx \lambda(-x) \sinh \Theta(-x) \left(\hat{c}_2^\dagger(-x) + \hat{c}_2(-x) \right) \end{aligned}$$

We now define an effective temperature-dependent coupling $\lambda_\beta(x)$ as

$$\lambda_\beta(x) = \begin{cases} \lambda(x) \cosh(\Theta(x)) & \text{for } x \geq 0 \\ \lambda(|x|) \sinh(\Theta(|x|)) & \text{for } x < 0 \end{cases}, \quad (7.18)$$

with support extended to negative $x \in [-1, +1]$. We further define in a similar way new bosonic operators as

$$\hat{c}(x) = \begin{cases} \hat{c}_1(x) & \text{for } x \geq 0 \\ \hat{c}_2(|x|) & \text{for } x < 0 \end{cases}. \quad (7.19)$$

The Hamiltonian can then be written as

$$\hat{H} = \hat{H}_{\text{LZS}} + \hbar\omega_c \int_{-1}^{+1} dx x \hat{c}^\dagger(x) \hat{c}(x) + \hbar\omega_c \hat{A} \otimes \int_{-1}^{+1} dx \lambda_\beta(x) \left(\hat{c}^\dagger(x) + \hat{c}(x) \right). \quad (7.20)$$

Notice that essentially we just mapped all the modes \hat{c}_2 to negative frequencies. With the Hamiltonian in this form, we have just a single environment coupled to the TLS, with dispersion $g(x) = x$ and temperature-dependent coupling $\lambda_\beta(x)$. Using Eq. (7.16) this translates into an effective spectral function [109]

$$\mathcal{J}_\beta(\omega) = \frac{\text{sgn}(\omega) \mathcal{J}(|\omega|)}{2} \left(1 + \coth(\beta\omega/2) \right), \quad (7.21)$$

which is obtained by rewriting Eq. (7.18) into a single function. Hence, it suffices to replace the spectral function by the effective spectral function \mathcal{J}_β to simulate baths at finite temperature, which is one of the important results of Tamascelli *et al.* [109].

7.3.3. Chain mapping

As a final step, we map the Hamiltonian Eq. (7.20) into a tight-binding chain with only nearest-neighbor interaction, which is very well suited for simulations with matrix

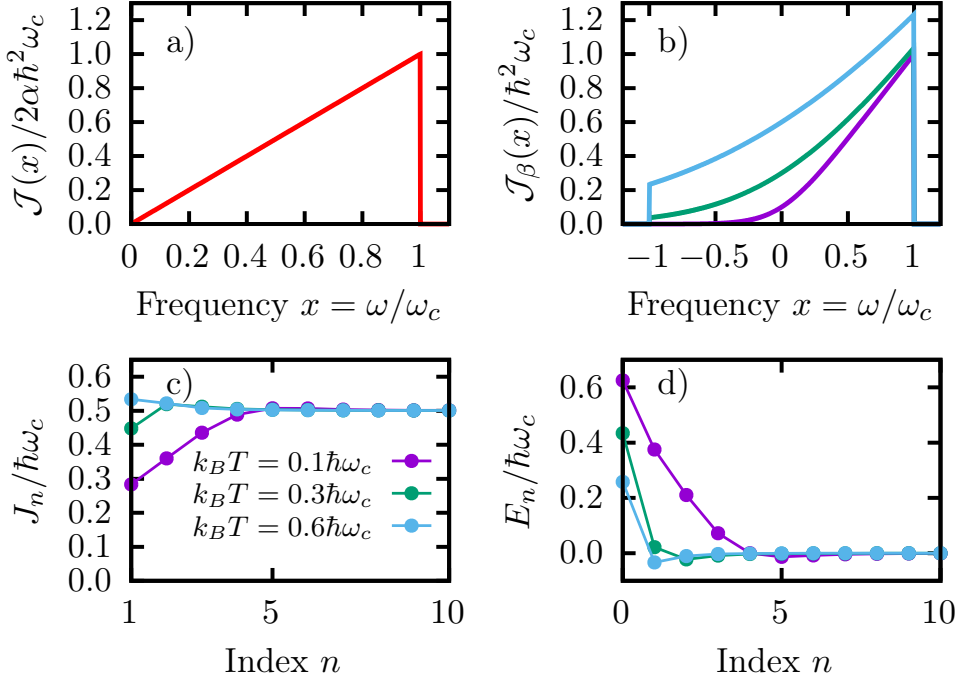


Figure 7.3.: Chain coefficients for ohmic spectral function. a) Ohmic spectral density $\mathcal{J}(\omega) = 2\alpha\hbar^2\omega\Theta(\omega - \omega_c)$ with hard cut-off frequency ω_c . b) Effective spectral density \mathcal{J}_β for various temperatures, with support extended to negative energies. c+d) Nearest-neighbor hoppings (c) and on-site energies (d) of the chain sites for the effective spectral densities in panel (b).

product states. As discussed in Chapter 3 there are essentially two different possibilities for the chain mapping: i) One can discretize the continuous bath and map the discrete bath modes into a chain, using Lanczos' tridiagonalization algorithm. ii) By exploiting the theory of orthogonal polynomials, the continuum bath is directly mapped into a chain without prior discretization. This can be advantageous especially when the bath spectral function has sharp features.

Due to its simplicity, which also avoids checking convergence in the discretization, we decided to work with orthogonal polynomials. We simply need to choose the chain long enough such that no excitation reaches its end [123], to avoid the introduction of finite size effects.

Let us briefly summarize the chain mapping, which is similar to the fermionic case in Section 3.3. The star-like bath maps into a chain through a unitary transformation, where new bosonic modes \hat{a}_n are introduced as

$$\hat{a}_n = \int_{-1}^{+1} dx U_n(x) \hat{c}(x), \quad (7.22)$$

with inverse transformation

$$\hat{c}(x) = \sum_{n=0}^{\infty} U_n(x) \hat{a}_n(x). \quad (7.23)$$

The transformation coefficients $U_n(x) = \lambda(x) p_n(x)$ are built from the coupling function $\lambda_\beta(x)$ and normalized orthogonal polynomials $p_n(x)$ fulfilling the orthonormality condition

$$\int_{-1}^{+1} dx \lambda_\beta^2(x) p_n(x) p_m(x) = \delta_{n,m}. \quad (7.24)$$

Notice that polynomials p_n are orthonormal with respect to the weighting function $\lambda_\beta^2(x)$. The crucial identity that allows us to map the star-like bath into a chain is the three term recurrence relation

$$\pi_{n+1}(x) = (x - \alpha_n) \pi_n(x) - \beta_n \pi_{n-1}(x), \quad (7.25)$$

with recurrence coefficients α_n, β_n and the monic polynomials ² $\pi_n(x)$.

By exploiting the previous recurrence relation it is easy to show [54] that the bath maps into a tight binding chain, and the Hamiltonian becomes

$$\hat{H} = \hat{H}_{\text{LZS}} + J_0 \hat{A} \otimes (\hat{a}_0^\dagger + \hat{a}_0) + \sum_{n=1}^{\infty} J_n (\hat{a}_n^\dagger \hat{a}_{n-1} + \text{H.c.}) + \sum_{n=0}^{\infty} E_n \hat{a}_n^\dagger \hat{a}_n, \quad (7.26)$$

with chain coefficients

$$J_{n=0} = \hbar \omega_c \sqrt{\int_{-1}^{+1} dx \lambda_\beta^2(x)} \quad J_{n \geq 1} = \hbar \omega_c \sqrt{\beta_n} \quad E_{n \geq 0} = \hbar \omega_c \alpha_n. \quad (7.27)$$

Hence, all we need are the recurrence coefficients α_n and β_n corresponding to the weighting function $\lambda^2(x)$. Notice that the coupling strength α only affects the coupling J_0 between system and first chain site, and hence does not affect any of the remaining chain coefficients. For certain special cases at zero temperature analytic solutions are known for the recurrence coefficients. In most cases, however, we need to calculate them numerically. Here, we use the Matlab packages of Gautschi [133, 134].

7.4. Results: Dissipative Stückelberg interference

We investigate the effect of dissipation on the interference dynamics. In particular, we study the ground state occupation P_{gs} , which in presence of the bath is given by

$$P_{\text{gs}}(t) = |\langle \text{GS}(t) | \psi(t) \rangle|^2 = \text{Tr} \left(|\text{GS}(t)\rangle \langle \text{GS}(t)| \hat{\rho}_{\text{S}}(t) \right), \quad (7.28)$$

²These polynomials are related to the normalized polynomials $p_n(x)$ through a rescaling, such that the coefficient a_n of the leading power of $\pi_n(x) = a_n x^n + a_{n-1} x^{n-1} + \dots + a_0$ is equal to one, $a_n = 1$.

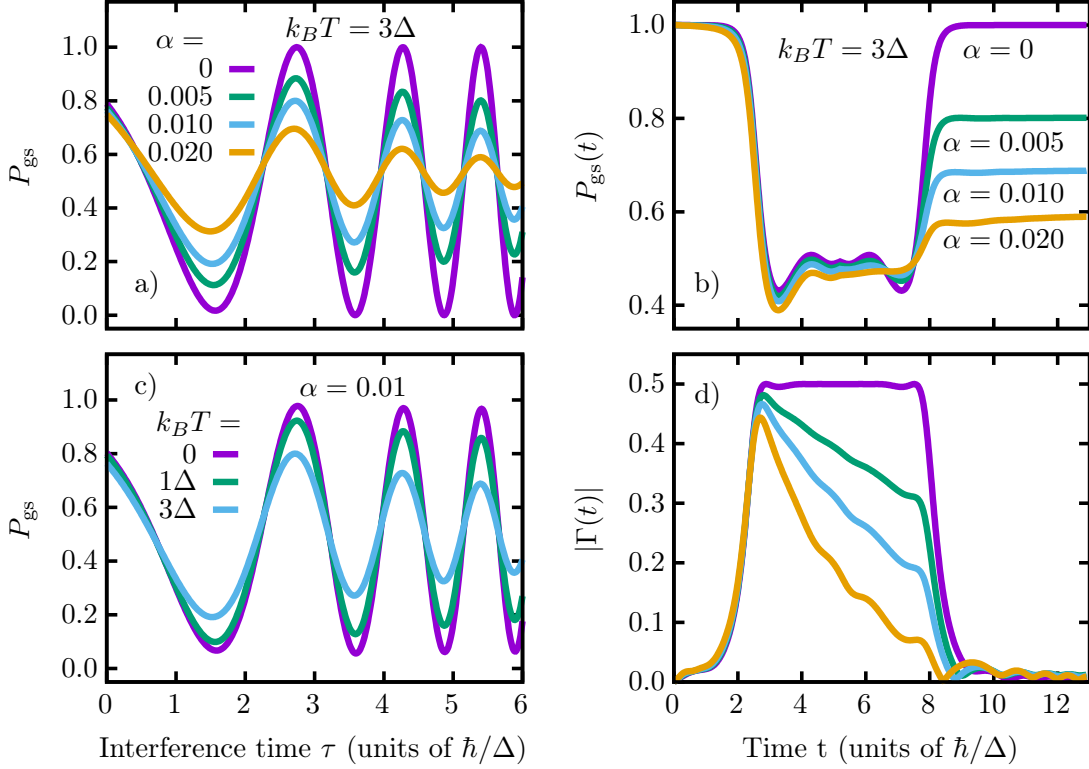


Figure 7.4.: Dissipative LZS interference. a+c) Probability to find the TLS in its ground state at the end of the annealing as a function of the interference time τ . Stückelberg oscillations are suppressed as the system-bath coupling α (a) or temperature T (c) is increased. b) Dynamics of the instantaneous ground state probability for different system-bath couplings α . The dynamics shows strong α -dependence only after the second LZ crossing, where interference takes place. d) Dynamics of the coherence $|\Gamma(t)|$, Eq. (7.29), which is the off-diagonal matrix element of the reduced density matrix of the TLS in the instantaneous eigenbasis. The decay of coherence takes place between the two LZ crossings and is responsible for the disappearance of interference effects. The color code is the same as in panels (a,b). In panels (b+d) the temperature is $k_B T = 3\Delta$ and the interference time is fixed to $\tau = 5.4\hbar/\Delta$.

where $|\psi(t)\rangle$ is the pure state of the TLS-plus-bath, and $\hat{\rho}_S(t) = \text{Tr}_{\text{bath}} |\psi(t)\rangle\langle\psi(t)|$ is the TLS's reduced density matrix obtained by tracing out the bath.

As we have seen previously for the coherent (non-dissipative) case, P_{gs} taken at the end of the dynamics shows Stückelberg oscillations as we change the duration of interference τ . Turning on the system-bath coupling α , we find that the amplitude of the Stückelberg oscillations decays as we increase α , see Fig. 7.4(a). Moreover, we find the oscillation amplitude to decrease even stronger for long interference times, which is easy to understand. As we increase the interference time τ between the avoided crossings, the bath can act longer on the dynamics of the TLS. Hence, it is beneficial to keep the interference time as short as possible in order to observe Stückelberg oscillations. Usually, the coupling strength is determined by the underlying physics,

and can not be controlled experimentally. The temperature of the environment, on the other hand, can be accessed and sometimes even controlled, e.g., when the bosonic environment describes the vibration (phonons) of a molecule. As shown in Fig. 7.4(c), the temperature of the environment plays an important role for the observation of Stückelberg oscillations. As one might expect, high temperature is detrimental for the observation of quantum effects, and hence leads to a suppression of interference effects as well, similar to the increase of system-bath coupling. Note that even the coupling to an environment at zero temperature leads to dissipation. Here, the environment acts as a vacuum in spontaneous emission, allowing the quantum system to lose excitations incoherently into the bath.

To understand the mechanism that leads to the decay of Stückelberg oscillations, let us investigate the dynamics of the instantaneous ground state occupation, see Fig. 7.4(b), for a fixed interference time with maximum interference at $\alpha = 0$. The dynamics shows very little α -dependence up to the second LZ avoided crossing. Hence, the bath is too weak to drive a transition from the ground to the excited state or vice-versa. However, after the second LZ transition where interference takes place, the curves strongly deviate from each other. While the bath is not strong enough to drive a direct transition between the energy eigenstates of the TLS, it can destroy interference. This can be understood from the dynamics of the *quantum coherence*, which is defined as the off-diagonal element of the reduced density matrix of the TLS, $\hat{\rho}_S$, in the instantaneous eigenbasis

$$\Gamma(t) = \text{Tr} \left(|\text{GS}(t)\rangle \langle \text{EXC}(t)| \hat{\rho}_S(t) \right). \quad (7.29)$$

Interference can only be observed if there is a well-defined phase between the two interfering states, the ground and the excited state of the TLS. This phase is encoded in the coherence $\Gamma(t)$, and hence its magnitude $|\Gamma(t)|$ quantifies the ability of the system to show interference. In absence of the environment, $|\Gamma(t)|$ takes its maximum value 0.5 between the LZ transitions, corresponding to a coherent 50:50 occupation of ground and excited state. In contrast to the populations, the coherence is strongly affected by the presence of the bath, and decays in time, Fig. 7.4(d), thereby reducing the systems ability to show interference.

Clearly, the decay of coherence is caused by the interaction of the TLS with the environment. While the TLS is initially decoupled from the environment, and hence they are not entangled, the interaction unavoidably creates entanglement between them. We can quantify the system-bath entanglement of the state $|\psi\rangle$ using the entanglement entropy

$$S = - \sum_j \lambda_j^2 \log \lambda_j^2, \quad (7.30)$$

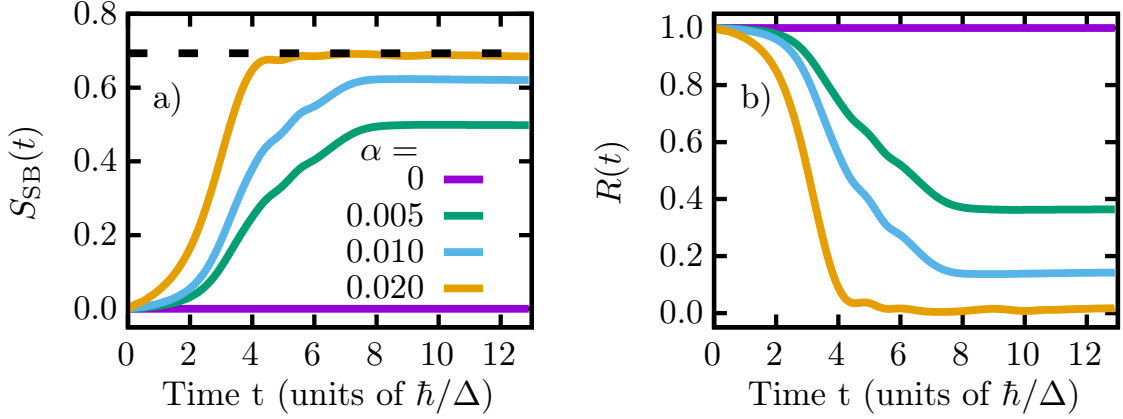


Figure 7.5.: System-bath entanglement and purity of the TLS. a) Dynamics of the entanglement entropy between the two-level system and the thermal bath, for different system bath couplings α . The dashed line represents the maximum possible entanglement entropy $S = \log(2)$. b) Length of the Bloch vector of the TLS, quantifying its purity. The interference time is $\tau = 5.4\hbar/\Delta$ and the bath temperature is $k_B T = 3\Delta$.

where λ_j are the Schmidt coefficients of the Schmidt decomposition of the state $|\psi\rangle$

$$|\psi\rangle = \sum_j \lambda_j |\phi_j^S\rangle \otimes |\phi_j^B\rangle. \quad (7.31)$$

As one might expect, the rate at which entanglement builds up increases with the interaction strength α , see Fig. 7.5(a), and similarly with temperature (not shown). Notice that even a coupling of $\alpha = 0.020$ almost leads to the maximum possible entanglement entropy of $\log(2)$. Hence, using a weak coupling approach that exploits the Born approximation would not be valid here, and might eventually fail.

In our approach, the TLS and the bath are considered a closed quantum system. Hence, the initially pure state of the TLS is getting mixed as a consequence of the creation of entanglement. Its reduced density matrix is given by

$$\hat{\rho}_S = \sum_j \lambda_j^2 |\phi_{S,j}\rangle \langle \phi_{S,j}|. \quad (7.32)$$

We quantify the purity of the TLS through the length of the Bloch vector $R = \sqrt{\langle \hat{\sigma}_x \rangle^2 + \langle \hat{\sigma}_y \rangle^2 + \langle \hat{\sigma}_z \rangle^2}$. In general, $R = 1$ for a pure state, while any state with $R < 1$ is mixed. We find R to start from $R = 1$ and decay in time. Again, the decay is faster for stronger system-bath coupling with a lower final value. For our strongest coupling, the TLS is almost in the fully mixed state, characterized by $R = 0$, in agreement with the entanglement entropy being close to its maximum possible value.

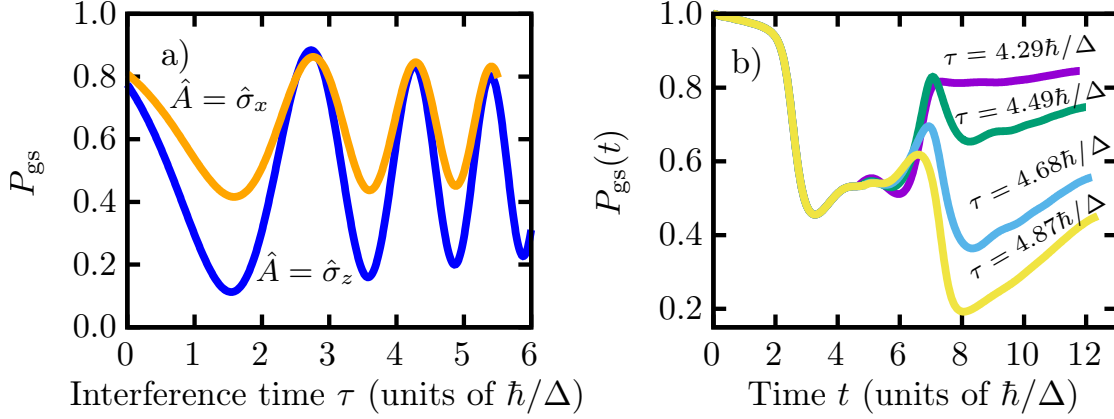


Figure 7.6.: Effect of the systems coupling operator \hat{A} . a) Probability to find the system in its ground state at the end of the dynamics for different interaction operators \hat{A} , at fixed system-bath interaction $\alpha = 0.005$ and bath temperature $k_B T = 3\Delta$. The coupling $\hat{A} = \hat{\sigma}_x$ reduces Stückelberg oscillations as compared to $\hat{A} = \hat{\sigma}_z$. b) Dynamics of the ground state population for different τ and coupling to the bath through $\hat{A} = \hat{\sigma}_x$.

7.4.1. Effect of the coupling operator \hat{A}

So far, we have considered only the case where the TLS is coupled to the bath through the Pauli operator $\hat{A} = \hat{\sigma}_z$. Here we study the effect of the choice $\hat{A} = \hat{\sigma}_x$. We find that this coupling leads to reduced Stückelberg oscillations as compared to our standard case $\hat{A} = \hat{\sigma}_z$, with an additional shift upwards. While the local maxima show little Θ -dependence, the minima tend to move to higher ground state populations. We can easily understand this trend from the dynamics of the ground state occupation (see Fig. 7.6(a)). Up to the second avoided crossing the dynamics is barely affected by the coupling angle Θ . After the second LZ process, however, the bath pushes the TLS towards the ground state, leading to a linear increase of P_{gs} . This is not possible for $\hat{A} = \hat{\sigma}_z$ as the instantaneous eigenstates of the TLS are approximately eigenstates of \hat{A} for $\hbar(t) \gg \Delta$ and hence the populations are conserved.

7.4.2. Sub- and Super-ohmic spectral functions

Thanks to the flexibility of the method employed, we are able to use basically any spectral function [55], and hence we can study the effect of the functional form of $\mathcal{J}(\omega)$. Here, we consider power-law spectral functions with a sharp cut-off ω_c , characterized through the exponent s , see Eq. (7.8).

In Fig. 7.7 we show the dependence of the Stückelberg oscillations with s : At fixed coupling and temperature, we find that the amplitude of the oscillations is strongly reduced in the sub-ohmic regime, while dissipative effects are less pronounced at super-ohmic coupling. Qualitatively this is consistent with the reduction of the critical cou-

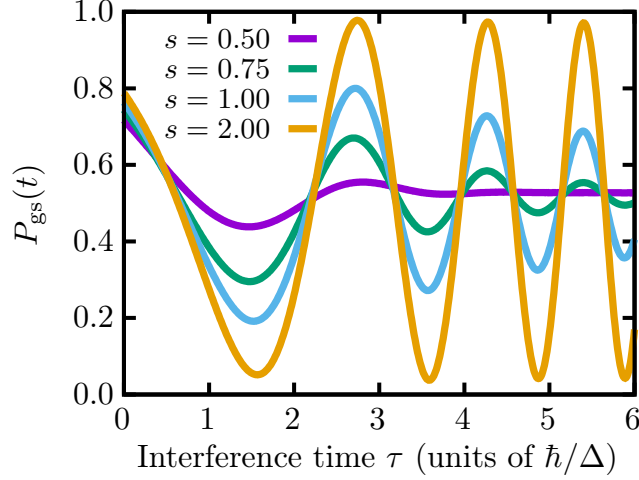


Figure 7.7.: Sub- and super-ohmic spectral functions. Stückelberg oscillations for sub- and super-ohmic spectral functions, characterized through the exponent s . System-bath coupling is $\alpha = 0.01$ and environmental temperature is $k_B T = 3\Delta$. At fixed coupling, sub-ohmic spectral functions suppress interference effects much stronger than ohmic and super-ohmic spectral functions.

pling α_c separating the localized and delocalized phase at $T = 0$: Effectively, sub-ohmic spectral functions couple stronger to the TLS, and hence reduce the Stückelberg oscillations even more.

7.5. Optimal annealing velocity

So far we have considered the annealing velocity to be fixed such that a single perfect Landau-Zener sweep leads to a ground state population of $1/2$. In absence of dissipation, we find perfect Stückelberg oscillations for this choice. However, dissipation reduces the amplitude of these oscillations, with a damping effect that increases with the interference time. If we are interested in the observation of interference effects, it is beneficial to keep the interference time as short as possible. In this section, we analyze how the modification of the annealing velocity affects the visibility, a measure for the oscillation amplitude.

We focus on the first Stückelberg oscillation, around $\tau = 3\hbar/\Delta$ for $v = v_{\text{opt}}$, and observe the ground state occupation to be shifted upwards as we increase v , see Fig. 7.8. This shift is due to modified LZ probabilities. A fast LZ sweep increases the population of the excited state after the first avoided crossing, but then leads to increased ground state occupation after the second LZ transition. On the other hand, the oscillation period is reduced, and hence the first oscillation locates at smaller interference times τ . Let us define the *visibility* to be the difference in ground state population at the local minimum and maximum, see Fig. 7.8(a). Note that very fast annealing reduces

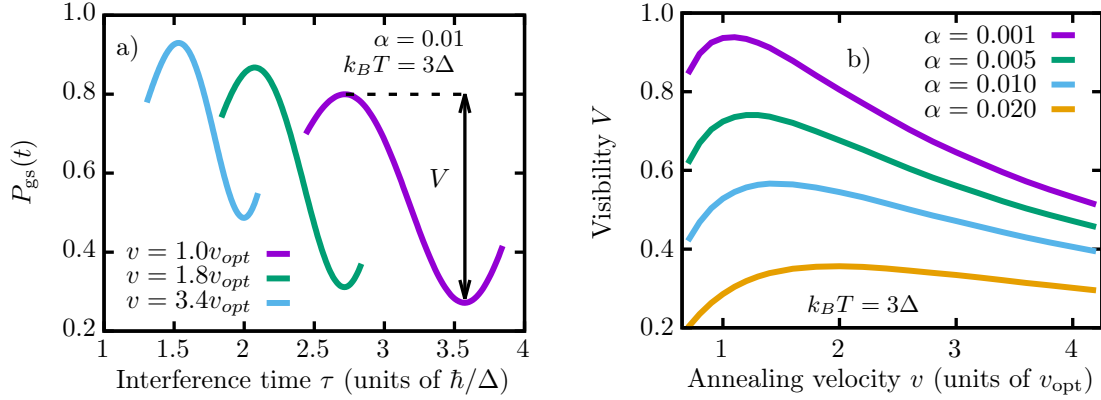


Figure 7.8.: Optimal working point for visibility: a) Probability to end up in the systems ground state, for different annealing velocities. Faster annealing reduces the period of Stückelberg oscillations and shifts the curves upwards. We define the visibility to be the difference between maximum and minimum of the first full oscillation. b) Visibility as a function of the annealing velocity v for different system-bath couplings α .

the system’s ability to show interference between ground and excited state, due to the modified LZ probabilities. On the other hand, fast annealing reduces the overall time of the protocol, giving the environment less time to destroy coherence. Those two opposite effects lead to an optimal annealing velocity, where the visibility is maximum, see Fig. 7.8(b). Similar observations were made in the context of dissipative adiabatic quantum annealing, where the competition between adiabaticity and dissipation results in an optimal annealing time [166]. With this intuitive understanding in mind, it is not surprising that the optimal annealing velocity increases with the system-bath coupling strength α .

7.6. Conclusions

In this chapter we have studied the effect of dissipation on the LZS interferometer employing a numerically exact technique based on matrix product states, see Ref. [109]. We have shown that, as one would expect, interference effects are suppressed once the two-level system is coupled to an environment, due to the rapid decay of coherence. The Stückelberg oscillations decrease in a very similar manner as the system-bath coupling or the temperature of the bath are increased. Even at system-bath couplings of the order of $\alpha = 0.01$ — which are usually still considered small — we found the TLS to become strongly entangled with the bath, implying an almost fully mixed state for the TLS. We have shown that the interferometer has an optimal working point for the annealing velocity, where interference effects can be observed best. This optimal working point emerges from the competition of the optimal velocity in the coherent case and dissipation. In absence of the bath, the visibility is maximum when the annealing velocity leads to a 50:50 population of ground and excited state between

the two avoided crossings. On the other hand, the effects of dissipation favor a short interference time, to reduce the loss of coherence. Hence, the globally best annealing velocity is higher than in the coherent case.

Experimentally it might be possible to realize the LZS interferometer also with highly controllable systems of trapped ions. Rather than exploiting internal electronic levels to build the qubit, one could use the ion in an effective double-well potential as a two-level system [169]. Here, the two levels correspond to the particle being in the left or right well, and the time-dependence could be realized through suitable manipulation of the external potential. Similar experimental setups [170–173] were employed to study (classical) friction [174, 175], but might be extended to study quantum effects as well. Indeed, it would be particularly interesting to see if such a system does show quantum effects such as LZS interference.

7.7. Outlook

In this chapter, we have explored the possibility to carry out time-dependent numerically exact simulations of the spin-boson model. However, due to the LZS interferometer showing signatures of interference only at weak coupling, $\alpha \ll 0.1$, we have restricted ourselves to this regime. To demonstrate the capabilities of the method, let us now discuss the combination of time-dependent driving plus strong coupling for future applications. Consider the spin-boson model, see Section 7.2, with strongly driven time-dependent $\hat{\sigma}_z$ coupling

$$h(t) = \varepsilon_{dr} \cos(\omega_{dr}t) , \quad (7.33)$$

where ε_{dr} and ω_{dr} define the driving power and frequency, respectively. This model has been realized already with a superconducting qubit that is coupled to an electromagnetic environment [7]. After initializing the qubit in state $|\uparrow\rangle$ and the bath in its thermal state with no correlation between them, we are interested in the dynamics of the qubit's expectation value $\langle \hat{\sigma}_z \rangle$, which is the relevant quantity that relates to the experimentally accessible transmission. We fix a temperature of $k_B T = 0.26\Delta$, corresponding to the experimental values $\Delta/2\pi\hbar = 7.23\text{GHz}$ and $T = 90\text{mK}$, a high energy cut-off $\hbar\omega_c = 10\Delta$, a driving frequency $\hbar\omega_{dr} = 1.5\Delta$ and the experimental system bath coupling $\alpha = 0.21$, which is one order of magnitude larger than previously.

At zero driving power, we find the spin to relax towards $\langle \hat{\sigma}_z \rangle = 0$, as known from the static case [123], with only little oscillations. As the driving power increases, we find oscillations to emerge around the static curve, with amplitudes increasing with the driving power. The results demonstrate our capabilities to simulate non-equilibrium open system dynamics in experimentally relevant regimes.

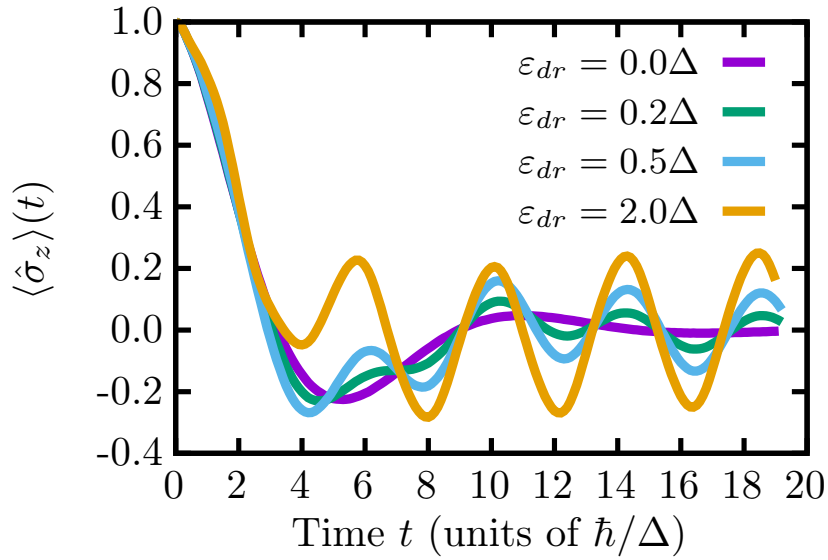


Figure 7.9.: Two-level system dynamics. Dynamics of the spin expectation value $\langle \hat{\sigma}_z \rangle$ for different driving powers ε_{dr} , at fixed system bath coupling strength $\alpha = 0.21$, driving frequency $\omega_{dr} = 1.5\Delta$ and temperature $k_B T = 0.26\Delta$, similar to the values in the experimental realization of Ref. [7]. In absence of driving, the spin dynamics relaxes, due to the coupling to the environment, while at stronger driving spin-oscillations are visible.

8. Conclusions

In this thesis, we have discussed how to efficiently simulate real-time dynamics of quantum systems interacting with finite temperature macroscopic environments using matrix product states. We have focused on essentially two cases, where macroscopic environments of free particles play a crucial role: The Anderson impurity model, relevant in the context of the Kondo effect and dynamical mean-field theory, and the spin-boson model, as a paradigmatic realization of an open quantum system.

Starting with the Anderson model in Chapter 3, we have recapitulated the two major existing simulation geometries that can be employed in MPS simulations: The star geometry and the chain geometry. We have argued that an independent chain mapping for bath modes above and below the baths' chemical potential combines the advantages of the two geometries, namely low entanglement and short-range interactions. Furthermore, we have shown that this approach neatly generalizes to finite temperatures when exploiting the so-called thermofield transformation, which allows us to represent finite temperature density matrices as pure states of an extended Hilbert space.

In Chapter 4 we have presented a detailed numerical analysis of the chain mapping approach developed in Chapter 3. In particular, we have addressed the question of how to order the fermionic sites within an MPS, for the example of a sudden quench in the SIAM. We have shown that the naive implementation of the Hamiltonian according to its geometric structure leads to a massive growth of entanglement within the MPS at finite temperature, due to the creation of particle-hole pairs in the two chains. As a solution to this problem, we have introduced an interleaved ordering, where the chains are merged by alternating sites from the two chains. Due to particle-hole pairs staying localized in this geometry, entanglement is significantly reduced, allowing for much longer simulations at lower numerical cost. We exploited this technique to study the dynamics not only of the impurity, but also the macroscopic bath, revealing clear signatures of many-body effects.

Chapter 5 has been devoted to the calculation of Green's and spectral functions, as relevant for Kondo-related problems and the dynamical mean-field theory. We provided evidence that the separated chain mapping reduces the amount of entanglement as compared to both the star and chain geometry at $T = 0$, while additionally allowing for finite temperatures. Furthermore, at finite temperatures, we have shown that the equilibrium state required for the calculation of Green's functions can be prepared through real-time evolution. However, it is still an open question whether or not there

are more efficient ways to prepare finite temperature steady states, as will be discussed below.

In Chapter 6 we have employed the previously developed technique to compute dissipation in the driven single impurity Anderson model, as relevant for currently ongoing pendulum AFM experiments [157]. We have shown that it is possible to simulate the real-time dynamics with explicit time-dependence and to calculate the dissipation from the total energy of the system. Preliminary results indicate that the mechanism of moving the impurity energy level contains little contribution of the Kondo effect, in contrast to mechanisms where the hybridization is modified in time [153, 154]. However, further research is required on these issues, especially when experimental results are available.

The last chapter instead deals with bosonic environments, as regularly employed to model open quantum systems. We have explored the possibility to simulate real-time dynamics with explicit time-dependence employing the numerically exact technique developed in Ref. [109], which is very similar to the approach we chose for fermionic baths but exploits additional properties of the spin-boson model. We have shown that the presence of a dissipative bath heavily reduces interference effects in quantum interferometry, due to the increasing system-bath entanglement. The presence of dissipation also leads to an optimal working point in the annealing velocity, due to the competition of dissipation and coherent dynamics, where interference effects are maximum.

8.1. Future perspectives

Clearly, there are still several open questions and problems.

On the physical side, further analysis of the issue regarding dissipation in presence of the Kondo effect is required. It is currently unclear in which scenarios one can detect signatures of the Kondo effect in dissipation measurements, both in theoretical models and in pendulum AFM experiments. Most importantly, the role of the slow driving of the tip in the experiment and its relation to the typical time scales of the Kondo effect are unknown and require further investigation.

On the technological side, further improvements for DMFT impurity solvers, the simulation of multi-bath models for quantum transport, and the efficient computation of steady states are possible, as discussed in more detail below.

Multi-orbital DMFT. Regarding the topic of DMFT impurity solvers, it is clear that in the next step one should implement the actual DMFT loop, which we have not done so far. Indeed, it would be very interesting to consider directly the two orbital case.

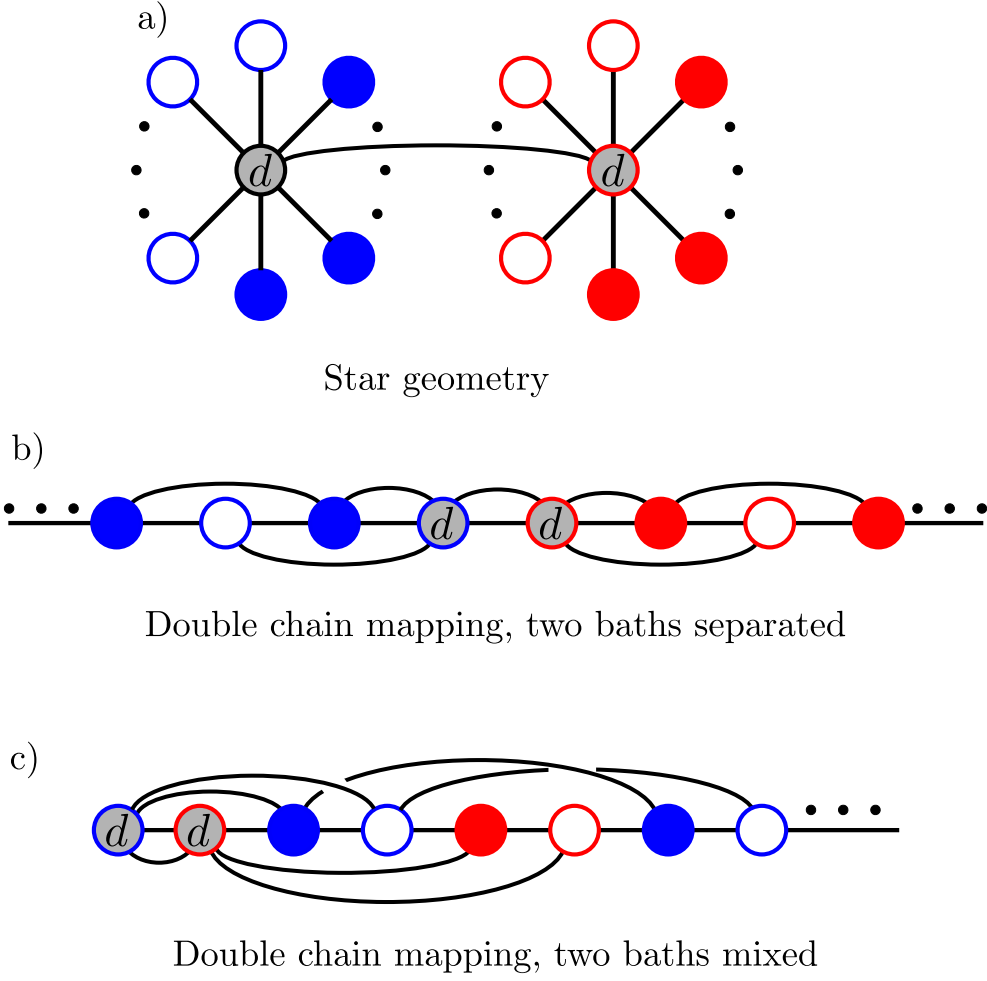


Figure 8.1.: Possible orderings for a two-orbital model. Two SIAMs are interacting through the impurities. b) Chain mapping using the double-chain method with alternating filled and empty chain sites. The baths corresponding to the impurities are spatially separated. c) Chain ordering with additional alternation of the two baths, introducing interactions over a longer range. Such ordering might be able to better capture the dynamics of excitations.

Consider the two band model

$$\hat{H}_{2\text{-band}} = \hat{H}_{\text{SIAM},1} + \hat{H}_{\text{SIAM},2} + \hat{H}_{d-d} , \quad (8.1)$$

built from two SIAMs, $\hat{H}_{\text{SIAM},1}$ and $\hat{H}_{\text{SIAM},2}$, and an interaction between the impurities, \hat{H}_{d-d} , which we do not specify explicitly here. Since similar “dimeric” structures have been successfully studied with the original chain mapping [38], it should be doable without any major issues with our two-chain approach as well. This model is indeed of crucial importance. As pointed out in Ref. [40], in multi-orbital scenarios the entanglement grows the most between different SIAMs. Hence, understanding the entanglement dynamics in more detail is key to further improve tensor-network-based impurity solvers. For example, we have seen that at finite temperature it can be highly beneficial to merge the two chains of the SIAM, which emerge from the thermofield

transformation. Similarly, one could ask if improvements are possible by merging the two baths corresponding to different SIAMs.

In Fig. 8.1(a) the model is visualized in the star-geometry. Again, a direct simulation of such a model is indeed possible [35, 53] and provides a promising path for future development. On the other hand, we can once again employ a chain mapping, with independent mappings for filled and empty chains of the two baths, see Fig. 8.1(b). Here we have already visualized it with interleaved empty and filled chains corresponding to the same bath, but with separation of the two baths. Since entanglement tends to grow most in between different impurity models [40], it is clear that further improvements are only possible when merging the baths in some way. In the chain geometry, this could be achieved by simply merging not only empty and filled chains, but also chains corresponding to different baths, see Fig. 8.1(c). Of course, this will make the interactions more long-ranged, but might eventually reduce the growth of entanglement. Notice that for the special case of zero or weak interaction between the impurities such ordering would be inefficient as entanglement would only grow slowly between the two SIAMs, but might be beneficial at stronger interactions. However, further analysis is required on these issues.

Equilibrium steady state. For the calculation of the spectral function in Chapter 5 we have prepared the finite temperature equilibrium state through real-time evolution: After turning on the hybridization between impurity and free electron bath at finite temperature, the system is evolved until reaching the equilibrium state. While the obtained results have been very accurate, such procedure clearly is numerically demanding, due to the requirement for long real-time dynamics. Hence, it would be a major improvement if the equilibrium state could be determined through a variational algorithm, similar to DMRG for ground states. In this paragraph, we discuss some thoughts and ideas on how this might be achieved.

Consider the SIAM with chain mapping and interleaved MPS ordering, see Fig. 8.2(a), as discussed in Chapter 4. In Section 5.4 we have shown that in the chain geometry, after turning on the hybridization interaction, local observables of chain sites converge towards a steady-state value. In particular, chain sites close to the impurity are found to equilibrate faster than sites far away from the impurity, as one would expect intuitively. Consequently, it is reasonable to expect the reduced density matrix of impurity and chain sites to converge in the long-time limit, where, once again, chain sites closer to the impurity equilibrate faster. Suppose that we let the system evolve for some time until chain sites within the box of Fig. 8.2(a) have equilibrated. Then the corresponding MPS tensors should be constant in time up to some global phase.

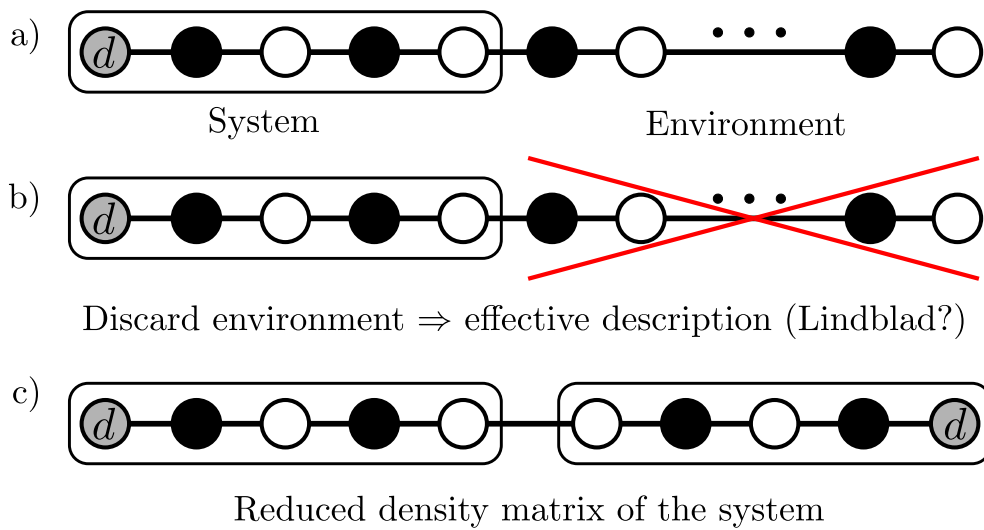


Figure 8.2.: MPS equilibration in chain geometry. a) The SIAM in chain geometry with separate chain mapping for filled and empty modes. The MPS is ordered with interleaved geometry, see also Chapter 4. The box encircles the impurity and the first two chains sites of both filled and empty chains, representing the "system", while the remaining sites of the chains are considered an effective environment. b) One idea to deal with the infinitely long chain is to replace the environment section with an effective description, hence discarding the chain, for example using Lindblad operators. c) The reduced density matrix of the encircled sites can be built by mirroring the system and connecting the open bond links of the MPS. Notice that no physical legs are drawn here.

Question

Can we design a DMRG-like variational algorithm that directly yields the equilibrium MPS tensors of chain sites that are "close" to the impurity?

One way to look at the problem is to treat the impurity and several chain sites as the "system", as visualized by the box in Fig. 8.2(a), while the rest of the infinitely long chain is considered to be an effective environment. It is currently an open question how to deal with this effective environment. For example, one might simply replace the infinitely long chains with Lindblad operators, see Fig. 8.2(b), which could deliver particles and holes into the filled and empty chains of the system. Such an approach requires working with the reduced density matrix of the "system", as visualized in Fig. 8.2(c). The condition for the steady-state reduced density matrix, $\frac{d}{dt}\hat{\rho} = 0$, can then be translated into a ground state search problem that can be solved via DMRG [176]. The crucial part of this idea, however, is to find an accurate and efficient way to mimic the infinitely long chains and to replace them. However, it is currently unclear if this can be done with Lindblad operators in some way, or if there are other possibilities.

A. Tensor network operations and algorithmic details

In this chapter we provide some additional information on elementary tensor network operations and the algorithms discussed in Chapter 2. In Appendix A.1 we discuss the reshaping procedure to transform a tensor into a vector and vice versa. This is very important as linear algebra routines such as singular value decomposition (SVD) or eigendecomposition usually work with matrices and vectors, and hence we need to reshape our tensors. The particular example of an SVD is presented in Appendix A.2, where we discuss different possibilities to carry out an SVD of a rank-3 tensor depending on how the indices are merged. Understanding these differences is crucial in MPS algorithms, as it affects the resulting tensors and their orthogonality properties. Finally, in Appendix A.3 we show how the TDVP equations in Eq. (2.31) can be solved efficiently.

A.1. Reshaping

In tensor networks we often deal with tensors of rank $r > 2$. However, mathematical routines such as QR or singular value decomposition are built for matrices only. Hence, we need to reshape the tensors into matrices or vectors before applying linear algebra routines on them. Consider a tensor with at least two indices, which are called i and j . Merging those two indices into a single index k corresponds to the mapping given in Table A.1: Every combination of index values i and j is labeled by a unique value of the index k . This procedure is similar to the creation of a Hilbert space from two smaller subsystem through the use of the tensor product.

Notice that the reverse is possible as well: The index k can be split into indices i and j through the mapping in Table A.1. The usual procedure we encounter in tensor network algorithms is as follows: 1) We merge the indices of a tensor to obtain either a matrix or a vector as required. 2) We perform a single or multiple linear algebra operations on the matrix/ vector, such as an QR decomposition, SVD, numerical optimization or time evolution. 3) We split the indices to bring the MPS in its original form.

Table A.1.: Merging two tensor indices: Any two indices i and j of a tensor can be merged into a single (vector-)index k . To this end we label all possible combinations of i and j with a unique number k . In this example, $i = 1, 2$ and $j = 1, 2, 3$.

Tensor indices i, j	Vector index k
1,1	1
1,2	2
1,3	3
2,1	4
2,2	5
2,3	6

A.2. Singular value decomposition for tensors

The singular value decomposition is one of the most important routines in tensor network algorithms. We can compute the SVD for any arbitrary matrix $A \in \mathbb{C}^{m \times n}$, which is given by

$$A = UDV^\dagger, \quad (\text{A.1})$$

where $U \in \mathbb{C}^{m \times \min(m,n)}$ has orthonormal columns, $V^\dagger \in \mathbb{C}^{\min(m,n) \times n}$ has orthonormal rows, and $D = \text{diag}(\lambda_1, \dots, \lambda_{\min(m,n)})$ is real diagonal. This implies $U^\dagger U = \mathbb{1}$ and $V^\dagger V = \mathbb{1}$, a property that is essential in tensor network algorithms as it allows to set the orthogonality center of the (loopfree) network. Consider now a rank-3 tensor A with elements A_{i_1, i_2, i_3} . There are multiple ways to compute the SVD of this tensor, depending on how we merge the indices. For example, we can merge i_1 and i_2 to build the row index of the matrix, while the column index is i_3 . Then the SVD is given by

$$A_{i_1, i_2, i_3} = \sum_{k_1, k_2} U_{i_1, i_2, k_1} D_{k_1, k_2} V_{k_2, i_3}^\dagger, \quad (\text{A.2})$$

as visualized in Fig. A.1(a). Note that i_1 and i_2 are indices of the tensor U , while i_3 is an index of V^\dagger . The orthogonality property of the SVD matrices U and V^\dagger translates into

$$\sum_{i_1, i_2} U_{i_1, i_2, k_1} U_{i_1, i_2, k'_1}^* = \delta_{k_1, k'_1} \quad \text{and} \quad \sum_{i_3} V_{k_2, i_3}^\dagger (V_{k'_2, i_3}^\dagger)^* = \delta_{k_2, k'_2} \quad (\text{A.3})$$

Graphically the orthogonality property of a tensor is visualized by the triangular shape, where legs going into the triangle are those we sum over in the orthogonality condition Eq. (A.3) (here i_1 and i_2). Alternatively, we can do the SVD in a different way: For example, we can merge i_2 and i_3 to build the column index and use i_1 as row index. In this case the SVD yields

$$A_{i_1, i_2, i_3} = \sum_{k_1, k_2} \tilde{U}_{i_1, k_1} \tilde{D}_{k_1, k_2} \tilde{V}_{k_2, i_2, i_3}^\dagger. \quad (\text{A.4})$$

Fig. A.1(b) shows that the leg i_2 is now an index of \tilde{V}^\dagger . Hence, by properly merging indices prior to the SVD, we are able to choose if an index will be in U or V^\dagger .

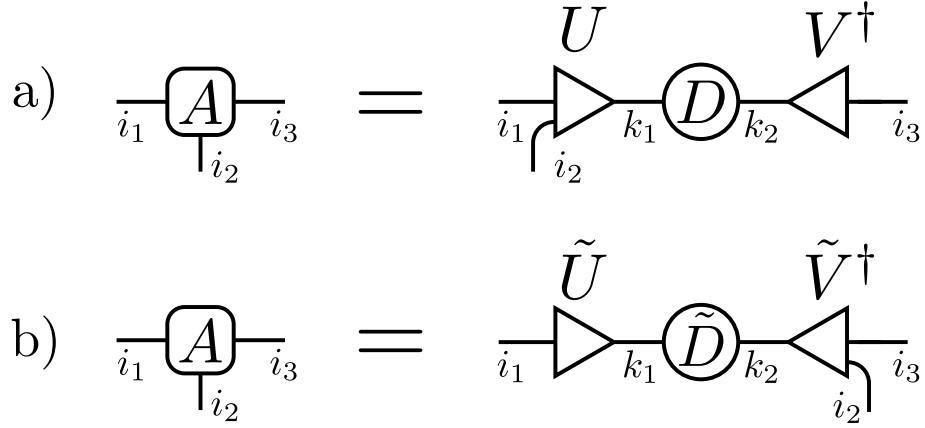


Figure A.1.: SVD of a rank-3 tensor: a) The SVD is performed on the matrix with joint row index (i_1, i_2) and column index i_3 . Hence, i_1 and i_2 are indices of U , while i_3 is an index of V^\dagger . Tensors U and V^\dagger satisfy the orthogonality condition Eq. (A.3), indicated by the triangular shape in graphical notation. b) SVD of tensor A when merging i_2 and i_3 to build the column index, while row index is just i_1 . Consequently, i_2 is now an index of \tilde{V}^\dagger .

A.3. Solving a TDVP equation

In this section we discuss in some detail how the TDVP equations in Eq. (2.31) can be solved efficiently, following the ideas of Ref. [116]. First, we notice that there are two types of differential equations (DEs), corresponding to the two types of projectors, $P_m^{(+)}$ and $P_m^{(-)}$. In this section, however, we will restrict ourselves on the differential equations containing $P_m^{(+)}$, as the case for $P_m^{(-)}$ is similar. Consider the differential equation

$$i\hbar \frac{\partial}{\partial t} |\psi(t)\rangle = \hat{P}_m^{(+)} \hat{H} |\psi(t)\rangle \quad (\text{A.5})$$

with $\hat{P}_m^{(+)}$ as given in Eq. (2.27) and Fig. 2.9.

In the first step we build the 2-site orthogonality center by contracting the two tensors to evolve, drawn in red, Fig. A.2(a). This is necessary so solve the differential equation later on. Before moving on with the details of the algorithm, let us introduce the notation we use throughout the section. The MPS can be split into three important parts, as indicated by different colors in Fig. A.2(a). The three parts are the left-orthogonal tensors with physical indices i_1, \dots, i_{m-1} (blue), the 2-site orthogonality center $T^{(m)}$ with physical indices i_m and i_{m+1} (red), see Eq. (2.18), and the right orthogonal tensors with indices i_{m+2}, \dots, i_L (green). We simplify the notation by representing each of the three parts by just a single tensor symbol. Notice that the contraction of right (left) orthogonal tensors remains right (left) orthogonal, and hence is represented by a triangle as well. In practical applications, however, the contraction of left and right orthogonal tensors is — in contrast to the contraction of the two center sites — never carried out, as it is highly inefficient.

Let us now go back to the TDVP equation of interest, Eq. (A.5). The left hand side, $i\hbar \frac{\partial}{\partial t} |\psi(t)\rangle$ contains the derivative of the state with respect to time. Employing the simplified MPS notation, the derivative is given in Fig. A.2(b), where the product rule has been used. We obtain three terms, each of them containing a derivative of a tensor with respect to time, as indicated by the dot above the corresponding tensor. The right hand side of Eq. (A.5) contains the application of the Hamiltonian \widehat{H} and the projector $\widehat{P}_m^{(+)}$ on the state $|\psi(t)\rangle$, visualized in Fig. A.2(c). Notice that the projector is the same as in Fig. 2.9(a), but represented in the simplified notation. In the orange box we identify the effective Hamiltonian, obtained when contracting the left and right orthogonal tensors into the Hamiltonian. It acts solely on the 2-site orthogonality center $T^{(m)}$, and produces a new tensor that is inserted in between the left and right orthogonal tensors.

To solve the TDVP equation, Eq. (A.5), we need the left and right hand side to be equal (dropping the factor $i\hbar$ for the moment). Comparing Fig. A.2(b) and Fig. A.2(c) we realize that they can be made equal by choosing the derivative of the blue and green tensors to be zero. Hence, only the second term of the product rule in Fig. A.2(b) remains, where the derivative of $T^{(m)}$ is taken. Comparing this term with Fig. A.2(c), we find that the two diagrams are equal, and hence the TDVP equation is solved, provided

$$i\hbar \frac{d}{dt} \mathbf{T}^{(m)} = + \widehat{H}_{\text{eff}}^{(m)} \mathbf{T}^{(m)}, \quad (\text{A.6})$$

as visualized in Fig. A.2(d). Hence, the TDVP equation can indeed be solved by making only the orthogonality center $T^{(m)}$ time-dependent, keeping all the remaining tensors constant. For the second type of TDVP equation,

$$i\hbar \frac{\partial}{\partial t} |\psi(t)\rangle = -\widehat{P}_m^{(-)} \widehat{H} |\psi(t)\rangle \quad (\text{A.7})$$

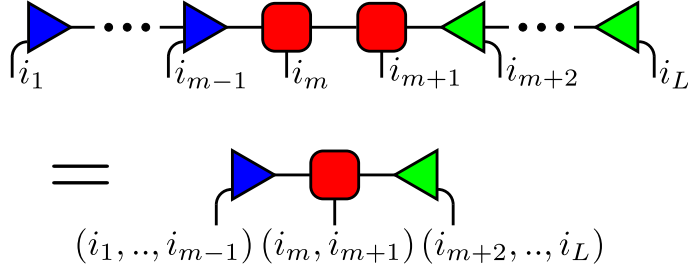
$$(\text{A.8})$$

a similar analysis can be carried out. One finds that the DE is solved by making only the single site orthogonality center $\mathbf{A}^{(m+1)}$ time-dependent, evolving it as

$$i\hbar \frac{d}{dt} \mathbf{A}^{(m+1)} = -K^{(m+1)} \mathbf{A}^{(m+1)}. \quad (\text{A.9})$$

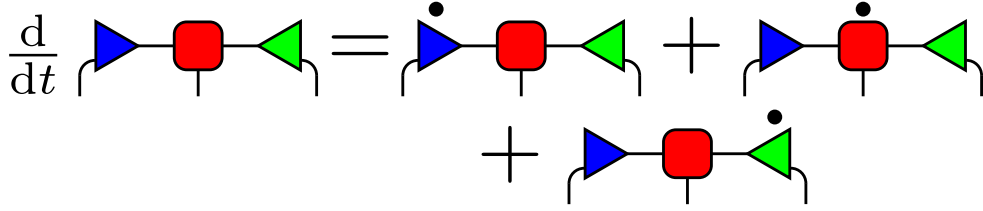
Here, $K^{(m+1)}$ is the corresponding single site effective Hamiltonian as given in Fig. 2.7(d). As discussed in the main text, the effective DEs for the 2-site orthogonality center and 1-site orthogonality center can be solved numerically using Krylov subspace techniques. However, there is one additional step to be taken when solving the DE for the 2-site tensor $T^{(m)}$: In order to restore the MPS format, it needs to be split into two tensors again by means of an SVD.

a) Simplify notation and contract center sites (red)



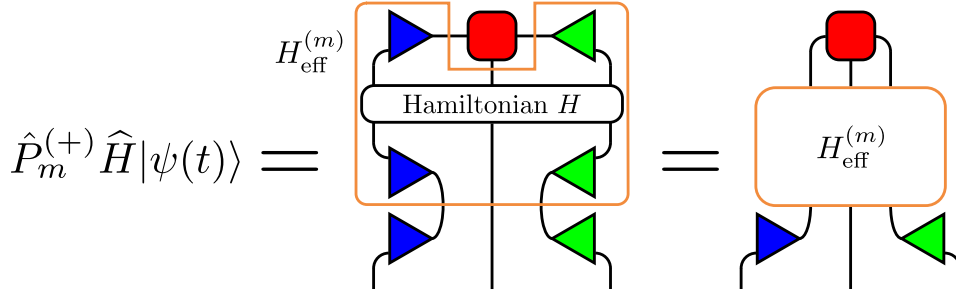
$$\begin{aligned}
& \text{Diagram showing contraction of two adjacent red tensors in an MPS chain.} \\
& \text{Top: } \dots \text{ (blue triangle } i_1 \text{)} \dots \text{ (blue triangle } i_{m-1} \text{)} \text{ (red square } i_m \text{)} \text{ (red square } i_{m+1} \text{)} \text{ (green triangle } i_{m+2} \text{)} \dots \text{ (green triangle } i_L \text{)} \\
& \text{Bottom: } \text{ (blue triangle } (i_1, \dots, i_{m-1}) \text{)} \text{ (red square } (i_m, i_{m+1}) \text{)} \text{ (green triangle } (i_{m+2}, \dots, i_L) \text{)}
\end{aligned}$$

b) Left hand side of TDVP equation



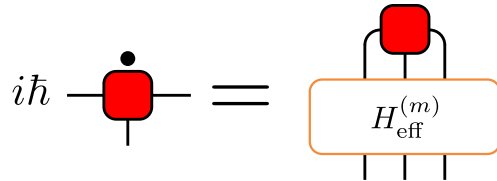
$$\frac{d}{dt} \text{ (blue triangle - red square - green triangle)} = \text{ (blue triangle with dot - red square - green triangle)} + \text{ (blue triangle - red square with dot - green triangle)} + \text{ (blue triangle - red square - green triangle with dot)}$$

c) Right hand side of TDVP equation



$$\hat{P}_m^{(+)} \hat{H} |\psi(t)\rangle = \text{Diagram with Hamiltonian } H \text{ and projector } \hat{P}_m^{(+)} \text{ boxes} = \text{Diagram with effective Hamiltonian } H_{\text{eff}}^{(m)} \text{ box}$$

d) Differential equation for orthogonality center



$$i\hbar \text{ (red square with dot)} = \text{ (red square with dot inside } H_{\text{eff}}^{(m)} \text{ box)}$$

Figure A.2.: How to solve a TDVP equation: a) MPS in mixed canonical gauge. For the sake of simple notation we represent all left orthogonal tensors (blue), and the right orthogonal tensors (green) in a single tensor each. In the short notation each physical index is a joint index representing several physical sites as given in brackets. Further, we carry out a real contraction of the center tensors $A^{(m)}$ and $A^{(m+1)}$ (red) to form the 2-site orthogonality center $T^{(m)}$ (red), see also Eq. (2.18). b) Left hand side of the TDVP equation, Eq. (A.5). Using the product rule for derivatives we have three terms, where in each term there is a derivative of a tensor with respect to time, as indicated by the dot. c) Right hand side of Eq. (A.5), where the Hamiltonian \hat{H} and the tangent space projector $\hat{P}_m^{(+)}$ are applied on the MPS. The tensors in the orange box define an effective Hamiltonian for the orthogonality center (red tensor). d) Differential equation for the orthogonality center, see Eq. (A.6).

B. Additional details for Chapter 5

We provide here additional details for the simulations discussed in Section 5.3.

B.1. Parameters and numerical details

In our tensor network simulations we have two crucial parameters to restrict the number of states kept in the MPS: 1) first, we have the truncated weight, corresponding to the summed probability of discarded states; 2) second, we also use a hard cutoff on the number of states we keep, the so-called *bond dimension*. We use a small truncated weight, of $w_t = 10^{-12}$, and a maximum bond dimension of, typically, $D = 150$. Only for the zero temperature simulations with the standard chain mapping, the bond dimension was increased to $D = 400$, in order to deal with the increase of entanglement. For all real time evolutions we use time steps in the range $\Delta t = 0.01 - 0.02\hbar/\Gamma$. (The largest energy scale in our system is given by the half bandwidth $W = 10\Gamma$.) We verified that our results are converged in all relevant numerical parameters. We further found that setting a minimum bond dimension of $D_{\min} \cong 20$ (i.e., keeping even some states with low probability) can be beneficial for the numerical stability of the time-dependent variation principle (TDVP) approach we have adopted when dealing with next-nearest neighbor interactions, see also Section 4.4.4 for details. We confirmed that 2-site TDVP delivers accurate results, by comparison of different MPS orderings. We compared our results with simulations employing the two separated chains ordering (see Fig.1(d) in the main text). Here, projection errors are absent due to the Hamiltonian terms being at most nearest neighbor in distance [50]. The “separated chains” ordering works fine at low temperatures, where we carried out the comparison, but shows strong entanglement growth for higher temperatures, see Chapter 4.

In our simulations, we explicitly exploit conservation of particle number and spin to speed-up the calculations [120, 177, 178]. We have previously seen that equilibration is faster for higher temperature. For this reason, we use different equilibration times $\tau = 32\hbar/\Gamma$ ($k_B T = 0.05\Gamma$), $\tau = 12\hbar/\Gamma$ ($k_B T = 0.15\Gamma$), $\tau = 6\hbar/\Gamma$ ($k_B T = 0.5\Gamma$), and $\tau = 4\hbar/\Gamma$ ($k_B T = 4\Gamma$). Green’s functions are computed up to time $t_f = 7.5\hbar/\Gamma$ (finite T), $t_f = 30\hbar/\Gamma$ ($T = 0, U = 2.5\pi\Gamma$) and $t_f = 40\hbar/\Gamma$ ($T = 0, U = 3.25\pi\Gamma$) before applying the “linear prediction method” to extrapolate the exponential tail [38, 141, 142], as explained in Appendix B.3.

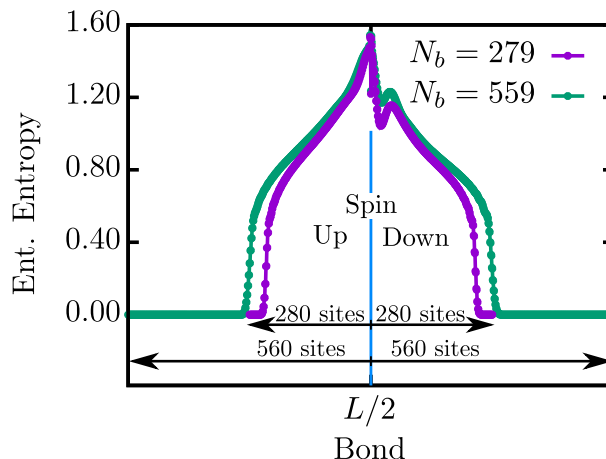


Figure B.1.: Entanglement entropy along the MPS at our final time $t = 30\hbar/\Gamma$ at zero temperature, for the symmetric SIAM. At $T = 0$ we separate spin-up and spin-down degrees of freedom into two chains, connected in the middle (see also Fig. B.3). Two different bath sizes $N_b = 279$ and $N_b = 559$ are considered, where $L/2$ labels the middle of the MPS. Note that the curves are centered around $L/2$ such that the smaller N_b curve does not extend to the boundaries of the window. During time evolution the nonzero entanglement region grows continuously (see Fig. B.3) and almost reaches the end of the $N_b = 279$ chains. Hence, any further evolution with this discretization would lead to significant errors in the dynamics.

Finally, let us discuss the discretization issue. In the dynamical case, which employs the equilibration procedure, we are able to work directly in the continuum limit $N_b \rightarrow \infty$ using orthogonal polynomials, as discussed previously. In practice, we truncate the infinitely long chain such that no excitation — being either a particle in the empty chain or a hole in the filled chain — does reach the end of the chain during the dynamics [123]. Clearly, this does not introduce any error, since the truncation does not have any impact on the quantum state at any time (as long as the chain is long enough). At $T = 0$ instead, where DMRG can be used to calculate the equilibrium (ground) state, we use linear discretization of the bath. This turned out to yield more accurate results for the ground state. For the calculations of Green’s functions at $T = 0$ we linearly discretized the bath into $N_b = 559$ modes, mapping 280 modes to the empty chain and 279 modes to the filled chain in our approach. We observed convergence with respect to N_b .

B.1.1. Performance dependence on bath size

For practical applications it can be crucial to have a fine discretization of the bath, in order to sample the hybridization function as accurate as possible. However, fine discretization translates into a large bath with many discrete conduction band levels. For an algorithm to be efficient, we require it to scale well with the number of bath modes. We investigate this issue by analyzing the entanglement entropy at the end of our zero-temperature Green’s function calculation (see Fig. B.1). We find that the number of bath sites — translating into the equivalent number of chain sites — barely

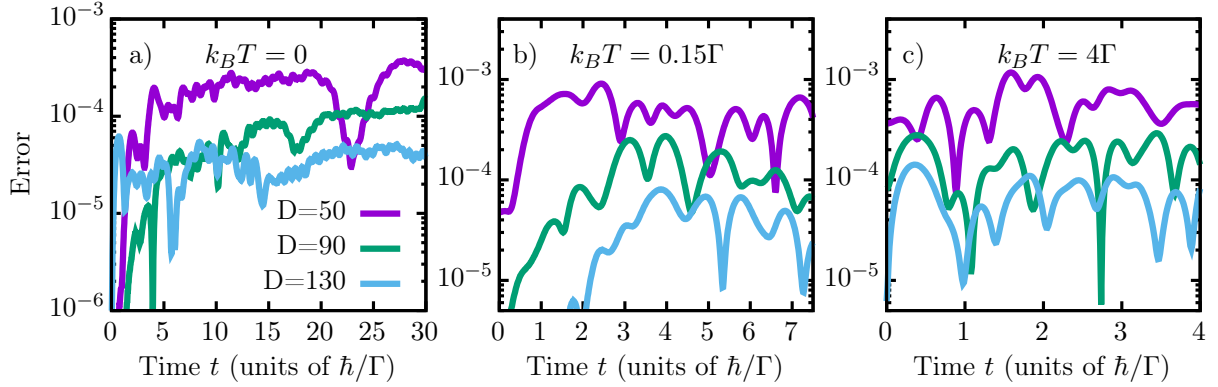


Figure B.2.: Error $|G_{\text{ref}}^<(t) - G_D^<(t)|$ in the lesser Green's function as compared to the reference simulation ($D = 250, w_t = 10^{-14}$), for different bond dimensions D ($w_t = 10^{-12}$). The symmetric SIAM is considered, with $\varepsilon_d = -1.25\pi\Gamma$ and $U = 2.5\pi\Gamma$, and temperatures $k_B T = 0$ (a), $k_B T = 0.15\Gamma$ (b) and $k_B T = 4\Gamma$ (c). We consider different maximum simulation times depending on temperature due to the faster decay of the Green's function at higher temperature.

affects the entanglement structure in the MPS. Within the region reached by excitations (nonzero entanglement) differences between the two curves are negligible. The larger bath has an extended region not reached by any excitation, and, since the state has zero entanglement there, time evolution is very efficient. Hence, our approach shows excellent scaling with the number of sites and allows to accurately simulate discretized baths without any significant increase of computational costs.

B.1.2. Convergence with bond dimension D

In tensor network algorithms, the bond dimension D is the key numerical parameter, defining how many states are kept at each bond, hence determining the accuracy of the simulation. For an algorithm to be efficient, it is crucial that the results converge sufficiently fast with respect to the bond dimension. Since no exact results are available, we investigate the convergence of the Green's function as compared to a reference simulation with large bond dimension $D = 250$ and small truncated weight $w_t = 10^{-14}$. We define the error to be the difference $|G_{\text{ref}}^<(t) - G_D^<(t)|$ between the reference simulation and simulations with bond dimension D and the usual truncated weight $w_t = 10^{-12}$. In Fig. B.2 we show the convergence of the lesser Green's function with respect to the bond dimension at different temperatures. We find already qualitatively good results at bond dimensions as low as $D \sim 50$, improving further when increasing D , as expected. For our simulations in the main paper we used $D = 150$, to reduce numerical errors to a minimum.

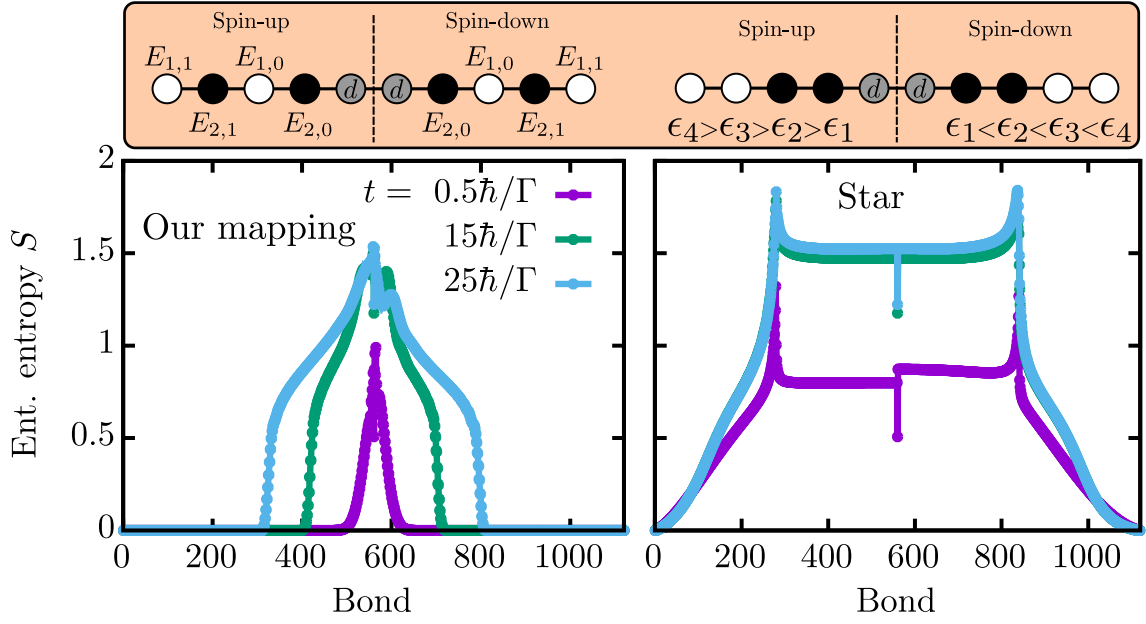


Figure B.3.: Top: Ordering of the sites in the MPS for our chain mapping based method (left) and the star geometry (right). At $T = 0$ we split spin degrees of freedom into two chains, due to the reduced amount of entanglement. Grey symbols represent impurity sites, while black and white symbols correspond to modes that are filled and empty (in absence of hybridization), respectively. Bottom: Entanglement entropy along the MPS during the calculation of the greater Green's function at $T = 0$ and different times t , for the symmetric SIAM.

B.2. Comparison with the star geometry

In the main text we already discussed the entanglement entropy of our approach, showing that it is significantly lower as compared to the original chain mapping. However, it has been shown by Wolf *et al.*[39] that the original chain-mapping-based approach is rather inefficient, and a direct simulation in the star geometry can reduce the entanglement in the MPS. For our comparison we employ the MPS ordering of Ref.[40], which includes an additional splitting of spin-up and spin-down, as compared to Ref. [39]. We found this splitting of spin degrees of freedom to lower the entanglement in the scenario considered here. Hence, the star geometry MPS consists of two impurity sites in the middle, one for spin-up and one for spin-down (see Fig. B.3). Both impurity sites are coupled to their individual conduction modes, represented in the star geometry: Conduction modes are ordered according to their energy, starting with the lowest energy mode next to the corresponding impurity, and increasing in energy as we move away from the impurity sites. For simplicity, we restrict our analysis to $T = 0$, where neither the thermofield transformation nor the equilibration process are needed.

For the star geometry, we find the entanglement to show a plateau in the middle of the MPS (see Fig. B.3), with almost constant entanglement. We believe that this plateau is due to the entanglement between the impurity and the conduction modes close to

the Fermi energy. These modes, however, are located in the middle of each bath, where we also find entanglement peaks (one for spin-up and one for spin-down). In our chain-mapping-based method we find clearly lower entanglement along the MPS, leading to much faster simulations. However, the entanglement structure highly depends on the ordering of the sites in the MPS, especially in the star geometry, and different orderings might reduce the entanglement. Here, the main disadvantage of the star geometry seems to be the spacial separation of the impurity and modes close to the Fermi energy, leading to significantly worse scaling with the number of bath sites, as compared to our chain-mapping-based approach. This might be avoided by moving to a nonlinear tensor network [53]. We further note that we have concentrated on the Kondo regime here, and that the entanglement can strongly depend on the physical parameters. Hence, further analysis is needed on these issues.

B.3. Linear prediction

The calculation of Greens functions through real time evolution is usually limited by the numerical resources available. Hence, in many cases we are only able to compute it up to some finite time, while the tail is inaccessible due to the requirement for long simulations. However, long tails of the Greens function can be important to calculate the spectral function accurately. The linear prediction method discussed here is a very simple tool to extrapolate a set of data points, thereby improving the accuracy of the spectral function [38, 141, 142]. Below we present some details of the linear prediction technique, following Ref.[38] with some additional details.

Let us assume that the simulations yields a sequence of $2N$ equidistant data points x_1, \dots, x_{2N} . In the framework of linear prediction a new data point \tilde{x}_n is predicted as a linear combination of the previous N values:

$$\tilde{x}_n = - \sum_{i=1}^N a_i x_{n-i} \quad \forall n > N, \quad (\text{B.1})$$

where a_1, \dots, a_N are unknown constants. Notice that we use the tilde to indicate that the value is obtained through linear prediction, while non-tilde variables are data points from the original simulation. Before predicting new data points, we first have to find the rule after which the new points are computed. Hence, we need to find the coefficients a_i based on the available data. To this end we split the data set into two halves, x_1, \dots, x_N and x_{N+1}, \dots, x_{2N} . Now pretend that we only know the first N points, while the second set should be predicted from those points. Since in fact we also know the correct values of the second half, we can define a cost/loss function using square errors:

$$\mathcal{L} = \sum_{n=N+1}^{2N} |\tilde{x}_n - x_n|^2 \quad (\text{B.2})$$

Here, any predicted value \tilde{x}_n of the second half is compared to its true value x_n . The coefficients a_1, \dots, a_N can then be found through minimization of the loss function

$$\mathcal{L} = \sum_{n=N+1}^{2N} (\tilde{x}_n - x_n)(\tilde{x}_n - x_n)^* \quad (\text{B.3})$$

$$= \sum_{n=N+1}^{2N} \tilde{x}_n \tilde{x}_n^* - \tilde{x}_n x_n^* - x_n \tilde{x}_n^* + x_n x_n^*. \quad (\text{B.4})$$

Let us carry out the minimization explicitly by setting the derivatives of the loss function with respect to the coefficients a_i and their complex conjugates a_i^* equal to zero. The derivatives are given by

$$\begin{aligned} \frac{\partial \mathcal{L}}{\partial a_k} &= \sum_{n=N+1}^{2N} -x_{n-k} \tilde{x}_n^* + x_{n-k} x_n^* \\ &= \sum_{n=N+1}^{2N} x_{n-k} \left(\sum_{j=1}^N a_j^* x_{n-j}^* \right) + x_{n-k} x_n^* \end{aligned} \quad (\text{B.5})$$

$$\begin{aligned} \frac{\partial \mathcal{L}}{\partial a_k^*} &= \sum_{n=N+1}^{2N} -\tilde{x}_n x_{n-k}^* + x_n x_{n-k}^* \\ &= \sum_{n=N+1}^{2N} \left(\sum_{j=1}^N a_j x_{n-j} \right) x_{n-k}^* + x_n x_{n-k}^* \end{aligned}$$

where we have used that

$$\frac{\partial \tilde{x}_n}{\partial a_k} = -x_{n-k}, \quad \frac{\partial \tilde{x}_n^*}{\partial a_k^*} = -x_{n-k}^*, \quad \text{and} \quad \frac{\partial \tilde{x}_n^*}{\partial a_k} = \frac{\partial \tilde{x}_n}{\partial a_k^*} = 0. \quad (\text{B.6})$$

Notice that the two derivatives are complex conjugates of each other since the cost function is real, and hence we can continue with just one of them. Setting the derivative equal to zero, we find a linear system of equations

$$\sum_{j=1}^N \sum_{n=N+1}^{2N} x_{n-j} x_{n-k}^* a_j = -x_n x_{n-k}^*, \quad (\text{B.7})$$

which is typically written in matrix notation as

$$\mathbf{R}\mathbf{a} = -\mathbf{r} \quad (\text{B.8})$$

with

$$R_{kj} = \sum_{n=N+1}^{2N} x_{n-k}^* x_{n-j}, \quad r_k = \sum_{n=N+1}^{2N} x_{n-k}^* x_n. \quad (\text{B.9})$$

Calculating the pseudo-inverse of R we can invert Eq. (B.8) and finally obtain the coefficients a_1, \dots, a_N . In practice, the pseudo-inverse is calculated through a singular value decomposition, with cutoff δ to truncate small singular values for reasons of numerical stability. In our calculations we use the cutoff $\delta = 10^{-8}$ relative to the largest singular value (see documentation of numpy function 'numpy.linalg.pinv'). Before predicting new data points, there is one more issue to discuss: Let introduce an alternative way to write the prediction of new values in Eq. (B.1). To simplify the notation, we drop the tilde and treat predicted values the same way as the original simulation data. Rewriting Eq. (B.1) as vector product, we have

$$x_n = -\mathbf{a}^T \mathbf{x}^{(n-1)}, \quad (\text{B.10})$$

where $\mathbf{a}^T = (a_1, a_2, \dots, a_N)$ and

$$\mathbf{x}^{(n-1)} = \begin{pmatrix} x_{n-1} \\ x_{n-2} \\ \vdots \\ x_{n-N} \end{pmatrix}. \quad (\text{B.11})$$

Notice that $\mathbf{x}^{(n)}$ is only defined for indices $n \geq N$. If we want to predict a data point x_n , we are looking for the vector $\mathbf{x}^{(n)}$, which contains x_n as its first element. This vector on the other hand, is related to the previous one through the relation

$$\mathbf{x}^{(n)} = \begin{pmatrix} x_n \\ x_{n-1} \\ \vdots \\ x_{n-N+2} \\ x_{n-N+1} \end{pmatrix} = \underbrace{\begin{pmatrix} -a_1 & -a_2 & -a_3 & \dots & -a_N \\ 1 & 0 & 0 & \dots & 0 \\ 0 & 1 & 0 & \dots & 0 \\ \vdots & \ddots & \ddots & \ddots & \vdots \\ 0 & 0 & \dots & 1 & 0 \end{pmatrix}}_M \underbrace{\begin{pmatrix} x_{n-1} \\ x_{n-2} \\ \vdots \\ x_{n-N+1} \\ x_{n-N} \end{pmatrix}}_{\mathbf{x}^{(n-1)}} = M \mathbf{x}^{(n-1)} \quad (\text{B.12})$$

Hence, any vector $\mathbf{x}^{(n)}$ can be obtained from the previous one by multiplication with the Matrix M . Since M is independent of n we find for $k \geq 1$

$$\mathbf{x}^{(N+k)} = M^k \mathbf{x}^{(N)}, \quad (\text{B.13})$$

where $\mathbf{x}^{(N)}$ contains the first N data points as obtained from the simulation. Any predicted data point is given by the first element of the corresponding vector (see Eq. (B.11)), i.e

$$x_{N+k} = [\mathbf{x}^{(N+k)}]_1 = [M^k \mathbf{x}^{(N)}]_1. \quad (\text{B.14})$$

It is clear that any eigenvalue of M larger than one will lead to a diverging prediction, which needs to be taken care of. While alternative schemes are possible, we simply eliminate any eigenvalue larger than one, which has proven to work well.

B.3.1. Example: Symmetric Anderson impurity model

Let us discuss an example to show give some idea of what linear prediction can do. We consider the symmetric Anderson impurity model with semi-circular hybridization, see Section 3.4, with $\Gamma = 0.5W$. The impurity Hamiltonian is defined through the energy level $\varepsilon_d = -W$ and Coulomb interaction $U = 2W = 4\Gamma$, which is a popular choice in the context of DMFT impurity solvers [39]. We choose to work at zero temperature, and calculate the initial state via DMRG ground state search. The retarded Green's function, defined in Section 5.1, is computed up to time $t = 25\hbar/W$, and additional data points up to time $t = 100\hbar/W$ are obtained from linear prediction. Results for the Greens function and the corresponding spectral function are shown in Fig. B.4. At the final simulation time $t = 25\hbar/W$ the Greens function is clearly different from zero. Hence, the spectral function does show unphysical oscillations. Employing linear prediction, the oscillations disappear in the spectral function, with additional adjustments of the height of the side peaks, significantly improving the spectral functions quality.

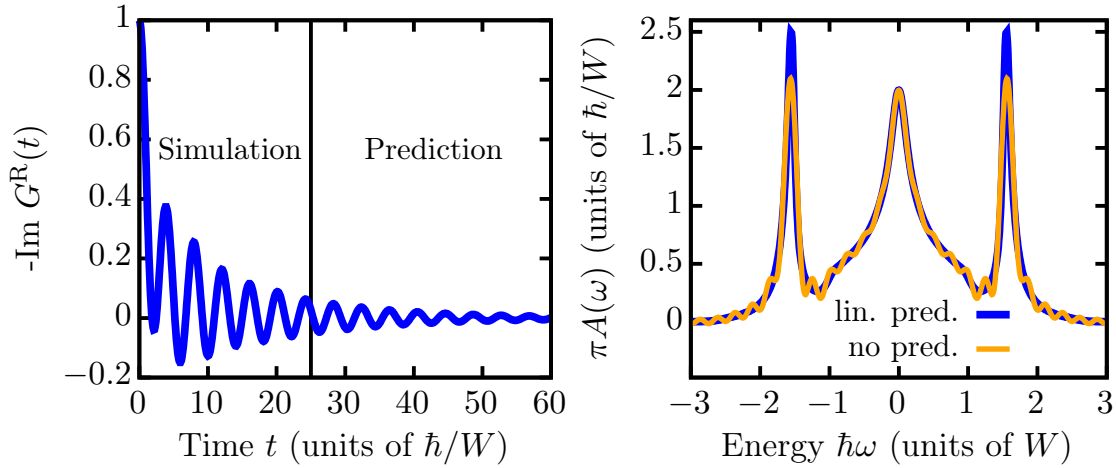


Figure B.4.: Linear prediction example: a) Retarded Green's function of the symmetric SIAM with hybridization coupling $\Gamma = 0.5W$, impurity energy level $\varepsilon_d = -W$ and interaction $U = -2\varepsilon_d = 4\Gamma$. Time evolution is carried out up to $t = 25\hbar/W$, while additional data points are obtained from linear prediction. b) Spectral function with and without linear prediction. Unphysical oscillations are removed and peak heights are adjusted when employing linear prediction.

C. Additional details for Chapter 7

C.1. Proof that the Gibbs state is represented by the thermofield vacuum

We have previously seen that the thermofield vacuum $|\emptyset\rangle$ indeed provides the correct boson occupation for the physical bath, $\langle\emptyset|\hat{b}_{1k}^\dagger\hat{b}_{1k}|\emptyset\rangle = f_B(\epsilon_k)$. Let us now prove directly that the reduced density matrix of the physical bath in the thermofield vacuum $|\emptyset\rangle$ is the Gibbs state, which, to the best of our knowledge, has not been presented explicitly in literature so far. The proof is done in two steps:

(i) Let us define the maximally entangled state (not normalized) $|I\rangle = \sum_l |l\rangle|l\rangle$ on the extended Hilbert space, with $|l\rangle|l\rangle = |l\rangle_S \otimes |l\rangle_{\text{anc}}$ being the product of eigenstates $|l\rangle_S$ and $|l\rangle_{\text{anc}}$ of bath Hamiltonians $\sum_k \epsilon_k \hat{b}_{1k}^\dagger \hat{b}_{1k}$ and $\sum_k \epsilon_k \hat{b}_{2k}^\dagger \hat{b}_{2k}$, respectively. Consider now the state $|\phi\rangle = \mathcal{N} e^{-\beta \hat{H}_S/2} |I\rangle$, with $\hat{H}_S = \sum_k \epsilon_k \hat{b}_{1k}^\dagger \hat{b}_{1k}$ being the *physical* bath Hamiltonian. The reduced density matrix of the physical bosons – obtained when tracing over the ancillary ones – equals the thermal state $\text{Tr}_{\text{anc}} |\phi\rangle\langle\phi| = |\mathcal{N}|^2 e^{-\beta \hat{H}_S}$, since the exponential does not act on the ancillary bath and $\text{Tr}_{\text{anc}} |I\rangle\langle I| = \mathbb{1}_S$.

(ii) It remains to show that $|\phi\rangle$ is the vacuum state in the transformed basis. The vacuum state $|\emptyset\rangle$ is uniquely defined through the property $\hat{c}_{1k}|\emptyset\rangle = 0$ and $\hat{c}_{2k}|\emptyset\rangle = 0$. Hence, we show below that $\hat{c}_{1k}|\phi\rangle = 0$. The proof for \hat{c}_{2k} is omitted but can be done similarly. For the sake of brevity we drop the normalization constant \mathcal{N} from here on. We start by rewriting the annihilation operator (see Eq. (7.10)) and apply the exponential on the states $|l\rangle|l\rangle$:

$$\begin{aligned} \hat{c}_{1k} e^{-\beta \hat{H}_S/2} |I\rangle &= \cosh \Theta_k \hat{b}_{1k} e^{-\beta \hat{H}_S/2} \sum_l |l\rangle|l\rangle - \sinh \Theta_k \hat{b}_{2k}^\dagger e^{-\beta \hat{H}_S/2} \sum_l |l\rangle|l\rangle \\ &= \cosh \Theta_k \hat{b}_{1k} \sum_l |l\rangle|l\rangle e^{-\beta E_l/2} - \sinh \Theta_k \hat{b}_{2k}^\dagger \sum_l |l\rangle|l\rangle e^{-\beta E_l/2}. \end{aligned}$$

The eigenstates $|l\rangle$ of the free boson Hamiltonians can be characterized through the particle occupations of the different modes, $|l\rangle = |n_{l1}, n_{l2}, n_{l3}, \dots\rangle$, where n_{lk} is the number of bosons in mode k of eigenstate l . In this notation the application of \hat{b}_{1k} and \hat{b}_{2k}^\dagger on $|l\rangle|l\rangle$ yields $\hat{b}_{1k}|l\rangle|l\rangle = \sqrt{n_{lk}} |n_{l1}, \dots, n_{lk} - 1, \dots\rangle|l\rangle$ and $\hat{b}_{2k}^\dagger|l\rangle|l\rangle = \sqrt{n_{lk} + 1} |l\rangle|n_{l1}, \dots, n_{lk} + 1, \dots\rangle$,

and hence:

$$\begin{aligned} \hat{c}_{1k} e^{-\beta \hat{H}_S/2} |I\rangle &= \cosh \Theta_k \sum_l \sqrt{n_{lk}} |n_{l1}, \dots, n_{lk} - 1, \dots\rangle |l\rangle e^{-\beta E_l/2} \\ &\quad - \sinh \Theta_k \sum_l \sqrt{n_{lk} + 1} |l\rangle |n_{l1}, \dots, n_{lk} + 1, \dots\rangle e^{-\beta E_l/2}. \end{aligned}$$

We carry out an index shift $l \rightarrow l'$ in the second term such that eigenstate $|l'\rangle$ has one boson more in mode k than $|l\rangle$, $n_{l'k} = n_{lk} + 1$. We find

$$\begin{aligned} \hat{c}_{1k} e^{-\beta \hat{H}_S/2} |I\rangle &= \cosh \Theta_k \sum_l \sqrt{n_{lk}} |n_{l1}, \dots, n_{lk} - 1, \dots\rangle |l\rangle e^{-\beta E_l/2} \\ &\quad - \sinh \Theta_k \sum_{l'} \sqrt{n_{l'k}} |n_{l'1}, \dots, n_{l'k} - 1, \dots\rangle |l'\rangle e^{-\beta(E_{l'} - \epsilon_k)/2} \\ &= 0, \end{aligned}$$

which completes the proof. Notice that for the last step we used the identity $\cosh \Theta_k = \sinh \Theta_k e^{\beta \epsilon_k/2}$ as obtained from the definition of the transformation Eq. (7.13).

C.2. Bloch vector and Schmidt decomposition

The entanglement entropy is defined through the Schmidt values of the corresponding bipartition. In this section we show that the length of the Bloch vector — a measurement for the pureness of a two-level system — depends only on the Schmidt values as well. To this end, let us evaluate the expectation value of the Pauli matrices using the Schmidt decomposition of the state given in Eq. (7.31). We find that

$$\langle \psi | \hat{\sigma}_\alpha | \psi \rangle = \lambda_1^2 \langle \phi_1^S | \hat{\sigma}_\alpha | \phi_1^S \rangle + \lambda_2^2 \langle \phi_2^S | \hat{\sigma}_\alpha | \phi_2^S \rangle$$

where we have used the orthonormality of bath states, $\langle \phi_1^B | \phi_2^V \rangle = 0$, and $\alpha \in \{x, y, z\}$. Since $|\phi_1^S\rangle$ and $|\phi_2^S\rangle$ are orthogonal, the expectation values differ in sign, $\langle \phi_2^S | \hat{\sigma}_\alpha | \phi_2^S \rangle = -\langle \phi_1^S | \hat{\sigma}_\alpha | \phi_1^S \rangle$, and hence

$$\langle \psi | \hat{\sigma}_\alpha | \psi \rangle = (\lambda_1^2 - \lambda_2^2) \langle \phi_1^S | \hat{\sigma}_\alpha | \phi_1^S \rangle.$$

We can then write the length of the Bloch vector as a function of the Schmidt coefficients

$$R^2 = \sum_\alpha \langle \psi | \hat{\sigma}_\alpha | \psi \rangle^2 = (\lambda_1^2 - \lambda_2^2)^2 \sum_\alpha \langle \phi_1^S | \hat{\sigma}_\alpha | \phi_1^S \rangle^2 \quad (\text{C.1})$$

$$= (\lambda_1^2 - \lambda_2^2)^2, \quad (\text{C.2})$$

which explains the similarity between the entanglement entropy and R .

C.3. Numerical details and parameters

Working with bosonic sites requires the truncation of the maximum boson occupation. The local dimension has major impact on the simulation efficiency, and hence it should be chosen as small as possible, but large enough to keep the relevant states. Since the TLS is coupled only to the first chain site and the bosons travel at finite speed along the chain, we choose larger maximum occupations for sites close to the TLS. In particular, for a chain with L bosonic sites we choose for $n = 0, \dots, L - 1$

$$d(n) = d_{\max} - \text{round} \left(\frac{(d_{\max} - d_{\min})n}{L - 1} \right),$$

with local dimension $d(0) = d_{\max}$ at the first chain site and local dimension $d(L - 1) = d_{\min}$ at the end of the chain. Notice that in cases where large local dimensions are necessary for an accurate simulation, numerical efficiency can be increased by using randomized SVDs in 2-site TDVP and TEBD algorithms [179, 180]. Those randomized SVDs only compute the largest singular values and corresponding singular vectors, and are more efficient than a full SVD whenever a small fraction of the singular values is retained. In 2-site TDVP and also TEBD, the SVD is carried out on a two-tensor block with dimension $dD \times dD$, with local dimension d and bond dimension D . Hence, the matrix to decompose has a total of dD singular values, while only D of them are kept, the fraction of kept singular values therefore being $1/d$. The randomized SVD algorithms typically show beneficial over a full SVD for $d \gtrsim 10$ [180].

In our simulations, we compute the dynamics of the MPS using the 2-site version of the time-dependent variational principle (TDVP) [115–117], which allows to increase the bond dimension on the fly. We employ a maximum bond dimension of only $D = 10$, where results are already converged, a time step $\Delta t = 0.005\hbar/\Delta$, and local dimensions of typically $d_{\max} = 6$ and $d_{\min} = 4$.

Bibliography

- [1] L. Kohn and G. E. Santoro, *Efficient mapping for Anderson impurity problems with matrix product states*, *Phys. Rev. B* **104**, 014303 (2021).
- [2] L. Kohn and G. E. Santoro, *Quenching the Anderson impurity model at finite temperature: Entanglement and bath dynamics using matrix product states*, (2021), [arXiv:2107.02807](https://arxiv.org/abs/2107.02807) .
- [3] L. Kohn, P. Silvi, M. Gerster, M. Keck, R. Fazio, G. E. Santoro, and S. Montangero, *Superfluid-to-mott transition in a Bose-Hubbard ring: Persistent currents and defect formation*, *Phys. Rev. A* **101**, 023617 (2020).
- [4] L. Arceci, L. Kohn, A. Russomanno, and G. E. Santoro, *Dissipation assisted Thouless pumping in the Rice–Mele model*, *Journal of Statistical Mechanics: Theory and Experiment* **2020**, 043101 (2020).
- [5] M. Greiner, O. Mandel, T. Esslinger, T. W. Hänsch, and I. Bloch, *Quantum phase transition from a superfluid to a Mott insulator in a gas of ultracold atoms*, *Nature* **415**, 39 (2002).
- [6] S. Trotzky, Y.-A. Chen, A. Flesch, I. P. McCulloch, U. Schollwöck, J. Eisert, and I. Bloch, *Probing the relaxation towards equilibrium in an isolated strongly correlated one-dimensional Bose gas*, *Nature Physics* **8**, 325 (2012).
- [7] L. Magazzù, P. Forn-Díaz, R. Belyansky, J.-L. Orgiazzi, M. A. Yurtalan, M. R. Otto, A. Lupascu, C. M. Wilson, and M. Grifoni, *Probing the strongly driven spin-boson model in a superconducting quantum circuit*, *Nature Communications* **9**, 1403 (2018).
- [8] F. Becca and S. Sorella, *Quantum Monte Carlo approaches for correlated systems* (Cambridge University Press, 2017).
- [9] R. Bulla, T. A. Costi, and T. Pruschke, *Numerical renormalization group method for quantum impurity systems*, *Rev. Mod. Phys.* **80**, 395 (2008).
- [10] A. Georges, G. Kotliar, W. Krauth, and M. Rozenberg, *Dynamical mean-field theory of strongly correlated fermion systems and the limit of infinite dimensions*, *Rev. Mod. Phys.* **68**, 13 (1996).

- [11] G. Carleo and M. Troyer, *Solving the quantum many-body problem with artificial neural networks*, *Science* **355**, 602 (2017).
- [12] S. R. White, *Density matrix formulation for quantum renormalization groups*, *Phys. Rev. Lett.* **69**, 2863 (1992).
- [13] S. R. White, *Density-matrix algorithms for quantum renormalization groups*, *Phys. Rev. B* **48**, 10345 (1993).
- [14] U. Schollwöck, *The density-matrix renormalization group*, *Rev. Mod. Phys.* **77**, 259 (2005).
- [15] I. Oseledets, *Tensor-train decomposition*, *SIAM Journal on Scientific Computing* **33**, 2295 (2011).
- [16] D. Perez-Garcia, F. Verstraete, M. M. Wolf, and J. I. Cirac, *Matrix product state representations*, *Quantum Information and Computation* **7**, 401 (2007), [arXiv:quant-ph/0608197](#) .
- [17] U. Schollwöck, *The density-matrix renormalization group in the age of matrix product states*, *Annals of Physics* **326**, 96 (2011).
- [18] S. Montangero, *Introduction to Tensor Network Methods* (Springer International Publishing, 2018).
- [19] R. Orús, *Tensor networks for complex quantum systems*, *Nature Reviews Physics* **1**, 538 (2019).
- [20] F. Verstraete and J. I. Cirac, *Renormalization algorithms for quantum-many body systems in two and higher dimensions*, (2004), [arXiv:cond-mat/0407066](#) .
- [21] F. Verstraete, M. M. Wolf, D. Perez-Garcia, and J. I. Cirac, *Criticality, the area law, and the computational power of projected entangled pair states*, *Phys. Rev. Lett.* **96**, 220601 (2006).
- [22] J. Jordan, R. Orús, G. Vidal, F. Verstraete, and J. I. Cirac, *Classical simulation of infinite-size quantum lattice systems in two spatial dimensions*, *Phys. Rev. Lett.* **101**, 250602 (2008).
- [23] R. Orús, *A practical introduction to tensor networks: Matrix product states and projected entangled pair states*, *Annals of Physics* **349**, 117 (2014).
- [24] Y.-Y. Shi, L.-M. Duan, and G. Vidal, *Classical simulation of quantum many-body systems with a tree tensor network*, *Phys. Rev. A* **74**, 022320 (2006).
- [25] M. Gerster, P. Silvi, M. Rizzi, R. Fazio, T. Calarco, and S. Montangero, *Unconstrained tree tensor network: An adaptive gauge picture for enhanced performance*, *Phys. Rev. B* **90**, 125154 (2014).

-
- [26] L. Tagliacozzo, G. Evenbly, and G. Vidal, *Simulation of two-dimensional quantum systems using a tree tensor network that exploits the entropic area law*, *Phys. Rev. B* **80**, 235127 (2009).
- [27] M. Gerster, M. Rizzi, P. Silvi, M. Dalmonte, and S. Montangero, *Fractional quantum Hall effect in the interacting Hofstadter model via tensor networks*, *Phys. Rev. B* **96**, 195123 (2017).
- [28] G. Vidal, *Entanglement renormalization*, *Phys. Rev. Lett.* **99**, 220405 (2007).
- [29] F. Verstraete, J. J. García-Ripoll, and J. I. Cirac, *Matrix product density operators: Simulation of finite-temperature and dissipative systems*, *Phys. Rev. Lett.* **93**, 207204 (2004).
- [30] M. Zwolak and G. Vidal, *Mixed-state dynamics in one-dimensional quantum lattice systems: A time-dependent superoperator renormalization algorithm*, *Phys. Rev. Lett.* **93**, 207205 (2004).
- [31] A. H. Werner, D. Jaschke, P. Silvi, M. Kliesch, T. Calarco, J. Eisert, and S. Montangero, *Positive tensor network approach for simulating open quantum many-body systems*, *Phys. Rev. Lett.* **116**, 237201 (2016).
- [32] S. Sachdev, *Quantum phase transitions* (Cambridge university press, 2011).
- [33] C. Kollath, A. M. Läuchli, and E. Altman, *Quench dynamics and nonequilibrium phase diagram of the Bose-Hubbard model*, *Phys. Rev. Lett.* **98**, 180601 (2007).
- [34] F. A. Wolf, A. Go, I. P. McCulloch, A. J. Millis, and U. Schollwöck, *Imaginary-time matrix product state impurity solver for dynamical mean-field theory*, *Phys. Rev. X* **5**, 041032 (2015).
- [35] N.-O. Linden, M. Zingl, C. Hubig, O. Parcollet, and U. Schollwöck, *Imaginary-time matrix product state impurity solver in a real material calculation: Spin-orbit coupling in Sr_2RuO_4* , *Phys. Rev. B* **101**, 041101(R) (2020).
- [36] D. J. García, K. Hallberg, and M. J. Rozenberg, *Dynamical mean field theory with the density matrix renormalization group*, *Phys. Rev. Lett.* **93**, 246403 (2004).
- [37] F. A. Wolf, I. P. McCulloch, O. Parcollet, and U. Schollwöck, *Chebyshev matrix product state impurity solver for dynamical mean-field theory*, *Phys. Rev. B* **90**, 115124 (2014).
- [38] M. Ganahl, M. Aichhorn, H. G. Evertz, P. Thunström, K. Held, and F. Verstraete, *Efficient DMFT impurity solver using real-time dynamics with matrix product states*, *Phys. Rev. B* **92**, 155132 (2015).
- [39] F. A. Wolf, I. P. McCulloch, and U. Schollwöck, *Solving nonequilibrium dynamical mean-field theory using matrix product states*, *Phys. Rev. B* **90**, 235131 (2014).

- [40] D. Bauernfeind, M. Zingl, R. Triebl, M. Aichhorn, and H. G. Evertz, *Fork tensor-product states: Efficient multiorbital real-time DMFT solver*, **Phys. Rev. X** **7**, 031013 (2017).
- [41] A. W. Chin, J. Prior, R. Rosenbach, F. Caycedo-Soler, S. F. Huelga, and M. B. Plenio, *The role of non-equilibrium vibrational structures in electronic coherence and recoherence in pigment–protein complexes*, **Nature Physics** **9**, 113 (2013).
- [42] S. Szalay, M. Pfeffer, V. Murg, G. Barcza, F. Verstraete, R. Schneider, and Ö. Legeza, *Tensor product methods and entanglement optimization for ab initio quantum chemistry*, **International Journal of Quantum Chemistry** **115**, 1342 (2015).
- [43] E. M. Stoudenmire and D. J. Schwab, *Supervised learning with tensor networks*, in *Advances in Neural Information Processing Systems*, Vol. 29, edited by D. Lee, M. Sugiyama, U. Luxburg, I. Guyon, and R. Garnett (Curran Associates, Inc., 2016).
- [44] E. M. Stoudenmire, *Learning relevant features of data with multi-scale tensor networks*, **Quantum Science and Technology** **3**, 034003 (2018).
- [45] T. Felser, M. Trenti, L. Sestini, A. Gianelle, D. Zuliani, D. Lucchesi, and S. Montangero, *Quantum-inspired machine learning on high-energy physics data*, **npj Quantum Information** **7**, 111 (2021).
- [46] S. Cavinato, T. Felser, M. Fusella, M. Paiusco, and S. Montangero, *Optimizing radiotherapy plans for cancer treatment with tensor networks*, **Physics in Medicine & Biology** **66**, 125015 (2021).
- [47] G. Vidal, *Efficient simulation of one-dimensional quantum many-body systems*, **Phys. Rev. Lett.** **93**, 040502 (2004).
- [48] A. J. Daley, C. Kollath, U. Schollwöck, and G. Vidal, *Time-dependent density-matrix renormalization-group using adaptive effective hilbert spaces*, **Journal of Statistical Mechanics: Theory and Experiment** **2004**, P04005 (2004).
- [49] S. R. White and A. E. Feiguin, *Real-time evolution using the density matrix renormalization group*, **Phys. Rev. Lett.** **93**, 076401 (2004).
- [50] S. Paeckel, T. Köhler, A. Swoboda, S. R. Manmana, U. Schollwöck, and C. Hubig, *Time-evolution methods for matrix-product states*, **Annals of Physics** **411**, 167998 (2019).
- [51] J. Preskill, *Lecture notes on Quantum Computation*, (2015), available on the web.
- [52] J. Eisert, M. Cramer, and M. B. Plenio, *Colloquium: Area laws for the entanglement entropy*, **Rev. Mod. Phys.** **82**, 277 (2010).

-
- [53] M. M. Rams and M. Zwolak, *Breaking the entanglement barrier: Tensor network simulation of quantum transport*, *Phys. Rev. Lett.* **124**, 137701 (2020).
- [54] A. W. Chin, Á. Rivas, S. F. Huelga, and M. B. Plenio, *Exact mapping between system-reservoir quantum models and semi-infinite discrete chains using orthogonal polynomials*, *Journal of Mathematical Physics* **51**, 092109 (2010).
- [55] J. Prior, A. W. Chin, S. F. Huelga, and M. B. Plenio, *Efficient simulation of strong system-environment interactions*, *Physical review letters* **105**, 050404 (2010).
- [56] J. Kondo, *Resistance minimum in dilute magnetic alloys*, *Progress of theoretical physics* **32**, 37 (1964).
- [57] A. C. Hewson, *The Kondo problem to heavy fermions* (Cambridge University Press, 1997).
- [58] P. W. Anderson, *Localized magnetic states in metals*, *Phys. Rev.* **124**, 41 (1961).
- [59] W. G. van der Wiel, S. D. Franceschi, T. Fujisawa, J. M. Elzerman, S. Tarucha, and L. P. Kouwenhoven, *The Kondo effect in the unitary limit*, *Science* **289**, 2105 (2000).
- [60] S. Sasaki, S. De Franceschi, J. M. Elzerman, W. G. van der Wiel, M. Eto, S. Tarucha, and L. P. Kouwenhoven, *Kondo effect in an integer-spin quantum dot*, *Nature* **405**, 764 (2000).
- [61] S. M. Reimann and M. Manninen, *Electronic structure of quantum dots*, *Rev. Mod. Phys.* **74**, 1283 (2002).
- [62] M. Braun, J. König, and J. Martinek, *Theory of transport through quantum-dot spin valves in the weak-coupling regime*, *Phys. Rev. B* **70**, 195345 (2004).
- [63] F. Schwarz, I. Weymann, J. von Delft, and A. Weichselbaum, *Nonequilibrium steady-state transport in quantum impurity models: A thermofield and quantum quench approach using matrix product states*, *Phys. Rev. Lett.* **121**, 137702 (2018).
- [64] T. Kato, *On the adiabatic theorem of quantum mechanics*, *Journal of the Physical Society of Japan* **5**, 435 (1950).
- [65] Y. Takahashi and H. Umezawa, *Thermo field dynamics*, *Collective Phenomena* **2**, 55 (1975).
- [66] I. de Vega and M.-C. Bañuls, *Thermofield-based chain-mapping approach for open quantum systems*, *Phys. Rev. A* **92**, 052116 (2015).
- [67] Y. Lu, M. Höppner, O. Gunnarsson, and M. W. Haverkort, *Efficient real-frequency solver for dynamical mean-field theory*, *Phys. Rev. B* **90**, 085102 (2014).

- [68] E. Gull, A. J. Millis, A. I. Lichtenstein, A. N. Rubtsov, M. Troyer, and P. Werner, *Continuous-time Monte Carlo methods for quantum impurity models*, *Rev. Mod. Phys.* **83**, 349 (2011).
- [69] A. N. Rubtsov, V. V. Savkin, and A. I. Lichtenstein, *Continuous-time quantum Monte Carlo method for fermions*, *Phys. Rev. B* **72**, 035122 (2005).
- [70] P. Werner, A. Comanac, L. de' Medici, M. Troyer, and A. J. Millis, *Continuous-time solver for quantum impurity models*, *Phys. Rev. Lett.* **97**, 076405 (2006).
- [71] R. Bulla, *Zero temperature metal-insulator transition in the infinite-dimensional Hubbard model*, *Phys. Rev. Lett.* **83**, 136 (1999).
- [72] R. Zitko and T. Pruschke, *Energy resolution and discretization artifacts in the numerical renormalization group*, *Phys. Rev. B* **79**, 085106 (2009).
- [73] X. Deng, J. Mravlje, R. Zitko, M. Ferrero, G. Kotliar, and A. Georges, *How bad metals turn good: Spectroscopic signatures of resilient quasiparticles*, *Phys. Rev. Lett.* **110**, 086401 (2013).
- [74] F. B. Anders, *A numerical renormalization group approach to non-equilibrium Green functions for quantum impurity models*, *Journal of Physics: Condensed Matter* **20**, 195216 (2008).
- [75] A. K. Mitchell, M. R. Galpin, S. Wilson-Fletcher, D. E. Logan, and R. Bulla, *Generalized Wilson chain for solving multichannel quantum impurity problems*, *Phys. Rev. B* **89**, 121105(R) (2014).
- [76] K. M. Stadler, Z. P. Yin, J. von Delft, G. Kotliar, and A. Weichselbaum, *Dynamical mean-field theory plus numerical renormalization-group study of spin-orbital separation in a three-band Hund metal*, *Phys. Rev. Lett.* **115**, 136401 (2015).
- [77] A. Horvat, R. Zitko, and J. Mravlje, *Low-energy physics of three-orbital impurity model with Kanamori interaction*, *Phys. Rev. B* **94**, 165140 (2016).
- [78] F. B. Kugler, M. Zingl, H. U. R. Strand, S.-S. B. Lee, J. von Delft, and A. Georges, *Strongly correlated materials from a numerical renormalization group perspective: How the Fermi-liquid state of Sr_2RuO_4 emerges*, *Phys. Rev. Lett.* **124**, 016401 (2020).
- [79] M. Srednicki, *Chaos and quantum thermalization*, *Phys. Rev. E* **50**, 888 (1994).
- [80] E. Canovi, D. Rossini, R. Fazio, G. E. Santoro, and A. Silva, *Quantum quenches, thermalization, and many-body localization*, *Phys. Rev. B* **83**, 094431 (2011).
- [81] J. Eisert, M. Friesdorf, and C. Gogolin, *Quantum many-body systems out of equilibrium*, *Nature Physics* **11**, 124 (2015).

-
- [82] R. Nandkishore and D. A. Huse, *Many-body localization and thermalization in quantum statistical mechanics*, *Annual Review of Condensed Matter Physics* **6**, 15 (2015).
- [83] L. D'Alessio, Y. Kafri, A. Polkovnikov, and M. Rigol, *From quantum chaos and eigenstate thermalization to statistical mechanics and thermodynamics*, *Advances in Physics* **65**, 239 (2016).
- [84] H.-P. Breuer and F. Petruccione, *The theory of open quantum systems* (Oxford University Press on Demand, 2002).
- [85] A. Rivas and S. F. Huelga, *Open quantum systems*, Vol. 10 (Springer, 2012).
- [86] U. Weiss, *Quantum dissipative systems*, Vol. 13 (World scientific, 2012).
- [87] S. Lloyd, *Universal quantum simulators*, *Science* **273**, 1073 (1996).
- [88] L. Arceci, S. Barbarino, R. Fazio, and G. E. Santoro, *Dissipative Landau-Zener problem and thermally assisted quantum annealing*, *Phys. Rev. B* **96**, 054301 (2017).
- [89] G. M. Palma, K.-A. Suominen, and A. Ekert, *Quantum computers and dissipation*, *Proceedings of the Royal Society of London. Series A: Mathematical, Physical and Engineering Sciences* **452**, 567 (1996).
- [90] D. P. DiVincenzo and D. Loss, *Quantum computers and quantum coherence*, *Journal of Magnetism and Magnetic Materials* **200**, 202 (1999).
- [91] I. M. Georgescu, S. Ashhab, and F. Nori, *Quantum simulation*, *Rev. Mod. Phys.* **86**, 153 (2014).
- [92] A. Caldeira and A. Leggett, *Quantum tunnelling in a dissipative system*, *Annals of Physics* **149**, 374 (1983).
- [93] A. J. Leggett, S. Chakravarty, A. T. Dorsey, M. P. A. Fisher, A. Garg, and W. Zwerger, *Dynamics of the dissipative two-state system*, *Rev. Mod. Phys.* **59**, 1 (1987).
- [94] A. Shnirman, Y. Makhlin, and G. Schön, *Noise and decoherence in quantum two-level systems*, *Physica Scripta* **T102**, 147 (2002).
- [95] V. Gorini, A. Kossakowski, and E. C. G. Sudarshan, *Completely positive dynamical semigroups of n -level systems*, *Journal of Mathematical Physics* **17**, 821 (1976).
- [96] G. Lindblad, *On the generators of quantum dynamical semigroups*, *Communications in Mathematical Physics* **48**, 119 (1976).

- [97] H.-P. Breuer, E.-M. Laine, J. Piilo, and B. Vacchini, *Colloquium: Non-Markovian dynamics in open quantum systems*, *Rev. Mod. Phys.* **88**, 021002 (2016).
- [98] D. Newman, F. Mintert, and A. Nazir, *Performance of a quantum heat engine at strong reservoir coupling*, *Phys. Rev. E* **95**, 032139 (2017).
- [99] S. Deffner and S. Campbell, *Quantum Thermodynamics*, 2053-2571 (Morgan & Claypool Publishers, 2019).
- [100] G. S. Engel, T. R. Calhoun, E. L. Read, T.-K. Ahn, T. Manvcal, Y.-C. Cheng, R. E. Blankenship, and G. R. Fleming, *Evidence for wavelike energy transfer through quantum coherence in photosynthetic systems*, *Nature* **446**, 782 (2007).
- [101] G. Panitchayangkoon, D. Hayes, K. A. Fransted, J. R. Caram, E. Harel, J. Wen, R. E. Blankenship, and G. S. Engel, *Long-lived quantum coherence in photosynthetic complexes at physiological temperature*, *Proceedings of the National Academy of Sciences* **107**, 12766 (2010).
- [102] P. Forn-Díaz, J. J. García-Ripoll, B. Peropadre, J.-L. Orgiazzi, M. A. Yurtalan, R. Belyansky, C. M. Wilson, and A. Lupascu, *Ultrastrong coupling of a single artificial atom to an electromagnetic continuum in the nonperturbative regime*, *Nature Physics* **13**, 39 (2017).
- [103] I. de Vega and D. Alonso, *Dynamics of non-Markovian open quantum systems*, *Rev. Mod. Phys.* **89**, 015001 (2017).
- [104] Y. Tanimura and R. Kubo, *Time evolution of a quantum system in contact with a nearly Gaussian-Markoffian noise bath*, *Journal of the Physical Society of Japan* **58**, 101 (1989).
- [105] Y. Tanimura, *Nonperturbative expansion method for a quantum system coupled to a harmonic-oscillator bath*, *Phys. Rev. A* **41**, 6676 (1990).
- [106] D. E. Makarov and N. Makri, *Path integrals for dissipative systems by tensor multiplication. condensed phase quantum dynamics for arbitrarily long time*, *Chemical Physics Letters* **221**, 482 (1994).
- [107] N. Makri, *Numerical path integral techniques for long time dynamics of quantum dissipative systems*, *Journal of Mathematical Physics* **36**, 2430 (1995).
- [108] S. Shevchenko, S. Ashhab, and F. Nori, *Landau-Zener-Stückelberg interferometry*, *Physics Reports* **492**, 1 (2010).
- [109] D. Tamascelli, A. Smirne, J. Lim, S. F. Huelga, and M. B. Plenio, *Efficient simulation of finite-temperature open quantum systems*, *Phys. Rev. Lett.* **123**, 090402 (2019).

-
- [110] H. F. Trotter, *On the product of semi-groups of operators*, *Proceedings of the American Mathematical Society* **10**, 545 (1959).
- [111] M. Suzuki, *Generalized Trotter's formula and systematic approximants of exponential operators and inner derivations with applications to many-body problems*, *Communications in Mathematical Physics* **51**, 183 (1976).
- [112] M. P. Zaletel, R. S. K. Mong, C. Karrasch, J. E. Moore, and F. Pollmann, *Time-evolving a matrix product state with long-ranged interactions*, *Phys. Rev. B* **91**, 165112 (2015).
- [113] Y. Saad, *Iterative methods for sparse linear systems* (SIAM, 2003).
- [114] M. Hochbruck and C. Lubich, *On Krylov subspace approximations to the matrix exponential operator*, *SIAM Journal on Numerical Analysis* **34**, 1911 (1997).
- [115] J. Haegeman, J. I. Cirac, T. J. Osborne, I. Pizorn, H. Verschelde, and F. Verstraete, *Time-dependent variational principle for quantum lattices*, *Phys. Rev. Lett.* **107**, 070601 (2011).
- [116] C. Lubich, I. Oseledets, and B. Vandereycken, *Time integration of tensor trains*, *SIAM Journal on Numerical Analysis* **53**, 917 (2015).
- [117] J. Haegeman, C. Lubich, I. Oseledets, B. Vandereycken, and F. Verstraete, *Unifying time evolution and optimization with matrix product states*, *Phys. Rev. B* **94**, 165116 (2016).
- [118] S. R. White, *Density matrix renormalization group algorithms with a single center site*, *Phys. Rev. B* **72**, 180403 (2005).
- [119] C. Hubig, I. P. McCulloch, U. Schollwöck, and F. A. Wolf, *Strictly single-site DMRG algorithm with subspace expansion*, *Phys. Rev. B* **91**, 155115 (2015).
- [120] P. Silvi, F. Tschirsich, M. Gerster, J. Jünemann, D. Jaschke, M. Rizzi, and S. Montangero, *The Tensor Networks Anthology: Simulation techniques for many-body quantum lattice systems*, *SciPost Phys. Lect. Notes* **8** (2019).
- [121] E. R. Davidson, *The iterative calculation of a few of the lowest eigenvalues and corresponding eigenvectors of large real-symmetric matrices*, *Journal of Computational Physics* **17**, 87 (1975).
- [122] D. Bauernfeind and M. Aichhorn, *Time Dependent Variational Principle for Tree Tensor Networks*, *SciPost Phys.* **8**, 24 (2020).
- [123] F. A. Y. N. Schröder and A. W. Chin, *Simulating open quantum dynamics with time-dependent variational matrix product states: Towards microscopic correlation of environment dynamics and reduced system evolution*, *Phys. Rev. B* **93**, 075105 (2016).

- [124] E. Hairer, C. Lubich, and G. Wanner, *Geometric numerical integration: structure-preserving algorithms for ordinary differential equations*, Vol. 31 (Springer Science & Business Media, 2006).
- [125] P. Jordan and E. P. Wigner, *Über das paulische äquivalenzverbot*, *Zeitschrift für Physik* **47**, 631 (1928).
- [126] M. Fishman, S. R. White, and E. M. Stoudenmire, *The ITensor software library for tensor network calculations*, (2020), [arXiv:2007.14822](https://arxiv.org/abs/2007.14822).
- [127] W. Metzner and D. Vollhardt, *Correlated lattice fermions in $d = \infty$ dimensions*, *Phys. Rev. Lett.* **62**, 324 (1989).
- [128] K. G. Wilson, *The renormalization group: Critical phenomena and the Kondo problem*, *Rev. Mod. Phys.* **47**, 773 (1975).
- [129] J. Krones, *Effective Models for the Single Impurity Anderson and Kondo Model from Continuous Unitary Transformations*, *Ph.D. thesis*, Universitätsbibliothek Dortmund (2014).
- [130] R. Bulla, T. Pruschke, and A. C. Hewson, *Anderson impurity in pseudo-gap Fermi systems*, *Journal of Physics: Condensed Matter* **9**, 10463 (1997).
- [131] I. de Vega, U. Schollwöck, and F. A. Wolf, *How to discretize a quantum bath for real-time evolution*, *Phys. Rev. B* **92**, 155126 (2015).
- [132] M. P. Woods, R. Groux, A. W. Chin, S. F. Huelga, and M. B. Plenio, *Mappings of open quantum systems onto chain representations and Markovian embeddings*, *Journal of Mathematical Physics* **55**, 032101 (2014).
- [133] W. Gautschi, *ORTHPOL—a package of routines for generating orthogonal polynomials and Gauss-type quadrature rules*, *ACM Transactions on Mathematical Software (TOMS)* **20**, 21 (1994).
- [134] W. Gautschi, *Orthogonal polynomials: Computation and Approximation* (Oxford University Press, New York, 2004).
- [135] C. Raas, *Dynamic Density-Matrix Renormalization for the Symmetric Single Impurity Anderson Model*, *Ph.D. thesis*, Universität zu Köln (2005).
- [136] A. Nüßeler, I. Dhand, S. F. Huelga, and M. B. Plenio, *Efficient simulation of open quantum systems coupled to a fermionic bath*, *Phys. Rev. B* **101**, 155134 (2020).
- [137] T. Chen, V. Balachandran, C. Guo, and D. Poletti, *Steady-state quantum transport through an anharmonic oscillator strongly coupled to two heat reservoirs*, *Phys. Rev. E* **102**, 012155 (2020).

-
- [138] A. Haller, M. Rizzi, and M. Filippone, *Drude weight increase by orbital and repulsive interactions in fermionic ladders*, *Phys. Rev. Research* **2**, 023058 (2020).
- [139] D. Contessi, D. Romito, M. Rizzi, and A. Recati, *Collisionless drag for a one-dimensional two-component Bose-Hubbard model*, *Phys. Rev. Research* **3**, L022017 (2021).
- [140] Z. He and A. J. Millis, *Entanglement entropy and computational complexity of the Anderson impurity model out of equilibrium: Quench dynamics*, *Phys. Rev. B* **96**, 085107 (2017).
- [141] T. Barthel, U. Schollwöck, and S. R. White, *Spectral functions in one-dimensional quantum systems at finite temperature using the density matrix renormalization group*, *Phys. Rev. B* **79**, 245101 (2009).
- [142] S. R. White and I. Affleck, *Spectral function for the $s = 1$ Heisenberg antiferromagnetic chain*, *Phys. Rev. B* **77**, 134437 (2008).
- [143] B. Horvatic, D. Sokcevic, and V. Zlatic, *Finite-temperature spectral density for the Anderson model*, *Phys. Rev. B* **36**, 675 (1987).
- [144] H. Saberi, A. Weichselbaum, and J. von Delft, *Matrix-product-state comparison of the numerical renormalization group and the variational formulation of the density-matrix renormalization group*, *Phys. Rev. B* **78**, 035124 (2008).
- [145] A. Serafini, *Quantum continuous variables: a primer of theoretical methods* (CRC Press, 2017).
- [146] P. W. Anderson, *Infrared catastrophe in Fermi gases with local scattering potentials*, *Phys. Rev. Lett.* **18**, 1049 (1967).
- [147] H. E. Türeci, M. Hanl, M. Claassen, A. Weichselbaum, T. Hecht, B. Braunecker, A. Govorov, L. Glazman, A. Imamoglu, and J. von Delft, *Many-body dynamics of exciton creation in a quantum dot by optical absorption: A quantum quench towards Kondo correlations*, *Phys. Rev. Lett.* **106**, 107402 (2011).
- [148] A. M. Kaufman, M. E. Tai, A. Lukin, M. Rispoli, R. Schittko, P. M. Preiss, and M. Greiner, *Quantum thermalization through entanglement in an isolated many-body system*, *Science* **353**, 794 (2016).
- [149] B. Gotsmann, C. Seidel, B. Anczykowski, and H. Fuchs, *Conservative and dissipative tip-sample interaction forces probed with dynamic AFM*, *Phys. Rev. B* **60**, 11051 (1999).
- [150] M. Kisiel, E. Gnecco, U. Gysin, L. Marot, S. Rast, and E. Meyer, *Suppression of electronic friction on Nb films in the superconducting state*, *Nature Materials* **10**, 119 (2011).

- [151] M. Langer, M. Kisiel, R. Pawlak, F. Pellegrini, G. E. Santoro, R. Buzio, A. Gerbi, G. Balakrishnan, A. Baratoff, E. Tosatti, and E. Meyer, *Giant frictional dissipation peaks and charge-density-wave slips at the NbSe₂ surface*, *Nature Materials* **13**, 173 (2014).
- [152] M. Kisiel, F. Pellegrini, G. E. Santoro, M. Samadashvili, R. Pawlak, A. Benassi, U. Gysin, R. Buzio, A. Gerbi, E. Meyer, and E. Tosatti, *Noncontact atomic force microscope dissipation reveals a central peak of SrTiO₃ structural phase transition*, *Phys. Rev. Lett.* **115**, 046101 (2015).
- [153] P. P. Baruselli, M. Fabrizio, and E. Tosatti, *Nanomechanical dissipation at a tip-induced Kondo onset*, *Phys. Rev. B* **96**, 075113 (2017).
- [154] P. P. Baruselli and E. Tosatti, *Finite-frequency dissipation in a driven Kondo model*, (2018), [arXiv:1804.04999](https://arxiv.org/abs/1804.04999).
- [155] P. Jacobson, M. Muenks, G. Laskin, O. Brovko, V. Stepanyuk, M. Ternes, and K. Kern, *Potential energy-driven spin manipulation via a controllable hydrogen ligand*, *Science Advances* **3** (2017).
- [156] R. Pawlak, W. Ouyang, A. E. Filippov, L. Kalikhman-Razvozov, S. Kawai, T. Glatzel, E. Gnecco, A. Baratoff, Q. Zheng, O. Hod, M. Urbakh, and E. Meyer, *Single-molecule tribology: Force microscopy manipulation of a Porphyrin derivative on a Copper surface*, *ACS Nano* **10**, 713 (2016).
- [157] *Ultra-sensitive mechanical dissipation in classical, quantum and non-equilibrium nanocontacts*, European Research Council.
- [158] T. A. Costi, *Kondo effect in a magnetic field and the magnetoresistivity of Kondo alloys*, *Phys. Rev. Lett.* **85**, 1504 (2000).
- [159] P. B. Wiegmann and A. M. Tsel'ick, *Exact solution of the Anderson model: I*, *Journal of Physics C: Solid State Physics* **16**, 2281 (1983).
- [160] T. D. Ladd, F. Jelezko, R. Laflamme, Y. Nakamura, C. Monroe, and J. L. O'Brien, *Quantum computers*, *Nature* **464**, 45 (2010).
- [161] C. Zener, *Non-adiabatic crossing of energy levels*, *Proceedings of the Royal Society of London. Series A, Containing Papers of a Mathematical and Physical Character* **137**, 696 (1932).
- [162] Z. Wang, W.-C. Huang, Q.-F. Liang, and X. Hu, *Landau-Zener-Stückelberg interferometry for Majorana qubit*, *Scientific reports* **8**, 1 (2018).
- [163] J. Stehlik, Y. Dovzhenko, J. R. Petta, J. R. Johansson, F. Nori, H. Lu, and A. C. Gossard, *Landau-Zener-Stückelberg interferometry of a single electron charge qubit*, *Phys. Rev. B* **86**, 121303 (2012).

-
- [164] G. D. Fuchs, G. Burkard, P. V. Klimov, and D. D. Awschalom, *A quantum memory intrinsic to single nitrogen–vacancy centres in diamond*, *Nature Physics* **7**, 789 (2011).
- [165] P. Nalbach, J. Knörzer, and S. Ludwig, *Nonequilibrium Landau-Zener-Stückelberg spectroscopy in a double quantum dot*, *Phys. Rev. B* **87**, 165425 (2013).
- [166] M. Keck, S. Montangero, G. E. Santoro, R. Fazio, and D. Rossini, *Dissipation in adiabatic quantum computers: lessons from an exactly solvable model*, *New Journal of Physics* **19**, 113029 (2017).
- [167] L. Arceci, S. Barbarino, D. Rossini, and G. E. Santoro, *Optimal working point in dissipative quantum annealing*, *Phys. Rev. B* **98**, 064307 (2018).
- [168] A. O. Caldeira and A. J. Leggett, *Influence of dissipation on quantum tunneling in macroscopic systems*, *Phys. Rev. Lett.* **46**, 211 (1981).
- [169] T. Zanica, F. Pellegrini, G. E. Santoro, and E. Tosatti, *Frictional lubricity enhanced by quantum mechanics*, *Proceedings of the National Academy of Sciences* **115**, 3547 (2018).
- [170] A. Bylinskii, D. Gangloff, and V. Vuletić, *Tuning friction atom-by-atom in an ion-crystal simulator*, *Science* **348**, 1115 (2015).
- [171] D. Gangloff, A. Bylinskii, I. Counts, W. Jhe, and V. Vuletić, *Velocity tuning of friction with two trapped atoms*, *Nature Physics* **11**, 915 (2015).
- [172] A. Bylinskii, D. Gangloff, I. Counts, and V. Vuletić, *Observation of Aubry-type transition in finite atom chains via friction*, *Nature Materials* **15**, 717 (2016).
- [173] I. Counts, D. Gangloff, A. Bylinskii, J. Hur, R. Islam, and V. Vuletić, *Multislip friction with a single ion*, *Phys. Rev. Lett.* **119**, 043601 (2017).
- [174] A. Benassi, A. Vanossi, and E. Tosatti, *Nanofriction in cold ion traps*, *Nature Communications* **2**, 236 (2011).
- [175] D. Mandelli, A. Vanossi, and E. Tosatti, *Stick-slip nanofriction in trapped cold ion chains*, *Phys. Rev. B* **87**, 195418 (2013).
- [176] J. Cui, J. I. Cirac, and M. C. Bañuls, *Variational matrix product operators for the steady state of dissipative quantum systems*, *Phys. Rev. Lett.* **114**, 220601 (2015).
- [177] S. Singh, R. N. C. Pfeifer, and G. Vidal, *Tensor network decompositions in the presence of a global symmetry*, *Phys. Rev. A* **82**, 050301(R) (2010).
- [178] S. Singh, R. N. C. Pfeifer, and G. Vidal, *Tensor network states and algorithms in the presence of a global $U(1)$ symmetry*, *Phys. Rev. B* **83**, 115125 (2011).

- [179] D. Tamascelli, R. Rosenbach, and M. B. Plenio, *Improved scaling of time-evolving block-decimation algorithm through reduced-rank randomized singular value decomposition*, *Phys. Rev. E* **91**, 063306 (2015).
- [180] L. Kohn, F. Tschirsich, M. Keck, M. B. Plenio, D. Tamascelli, and S. Montangero, *Probabilistic low-rank factorization accelerates tensor network simulations of critical quantum many-body ground states*, *Phys. Rev. E* **97**, 013301 (2018).